

Utah State University

DigitalCommons@USU

All Graduate Theses and Dissertations

Graduate Studies

5-2015

In Vitro, Non-Invasive Imaging and Detection of Single Living Mammalian Cells Interacting with Bio-Nano-Interfaces

Qifei Li

Utah State University

Follow this and additional works at: <https://digitalcommons.usu.edu/etd>



Part of the [Biological Engineering Commons](#)

Recommended Citation

Li, Qifei, "In Vitro, Non-Invasive Imaging and Detection of Single Living Mammalian Cells Interacting with Bio-Nano-Interfaces" (2015). *All Graduate Theses and Dissertations*. 4520.

<https://digitalcommons.usu.edu/etd/4520>

This Dissertation is brought to you for free and open access by the Graduate Studies at DigitalCommons@USU. It has been accepted for inclusion in All Graduate Theses and Dissertations by an authorized administrator of DigitalCommons@USU. For more information, please contact digitalcommons@usu.edu.



IN VITRO, NON-INVASIVE IMAGING AND DETECTION OF SINGLE LIVING
MAMMALIAN CELLS INTERACTING WITH BIO-NANO-INTERFACES

by

Qifei Li

A dissertation submitted in partial fulfillment
of the requirements for the degree

of

DOCTOR OF PHILOSOPHY

in

Biological Engineering

Approved:

Anhong Zhou
Major Professor

S. Clay Isom
Committee Member

Xiaojun Qi
Committee Member

Charles D. Miller
Committee Member

Randy Lewis
Committee Member

Mark R. McLellan
Vice President for Research and
Dean of the School of Graduate Studies

UTAH STATE UNIVERSITY
Logan, Utah

2015

Copyright © Qifei Li 2015

All Rights Reserved

ABSTRACT

In vitro, Non-invasive Imaging and Detection of Single Living Mammalian Cells

Interacting with Bio-nano-interfaces

by

Qifei Li, Doctor of Philosophy

Utah State University, 2015

Major Professor: Dr. Anhong Zhou
Department: Biological Engineering

Understanding of bio-nano-interfaces of living mammalian cells will benefit the identification of cellular alterations (e.g. nucleic acids, amino acids, biomechanics, etc.) due to external stimuli, the design of biomaterials (e.g. nanoparticles, nanotubes) and the investigation of the interaction between cells and bio-nano-interfaces (e.g. cell differentiation on 3D nanostructured materials). Analytical techniques can be applied to evaluate the chemical, physical, and mechanical properties of mammalian cells when exposed to such bio-nano-interfaces. In this study, non-invasive advanced spectroscopy techniques including atomic force microscopy (AFM) and Raman microscopy (RM), in conjunction with traditional biological methods are utilized to elucidate specific characteristic information for biological samples and how these property changes reflect the interaction with external stimuli.

The focus of this dissertation is on the biophysical, biochemical and cytotoxic detection of mammalian cells interacting with bio-nano-interfaces, and this dissertation can be classified into three topics: biomechanics/cellular biopolymers measurement, bio-interfaces and nano-interfaces studies.

For the topic of biomechanics/cellular biopolymers measurement, cellular biophysical and biomechanical properties could be used as differentiation markers to classify cellular differentiation. For the bio-interfaces part, it was observed that BRMS1 expression changed cellular biochemical and biomechanical properties, and the expressions of reactive oxidative species (ROS), apoptosis and cell viability of five types of cells displayed similar patterns over doxorubicin (DOX) incubation time. Secondly, A549 cells were treated with diesel exhaust particles (DEP) and resveratrol (RES) to study the effect of RES on the DEP-induced cells, and it was found that RES can alleviate DEP intervention on cellular structure and increase DEP-induced biomechanical and inflammatory changes. For the nano-interfaces topic, first we synthesized a hybrid nanoparticle with the multimodal properties of fluorescence imaging, Surface-enhanced Raman spectroscopy (SERS) detection and photothermal therapy (PTT) for single living cell analysis of epidermal growth factor receptor (EGFR) and specifically killed cancer cells with high EGFR expression. Additionally, to increase surface area, light-heat conversion efficiency and biocompatibility, we developed a silica coated nanoparticle conjugated with anti-human epidermal growth factor receptor 2 (HER2) antibody. Finally, three-dimensional TiO₂ nanotubes with Au nanoparticles coating were synthesized and used to study trophoblast-derived stem-like cells growth on such 3D nanostructures.

(251 pages)

PUBLIC ABSTRACT

In vitro, Non-invasive Imaging and Detection of Single Living Mammalian Cells

Interacting with Bio-nano-interfaces

by

Qifei Li

Study of bio-nano-interfaces of living mammalian cells will help the identification of cellular alterations (e.g. nucleic acids, amino acids, biomechanics, etc.) due to external stimuli, the design of biomaterials (e.g. nanoparticles, nanotubes) and the investigation on the interaction between cells and bio-nano-interfaces (e.g. cell differentiation on 3D nanostructured materials). The chemical, physical, and mechanical changes of mammalian cells interacting with biomaterials can be investigated by analytical techniques. In this dissertation, cellular responses and property changes are evaluated by non-invasive spectroscopic technique, Raman microscopy (RM), and atomic force microscopy (AFM) combined with traditional biological methods.

This dissertation includes the biophysical, biochemical and cytotoxic measurement of cells interacting with bio-nano-interfaces, and this work can be divided into three topics: biomechanics/cellular biopolymers measurement, bio-interfaces and nano-interfaces studies.

Cellular biomechanical, biochemical and genetic changes were detected in the topic of biomechanics/cellular biopolymers measurement, and cellular differentiation can be identified by cellular biophysical and biochemical properties. For the bio-interfaces, cellular biochemical and biomechanical properties were affected by BRMS1 expression (a metastasis suppressor) through the study of five metastatic and non-metastatic cancer cells. However, both metastatic and non-metastatic cells exhibited similar patterns of reactive oxygen species (ROS), apoptosis expression and cell viability changes over doxorubicin (DOX) incubation

time. Then A549 cells were incubated with diesel exhaust particles (DEP) and an antioxidant resveratrol (RES) to study the effect from DEP and RES, and it was found that RES can decrease DEP-induced destructive effect on cellular structure and enhance DEP-induced biomechanical and inflammatory changes. For the nano-interfaces, hybrid nanoparticles were first developed with the function of fluorescence imaging, Surface-enhanced Raman spectroscopy (SERS) detection and photothermal therapy (PTT). These nanoparticles were applied for single living cells analysis of epidermal growth factor receptor (EGFR) distribution and cancer therapy with high EGFR expression. Additionally, silica coated nanoparticles conjugated with anti-human epidermal growth factor receptor 2 (HER2) were synthesized to increase surface area, light-heat conversion efficiency and biocompatibility. Cancer cells with high-HER2 expression were killed upon an 808 nm laser irradiation. Moreover, trophoblast-derived stem-like cells were cultured on three-dimensional TiO₂ nanotubes with Au to study cell viability, morphology and biochemical changes.

DEDICATION

To my grandparents Zhiqin Li, Fuxian Zhao, my parents Zhen Li, Yixiu Lin and my fiancée
Shiyu Luo I dedicate this dissertation.

ACKNOWLEDGMENTS

I would like to thank all those people who have helped me and made possible the completion of this doctoral program. First I would like to thank my major advisor, Dr. Anhong Zhou. We had numerous discussions on research for these 4 years and I am grateful that he shared many of his insights and knowledge with me. He is a patient advisor not only giving me valuable suggestions, but also guiding me to explore academic research. Besides, I would like to thank my committee members, Dr. Clay Isom, Dr. Charles Miller, Dr. Xiaojun Qi and Dr. Randy Lewis for their advice and support during the entire process.

My sincere appreciation goes to the people I have worked with. I would like to thank Dr. Yangzhe Wu, Mingjie Tang and Qian Chen, who trained me in Dr. Zhou's laboratory. With those detailed training and basic experiment skills I learned later, I am able to work independently. I also thank the excellent researcher, Dr. A. K. Parchur, for his help of nanoparticles synthesis (Chapter 5 and 6). Thanks to Edison Suasnavas and Sierra Heywood from Dr. Clay Isom's lab for trophoblast cells culture. Thanks to Dr. Xiaojun Qi for her help with principal component analysis of some of Raman spectra. Thanks to Fen-Ann Shen from Microscopy Core Facility. Thanks to Dr. Dane Hansen for confocal microscopy training, and thanks to Spencer Williams as lab manager for all his help. Also thanks to Dr. Sitaram Harihar and Dr. Danny Welch from University of Kansas Medical Center. I am very grateful to have spent wonderful time with my labmates, Lifu Xiao, Han Zhang, Neil Draper, Dr. Ruizhen Li and Dr. Wen Zhang. I also thank the financial support from National Science Foundation, Utah Agriculture Experimental Station, Utah Water Research Laboratory and China Scholarship Council.

Most importantly, I appreciate the support from my parents and my fiancée Shiyu Luo. You help me complete this challenging and rewarding adventure.

Qifei Li

CONTENTS

	Page
ABSTRACT.....	iii
PUBLIC ABSTRACT	v
DEDICATION.....	vii
ACKNOWLEDGMENTS	viii
LIST OF TABLES	xi
LIST OF FIGURES	xii
CHAPTER	
1. INTRODUCTION	1
2. LABEL-FREE AND NON-INVASIVE MONITORING OF PORCINE TROPHOBLAST-DERIVED STEM-LIKE CELLS: DIFFERENTIATION IN SERUM AND SERUM-FREE MEDIA.....	36
3. <i>IN VITRO</i> EVALUATION OF THE ROLE OF BREAST CANCER METASTASIS SUPPRESSOR 1 (BRMS1) IN BREAST CANCER CELLS TO CHEMOTHERAPY USING A MULTIMODAL APPROACH	62
4. DIESEL EXHAUST PARTICLES (DEP) INDUCED HUMAN LUNG CANCER CELLS DAMAGE AND THE PROTECTIVE EFFECT OF RESVERATROL (RES)	90
5. <i>IN-VITRO</i> BIOMECHANICAL PROPERTIES, FLUORESCENCE IMAGING, SURFACE-ENHANCED RAMAN SPECTROSCOPY, AND PHOTOTHERMAL THERAPY EVALUATION OF CaMoO ₄ :Eu@Au HYBRID NANORODS ON HUMAN LUNG ADENOCARCINOMA EPITHELIAL CELLS	122

6. NEAR-INFRARED PHOTOTHERMAL THERAPY OF PRUSSIAN BLUE (PB) COATED WITH MULTIFUNCTIONAL $\text{CaMoO}_4:\text{Eu}@\text{SiO}_2/\text{Au}$ NANOSTRUCTURES FOR TARGETING HUMAN EPIDERMAL GROWTH FACTOR RECEPTOR 2 (HER2) EXPRESSING CANCER CELLS	162
7. TROPHOBLAST DERIVED CELLS BIOPHYSICAL AND BIOCHEMICAL CHANGES ON TiO_2 NT ARRAYS COATED WITH GOLD NANOPARTICLES (TiO_2 NTs-Au)	195
8. SUMMARY AND FUTURE DIRECTION	213
APPENDIX	220
CURRICULUM VITAE.....	227

LIST OF TABLES

Table

	Page
2.1. Formulations for serum-containing and serum-free culture media	39
2.2. Forward and reverse primer of HAND1, KLF4, KRT8 and EIF4A1 (Forty (40) two-step cycles (95° C/15 s denaturation – 60° C/30 s anneal/extend) were used for amplification, followed by a melt curve analysis to confirm the identity of the fragments amplified	42
2.3. Tentative Raman band assignments of trophoblast cells	44
3.1. Tentative Raman band assignments of cancer cells.....	74

LIST OF FIGURES

Figure	Page
1.1. Diagram of IR absorption, Rayleigh scattering and Raman scattering (stokes scattering or anti-stokes scattering) processes [44]	9
1.2. Chemical structure of Doxorubicin [87]	12
1.3. Chemical structure of Resveratrol [98]	13
1.4. Schematic overview of three main topics covered in this dissertation	16
1.5. Trophoblast cells differentiation on Petri dish monitored by RM, AFM and qPCR	16
1.6. Cancer cells with or without BRMS1 expression treated with different time of DOX	17
1.7. Cancer cells treated with DEP only or RES first and then DEP exposure at different time	17
1.8. Surface modification and conjugation of Au nanorods on the surface of CaMoO ₄ :Eu nanoparticles and their applications.....	18
1.9. Schematic of silica coated nanoparticles and its application to PTT	19
1.10. Schematic illustration of TiO ₂ nanotube coated with Au nanoparticles and cellular responses	20

2.1. Nucleus diameter of trophoblast cells (A) and representative GFP images of cells (B) in serum-free and serum medium at day 3, 5, 7 and 10 (Error bars of (A) are standard deviation of the mean; $N \geq 50$, $*P < 0.05$)	43
2.2. Raman peak intensity analysis of trophoblast cells on DNA (A), RNA (B), tryptophan (C), phenylalanine (D), lipid/choline (E) and lipid (F) at day 3 (black), 5 (red), 7 (blue) and 10 (cyan) in serum and serum-free medium (Error bars are standard deviation of the mean; $N \geq 10$, $*P < 0.05$)	46
2.3. Raman peak ratio ($760 \text{ cm}^{-1}/786 \text{ cm}^{-1}$) in serum and serum-free medium (A) (Inset fluorescence images of trophoblast cells at day 10, scale bar: $50 \mu\text{m}$); distribution diagram of two protein/nucleic acid peak intensity ratios ($760/786 \text{ cm}^{-1}$ and $854/786 \text{ cm}^{-1}$) (B), and PCA plot (C) (Error bars of (A) are standard deviation of the mean; $N \geq 10$, $*P < 0.05$)	47
2.4. AFM deflection (A-H) and corresponding 3-D view (A'-H') images of cells in serum-free and serum medium at day 3, 5, 7 and 10. Insets in deflection images are the line profiling of nucleus height	48
2.5. Young's modulus of cells in serum-free and serum medium at day 3, 5, 7 and 10. Error bars are standard deviation of the mean; $N \geq 10$, $*P < 0.05$	51
2.6. Gene expression analysis of cells cultured 3 and 10 days in serum medium compared to serum-free medium by qPCR. All values are presented as a ratio of fold-change values: Serum/Non-serum fold-change. A) CYP17A1 levels. The ratio at day 10 was approach zero, which does not register on the scale used to present the data, but should not be interpreted as an absent or null value (as in panel B); B) HAND1 levels; C) KLF4 levels; D) Relative	

KRT8 levels. Error bars are standard error of the mean. (N = 3, * $P < 0.05$; N.S. = non-serum; N/A = fold change ratio not available because of a null value for non-serum group) 52

3.1. BRMS1 mainly distributed around the nucleus. Immunofluorescence images of (A) 435 and (B) 435/BRMS1 cells stained with anti-BRMS1 antibody (blue: nucleus; green: expression of BRMS1).....69

3.2. BRMS1 expression alters the biomechanical properties and the response of cancer cells to DOX. (A) Young's modulus and (B) adhesion force of 231, 231/BRMS1 (231/B), 435, 435/BRMS1 (435/B) and A549 cells without DOX treatment and treated with 4 h DOX group. Error bars are standard deviation of the mean (N ≥ 10 , ** $p < 0.01$; B represents BRMS1)70

3.3. Similar Raman peaks corresponding to DNA/RNA, lipids and proteins between cell lines have noticeable changes for all cancer cells after DOX treatment. The representative Raman video images of (A) 231, (B) 231/BRMS1, (C) 435, (D) 435/BRMS1 and (E) A549 (inset in each image is the average Raman spectra from nucleus of control and treated with DOX for 4 h, 12 h and 24 h). Spectra difference between different time (4h, 12h and 24h) of DOX treated cells and control cells of (A') 231, (B') 231/BRMS1, (C') 435, (D') 435/BRMS1 and (E') A549 (B represents BRMS1).....72

3.4. BRMS1 expression has little impact on the biochemical changes of cancer cells to DOX. Raman intensity analysis of five cancer cell lines at (A) 786 cm^{-1} (pyrimidine), (B) 1313 cm^{-1} (guanine), (C) 1095 cm^{-1} (lipid), (D) 1450 cm^{-1} (CH_2 deformation of lipid), (E) 937 cm^{-1} (α -helix), (F) 1006 cm^{-1} (phenylalanine) and (G) 1608 cm^{-1} (phenylalanine and tryptophan) at different DOX exposure times (control, 4 h, 12 h and 24 h). Error bars are standard deviation

of the mean. The band area of 1200-1300 cm^{-1} (H) and the intensity ratio (I) between the 1450 cm^{-1} and 1006 cm^{-1} bands (A_{1450}/A_{1006}) of 231, 231/BRMS1, 435, 435/BRMS1 and A549 cells at different DOX exposure times ($N \geq 6$, $**p < 0.01$, B represents BRMS1).....75

3.5. The expression of cytokine and chemokine was affected by BRMS1. Cytokines and chemokines analysis of (A) IL-8, (B) IL-15, (C) RANTES, (D) MCP-1, (E) $\text{GRO}\alpha$, (F) GM-CSF, (G) IL-2 and (H) $\text{TNF}\alpha$ released from 231, 231/BRMS1, 435, 435/BRMS1 and A549 cells. Cells were exposed to DOX for 0 h (control), 4 h, 12 h and 24 h before measurement. Unit of Y-axis: pg/mL. Error bars are standard deviation of the mean ($N = 3$, $**p < 0.01$, B represents BRMS1)77

3.6. BRMS1 expression has little influence on apoptosis, ROS expression and cell viability of cancer cells from DOX. The representative (A) Apoptosis, (B) ROS expression and (C) cell viability images and the histogram of (A') Apoptosis, (B') ROS expression and (C') cell viability percentage from 231, 231/BRMS1, 435, 435/BRMS1 and A549 cells without DOX treatment and treated with 4 h, 12 h and 24 h DOX (Error bars are standard deviation of the mean; $N = 3$, $**p < 0.01$, B represents BRMS1)80

4.1. Energy-dispersive X-ray spectroscopy of DEP (A) used in this study (inset is the representative SEM image of DEP). Representative SEM images of A549 cells without treatment (B), treated with 24 h DEP (C) and treated with 24 h RES and 24 h DEP (D) (black arrow points to DEP)99

4.2. Differential interference contrast (DIC) images (row 1 and row 3) and corresponding fluorescence (FL) confocal images (row 2 and row 4) of A549 cells treated with DEP for different time and treated with RES and DEP for different time (scale bar: 10 μm ; DEP:

black spot in DIC images; nucleus: DAPI, blue; cytoskeleton: fluorescein phalloidin, green)

.....101

4.3. Representative AFM deflection images and corresponding 3-D images of A549 treated with 10 $\mu\text{g}/\text{mL}$ DEP (A) and treated with 10 μM RES and 10 $\mu\text{g}/\text{mL}$ DEP (B) for different times. Histograms of Young's modulus (C) and adhesion force (D) of A549 cells treated with different groups. The data of histograms were obtained from multiple individual cells (Error bars are standard deviation of the mean; $N \geq 10$, $**p < 0.01$).....104

4.4. Raman bright-field images and spectra of A549 cells with 0 h, 4 h, 16 h and 48 h DEP treatment (A) and treated with 24 h RES in advance, followed by 0 h, 4 h, 16 h and 48 h DEP treatment (B). In row 1 of (A) and (B) white dash line illustrates cellular morphology; black arrow points to nucleus; red arrow points to cytoplasm; blue arrow points to membrane. Row 2 of (A) and (B) is the corresponding confocal Raman spectra at different cellular locations as assigned by different color: nucleus (black); cytoplasm (red) and cell membrane (blue). A representative Raman spectrum of A549 cells without treatment (C). Raman peak intensity changes for nucleus (D), cytoplasm (E) and membrane (F) at Raman peaks 786 and 1660 cm^{-1} (Error bars of (D–F) are standard deviation of the mean; $N \geq 4$, $**p < 0.01$)105

4.5. RES induced cytokines and chemokines release from A549 cells. Histograms of IL-6, IL-8, MCP-1, RANTES, GRO α , GM-CSF and Eotaxin (A-G) showed mean values of three independent experiments of both types of cells. Cells were exposed to 10 μM RES for 24 h and 10 $\mu\text{g}/\text{mL}$ DEP for 0 h (no DEP treatment), 4 h, 8 h, 16 h, 24 h and 48 h, or only treated by 10 $\mu\text{g}/\text{mL}$ DEP 0 h (no DEP treatment), 4 h, 8 h, 16 h, 24 h and 48 h for before measurement (Error bars are standard deviation of the mean; $N = 3$, $**p < 0.01$).....107

4.6. Changes of plasma membrane potential (A) (control group was normalized as 1) and cell cycle (B) of A549 cells treated with 10 $\mu\text{g/mL}$ DEP and treated with 10 μM RES and 10 $\mu\text{g/mL}$ DEP assayed by flow cytometry. Results represent the means of three separate experiments, and error bars represent the standard error of the mean. All experimental groups significantly differs from control group (Error bars are standard deviation of the mean; $N = 3$, $**p < 0.01$).....109

5.1. (A) TEM and (B) HRTEM images of CMO:Eu@GNR. (C) HRTEM image of $\text{CaMoO}_4\text{:Eu}$ NPs and (D) SAED pattern for (A). (E) UV-visible and (F) photoluminescence ($\lambda_{\text{ex}} = 464 \text{ nm}$) spectra of CMO:Eu@GNR without (black) and with Ab (red). Inset in (E) shows the comparison of normalized absorption spectrum at an SPR of $\sim 790 \text{ nm}$. Digital photograph of the $\text{CaMoO}_4\text{:Eu}$ NPs dispersed in PBS under a UV-lamp ($\lambda_{\text{ex}} = 254 \text{ nm}$), shown in the inset of (F)..... 135

5.2. (A) Infrared images of PBS and CMO:Eu@GNR aqueous solutions exposed to 808 nm laser (1 W cm^{-2}) for 900 s recorded at different time intervals. (B) Photothermal responses of CMO:Eu@GNR NPs at different concentrations in aqueous solution for 900 s NIR laser (808 nm, 1 W/cm^2). (C) Photothermal responses of 808 nm laser irradiation with different power densities for 900 s at fixed CMO:Eu@GNR NP concentration ($28 \mu\text{g/mL}$ GNR). (D) Temperature change of CMO:Eu@GNR solution at 1 W/cm^2 808 nm laser irradiation over six LASER ON/OFF cycles. Experiment was carried out at room temperature 138

5.3. Atomic force microscopy detection of A549 cells (A) without treatment, (B) treated with CMO:Eu@GNR, or (C) CMO:Eu@GNR-Ab for 2 h: (A'–C') are 3D view images of (A–C); (D) Young's modulus and (E) adhesion force of cells. Error bar:

standard deviation of the mean; $N \geq 20$, $**P < 0.01$	141
5.4. Phase, fluorescence, and overlay images of A549 cells without treatment and treated with CMO:Eu@GNR or CMO:Eu@GNR-Ab for 2 h and 16 h. Scale bar: 100 μm	142
5.5. (A) Raman bright-field images of A549 cells without treatment and treated with CMO:Eu@GNR-MBA or CMO:Eu@GNR-MBA-Ab for 2 h (peak at 1078 cm^{-1} from MBA was selected for mapping). Scale bar: 10 μm (horizontal), 5 μm (vertical). (B) Raman streamline mapping and (C) corresponding Raman spectra of A549 cells without treatment and treated with CMO:Eu@GNR-MBA or CMO:Eu@GNR-MBA-Ab NPs for 2 h	145
5.6. (A) Raman Bright-field images of AML12 cells without treatment and treated with 2-h CMO:Eu@GNR-MBA or CMO:Eu@GNR-MBA-Ab (peak at 1078 cm^{-1} from MBA was selected for mapping). Scale bar: 10 μm (horizontal), 5 μm (vertical). (B) Raman streamline mapping (Black cross: SERS negative; red cross: SERS positive) and (C) the corresponding Raman spectra of AML12 cells without treatment and treated with 2-h CMO:Eu@GNR-MBA or CMO:Eu@GNR-MBA-Ab NPs at $63\times$ water immersion objective	146
5.7. (A) Photothermal therapy. A549 cells were incubated without NPs (control), with CMO:Eu@GNR or CMO:Eu@GNR-Ab for 2 h; after that, cells were irradiated under 1 W/cm^2 808 nm laser for 5 min (green: live cells; red: dead cells. Scale bar: 100 μm). (B) Cell viability of A549 cells without treatment and treated with CMO:Eu@GNR or CMO:Eu@GNR-Ab for 2 h; after that, irradiation for 5 min under 1 W/cm^2 808 nm laser.	

Inset shows the fluorescence image of A549 cells treated with CMO:Eu@GNR-Ab NPs for 2 h, then irradiated without/with laser; Error bar: standard deviation of the mean; N = 3, ** $P < 0.01$	147
5.8. Fluorescence images of A549 and hepatocyte cells control without laser and with 5 min 1 W/cm ² 808 nm laser irradiation and treated with 2 h CMO:Eu@GNR or CMO:Eu@GNR-Ab, then for 5 min 1 W/cm ² 808 nm laser irradiation (Green: live cells; red: dead cells. Scale bar: 100 μm)	149
5.9. Zeta potentials of different samples at pH ~7	150
5.10. DLS data of CMO:Eu@GNR NPs	151
5.11. The effect of different treatments on the WBC counts (NPs: CMO:Eu@GNR; ** $p < 0.01$, N = 3, error bar: standard deviation of the mean)	153
6.1. (A) XRD (B) SEM of Silica coated CMO nanoparticles and (C) Silica coated CMO nanoparticles conjugated with gold nanorods, Inset of (B) shows the STEM of CMO@SiO ₂ ; Inset of (C) shows the SEM of single CMO@SiO ₂ @GNR. (D) EDX spectrum of CMO@SiO ₂ . (E) Excitation, and (F) Luminescence spectra of CMO@SiO ₂ @GNR-PB nanoparticles under different excitations. (G) UV–visible spectra of GNR, CMO@SiO ₂ @GNR, PB and CMO@SiO ₂ @GNR-PB. (H) Photothermal responses of 808 nm laser irradiation with different power densities for 900 s at fixed CMO@SiO ₂ @GNR-PB concentration (28 μg/mL GNR). (I) Temperature change of CMO@SiO ₂ @GNR-PB solution with 28 μg/mL GNR at 0.8 W/cm ² 808 nm laser irradiation over seven LASER ON/OFF cycles. Experiment was carried out at room temperature	174

- 6.2. (A) Photothermal responses of PBS, GNR, PB, CMO@SiO₂@GNR and CMO@SiO₂@GNR-PB for 900 s at fixed 0.8 W/cm². (B) The photothermal response of the CMO@SiO₂@GNR-PB solution (28 µg/mL GNR) was recorded for an NIR laser (808 nm, 0.8 W/cm²), and then the laser was turned off. (C) Temperature increase of synthesized CMO@SiO₂@GNR-PB solution as a function of laser power extinction176
- 6.3. (A) Representative SEM images of 435 cells without treatment, treated with HNP-PB or HNP-PB-Ab (black arrow points to NPs). (B) Corresponding energy-dispersive X-ray spectroscopy of 435 cells without treatment, treated with HNP-PB or HNP-PB-Ab179
- 6.4. Phase (PH), fluorescence (FL), and overlay images of 435 (A) and AML12 cells (B) without treatment and treated with HNP-PB or HNP-PB-Ab for 2 h. Scale bar: 100 µm 181
- 6.5. Raman streamline mapping of 435 (A) and AML12 cells (B) without treatment and treated with HNP-PB or treated with HNP-PB-Ab for 2 h (peak at 2152 cm⁻¹ from PB was selected for mapping). Scale bar: 10 µm 183
- 6.6. (A) Photothermal effect and biocompatibility. 435 and AML12 cells were incubated without NPs (control), with HNP-PB or HNP-PB-Ab for 2 h; after that, cells were irradiated under 0.8 W/cm² 808 nm laser for 5 min (green: live cells; red: dead cells. Scale bar: 100 µm). (C) Cell viability of 435 and AML12 cells (Error bar: standard deviation of the mean; N = 3, ***P* < 0.01). (D) Human white blood count 184
- 6.7. Cytotoxicity of synthesized HNP-PB. (A) The histograms show the percentages of ROS- (M1) and ROS+ (M2) for one experiment. 435 cells were incubated without NPs (control),

with HNP-PB or HNP-PB-Ab for 2 h; after that the formation of ROS was measured using the Muse flow cytometry-based oxidative stress assay™. (B) The scattered apoptosis blots represent one experiment. 435 cells were incubated without NPs (control), with HNP-PB or HNP-PB-Ab for 2 h; after that apoptosis was evaluated after staining with FITC-annexin-V/7ADD. (C) The graph displays the summary ROS+ cells from three independent experiments. (D) The graph represents the summary mean percentages \pm SD of apoptosis (early and late apoptosis) of three independent experiments. (E) Cell viability of 435 and AML12 cells: control and treated with different concentrations of HNP-PB for 24 h (Error bars are standard deviation of the mean; N = 3, ** $P < 0.01$).....	186
7.1. (A) The SEM top view of TiO ₂ NTs, (B) cross section of TiO ₂ NTs, (C) the top view of TiO ₂ NTs-Au, (D) the enlarged top view of TiO ₂ NTs-Au	202
7.2. Raman spectra of trophoblast-derived stem-like cells grown on TiO ₂ NTs-Au NPs, TiO ₂ NTs and MgF ₂ substrates (black dash line indicates the peak from TiO ₂).....	203
7.3. Raman spectra of trophoblast-derived stem-like cells on TiO ₂ NTs-Au at day 3, 5, 7, 10, 15 and 30 on (A) serum-free and (B) serum media.....	205
7.4. Cell viability of trophoblast-derived stem-like cells on TiO ₂ NTs-Au at day 3, 5, 7, 10, 15 and 30 on (A) serum-free and (B) serum media (green: live; red: dead; scale bar: 100 μ m)	207
7.5. SEM images of trophoblast-derived stem-like cells on (A) TiO ₂ NTs-Au NPs, (B) TiO ₂ NTs and (C) Petri dish substrate (Cells were grown in serum-free medium).....	208

CHAPTER 1

INTRODUCTION

1.1 OVERVIEW

In biological systems the cell is the basic unit of life, and an understanding of cellular behavior is crucial for the area of bioengineering. Environmental stimuli (e.g. chemical and physical factors) affect cellular functions, and elucidation of cellular responses to environmental stimuli will help understand and discriminate cellular changes. Cellular biomechanics and biocomposition are two important parameters to reflect cellular responses to external stimuli or changes. Biomechanics plays an important role in cellular morphogenesis, focal adhesion, motility, and metastasis [1-4]. Cellular biomechanical properties including cell stiffness and cell adhesion directly reflect cell composition, affect or can be affected by internal structure (cytoskeleton, organelles, etc.) and external interactions (cell-cell and/or cell-ECM). Alterations in the mechanical properties of cells, therefore, can be used to detect changes in their cellular composition that occur during differentiation, aging, and other changes in physiological status [5, 6]. Not only do alterations in the mechanical properties of cells reflect their status but also the mechanical properties of their surroundings, extracellular matrix, and neighboring cells can directly induce changes in cell status [7]. Therefore, there has been an increasing interest in determining mechanical properties of cells.

A number of techniques have been used to measure the biomechanics of cells, such as the atomic force microscope (AFM) indentation, capillary aspiration, twisted bead and unconfined creep compression method [8]. Among these methods, AFM has proven itself to be a valuable tool for high resolution imaging of surface topography and for quantitative

measurement of the mechanical properties of cells without invasive labels. AFM is a scanning analytical technique that is based on the movement of a sharp tip scanning over the surface of a biological sample while measuring the near-field physical interactions between the sample and tip by a laser detector [9, 10]. AFM is able to image the topographic features of cytoskeleton, cellular microenvironments, and quantitatively measure cellular mechanical properties at nanometer scales *in situ* [11]. Therefore, AFM was applied to evaluate the biophysical properties of mammalian cells under the near-physiological conditions.

The biochemical information of cells is also important in biological systems. Biochemical processes generate the complexity of living organisms by controlling the biochemical signals and chemical energy through metabolism. To understand the whole organism, it is necessary to study how biochemical molecules that occur within living cells change. Techniques like Raman microspectroscopy (RM), infrared (IR) absorption spectroscopy and fluorescence microscopy can be applied to detect the biochemical information of organisms. Compared with other methods, RM is the prevalent approach to probe the relationship between structure and function of biocomponent (e.g. nucleic acids, proteins, pharmacologically relevant molecules, etc.) in the response to external changes [12] because it is noninvasive, nondestructive and free from water interference as well as maintaining chemical selectivity [13]. Based on inelastic scattering of the interaction between laser light and molecular vibrations or other excitations, RM is a spectroscopic technique that can identify chemical compositions through characteristic fingerprints in biological systems [14]. RM permits biochemistry assessment of single living cells *in situ* in a simple and rapid way, requiring minimal sample preparation and small sample volume, and it has been applied

in diagnostic, toxicological and biomedical areas [15]. Clearly, RM is suitable to monitor the biochemical changes in living mammalian cells.

Previously, our group has characterized the biomechanical and biochemical alterations of mammalian cells and their corresponding responses to external stimuli by AFM, RM and other approaches (e.g. qPCR, immunostaining, flow cytometry). Wu *et al.* demonstrated the potential to apply AFM and RM techniques for *in situ* biophysical and biochemical measurements of breast cancer cells with or without Breast Cancer Metastasis Suppressor 1 (BRMS1) expression [16]. Tang *et al.* evaluated the effects from short time exposure of diesel exhaust particles on normal epithelial cells and cancerous epithelial cells by AFM, RM and multiplex ELISA [17]. By utilizing AFM and RM, Xiao *et al.* investigated the potential relationship between biomechanics and cellular biopolymers of human lung epithelial cells upon anti-cancer drug treatments [18]. At the single cell level, Xiao *et al.* also studied the localization, spatial distribution and endocytosis of epidermal growth factor receptor (EGFR) by surface-enhanced Raman spectroscopy (SERS) [19]. Additionally, the differentiation of trophoblast-derived stem-like cells was successfully identified by measuring cellular biophysical and biochemical alterations with the help of AFM and RM [20]. These above works conducted in our research laboratory have demonstrated the applications of AFM and RM as noninvasive technologies to study the responses of mammalian cells to external stimuli.

The focus of this dissertation is to non-invasively image and detect single living mammalian cells interacting with bio-nano-interfaces *in vitro*, and this topic is classified into three categories from biomechanics/cellular biopolymers detection to bio-interfaces and nano-interfaces studies. First, the biophysical and biochemical properties between

undifferentiated cells and differentiated cells are distinguished by AFM and RM, respectively, and these biophysical and biochemical differences could be applied as “biomarkers” for identification purpose. Secondly, mammalian cells were reacted with bio-interfaces (e.g. anticancer drug, diesel exhaust particles, and antioxidant) to study cellular responses and changes. Thirdly, multifunctional hybrid nanoparticles (CaMoO₄:Eu@GNR and CaMoO₄:Eu@SiO₂-GNR-PB) and titanium nanotube were synthesized and characterized. Mammalian cells were exposed to nano-interfaces to evaluate how these nano-interfaces affect cellular responses. More details of this dissertation will be introduced in the following sections.

1.2 SIGNIFICANCE

The impact of this work presented in this dissertation could have profound implications. Detection of mammalian cells under different stimuli by traditional biological methods (qPCR, immunostaining, flow cytometry, etc.) requires the cell sample destruction (e.g., cell fixation in immunostaining), while AFM and RM applied in this study could measure *in situ* the cellular biophysical properties and biocomposition at single cell level under cellular physiological condition.

Recently biomechanical and biochemical properties of single cells were found to be akin to gene and protein detection. We are able to identify differences in cellular subpopulations, disease state, and cellular responses to drugs based on the biomechanical and biochemical properties of single cells [21-27]. Cellular behavior depends on the organization of subcellular structures and cellular composition, and detection of these changes by AFM and RM could facilitate the understanding of cellular structure-function relationship, reflecting cellular changes without modification.

The applications of AFM and RM could benefit the areas of disease study, exploration of new biomaterials, cellular differentiation and regenerative medicine. Combined with traditional biological methods, the new non-invasive techniques can provide additional information and new aspects to understand the changes of biological systems.

1.3 LITERATURE REVIEW

1.3.1 Techniques

1.3.1.1 Atomic force microscopy (AFM)

AFM is a high-resolution scanning probe first developed in 1986 by Binnig, *et al.* [28]. It can detect sample topography by the local attractive and repulsive forces interaction between the tip (mounted on silicon cantilever) and the sample in physiological conditions [11, 29, 30]. AFM can also measure the force-distance curves of a sample to characterize its biomechanical parameters by fitting theoretic model (e.g., the Hertz equation [31]). AFM is able to detect the surface topography of non-conductive samples at the nanoscale, and AFM can be operated in air, vacuum and liquid. Hence, AFM appeared suitable for biological samples.

Different from other light microscopy techniques, AFM requires a sharp, tiny probe that approaches the specimen surface to measure the physical parameters while the sensor is scanned line by line over the sample surface. To keep the probe signal constant, the feedback from the sensor maintains the strength of the interaction (current, force or amplitude) constant [32]. There are three AFM modes during operation: contact, non-contact and tapping mode (intermittent contact mode). In contact mode, the tip contacts with the sample surface softly, and Silicon Nitride tips are normally applied for contact mode. The tip either

scans at a constant force (force fixed) or a constant small height (height fixed) above the surface, and the motion of the scanner in z-direction is detected. “Atomic resolution” images can be obtained in contact mode. For contact mode imaging, the cantilever should be soft enough to be deflected by small forces and has a high enough resonant frequency to prevent vibrational instabilities. Under the non-contact mode the tips are silicon probes. The cantilever should have high spring constant (20-100 N/m) to prevent the tip from sticking to the specimen surface at small amplitudes. The tip-sample interaction can be ignored and the probe operates within the attractive force region. This mode allows scanning without affecting the shape of the specimen. In tapping or intermittent contact mode the probe operates in the repulsive force region, and the cantilever is oscillated close to its resonance frequency. The specimen surface is touched for a short time to minimize potential sample damage.

AFM has some advantages compared to other imaging approaches such as transmission electron microscopy and scanning electron microscopy. AFM possesses a high signal-to-noise ratio that does not need signal averaging for contrast enhancement [33]. In addition, AFM does not require quick-freezing, fixing and staining of the samples. The major difference of AFM is that it has no lens and beam irradiation, so it does not suffer from a limitation of space resolution. AFM measures the height of sample surface as a function of position generating a quantitative 3-dimensional image of the specimen surface, and AFM can accurately measure the lateral and vertical displacement by a computer-controlled piezo scanner that allows precise detection of distances and heights [34]. The resolution for a light microscope and an electron microscopy is limited by the wavelength of visible light and electrons respectively, but the resolution for AFM is restricted by the probe sharpness. Even

though AFM and electron microscopy normally have similar range of resolution, AFM usually provides a smaller resolution than obtained by electron microscopy [34]. One obvious advantage is that AFM can image samples in fluid condition, so biological samples can be measured in near physiological conditions. Additionally, AFM can image real-time processes of a biological sample.

AFM-based detection of mechanical properties of samples is a novel application in the biological field that potentially allows for a better understanding of biomechanics at different levels from the bio-interfaces of cellular structural organization to the nano-interfaces of complex interaction. Since the introduction of AFM, it has been used to distinguish the differences in cellular subpopulations, cellular proliferation and differentiation [35-37]. AFM is able to image and measure cellular biophysical properties at single living cell level is important in the research of life sciences. Of particular significance is the potential use in clinical applications, for example, for early cancer diagnosis before diseases progress [38]. AFM is applied here to characterize cellular biomechanics and topography. The applications of AFM have expanded as it has been used across multiple research areas [39].

1.3.1.2 Raman spectroscopy (RM)

RM is a spectroscopic technique first developed in 1928 by C.V. Raman [40]. Based on vibrational modes of molecules, RM can obtain biochemical information from single cells without other invasive steps, providing spectral information about the molecular compositions, structures, and quantities of cellular biopolymers with a minimal background signal from water [41]. The detected Raman spectral frequencies in wavenumber are proportional to vibrational energies of molecular polarizability [42].

The photons can either be absorbed or scattered when incident light strikes molecules. Infrared spectroscopy (IR) and ultraviolet-visible spectroscopy (UV-Vis spectroscopy) are two typical absorption spectroscopic approaches that are based on photon absorption phenomenon and they can measure the radiation loss as a function of frequency. RM is a spectroscopic technique that is based on photon scattering phenomenon with energy transfer. If there is no energy change of these photons, this scattering phenomenon is called elastic scattering (Rayleigh scattering). If there is a net energy transfer, it is called inelastic scattering (Raman scattering), as shown in Figure 1.1. Raman scattering is a low-probability case, only occurring among one per 10^6 - 10^8 scattered photons [43]. There are two types of Raman scattering: Stokes and anti-Stokes. If the molecule is excited from the ground state v_0 to a higher state v_1 , it is called Stokes scattering; if the molecule drops from a higher vibrational state down to a lower one, it is called anti-Stokes scattering. At room temperature anti-Stokes scattering is usually less intense because of fewer molecules in excited states. Thus, Stokes scattering is detected to acquire Raman spectra. However, if a strong fluorescence interference is present, anti-Stokes scattering is preferred.

The energy of a vibrational transition between two energy states is called the Raman shift (in cm^{-1}). RM probes the molecular vibrational transitions that rely on chemical bonds, so RM can detect “finger printing” information about chemical structure and conformation of molecules. It should be noted that only those vibrational modes that change molecule polarizability display Raman signal. The disadvantage of RM is that the Raman signal is usually very weak, and can be interfered with autofluorescence. However, RM has unique advantages over other techniques. First, RM can be combined with confocal microscopy [45] to provide high spatial resolution ($\sim 1 \mu\text{m}$). Another advantage of RM over other methods is

the non-invasive analysis of specimen without sample preparation (for example, no need of labels, contrast agents or dyes). Moreover, Raman scattering is free from water interference, which is important for cellular biopolymer spectroscopy over IR where water has strong interference because of its high absorbance at IR wavelengths [46].

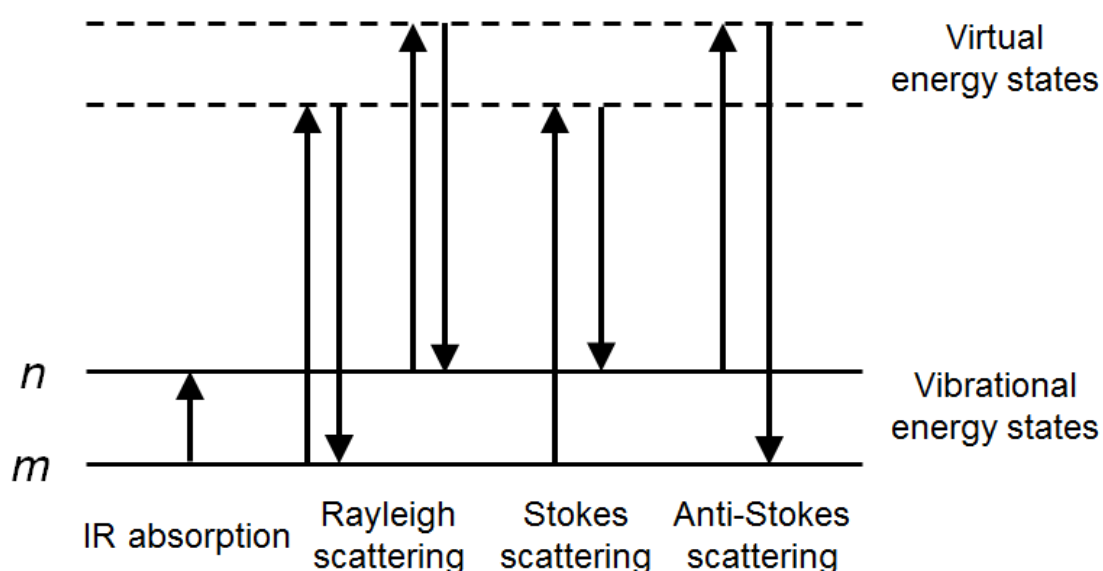


Figure 1.1 Diagram of IR absorption, Rayleigh scattering and Raman scattering (stokes scattering or anti-stokes scattering) processes [44].

RM has been applied in a range of industrial areas, including semiconductors [47], geosciences [48], archeology [49] and pharmaceuticals [50]. With the development of instrumentation, currently RM has been widely utilized in bioanalytical fields for chemistry [51], biology [52], and medicine studies [53]. Additionally, RM has gained increased popularity in the area of mammalian cell research. RM is suitable for biological samples by its successful applications in cell sorting, identification of cellular biopolymers, and assessing

differentiation status [54, 55]. RM has successfully discriminated undifferentiated stem cells from differentiated cells [56-58]. When distinct molecular components are selected, RM becomes a powerful tool to identify the differences between normal and dysplasia tissue [59] and principal component analysis can discriminate, through characteristic Raman bands, normal from abnormal oral squamous cell carcinoma [60]. Similar applications of RM have been performed for other types of cancer cell lines (e.g. liver [61], breast [62], prostate [63], ovarian [64], and so on).

Clearly, RM is a good instrumental technique to study the cellular biopolymer changes of mammalian cells. We utilized RM to track the biochemical changes (DNA/RNA, lipids, proteins, and carbohydrates) of mammalian cells interacting *in situ* with bio-nano-interfaces.

1.3.1.3 Surface-enhanced Raman spectroscopy (SERS)

SERS is a RM technique that can greatly increase Raman signal from Raman-active molecules that have been adsorbed onto certain specific metal surfaces (e.g. gold nanoparticles, silver nanoparticles, etc.). Increases in the intensity of Raman signal can be as much as 10^{10} to 10^{11} [65, 66]. RM is less effective for surface studies than SERS because the incident photons from laser light simply distribute through the bulk and the signal of the bulk overwhelms other Raman signal. However, the surface signal of SERS overwhelms the bulk signal because of surface enhancement mechanisms, largely suppressing bulk signal. An electromagnetic and a chemical enhancement are two primary mechanisms of enhancement for SERS. The electromagnetic enhancement relies on the metal feature that contributes more compared to chemical enhancement [67], while the chemical enhancement involves changes of the adsorbate electronic states [68]. Previous research has reported using SERS probes to

target cancer cells *in vitro* or *in vivo*, identifying the binding between probes and target cancer cells [19, 69-71]. In this study, SERS is applied to locate the distribution of epidermal growth factor receptor (EGFR) and human epidermal growth factor receptor 2 (HER2) at single living cells.

1.3.1.4 Quantitative polymerase chain reaction (qPCR)

Quantitative polymerase chain reaction (qPCR), is a laboratory technique to quantify targeted DNA molecules in molecular biology [72]. Due to the detection sensitivity, high throughput capabilities, accurate quantification and high degree of potential automation, qPCR is selected to monitor gene expression [73]. qPCR has been applied to detect the changes of biomechanics-related genes during the differentiation of mesenchymal stem cells and human tendon stem/progenitor cells [74, 75]. However, few applications have been conducted to sort out the potential correlation between the changes of cell biomechanics and the changes of biomechanics-related genes during stem cell differentiation. In this dissertation research, qPCR was used to assess the expression of biomechanics-related genes during the process of trophoblast cell differentiation.

1.3.1.5 Photothermal therapy (PTT)

PTT, also known as photothermal ablation, is a minimally invasive approach to cancer therapy. PTT requires photothermal conversion agents to generate rapid localized heat to ablate cancerous cells specifically by absorbing light and converting the absorbed light into heat [76]. Gold nanostructures are commonly applied as contrast agents because of their features to tune optical properties via the localized surface plasmon effect. Gold nanostructures with strong near-infrared (NIR) absorption are considered to be a relatively noninvasive and effective treatment of cancer compared to the current cancer treatments

(chemotherapy, radiotherapy, surgery, and so on), which usually result in severe adverse effects and cancer recurrence [77-80]. Previous studies have reported the application of gold nanostructures (e.g. Au nanoparticles [81], Au nanoshells [82], Au nanostar [83], etc.) for PTT. In this work, a novel hybrid nanostructure was developed for simultaneous molecular imaging and photothermal cancer therapy.

1.3.2 Treatment agents

1.3.2.1 Doxorubicin (DOX)

Doxorubicin (DOX, Figure 1.2), an antitumor antibiotic, has been widely used for treating a variety of cancers in clinical trials. Several mechanisms of DOX have been proposed, such as the inducement of DNA damage via the topoisomerase inhibition, intercalation into DNA, interference with the structure of DNA and helicase activity [84-86]. In this dissertation we use DOX to treat cancer cells with or without BRMS1 to study cellular responses.

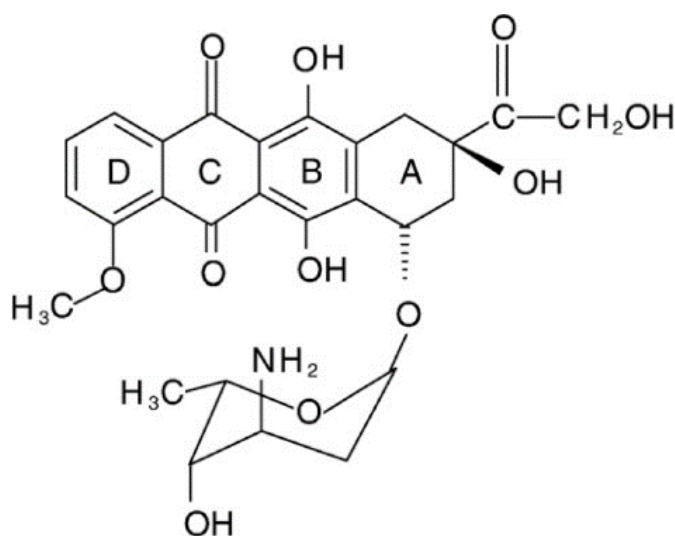


Figure 1.2 Chemical structure of doxorubicin [87].

1.3.2.2 Resveratrol (RES)

Resveratrol (trans-3, 4, 5-trihydroxystilbene, RES, Figure 1.3), a phenolic natural component from the skin of grapes, blueberries, raspberries and mulberries, has potential benefits to human health [88]. This natural compound has been found to possess many pharmacological effects, including modulatory lipoprotein metabolism, platelet antiaggregatory, anti-inflammatory, anti-fungal properties, cancer chemopreventive and anticancer properties [89-92]. Previous studies have shown that RES can effectively inhibit oxidative damage than other conventional antioxidants [93, 94] and has been shown to scavenge free radicals such as lipid hydroperoxyl, hydroxyl (-OH), and superoxide anion (O_2^-) radicals [95]. Interestingly, Birrell *et al.* [96] showed that RES inhibits lipopolysaccharide-induced airway neutrophilia and inflammation through an NF- κ B-independent and unidentified mechanism. The study conducted by King *et al.* [97] suggested that RES significantly decreased intracellular ROS accumulation induced by basal and H_2O_2 , reducing H_2O_2 induced extracellular signal regulated kinase activation in retinal pigment epithelial cells. In this study, the RES effect on DEP induced mammalian cells was detected and compared with control groups.

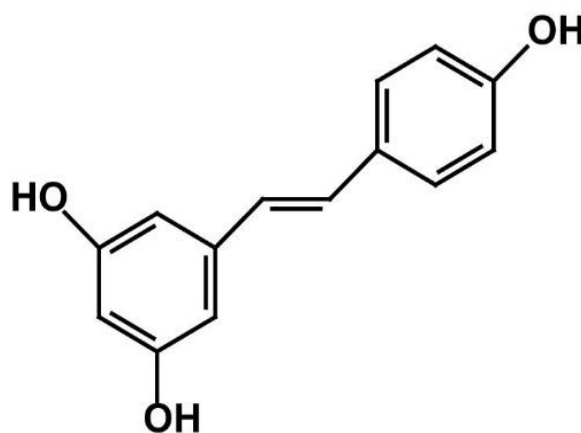


Figure 1.3 Chemical structure of resveratrol [98].

1.3.2.3 Diesel exhaust particles (DEP)

Diesel exhaust particles (DEP), mainly originated from the spark-ignition inside diesel engines, are characterized by a carbonic nucleus, in which about 18,000 high-molecular-weight organic compounds are adsorbed [99]. It is reported that there is a relationship between DEP and lung cancer incidence, cardiopulmonary deaths, and respiratory and cardiovascular diseases for adults living in metropolitan areas [100-103]. DEP induce a variety of cardiovascular and respiratory diseases, which lead to significant morbidity and mortality in susceptible populations [104, 105]. DEP exposure is associated with asthma [106] and might exacerbate allergic lung inflammation and induce functional lung changes [107]. On the cellular level, DEP exposure induces cytotoxic and pro-inflammatory responses [108], and significantly alters cytokine production [109]. In this study, DEP exposure at different time was utilized to stimulate cellular responses, and cellular biophysical and biochemical changes were measured.

1.3.2.4 Titanium nanotubes (TiO₂ NT)

Titanium surfaces have been widely applied in clinical titanium implantations for the purpose of bone, joint, or tooth replacements [110]. Compared with the titanium surface, a thin TiO₂ nanotube layer forms on Ti substrate has desirable bioactive (bone-growth) properties [111]. TiO₂ nanotube layer can improve the formation of fibrous tissue, alleviating the implant and inflammation. By anodization there was vertically aligned yet laterally arrayed nanoscale TiO₂ nanotopography grown on the titanium surfaces. The TiO₂ nanotubes largely enhanced the adhesion and propagation of the osteoblast with the filopodia of growing cells actually spreading into the nanotubes, inducing an interlocked cellular structure.

In comparison with titanium surfaces, the growth rate of osteoblast cells was significantly facilitated by as much as ~ 300–400% with the presence of the TiO₂ nanotopography [112]. It was found that as nanoscale spacing models TiO₂ nanotube surfaces can be utilized for size-dependent cellular response [113]. The nanotube structure also offered nano-scale cues to enhance cellular probing, cell sensing, and cell migration. For bovine aortic endothelial cells (BAECs) grown on TiO₂ nanotubes, it is of benefit to probe the surface and interlock cellular extensions. Extracellular matrix (ECM) deposition and more natural “vascular bed” were stimulated by TiO₂ nanostructures, which also induced unidirectional cytoskeletons and more organized lamellipodia, indicating the functionality of the TiO₂ nanotopography facilitating endothelialization and endothelial cell migration, especially in the raised formation of ECM and increased level of nitric oxide/endothelin ratio [114]. Due to the unique nanotopographical structures and biocompatibility of the TiO₂ nanotube surface on Ti foils, it can facilitate the mobility of endothelial cells [114]. In this study, trophoblast-derived stem-like cells were culture on TiO₂ nanotubes and cellular responses were detected.

1.4 DISSERTATION FORMAT

This dissertation is formatted in a multiple paper structure, and it can be divided into three main topics as shown in Figure 1.4: biomechanics/cellular biopolymers of native cells (Chapter 2); bio-interfaces (Chapter 3 - 4) and nano-interfaces (Chapter 5 - 7). All subsequent chapters have been formatted as publications. Chapter 2 was published prior to the completion of this dissertation. Chapters 3-5 were submitted and are under review.

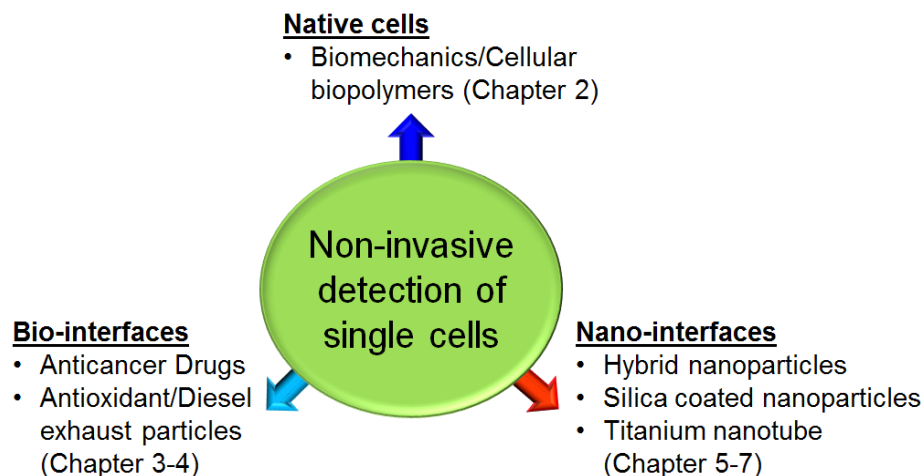


Figure 1.4 Schematic overview of three main topics covered in this dissertation.

In Chapter 2, AFM, RM and qPCR were applied to study the differentiation of porcine trophoblast-derive stem-like cells (TE) on Petri dishes in response to serum and serum-free media (Figure 1.5). Cellular biophysical properties were detected by AFM. RM was used to collect cellular biopolymers information. Cellular gene expression was measured by qPCR.

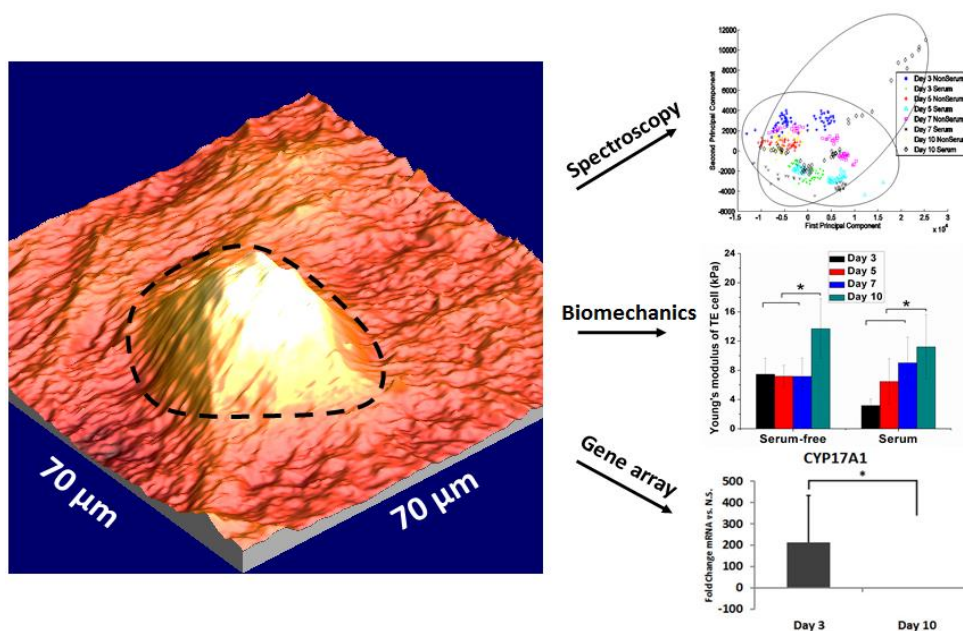


Figure 1.5 Trophoblast cells differentiation on Petri dish monitored by RM, AFM and qPCR.

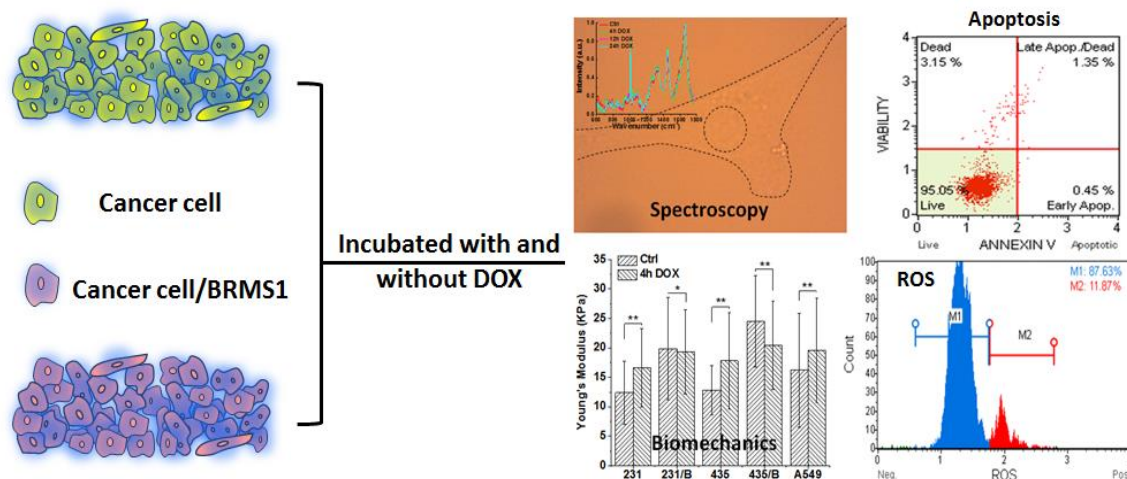


Figure 1.6 Cancer cells with or without BRMS1 expression treated with different time of DOX.

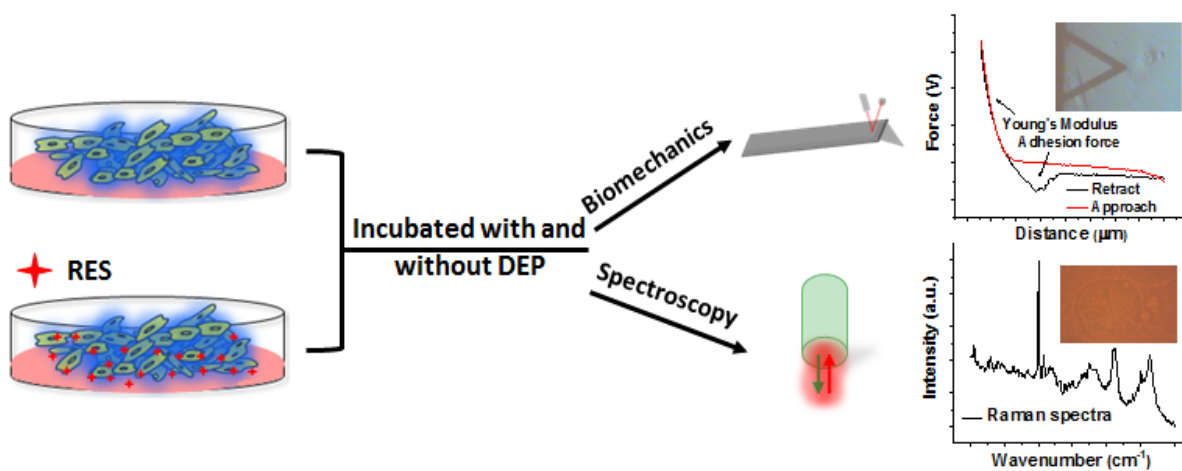


Figure 1.7 Cancer cells treated with DEP only or RES first and then DEP exposure at different time.

In Chapter 3, we evaluated the bio-interfaces interaction between human cancer cells and DOX that cancer cells with or without BRMS1 expression (MDA-MB-231, MDA-MB-435, MDA-MB-231/BRMS1, MDA-MB-435/BRMS1 and A549 cells) under different time

points of DOX exposure (Figure 1.6). Cellular Young's modulus and adhesion force were measured by AFM. The biochemical information of cells was measured by RM. Cellular viability, apoptosis expression and reactive oxygen species (ROS) level were analyzed with and without DOX treatments.

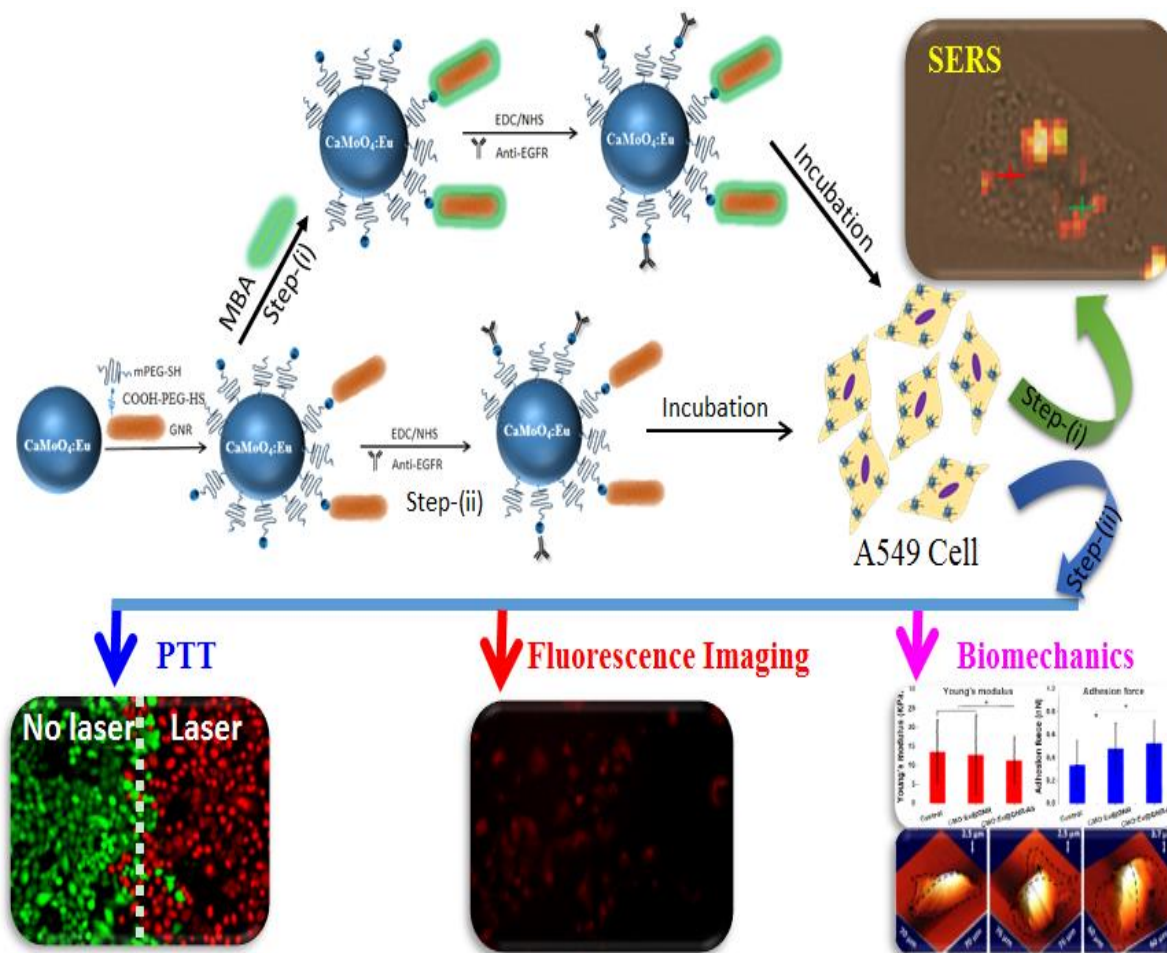


Figure 1.8 Surface modification and conjugation of Au nanorods on the surface of $\text{CaMoO}_4:\text{Eu}$ nanoparticles and their applications.

The focus of Chapter 4 was to study human lung cancer cells (A549) in response to diesel exhaust particles (DEP) and resveratrol (RES) (Figure 1.7). AFM and fluorescence

microscopy were used to collect cellular topography and fluorescence images. RM was applied to obtain the subcellular biochemical compositions. Plasma membrane potential and cell cycles were analyzed.

In Chapter 5 the nano-interfaces were studied, and we synthesized a hybrid nanoparticle (HNP) with multifunctional properties: fluorescence, SERS and PTT. We characterized this HNP and studied the effect of HNP on cellular biomechanical properties. HNPs and cancer biomarker (EGFR) distribution on cells were monitored by SERS mapping (Figure 1.8). The PTT effect from HNPs was investigated on cancer and non-cancer cells.

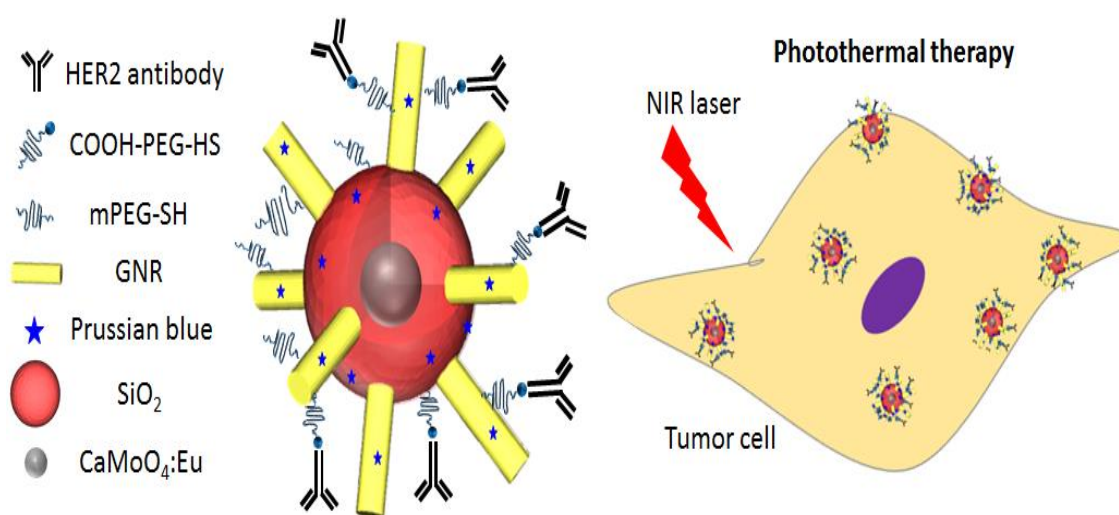


Figure 1.9 Schematic of silica coated nanoparticles and its application to PTT.

In Chapter 6, breast cancer cells (MDA-MB-435) were studied regarding their response to silica coated nanoparticles (Figure 1.9), and the applications of silica coated nanoparticles for fluorescence, SERS detection and photothermal effect were evaluated as well. The biocompatibility of this silica coated nanoparticle was evaluated by Muse cell analyzer.

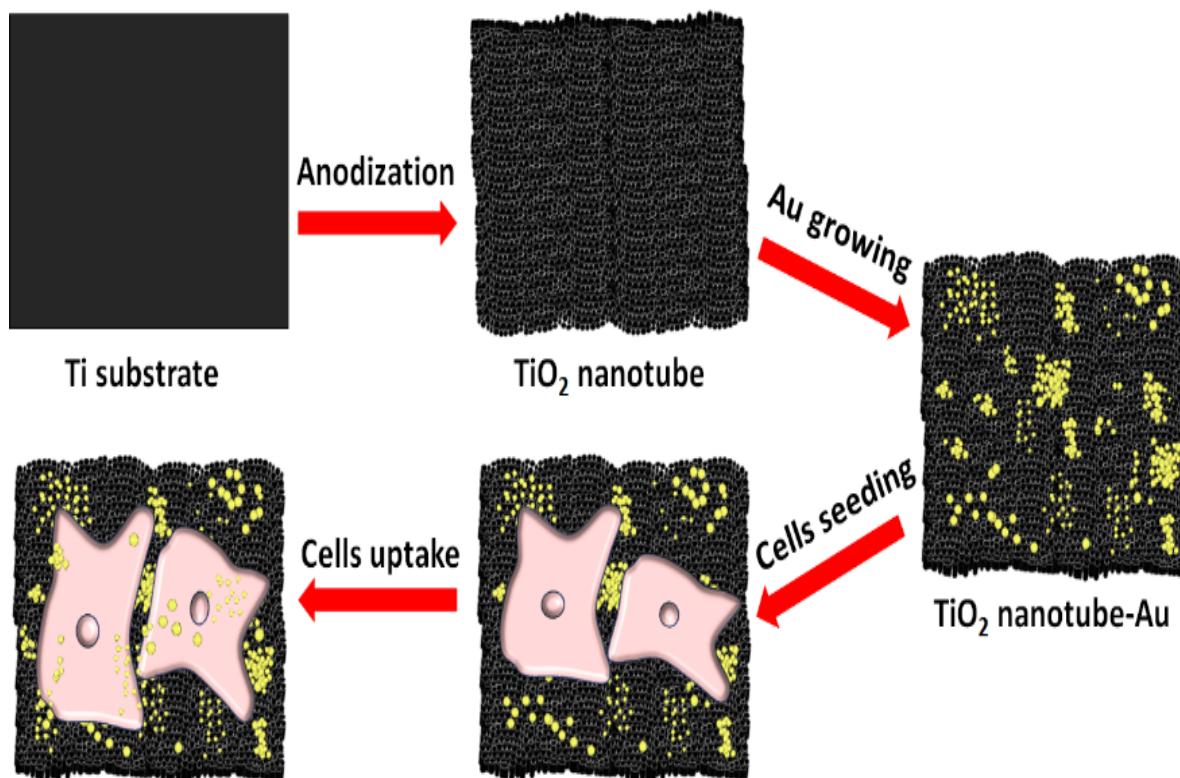


Figure 1.10 Schematic illustration of TiO₂ nanotube coated with Au nanoparticles and cellular responses.

In Chapter 7, my research focused on the morphological and biochemical changes of trophoblast cells grown on 3D TiO₂ nanotubes (NTs) with and without gold nanoparticles (Au) (Figure 1.10). Cellular morphology was recorded by scanning electron microscopy. The subcellular biochemical changes were measured by RM.

In Chapter 8, I presented a brief summary of my dissertation and discussed the potential research for future directions.

1.5 DISSERTATION OUTLINE

Technical Chapter	Title of Chapter	Objectives
Chapter 2	Identification of trophoblast-derived stem-like cell differentiation in serum or serum-free medium	Trophoblast stem-like cells have been induced by serum or serum-free medium to study cellular differentiation in physiological conditions.
Chapter 3	Breast cancer cells with or without BRMS1 in response to doxorubicin	Evaluate BRMS1 expression to cellular biomechanical and biochemical changes upon DOX treatment.
Chapter 4	Human lung cancer cells in response to diesel exhaust particles and resveratrol	Study cellular biomechanical and biochemical changes to diesel exhaust particles and resveratrol exposure.
Chapter 5	Human lung cancer cells and hepatocyte cells in response to hybrid nanoparticles and photothermal effect of nanoparticles	Hybrid nanoparticle with the properties of fluorescence imaging, surface-enhanced Raman spectroscopy detection and photothermal therapy were synthesized and its effects on cells were evaluated.
Chapter 6	Breast cancer cells and hepatocyte cells in response to silica coated nanoparticles	Silica coated nanoparticles were synthesized to increase light-heat conversion efficiency as well as biocompatibility, applying for fluorescence imaging, surface-enhanced Raman spectroscopy detection and photothermal therapy.
Chapter 7	Morphology and cell viability evaluation of trophoblast cells on TiO ₂ nanotubes coated with Au	Measure the viability, cellular topography and biochemical changes of trophoblast cells on TiO ₂ nanotubes coated with Au.

1.6 REFERENCES

1. Nelson CM, Jean RP, Tan JL, Liu WF, Sniadecki NJ, Spector AA, et al. Emergent patterns of growth controlled by multicellular form and mechanics. *Proc Natl Acad Sci U S A*. 2005; 102: 11594-9.
2. Tan JL, Tien J, Pirone DM, Gray DS, Bhadriraju K, Chen CS. Cells lying on a bed of microneedles: An approach to isolate mechanical force. *Proc Natl Acad Sci U S A*. 2003; 100: 1484-9.
3. du Roure O, Saez A, Buguin A, Austin RH, Chavrier P, Siberzan P, et al. Force mapping in epithelial cell migration. *Proc Natl Acad Sci U S A*. 2005; 102: 14122.
4. Suresh S. Biomechanics and biophysics of cancer cells. *Acta Biomater*. 2007; 3: 413-38.
5. Starodubtseva MN. Mechanical properties of cells and ageing. *Ageing Res Rev*. 2011; 10: 16-25.
6. Montell DJ. Morphogenetic Cell Movements: Diversity from Modular Mechanical Properties. *Science*. 2008; 322: 1502-5.
7. Discher DE, Mooney DJ, Zandstra PW. Growth Factors, Matrices, and Forces Combine and Control Stem Cells. *Science*. 2009; 324: 1673-7.
8. Keefer CL, Desai JP. Mechanical phenotyping of stem cells. *Theriogenology*. 2011; 75: 1426-30.
9. Binnig G, Quate CF, Gerber C. Atomic Force Microscope. *Phys Rev Lett*. 1986; 56: 930-3.
10. Dorobantu LS, Gray MR. Application of atomic force microscopy in bacterial research. *Scanning*. 2010; 32: 74-96.

11. Wu YZ, Yu T, Gilbertson TA, Zhou AH, Xu H, Nguyen KT. Biophysical Assessment of Single Cell Cytotoxicity: Diesel Exhaust Particle-Treated Human Aortic Endothelial Cells. *Plos One*. 2012; 7.
12. Schmitt M, Popp J. Raman spectroscopy at the beginning of the twenty-first century. *J Raman Spectrosc*. 2006; 37: 20-8.
13. Notingher L, Jell G, Notingher PL, Bisson I, Tsigkou O, Polak JM, et al. Multivariate analysis of Raman spectra for in vitro non-invasive studies of living cells. *J Mol Struct*. 2005; 744: 179-85.
14. Ling J, Weitman SD, Miller MA, Moore RV, Bovik AC. Direct Raman imaging techniques for study of the subcellular distribution of a drug. *Appl Opt*. 2002; 41: 6006-17.
15. Owen CA, Notingher I, Hill R, Stevens M, Hench LL. Progress in Raman spectroscopy in the fields of tissue engineering, diagnostics and toxicological testing. *J Mater Sci Mater Med*. 2006; 17: 1019-23.
16. Wu Y, McEwen GD, Harihar S, Baker SM, DeWald DB, Zhou A. BRMS1 expression alters the ultrastructural, biomechanical and biochemical properties of MDA-MB-435 human breast carcinoma cells: an AFM and Raman microspectroscopy study. *Cancer Lett*. 2010; 293: 82-91.
17. Tang MJ, Li QF, Xiao LF, Li YP, Jensen JL, Liou TG, et al. Toxicity effects of short term diesel exhaust particles exposure to human small airway epithelial cells (SAECs) and human lung carcinoma epithelial cells (A549). *Toxicol Lett*. 2012; 215: 181-92.

18. Xiao LF, Tang MJ, Li QF, Zhou AH. Non-invasive detection of biomechanical and biochemical responses of human lung cells to short time chemotherapy exposure using AFM and confocal Raman spectroscopy. *Anal Methods*. 2013; 5: 874-9.
19. Xiao LF, Harihar S, Welch DR, Zhou AH. Imaging of epidermal growth factor receptor on single breast cancer cells using surface-enhanced Raman spectroscopy. *Anal Chim Acta*. 2014; 843: 73-82.
20. Li Q, Suasnavas E, Xiao L, Heywood S, Qi X, Zhou A, et al. Label-free and non-invasive monitoring of porcine trophoblast derived cells: differentiation in serum and serum-free media. *J Biophotonics*. 2015; 8: 638-645.
21. Darling EM, Topel M, Zauscher S, Vail TP, Guilak F. Viscoelastic properties of human mesenchymally-derived stem cells and primary osteoblasts, chondrocytes, and adipocytes. *J Biomech*. 2008; 41: 454-64.
22. Darling EM, Pritchett PE, Evans BA, Superfine R, Zauscher S, Guilak F. Mechanical properties and gene expression of chondrocytes on micropatterned substrates following dedifferentiation in monolayer. *Cell Mol Bioeng*. 2009; 2: 395-404.
23. Darling EM, Zauscher S, Block JA, Guilak F. A thin-layer model for viscoelastic, stress-relaxation testing of cells using atomic force microscopy: Do cell properties reflect metastatic potential? *Biophys J*. 2007; 92: 1784-91.
24. Suresh S. Biomechanics and biophysics of cancer cells. *Acta Biomater*. 2007; 3: 413-38.
25. Schulze HG, Konorov SO, Caron NJ, Piret JM, Blades MW, Turner RFB. Assessing Differentiation Status of Human Embryonic Stem Cells Noninvasively Using Raman Microspectroscopy. *Anal Chem*. 2010; 82: 5020-7.

26. Verrier S, Notingher I, Polak JM, Hench LL. In situ monitoring of cell death using Raman microspectroscopy. *Biopolymers*. 2004; 74: 157-62.
27. Owen CA, Selvakumaran J, Notingher I, Jell G, Hench LL, Stevens MM. In vitro toxicology evaluation of pharmaceuticals using Raman micro-spectroscopy. *J Cell Biochem*. 2006; 99: 178-86.
28. Binnig G, Quate CF, Gerber C. Atomic force microscope. *Phys Rev Lett*. 1986; 56: 930-3.
29. McElfresh M, Baesu E, Balhorn R, Belak J, Allen MJ, Rudd RE. Combining constitutive materials modeling with atomic force microscopy to understand the mechanical properties of living cells. *Proc Natl Acad Sci U S A*. 2002; 99: 6493-7.
30. Wu YZ, McEwen GD, Harihar S, Baker SM, DeWald DB, Zhou AH. BRMS1 expression alters the ultrastructural, biomechanical and biochemical properties of MDA-MB-435 human breast carcinoma cells: An AFM and Raman microspectroscopy study. *Cancer Lett*. 2010; 293: 82-91.
31. Kuznetsova TG, Starodubtseva MN, Yegorenkov NI, Chizhik SA, Zhdanov RI. Atomic force microscopy probing of cell elasticity. *Micron*. 2007; 38: 824-33.
32. Miles M. Scanning probe microscopy - Probing the future. *Science*. 1997; 277: 1845-7.
33. Payton OD, Picco L, Miles MJ, Homer ME, Champneys AR. Improving the signal-to-noise ratio of high-speed contact mode atomic force microscopy. *Rev Sci Instrum*. 2012; 83.
34. Dufrene YF. Atomic force microscopy, a powerful tool in microbiology. *J Bacteriol*. 2002; 184: 5205-13.

35. Darling EM, Pritchett PE, Evans BA, Superfine R, Zauscher S, Guilak F. Mechanical Properties and Gene Expression of Chondrocytes on Micropatterned Substrates Following Dedifferentiation in Monolayer. *Cell Mol Bioeng.* 2009; 2: 395-404.
36. Shields KJ, Beckman MJ, Bowlin GL, Wayne JS. Mechanical properties and cellular proliferation of electrospun collagen type II. *Tissue Eng.* 2004; 10: 1510-7.
37. Seidlits SK, Khaing ZZ, Petersen RR, Nickels JD, Vanscoy JE, Shear JB, et al. The effects of hyaluronic acid hydrogels with tunable mechanical properties on neural progenitor cell differentiation. *Biomaterials.* 2010; 31: 3930-40.
38. Cross SE, Jin YS, Rao J, Gimzewski JK. Nanomechanical analysis of cells from cancer patients. *Nat Nanotechnol.* 2007; 2: 780-3.
39. Santos NC, Castanho MA. An overview of the biophysical applications of atomic force microscopy. *Biophys chem.* 2004; 107: 133-49.
40. Gardiner D, Graves P, Bowley H. *Practical Raman spectroscopy.* 1989. Springer-Verlag.
41. Chan JW, Lieu DK. Label-free biochemical characterization of stem cells using vibrational spectroscopy. *J Biophotonics.* 2009; 2: 656-68.
42. Ball DW. Theory of Raman spectroscopy. *Spectroscopy.* 2001; 16: 32-4.
43. Ellis DI, Brewster VL, Dunn WB, Allwood JW, Golovanov AP, Goodacre R. Fingerprinting food: current technologies for the detection of food adulteration and contamination. *Chem Soc Rev.* 2012; 41: 5706-27.
44. Smith E, Dent G. *Modern Raman spectroscopy: a practical approach:* John Wiley & Sons; 2013.

45. Everall NJ. Confocal Raman Microscopy: Performance, Pitfalls, and Best Practice. *Appl Spectrosc.* 2009; 63: 245a-62a.
46. Laane J. *Frontiers of molecular spectroscopy*: Elsevier; 2011.
47. Perkowitz S. *Optical characterization of semiconductors: infrared, Raman, and photoluminescence spectroscopy*: Elsevier; 2012.
48. Chalmers JM, Edwards HG, Hargreaves MD. *Infrared and Raman Spectroscopy in Forensic Science*: John Wiley & Sons; 2012.
49. Ropret P, Madariaga JM. Applications of Raman spectroscopy in art and archaeology. *J Raman Spectrosc.* 2014; 45: 985-92.
50. Paudel A, Raijada D, Rantanen J. Raman spectroscopy in pharmaceutical product design. *Adv Drug Deliv Rev.* 2015.
51. Kneipp K, Kneipp H, I I, Dasari RR, Feld MS. Ultrasensitive chemical analysis by Raman spectroscopy. *Chem Rev.* 1999; 99: 2957-76.
52. Movasaghi Z, Rehman S, Rehman IU. Raman spectroscopy of biological tissues. *Appl Spectrosc Rev.* 2007; 42: 493-541.
53. Choo-Smith LP, Edwards HGM, Endtz HP, Kros JM, Heule F, Barr H, et al. Medical applications of Raman spectroscopy: From proof of principle to clinical implementation. *Biopolymers.* 2002; 67: 1-9.
54. Konorov SO, Glover CH, Piret JM, Bryan J, Schulze HG, Blades MW, et al. In situ analysis of living embryonic stem cells by coherent anti-stokes Raman Microscopy. *Anal Chem.* 2007; 79: 7221-5.
55. Lin JQ, Xu H, Wu YZ, Tang MJ, McEwen GD, Liu P, et al. Investigation of Free Fatty Acid Associated Recombinant Membrane Receptor Protein Expression in

- HEK293 Cells Using Raman Spectroscopy, Calcium Imaging, and Atomic Force Microscopy. *Anal Chem.* 2013; 85: 1374-81.
56. Notingher I, Bisson I, Bishop AE, Randle WL, Polak JM, Hench LL. In situ spectral monitoring of mRNA translation in embryonic stem cells during differentiation in vitro. *Anal Chem.* 2004; 76: 3185-93.
57. Chan JW, Lieu DK, Huser T, Li RA. Label-Free Separation of Human Embryonic Stem Cells and Their Cardiac Derivatives Using Raman Spectroscopy. *Anal Chem.* 2009; 81: 1324-31.
58. Schulze HG, Konorov SO, Caron NJ, Piret JM, Blades MW, Turner RFB. Assessing Differentiation Status of Human Embryonic Stem Cells Noninvasively Using Raman Microspectroscopy. *Anal Chem.* 2010; 82: 5020-7.
59. Teh SK, Zheng W, Ho KY, Teh M, Yeoh KG, Huang Z. Diagnostic potential of near-infrared Raman spectroscopy in the stomach: differentiating dysplasia from normal tissue. *Brit J Cancer.* 2008; 98: 457-65.
60. Carvalho LFCS, Bonnier F, O'Callaghan K, O'Sullivan J, Flint S, Byrne HJ, et al. Raman micro-spectroscopy for rapid screening of oral squamous cell carcinoma. *Exp Mol Pathol.* 2015; 98: 502-9.
61. Hawi SR, Campbell WB, KajdacsyBalla A, Murphy R, Adar F, Nithipatikom K. Characterization of normal and malignant human hepatocytes by Raman microspectroscopy. *Cancer Lett.* 1996; 110: 35-40.
62. Haka AS, Shafer-Peltier KE, Fitzmaurice M, Crowe J, Dasari RR, Feld MS. Identifying microcalcifications in benign and malignant breast lesions by probing

- differences in their chemical composition using Raman spectroscopy. *Cancer Res.* 2002; 62: 5375-80.
63. Crow P, Barrass B, Kendall C, Hart-Prieto M, Wright M, Persad R, et al. The use of Raman spectroscopy to differentiate between different prostatic adenocarcinoma cell lines. *Brit J Cancer.* 2005; 92: 2166-70.
64. Maheedhar K, Bhat RA, Malini R, Prathima NB, Keerthi P, Kushtagi P, et al. Diagnosis of ovarian cancer by Raman spectroscopy: A pilot study. *Photomed Laser Surg.* 2008; 26: 83-90.
65. Blackie EJ, Le Ru EC, Etchegoin PG. Single-molecule surface-enhanced Raman spectroscopy of nonresonant molecules. *J Am Chem Soc.* 2009; 131: 14466-72.
66. Le Ru EC, Blackie E, Meyer M, Etchegoin PG. Surface enhanced Raman scattering enhancement factors: a comprehensive study. *J Phys Chem C.* 2007; 111: 13794-803.
67. Kambhampati P, Child CM, Foster MC, Campion A. On the chemical mechanism of surface enhanced Raman scattering: Experiment and theory. *J Chem Phys.* 1998; 108: 5013-26.
68. Srnova-Sloufova I, Vlckova B, Snoeck TL, Stufkens DJ, Matejka P. Surface-enhanced Raman scattering and surface-enhanced resonance Raman scattering excitation profiles of Ag-2,2'-bipyridine surface complexes and of [Ru(bpy)₃]²⁺ on Ag colloidal surfaces: manifestations of the charge-transfer resonance contributions to the overall surface enhancement of Raman scattering. *Inorg chem.* 2000; 39: 3551-9.

69. Lee S, Chon H, Lee J, Ko J, Chung BH, Lim DW, et al. Rapid and sensitive phenotypic marker detection on breast cancer cells using surface-enhanced Raman scattering (SERS) imaging. *Biosens Bioelectron.* 2014; 51: 238-43.
70. Dinish US, Balasundaram G, Chang YT, Olivo M. Actively Targeted In Vivo Multiplex Detection of Intrinsic Cancer Biomarkers Using Biocompatible SERS Nanotags. *Sci Rep.* 2014; 4: 4075.
71. Samanta A, Das RK, Park SJ, Maiti KK, Chang YT. Multiplexing SERS nanotags for the imaging of differentiated mouse embryonic stem cells (mESC) and detection of teratoma in vivo. *Am J Nucl Med Mol Imaging.* 2014; 4: 114-24.
72. Wong ML, Medrano JF. Real-time PCR for mRNA quantitation. *Biotechniques.* 2005; 39: 75-85.
73. Ragni E, Vigano M, Rebulli P, Giordano R, Lazzari L. What is beyond a qRT-PCR study on mesenchymal stem cell differentiation properties: how to choose the most reliable housekeeping genes. *J Cell Mol Med.* 2013; 17: 168-80.
74. O'Cearbhaill ED, Punchard MA, Murphy M, Barry FP, McHugh PE, Barron V. Response of mesenchymal stem cells to the biomechanical environment of the endothelium on a flexible tubular silicone substrate. *Biomaterials.* 2008; 29: 1610-9.
75. Yin Z, Chen X, Chen JL, Shen WL, Nguyen TMH, Gao L, et al. The regulation of tendon stem cell differentiation by the alignment of nanofibers. *Biomaterials.* 2010; 31: 2163-75.
76. Huang X, El-Sayed MA. Plasmonic photo-thermal therapy (PPTT). *Alexandria Journal of Medicine.* 2011; 47: 1-9.

77. Lu WT, Singh AK, Khan SA, Senapati D, Yu HT, Ray PC. Gold Nano-Popcorn-Based Targeted Diagnosis, Nanotherapy Treatment, and In Situ Monitoring of Photothermal Therapy Response of Prostate Cancer Cells Using Surface-Enhanced Raman Spectroscopy. *J Am Chem Soc.* 2010; 132: 18103-14.
78. Coates A, Abraham S, Kaye SB, Sowerbutts T, Frewin C, Fox RM, et al. On the Receiving End Patient Perception of the Side-Effects of Cancer-Chemotherapy. *Eur J Cancer.* 1983; 19: 203-8.
79. Zachariah B, Balducci L, Venkattaramanabalaji GV, Casey L, Greenberg HM, DelRegato JA. Radiotherapy for cancer patients aged 80 and older: A study of effectiveness and side effects. *Int J Radiat Oncol.* 1997; 39: 1125-9.
80. In H, Bilimoria KY, Stewart AK, Wroblewski KE, Posner MC, Talamonti MS, et al. Cancer Recurrence: An Important but Missing Variable in National Cancer Registries. *Ann Surg Oncol.* 2014; 21: 1520-9.
81. Mackey MA, Ali MR, Austin LA, Near RD, El-Sayed MA. The most effective gold nanorod size for plasmonic photothermal therapy: theory and in vitro experiments. *J Phys Chem B.* 2014; 118: 1319-26.
82. Trinidad AJ, Hong SJ, Peng Q, Madsen SJ, Hirschberg H. Combined Concurrent Photodynamic and Gold Nanoshell Loaded Macrophage-Mediated Photothermal Therapies: An In Vitro Study on Squamous Cell Head and Neck Carcinoma. *Laser Surg Med.* 2014; 46: 310-8.
83. Yuan H, Fales AM, Vo-Dinh T. TAT Peptide-Functionalized Gold Nanostars: Enhanced Intracellular Delivery and Efficient NIR Photothermal Therapy Using Ultralow Irradiance. *J Am Chem Soc.* 2012; 134: 11358-61.

84. Pang B, Qiao X, Janssen L, Velds A, Groothuis T, Kerkhoven R, et al. Drug-induced histone eviction from open chromatin contributes to the chemotherapeutic effects of doxorubicin. *Nat Commun.* 2013; 4: 1908.
85. Tacar O, Sriamornsak P, Dass CR. Doxorubicin: an update on anticancer molecular action, toxicity and novel drug delivery systems. *J Pharm Pharmacol.* 2013; 65: 157-70.
86. Gewirtz DA. A critical evaluation of the mechanisms of action proposed for the antitumor effects of the anthracycline antibiotics Adriamycin and daunorubicin. *Biochem Pharmacol.* 1999; 57: 727-41.
87. Guo J, Cai W, Du B, Qian M, Sun Z. Raman spectroscopic investigation on the interaction of malignant hepatocytes with doxorubicin. *Biophys Chem.* 2009; 140: 57-61.
88. Jasinski M, Jasinska L, Ogrodowczyk M. Resveratrol in prostate diseases - a short review. *Cent European J Urol.* 2013; 66: 144-9.
89. Soleas GJ, Diamandis EP, Goldberg DM. Resveratrol: A molecule whose time has come? And gone? *Clin Biochem.* 1997; 30: 91-113.
90. Middleton E, Kandaswami C, Theoharides TC. The effects of plant flavonoids on mammalian cells: Implications for inflammation, heart disease, and cancer. *Pharmacol Rev.* 2000; 52: 673-751.
91. Di Santo A, Mezzetti A, Napoleone E, Di Tommaso R, Donati MB, De Gaetano G, et al. Resveratrol and quercetin down-regulate tissue factor expression by human stimulated vascular cells. *J Thromb Haemost.* 2003; 1: 1089-95.

92. Baur JA, Sinclair DA. Therapeutic potential of resveratrol: the in vivo evidence. *Nat Rev Drug Discov.* 2006; 5: 493-506.
93. Pervaiz S. Resveratrol: from grapevines to mammalian biology. *Faseb J.* 2003; 17: 1975-85.
94. Sun AY, Simonyi A, Sun GY. The "French paradox" and beyond: Neuroprotective effects of polyphenols. *Free Radical Bio Med.* 2002; 32: 314-8.
95. Morelli R, Das S, Bertelli A, Bollini R, Lo Scalzo R, Das DK, et al. The introduction of the stilbene synthase gene enhances the natural antiradical activity of *Lycopersicon esculentum* mill. *Mol Cell Biochem.* 2006; 282: 65-73.
96. Birrell MA, McCluskie K, Wong SS, Donnelly LE, Barnes PJ, Belvisi MG. Resveratrol, an extract of red wine, inhibits lipopolysaccharide induced airway neutrophilia and inflammatory mediators through an NF-kappa B-independent mechanism. *Faseb J.* 2005; 19: 840-1.
97. King RE, Kent KD, Bomser JA. Resveratrol reduces oxidation and proliferation of human retinal pigment epithelial cells via extracellular signal-regulated kinase inhibition. *Chem-Biol Interact.* 2005; 151: 143-9.
98. Borra MT, Smith BC, Denu JM. Mechanism of human SIRT1 activation by resveratrol. *J Biol Chem.* 2005; 280: 17187-95.
99. Mazzearella G, Ferraraccio F, Prati MV, Annunziata S, Bianco A, Mezzogiorno A, et al. Effects of diesel exhaust particles on human lung epithelial cells: An in vitro study. *Resp Med.* 2007; 101: 1155-62.
100. Kunzli N, Kaiser R, Medina S, Studnicka M, Chanel O, Filliger P, et al. Public-health impact of outdoor and traffic-related air pollution: a European assessment. *Lancet.*

- 2000; 356: 795-801.
101. Samet JM, Dominici F, Curriero FC, Coursac I, Zeger SL. Fine particulate air pollution and mortality in 20 US Cities, 1987-1994. *New Engl J Med.* 2000; 343: 1742-9.
 102. Pope CA, Thun MJ, Namboodiri MM, Dockery DW, Evans JS, Speizer FE, et al. Particulate Air-Pollution as a Predictor of Mortality in a Prospective-Study of Us Adults. *Am J Resp Crit Care.* 1995; 151: 669-74.
 103. Brauer M, Henderson S. Diesel exhaust particles and related air pollution from traffic sources in the Lower Mainland. Health Canada, Environment and Sustainability Program: Willingdon Green. 2003: 1-28.
 104. Bayram H, Ito K, Issa R, Ito M, Sukkai M, Chung KF. Regulation of human lung epithelial cell numbers by diesel exhaust particles. *Eur Respir J.* 2006; 27: 705-13.
 105. Hales S, Salmond G, Town GI, Kjellstrom T, Woodward A. Daily mortality in relation to weather and air pollution in Christchurch, New Zealand. *Aust Nz J Publ Heal.* 2000; 24: 89-91.
 106. Li N, Wang MY, Oberley TD, Sempf JM, Nel AE. Comparison of the pro-oxidative and proinflammatory effects of organic diesel exhaust particle chemicals in bronchial epithelial cells and macrophages. *J Immunol.* 2002; 169: 4531-41.
 107. Matsumoto A, Hiramatsu K, Li YJ, Azuma A, Kudoh S, Takizawa H, et al. Repeated exposure to low-dose diesel exhaust after allergen challenge exaggerates asthmatic responses in mice. *Clin Immunol.* 2006; 121: 227-35.
 108. Muller L, Comte P, Czerwinski J, Kasper M, Mayer ACR, Schmid A, et al. Investigating the potential for different scooter and car exhaust emissions to cause

- cytotoxic and (pro-)inflammatory responses to a 3D in vitro model of the human epithelial airway. *Toxicol Environ Chem.* 2012; 94: 164-80.
109. Boland S, Baeza-Squiban A, Fournier T, Houcine O, Gendron MC, Chevrier M, et al. Diesel exhaust particles are taken up by human airway epithelial cells in vitro and alter cytokine production. *Am J Physiol-Lung C.* 1999; 276: L604-L13.
110. Linder L, Carlsson A, Marsal L, Bjursten LM, Branemark PI. Clinical aspects of osseointegration in joint replacement. A histological study of titanium implants. *J Bone Joint Surg Br.* 1988; 70: 550-5.
111. Satsangi A, Satsangi N, Glover R, Satsangi RK, Ong JL. Osteoblast response to phospholipid modified titanium surface. *Biomaterials.* 2003; 24: 4585-9.
112. Oh S, Daraio C, Chen L-H, Pisanic TR, Finones RR, Jin S. Significantly accelerated osteoblast cell growth on aligned TiO₂ nanotubes. *Journal of biomedical materials research Part A.* 2006; 78: 97-103.
113. Park J, Bauer S, Schlegel KA, Neukam FW, von der Mark K, Schmuki P. TiO₂ nanotube surfaces: 15 nm--an optimal length scale of surface topography for cell adhesion and differentiation. *Small.* 2009; 5: 666-71.
114. Brammer KS, Oh S, Gallagher JO, Jin S. Enhanced cellular mobility guided by TiO₂ nanotube surfaces. *Nano Lett.* 2008; 8: 786-93.

CHAPTER 2

LABEL-FREE AND NON-INVASIVE MONITORING OF PORCINE TROPHOBLAST DERIVED CELLS: DIFFERENTIATION IN SERUM AND SERUM-FREE MEDIA

2.1 ABSTRACT

Traditional approaches to characterize stem cell differentiation are time-consuming, lengthy and invasive. Here, Raman microspectroscopy (RM) and atomic force microscopy (AFM)—both considered as non-invasive techniques—are applied to detect the biochemical and biophysical properties of trophoblast derived stem-like cells incubated up to 10 days under conditions designed to induce differentiation. Significant biochemical and biophysical differences between control and differentiated cells were observed. Quantitative real time PCR was applied to analyze gene expression. The relationship between cell differentiation and associated cellular biochemical and biomechanical changes were discussed.

2.2 INTRODUCTION

In vitro characterization of cellular differentiation using traditional methods, including immunocytochemistry, fluorescence activated cell sorting and RNA in situ hybridization analysis, has limitations: all require large numbers of cells, lengthy steps and cellular lysis or fixation [1-3]. Recently, there has been a drive to characterize and monitor cellular differentiation processes *in situ* and in real-time by faster and non-invasive methods. Raman microspectroscopy (RM) and atomic force microscopy (AFM) are two highly sensitive analytical techniques able to characterize cellular biochemical [4] and biomechanical [5] properties in cell samples under near physiological conditions [6].

RM is a spectroscopic technique based on inelastic scattering that exhibits energy shift of laser photons corresponding to frequencies of vibration within molecules from samples. Raman shifts can serve as a "fingerprint" to provide information about the molecular compositions, structures, and quantities of cellular biopolymers with a minimal background signal from water [7, 8], allowing the study of living cells under physiological states, without labels or using other invasive steps [9]. Previous studies reported that Raman intensities of nucleic acids on undifferentiated stem cells were dominant in comparison with differentiated cells, while differentiated cells had larger spectral intensities of proteins and lipids than undifferentiated cells [6, 7, 10-18].

AFM is a high-resolution scanning probe microscopy that involves the movement of a sharp tip over the surface of a biological sample while detecting the near-field physical interactions between the sample and tip [19, 20]. AFM can image cytoskeleton, cellular microenvironments, and quantitatively detect cellular mechanical properties at nanometer scales in physiological condition [5, 21, 22]. It was found that stem cell stiffness will increase with differentiation [23-25] and cellular mechanical properties are indicative of stem cell differentiation potential [26, 27].

In the earliest stages of eutherian mammalian embryo development, all the cells (blastomeres) are functionally equivalent, and equally capable of giving rise to all cell types necessary for proper and complete embryonic/fetal growth and survival. However, at a species-specific timepoint (approximately day 3 in mice, day 5 in humans and pigs, and day 7 in cattle, e.g.), molecular and morphological transitions destine some of the cells for development into the primitive placenta (i.e. the trophoctoderm), while the remaining cells give rise to the embryo/fetus proper (i.e. the so-called embryonic stem cells) and retain a

relatively undifferentiated status [28-30]. Trophoblast cells are the first cells within the early developing embryo to undergo a recognizable differentiation event, and the proper formation and function of cells is essential to embryo and fetal survival. In fact, many instances of early embryo mortality – at least in in vitro-manipulated embryos – can be traced back to dysfunctional trophoblast cells [31-33]. Yet the process of trophoblast differentiation is poorly understood. A thorough appreciation of the biochemical and biophysical aspects of trophoblast differentiation may enhance trophoblast function for increased embryonic survival.

In this experiment, trophoblast stem-like cells derived from day 10 porcine embryos have been induced by serum and serum-free medium to study cellular differentiation in physiological conditions. This is the first work to combine RM and AFM to monitor and identify discrete biochemical and biomechanical changes during serum-induced differentiation.

2.3 HYPOTHESIS

The biochemical and biomechanical properties collected by RM and AFM could be used as differentiation indicators to distinguish between differentiated and undifferentiated trophoblast-derived stem-like cells.

2.4 MATERIALS AND METHODS

2.4.1 Preparation of trophoblast cells

The cells were collected from porcine embryos on gestational day 10 as described elsewhere [34] and were passaged without senescence or morphological changes until utilized for experiments. Cell colonies were transfected with an expression construct coding

for green fluorescent protein (GFP) using Jet Pei reagent (Polyplus transfection Inc., New York, NY, USA) according to instructions [34]. GFP cells help observe TE cells morphological changes on magnesium fluoride (MgF₂, United Crystals Co., Port Washington, NY, USA) over time without chemical label. Cells were cultured in serum-free medium to maintain undifferentiated, stem-like characteristics [35], whereas cells cultured in fetal bovine serum medium (15% [v:v]) underwent dramatic and predictable changes to cell morphology and behaviour. Table 2.1 lists formulations for serum-free and serum-containing medium.

Table 2.1 Formulations for serum-containing and serum-free culture media.

Component	Serum-containing	Non serum-containing
DMEM	85% (v:v)	50% (v:v)
F12 Nutrient Mixture	---	50% (v:v)
Fetal Bovine Serum	15% (v:v)	---
B27 Serum-free Supplement	---	1X working concentration
Epidermal Growth Factor	---	20 ng/mL
Fibroblast Growth Factor, Basic	2 ng/mL	40 ng/mL
Gentamicin	20 µg/mL	20 µg/mL

2.4.2 Fluorescence imaging of trophoblast cells

Bright field and fluorescence images were collected by Olympus IX71 inverted fluorescence microscope (Olympus America Inc., Center Valley, PA, USA) equipped with an

Olympus DP30BW CCD camera using DP-BSW Controller and Manager Software. Images were acquired via a 10× lens (Olympus), and cell samples grown on MgF₂ substrates were observed in medium. Fluorescence images were processed by ImageJ software and nucleus diameter measurements were performed on 50~100 cells.

2.4.3 Raman spectroscopy

The Raman spectra were measured by Renishaw inVia Raman spectrometer (WiRE 3.0 software, Renishaw, Wotton-under-Edge, Gloucestershire, UK) equipped with a 300 mW 785 nm near-IR laser that was focused through a 63 × (NA = 0.90) water immersion objective (Leica DMLM, Leica Microsystems, Buffalo Grove, IL, USA). Cells were cultured on MgF₂ and imaged in Earle's balanced salt solution (EBSS, Thermo Fisher Scientific, Waltham, MA, USA).

The Raman laser spot size is about 24 μm × 0.5 μm, focusing primarily on the cellular nuclear region. Raman spectra were collected at Raman static mode at 1 accumulation with 10s exposure time. For each treatment of the day, two MgF₂ windows with cells were measured. On each treatment group, 40 ~ 60 Raman spectra from multiple individual cells (10 ~ 15 cells, each cell collected 4 spectra but position was changed about 3 μm) were detected within 2 hours at room temperature. Renishaw Wire 3.3 software (Renishaw) performed for Raman spectra baseline corrected, spectral smoothed and normalized at maximum peaks. The processed spectra were imported to OriginPro 8 software (OriginLab Corp., Northampton, MA, USA) for Raman intensity analysis. The significance testing was employed by one-way ANOVA, and the data were reported as mean ± SD. Principal component analysis (PCA) was processed in Matlab R2012b using baseline corrected data.

2.4.4 Atomic force microscopy

Contact mode AFM controlled by Picoview software (Picoplus, Agilent Technologies, Santa Clara, CA, USA) was applied to trophoblast cells on MgF₂ in culture medium. Sharp silicon nitride AFM probes (tip radius, 20nm) were employed (Bruker Corp., Billerica, MA, USA). Spring constant of tips was calibrated as 0.10~0.11 N/m and deflection sensitivities were 45~50 nm/V.

Scanning Probe Image Processor (SPIP) software (Image Metrology, Hørsholm, Denmark) calculated Young's modulus by converting the force-distance curves to force-separation curves and fitting the Sneddon variation of Hertz model as below formula shows [36-38]:

$$E_{\text{cell}} = 4 \cdot F_{(\Delta Z)} \cdot (1 - \eta_{\text{cell}}^2)/3 \cdot (\Delta Z)^{1.5} \cdot \tan \theta$$
, where E_{cell} : Young's modulus; F : loading force; η_{cell} : Poisson ratio; ΔZ : indentation; θ : tip half cone opening angle.

The Poisson's ratio was 0.5 and the tip half cone opening angle was 36°. For each group, at least 20 force curves of each cell (the total cells are over 15) were collected, and detection was accomplished within 2 hours to approximate normal physiologic conditions. The AFM images were processed with WSXM software (Nanotec Electrónica S.L., Tres Cantos, Madrid, Spain) for deflection and 3-D view.

2.4.5 Quantitative real time PCR analysis

On days 3 and 10, total RNA was isolated from cells by the Total RNA kit I (Omega Bio-tek; Norcross, GA, USA) following protocol. mRNA was reverse transcribed using GoScript Reverse Transcription System kit from Promega (Madison, WI, USA). Quantitative PCR (qPCR) was performed on the Eppendorf Mastercycler Realplex2 machine

using Promega GoTaq qPCR master mix with primers (Table 2.2) for HAND1, KLF4, CYP17A1, KRT8 and EIF4A1 genes.

Table 2.2 Forward and reverse primer of HAND1, KLF4, KRT8 and EIF4A1 (Forty (40) two-step cycles (95° C/15 s denaturation – 60° C/30 s anneal/extend) were used for amplification, followed by a melt curve analysis to confirm the identity of the fragments amplified. The $\Delta\Delta$ CT method was used to analyze the qPCR data. EIF4A1 was used as a housekeeping gene to normalize CT values. The serum-free samples were used as control samples.

Gene	Forward primer	Reverse primer
HAND1	5'-GCGAGAGCAAGCGGAAAA-3'	5'-CCTGTGCGCCCTTTAATCC-3'
KLF4	5'-GGGAAGGGAGAAGACACTG-3'	5'-TCTTTGCTTCATGTGGGAGA-3'
CYP17A1	5'-GGACACAGATGTCGTCGTCAA-3'	5'-AAGCGCTCAGGCATGAACA-3'
KRT8	5'-AAGCGTACCGACATGGAGAA-3'	5'-TCCAGCTCGACCTTGTTCA-3'
EIF4A1	5'-AGGATCATGTCTGCGAGTCAGG-3'	5'-ATAGATGCCACGGAGGAGGGAC-3'

2.5 RESULTS AND DISCUSSION

2.5.1 Fluorescence imaging for trophoblast cells

Figure 2.1 compares nucleus diameter of the groups at different days (Figure 2.1(A)) and shows representative cell images on each group (Figure 2.1(B)). According to Figure 2.1(A), the nucleus diameter of serum-free cell maintains similar value with time, from 27.5

$\pm 4.6 \mu\text{m}$ at day 3 to $26.1 \pm 5.3 \mu\text{m}$ at day 10. On the contrary, the nucleus diameter of cells in serum gradually increases with time, from $41.6 \pm 9.5 \mu\text{m}$ at day 3 to $55.8 \pm 9.1 \mu\text{m}$ at day 7, maximizing at day 10 ($67.0 \pm 9.7 \mu\text{m}$).

Overall, the above observations indicate trophoblast cells maintain smaller nucleus diameter in serum-free medium up to 10 days.

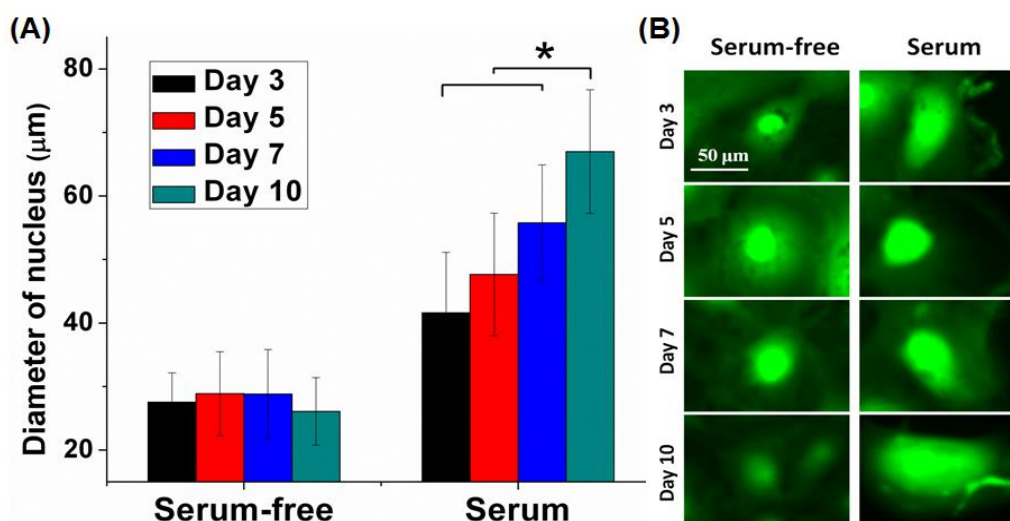


Figure 2.1 Nucleus diameter of trophoblast cells (A) and representative GFP images of cells (B) in serum-free and serum medium at day 3, 5, 7 and 10 (Error bars of (A) are standard deviation of the mean; $N \geq 50$, $*P < 0.05$).

2.5.2 Raman intensity comparison

After exposure to 785 nm laser in Raman detection (within 2 hrs), LIVE/DEAD Viability/Cytotoxicity was conducted by staining cells with Calcein AM (green, live cells)/ethidium homodimer-1 (red, dead cells) (Invitrogen). Few dead cells were observed, indicating little photodamage effect from Near Infrared light, which is consistent with previous studies [39-41].

Table 2.3 Tentative Raman band assignments of trophoblast cells.

Raman shift (cm ⁻¹)	Band assignment
624	Phenylalanine
643	C-C twist Phenylalanine
662	C-S stretching mode of cystine (collagen type I)
666	G, T-tyrosine-G backbone in RNA
672	C-S stretching mode of cytosine
717	CN ⁻ (CH ₃) ₃ (lipids)
719	C-C-N ⁺ symmetric stretching in phosphatidylcholine
720	DNA
760	Tryptophan
786	DNA & phosphodiester bands DNA
813	Phosphodiester bands RNA
832	PO ₂ ⁻ stretch nucleic acids
854	Tyrosine
881	Tryptophan
939	Skeletal modes (polysaccharides)
961	Phosphate of HA; Calcium-phosphate stretch band
1006	Phenylalanine
1031	Phenylalanine
1057	lipids
1066	PO ₂ ⁻ stretching; chain stretching; C-O, C-C stretching
1070-90	Symmetric PO ₂ ⁻ stretching of DNA
1095	Lipid; Phosphodioxo group (PO ₂ ⁻ in nucleic acids)
1129	C-C skeletal stretch transconformation
1158	Lipids and nucleic acids (C, G and A)
1179	Cytosine, guanine
1213	Tyrosine, phenylalanine
1254	Lipid; A,T breathing mode; Amide III (protein)
1304	CH ₂ deformation (lipid), adenine, cytosine
1306	C-N stretching aromatic amines
1317-9	Guanine (B,Z-marker)
1341	G (DNA/RNA); CH deformation
1400-30	γ(C=O) O- (amino acids aspartic & glutamic acid)
1451	CH ₂ deformation (nucleic acid, proteins, lipids)
1579	Pyrimidine ring (nucleic acids)
1608	Phenylalanine, Tryptophan
1660	Amide I
1740	Collagen III

Band assignment is based on [42-50].

Table 2.3 lists the tentative Raman band assignments of trophoblast cells. There are some remarkable differences among groups, for example, 717 cm^{-1} ($\text{CN}^{-1}(\text{CH}_3)_3$ (lipid/choline)), 760 cm^{-1} (Tryptophan), 786 cm^{-1} (DNA & phosphodiester bands DNA), 813 cm^{-1} (Phosphodiester bands RNA), 1006 cm^{-1} (Phenylalanine) and 1057 cm^{-1} (lipid). The mean Raman peaks intensities were extracted to quantitatively analyze the differences, as shown in Figure 2.2. For serum groups, the DNA intensity gradually decreases from 0.12 at day 3 to 0.09 at day 10 (Figure 2.2(A)). However, the DNA intensity of cells in serum-free medium fluctuates over time. Similar to DNA changes, the RNA intensity of serum groups (Figure 2.2(B)) slowly drops, while that of cells in serum-free medium fluctuates over times. The tryptophan (760 cm^{-1}) intensity of serum groups (Figure 2.2(C)) increases over time. However, for cells in serum-free medium the tryptophan intensity fluctuates. Similarly, for serum groups the phenylalanine (1006 cm^{-1}) intensity (Figure 2.2(D)) grows continuously, while that of cells in serum-free medium fluctuates with time. The lipid/choline intensities (717 cm^{-1} and 1057 cm^{-1}) fluctuates with time regardless cells in serum or serum-free medium (Figure 2.2(E-F)).

Our spectral results are similar to previous studies [10, 39, 51, 52] that an increase of protein peak intensity and decrease of nucleic acids peak intensity are related to the differentiation of stem cells. However, the lipid peak intensities exhibits an increasing trend. Regardless of the days in culture, the lipid peaks of serum groups (differentiated cells) are higher than those of serum-free groups (undifferentiated cells). The lipid peaks do not show a steady increase in trophoblast cell system, which is not consistent with those observation in multipotent and pluripotent stem cells [13]. The reason may be accounted for cell type

difference, and the lipid expression of trophoblast cells may be different from stem cells during their development.

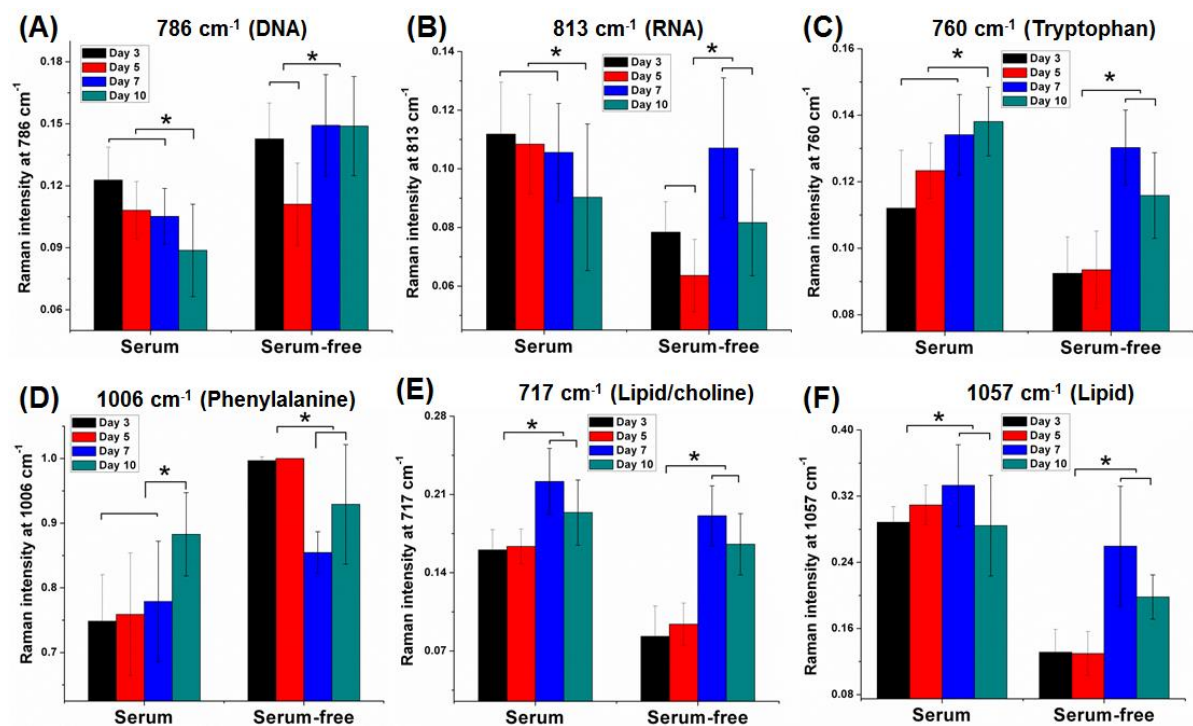


Figure 2.2 Raman peak intensity analysis of trophoblast cells on DNA (A), RNA (B), tryptophan (C), phenylalanine (D), lipid/choline (E) and lipid (F) at day 3 (black), 5 (red), 7 (blue) and 10 (cyan) in serum and serum-free medium (Error bars are standard deviation of the mean; $N \geq 10$, $*P < 0.05$).

2.5.3 Spectroscopic markers comparison and principal component analysis (PCA) of Raman spectra

Previous studies indicate increasing 757 cm^{-1} to 784 cm^{-1} intensity ratio is correlated with the reduction of *Oct4* and *Nanog* expression, which decrease rapidly with the differentiation of human embryonic stem cells (hESCs) [39, 53] and human induced

pluripotent stem cells (hiPSCs) [54]. Here, the peak intensity ratio of 760 cm^{-1} (tryptophan) to 786 cm^{-1} (DNA) was applied to assess trophoblast cells differentiation.

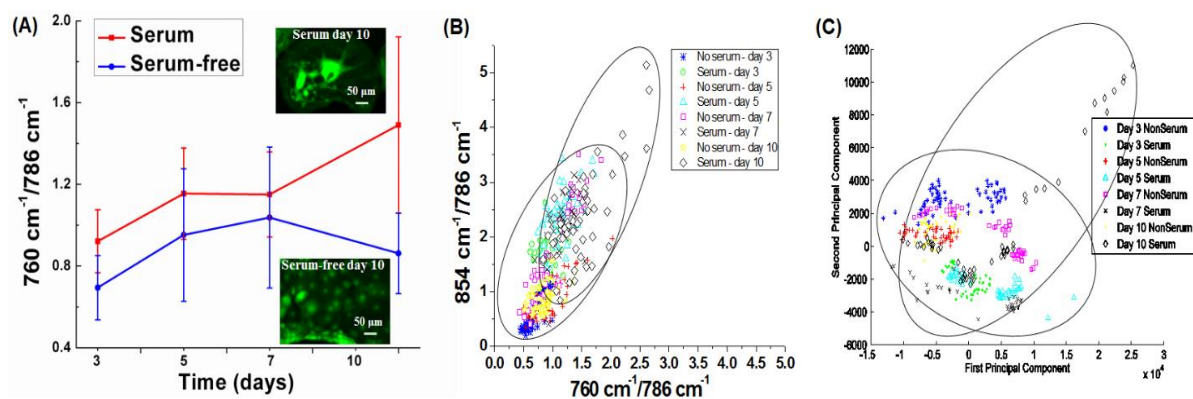


Figure 2.3 Raman peak ratio ($760\text{ cm}^{-1}/786\text{ cm}^{-1}$) in serum and serum-free medium (A) (Inset fluorescence images of trophoblast cells at day 10, scale bar: $50\text{ }\mu\text{m}$); distribution diagram of two protein/nucleic acid peak intensity ratios ($760/786\text{ cm}^{-1}$ and $854/786\text{ cm}^{-1}$) (B), and PCA plot (C) (Error bars of (A) are standard deviation of the mean; $N \geq 10$, $*P < 0.05$).

Peak intensity ratio ($760\text{ cm}^{-1}/786\text{ cm}^{-1}$) of trophoblast cells are presented in Figure 2.3(A) (inset fluorescence images of cells at day 10). The ratios in serum medium were larger than those in serum-free medium at each day. For serum groups the ratio increase in the first five days, then drops slightly, reaching the maximum at day 10. The ratio of serum-free groups grows in the first seven days, then decrease largely at day 10. This ratio of serum groups increased with time, probably suggesting the cellular differentiation. In contrast, the ratio fluctuated for serum-free groups, which may indicate cells still remain undifferentiated or differentiated slowly in serum-free medium.

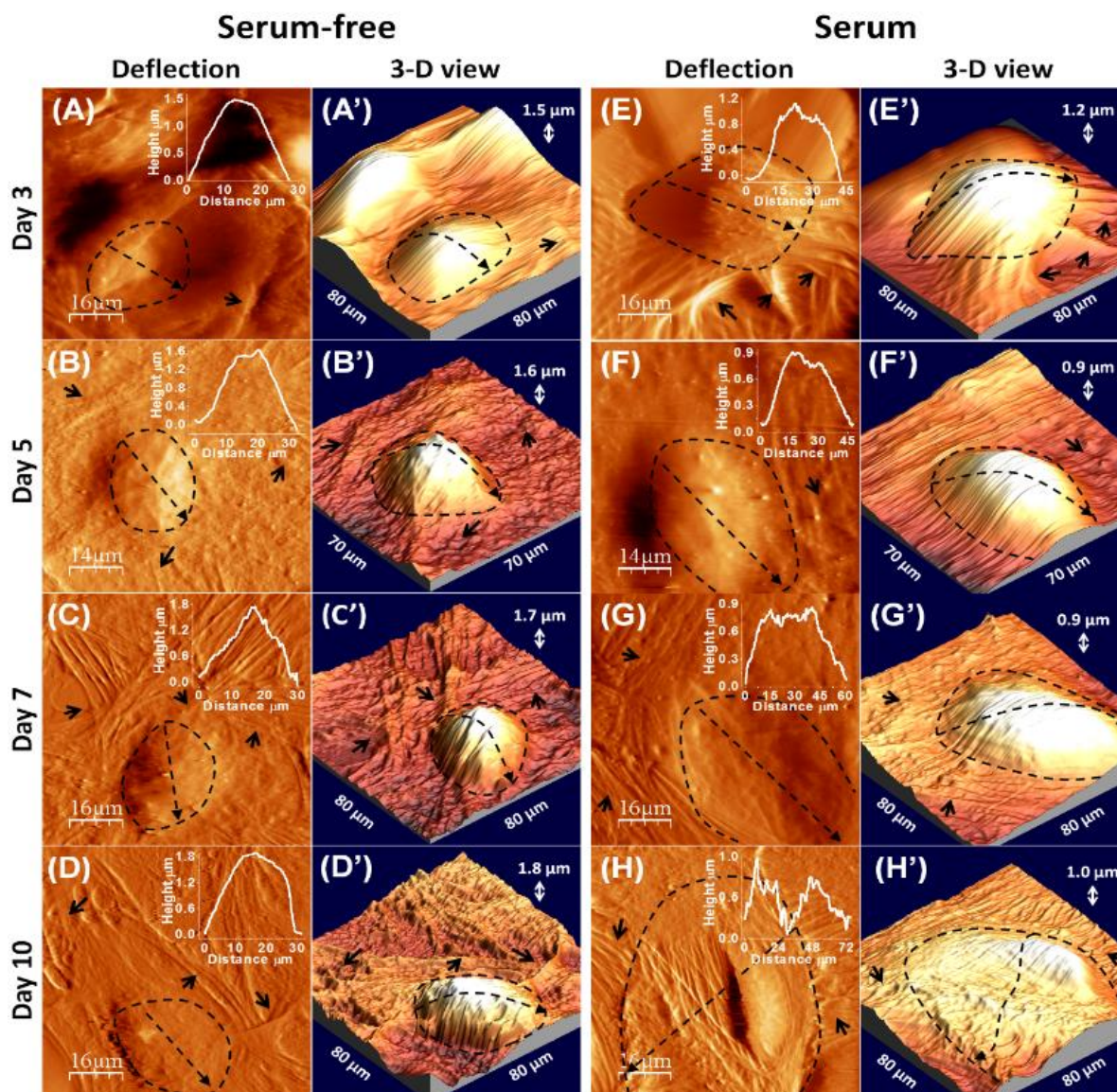


Figure 2.4 AFM deflection (A-H) and corresponding 3-D view (A'-H') images of cells in serum-free and serum medium at day 3, 5, 7 and 10. Insets in deflection images are the line profiling of nucleus height.

Turner et al. have successfully assessed hESCs differentiation by distribution diagram of two protein/nucleic acid intensity ratios ($757\text{ cm}^{-1}/784\text{ cm}^{-1}$ (tryptophan/nucleic acid) and $853\text{ cm}^{-1}/784\text{ cm}^{-1}$ (tyrosine/ nucleic acid)) [39]. We applied the same method, as shown in

Figure 2.3(B). The X-axis displays the peak intensity ratio of $760\text{ cm}^{-1}/786\text{ cm}^{-1}$, and Y-axis is the peak intensity ratio of $854\text{ cm}^{-1}/786\text{ cm}^{-1}$. The serum group at day 10 (upper right) has the largest distribution in comparison with other groups, even though over 50% of these points overlay with other points.

PCA is also applied to analyze Raman spectra difference for serum and serum-free groups (each group has ≈ 200 spectra). PCA simplifies the spectra by exhibiting the data with principal component (PC) variables ordered from the largest variance to the least variance [55]. The X-axis and Y-axis correspond to the 1st and the 2nd PC variables, respectively. These two PCs account for 87.58% of variance and mainly represent the Raman spectra of the cells. Similarly to Figure 2.3(B), the data points in serum group at day 10 (white diamond) are not closely clustered, even over 50% of these points overlay with other groups as shown in Figure 2.3(C). Clusters of other groups sit tightly with each other.

Our distribution diagram and PCA analysis (Figure 2.3(B, C) both imply that “Day 10 serum” group exhibits the largest distribution of cellular biocomponents (e.g., proteins/nucleic acids) among other groups.

2.5.4 Topography and biomechanics comparison

The nucleus diameter can be obtained by AFM, as shown in Figure 2.4. The inset is the line profiling of nucleus height crossed cells. The nucleus diameter of cells in serum-free medium (Figure 2.4 (A-D, A'-D')) remains the similar value over time, while its cytoskeleton structures (e.g., filamentous actin bundles) increase from over time. However, the nucleus diameter of serum group (Figure 2.4 (E-H, E'-H')) increases with time, and its surrounding cytoskeleton structures become less visible over time. At day 3, mesh-like structures are clearly visible on surface of cells in serum (Figure 2.4 (E, E')) black arrows

pointed) in comparison with those of serum-free group (Figure 2.4(A, A') one black arrow pointed). Meantime, the nucleus diameter ($\sim 42 \mu\text{m}$) of cells in serum medium is larger than that ($\sim 27 \mu\text{m}$) of cells in serum-free medium. At day 5, the nucleus diameter ($\sim 32 \mu\text{m}$) of cells in serum-free medium is still less than that ($48 \mu\text{m}$) of cells in serum medium. Similar trends are observed over 7 days (cells in serum medium have larger nucleus diameter than those in serum-free medium). For the height differences, the overall height (around $1.65 \mu\text{m}$) of cells in serum-free medium is higher than that (around $1.00 \mu\text{m}$) of cells in serum medium over time. The AFM image analysis confirms the result of nucleus diameter shown in Figure 2.1.

To analyze the biomechanics properties, we compare the Young's modulus (via AFM force-distance curve measurements) of different groups (Figure 2.5). Serum groups show a gradual increase in Young's modulus over time, from $3.16 \pm 0.90 \text{ kPa}$ at day 3 to $11.20 \pm 4.41 \text{ kPa}$ at day 10. However, Young's modulus of serum-free groups remains unchanged ($\sim 7.30 \text{ kPa}$) from day 3 to 7, then significantly increases to $13.70 \pm 4.11 \text{ kPa}$ at day 10.

The Young's modulus gradually increases in serum groups over time, which is similar to the mouse embryonic stem cells study conducted by Pillarisetti et al. [24]. However, that of serum-free groups maintains stable at first 7 days, followed by significant increase at day 10. Further studies are needed to investigate the reason leading to Young's modulus increase of undifferentiated cells at day 10.

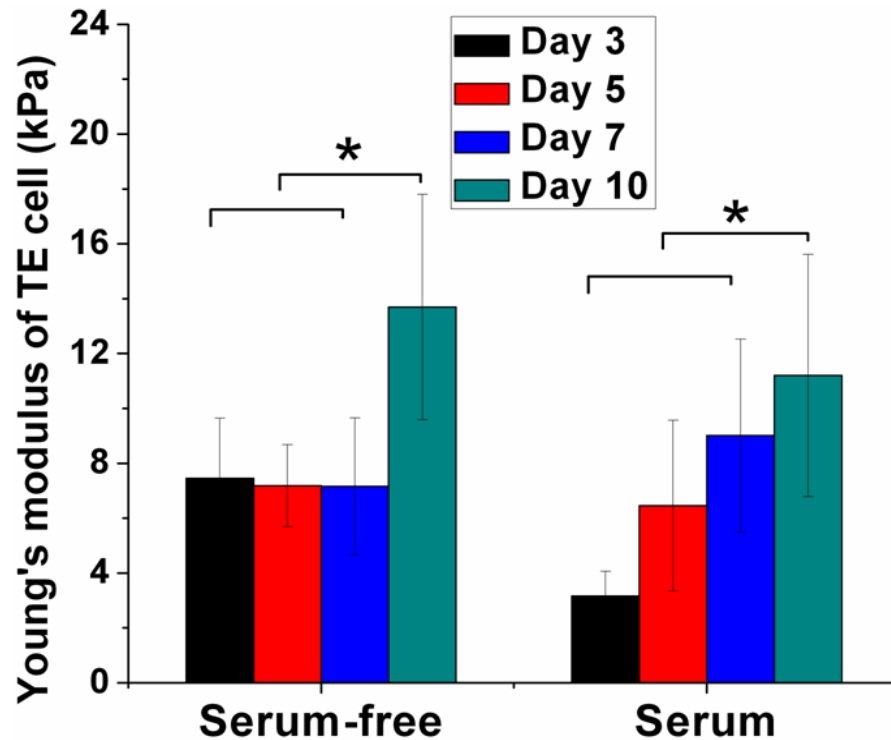


Figure 2.5 Young's modulus of cells in serum-free and serum medium at day 3, 5, 7 and 10.

Error bars are standard deviation of the mean; $N \geq 10$, $*P < 0.05$.

2.5.5 Analysis of gene expression by qPCR

Four genes were selected for qPCR: CYP17A1, HAND1, KLF4 and KRT8. The gene CYP17A1 is involved in the steroid biosynthetic pathway, testing for differentiation [56]. HAND1 is essential for placental development and to promote trophoblast giant cells differentiation [57]. The KLF4 gene is a transcription factor that regulates proliferation, differentiation, development and apoptosis [58]. KRT8 is prominent in simple single-layer epithelial cells, such as differentiated trophoblast [59].

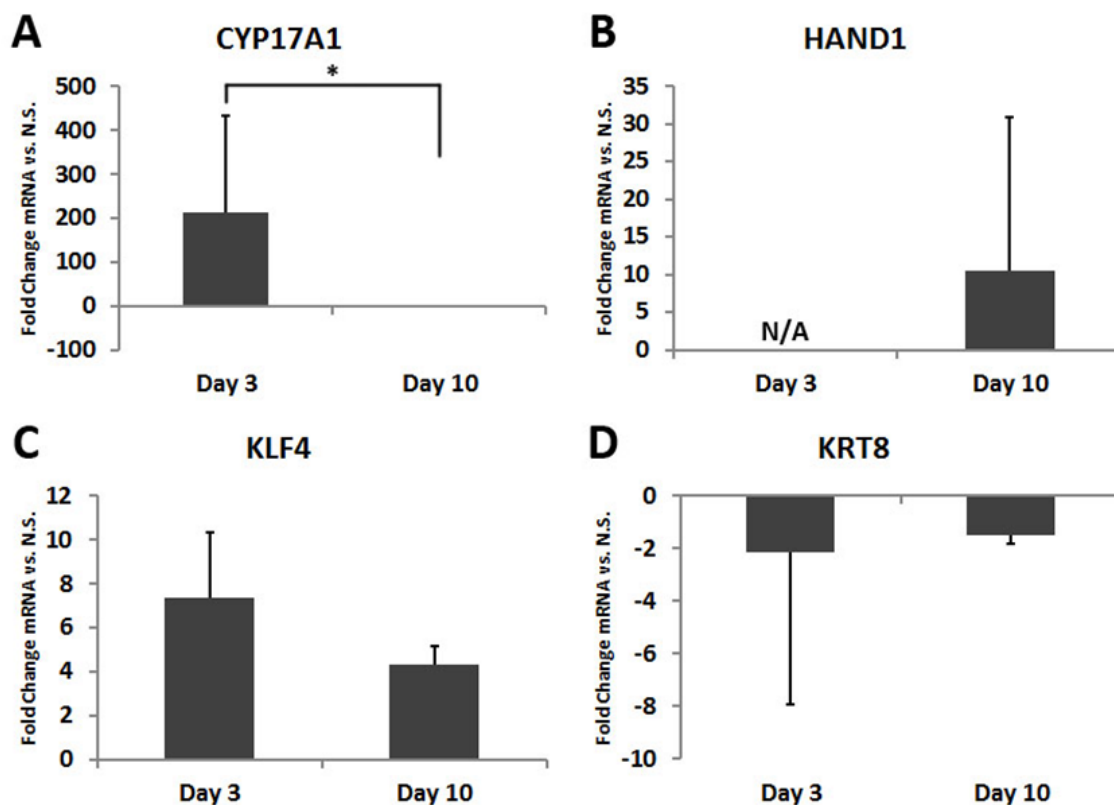


Figure 2.6 Gene expression analysis of cells cultured 3 and 10 days in serum medium compared to serum-free medium by qPCR. All values are presented as a ratio of fold-change values: Serum/Non-serum fold-change. A) CYP17A1 levels. The ratio at day 10 was approach zero, which does not register on the scale used to present the data, but should not be interpreted as an absent or null value (as in panel B); B) HAND1 levels; C) KLF4 levels; D) Relative KRT8 levels. Error bars are standard error of the mean. (N = 3, * $P < 0.05$; N.S. = non-serum; N/A = fold change ratio not available because of a null value for non-serum group).

In Figure 2.6, the X-axis displays time point and the Y-axis shows the expression ratio (fold-change; serum/non-serum). Figure 2.6(A) exhibits that on day 3 CYP17A1 are

approximately 200-fold higher for serum group than serum-free group, but this discrepancy has disappeared by day 10. Day 3 HAND1 from serum-treated cells are undetectable, thus there is insufficient data (N/A = not available) in Panel B. Panel C shows there is a numerical drop in relative KLF4 gene expression in serum- vs. un-treated cells, but this drop is not statistically significant and relative KRT8 gene expression levels do not change significantly across time in Panel D.

Cells express very low levels of CYP17A1 when cultured in serum-free conditions, but CYP17A1 is turned on when these cells are in serum medium. After three days the cells in serum medium showed a 200 fold upregulation of CYP17A1 compared to the serum-free groups. There is a significant decrease of CYP17A1 from day 3 to day 10. HAND1 transcripts were undetectable in serum groups on day 3, so expression ratio was not feasible. For day 10, the serum group had 12-fold higher HAND1 expression compared to the cells cultured in non-serum medium, which is consistent with the role played by HAND1 in cellular differentiation. qPCR results demonstrated a non-significant drop when analyzing KLF4 and KRT-8 genes. Thus, these genes might not have an impact on these cells. The medium and time differences might impact the expression of certain genes, and these biomacromolecules variations can also be observed in Figure 2.2.

Our initial qPCR results give us clues that we may seek and screen more genes related to cell biomechanics (e.g., cell adhesion, extracellular matrix) and cell differentiation to sort out such potential correlation.

2.6 CONCLUSION

Porcine trophoblast derived cells are interesting model for stem like cell research for their regenerative properties, indefinite passage, and foreign DNA receptivity. Trophoblast

cells exhibit different morphologies and functions with/without serum medium, providing a unique tool for studying trophoblast cell differentiation. This is the first work to combine RM and AFM to compare trophoblast cell differentiation, showing that RM and AFM are able to distinguish between undifferentiated and differentiated trophoblast cells. Meantime, this work evaluated the biochemical and biophysical changes of both undifferentiated and differentiating cells at the same day instead of only studying cellular differentiation over time. Characterization of trophoblast cells biochemical and biophysical properties extends the knowledge to further investigations as this area develops.

2.7 REFERENCES

1. Leahy A, Xiong JW, Kuhnert F, Stuhlmann H. Use of developmental marker genes to define temporal and spatial patterns of differentiation during embryoid body formation. *J Exp Zool.* 1999; 284: 67-81.
2. Alcock J, Sottile V. Dynamic distribution and stem cell characteristics of Sox1-expressing cells in the cerebellar cortex. *Cell Res.* 2009; 19: 1324-33.
3. Ratcliffe E, Thomas RJ, Williams DJ. Current understanding and challenges in bioprocessing of stem cell-based therapies for regenerative medicine. *Br Med Bull.* 2011; 100: 137-55.
4. Tang M, Li Q, Xiao L, Li Y, Jensen JL, Liou TG, et al. Toxicity effects of short term diesel exhaust particles exposure to human small airway epithelial cells (SAECs) and human lung carcinoma epithelial cells (A549). *Toxicol Lett.* 2012; 215: 181-92.
5. Wu YZ, McEwen GD, Harihar S, Baker SM, DeWald DB, Zhou AH. BRMS1 expression alters the ultrastructural, biomechanical and biochemical properties of

- MDA-MB-435 human breast carcinoma cells: An AFM and Raman microspectroscopy study. *Cancer Lett.* 2010; 293: 82-91.
6. Ghita A, Pascut FC, Mather M, Sottile V, Notingher I. Cytoplasmic RNA in Undifferentiated Neural Stem Cells: A Potential Label-Free Raman Spectral Marker for Assessing the Undifferentiated Status. *Anal Chem.* 2012; 84: 3155-62.
 7. Chan JW, Lieu DK. Label-free biochemical characterization of stem cells using vibrational spectroscopy. *J Biophotonics.* 2009; 2: 656-68.
 8. Zoladek A, Pascut FC, Patel P, Notingher I. Non-invasive time-course imaging of apoptotic cells by confocal Raman micro-spectroscopy. *J Raman Spectrosc.* 2011; 42: 251-8.
 9. Notingher I, Hench LL. Raman microspectroscopy: a noninvasive tool for studies of individual living cells in vitro. *Expert Rev Med Devic.* 2006; 3: 215-34.
 10. Notingher L, Bisson I, Polak JM, Hench LL. In situ spectroscopic study of nucleic acids in differentiating embryonic stem cells. *Vib Spectrosc.* 2004; 35: 199-203.
 11. Downes A, Mouras R, Elfick A. Optical Spectroscopy for Noninvasive Monitoring of Stem Cell Differentiation. *J Biomed Biotechnol.* 2010.
 12. Chiang HK, Peng FY, Hung SC, Feng YC. In situ Raman spectroscopic monitoring of hydroxyapatite as human mesenchymal stem cells differentiate into osteoblasts. *J Raman Spectrosc.* 2009; 40: 546-9.
 13. Pijanka JK, Kumar D, Dale T, Yousef I, Parkes G, Untereiner V, et al. Vibrational spectroscopy differentiates between multipotent and pluripotent stem cells. *Analyst.* 2010; 135: 3126-32.

14. Pascut FC, Goh HT, Welch N, BATTERY LD, Denning C, Notingher I. Noninvasive Detection and Imaging of Molecular Markers in Live Cardiomyocytes Derived from Human Embryonic Stem Cells. *Biophys J*. 2011; 100: 251-9.
15. Downes A, Mouras R, Bagnaninchi P, Elfick A. Raman spectroscopy and CARS microscopy of stem cells and their derivatives. *J Raman Spectrosc*. 2011; 42: 1864-70.
16. Aksoy C, Severcan F. Role of Vibrational Spectroscopy in Stem Cell Research. *Spectrosc-Int J*. 2012; 27: 167-84.
17. Notingher I, Bisson I, Bishop AE, Randle WL, Polak JMP, Hench LL. In situ spectral monitoring of mRNA translation in embryonic stem cells during differentiation in vitro. *Anal Chem*. 2004; 76: 3185-93.
18. McManus LL, Burke GA, McCafferty MM, O'Hare P, Modreanu M, Boyd AR, et al. Raman spectroscopic monitoring of the osteogenic differentiation of human mesenchymal stem cells. *Analyst*. 2011; 136: 2471-81.
19. Binnig G, Quate CF, Gerber C. Atomic Force Microscope. *Phys Rev Lett*. 1986; 56: 930-3.
20. Dorobantu LS, Gray MR. Application of atomic force microscopy in bacterial research. *Scanning*. 2010; 32: 74-96.
21. McElfresh M, Baesu E, Balhorn R, Belak J, Allen MJ, Rudd RE. Combining constitutive materials modeling with atomic force microscopy to understand the mechanical properties of living cells. *Proc Natl Acad Sci U S A*. 2002; 99: 6493-7.
22. Wu YZ, Yu T, Gilbertson TA, Zhou AH, Xu H, Nguyen KT. Biophysical Assessment of Single Cell Cytotoxicity: Diesel Exhaust Particle-Treated Human Aortic Endothelial Cells. *Plos One*. 2012; 7.

23. Pillarisetti. A, Keefer. C, Desai. JP. Mechanical Response of Embryonic Stem Cells Using Haptics-Enabled Atomic Force Microscopy. Springer Tracts in Advanced Robotics. 2009; 54: 261-9.
24. Pillarisetti A, Desai JP, Ladjal H, Schiffmacher A, Ferreira A, Keefer CL. Mechanical Phenotyping of Mouse Embryonic Stem Cells: Increase in Stiffness with Differentiation. Cell Reprogram. 2011; 13: 371-80.
25. Keefer CL, Desai JP. Mechanical phenotyping of stem cells. Theriogenology. 2011; 75: 1426-30.
26. Gonzalez-Cruz RD, Fonseca VC, Darling EM. Cellular mechanical properties reflect the differentiation potential of adipose-derived mesenchymal stem cells. Proc Natl Acad Sci U S A. 2012; 109: E1523-E9.
27. Kiss R, Bock H, Pells S, Canetta E, Adya AK, Moore AJ, et al. Elasticity of Human Embryonic Stem Cells as Determined by Atomic Force Microscopy. J Biomech Eng. 2011; 133.
28. Blomberg L, Hashizume K, Viebahn C. Blastocyst elongation, trophoblastic differentiation, and embryonic pattern formation. Reproduction. 2008; 135: 181-95.
29. Pfeffer PL, Pearton DJ. Trophoblast development. Reproduction. 2012; 143: 231-46.
30. Senner CE, Hemberger M. Regulation of early trophoblast differentiation - lessons from the mouse. Placenta. 2010; 31: 944-50.
31. Hill JR, Burghardt RC, Jones K, Long CR, Looney CR, Shin T, et al. Evidence for placental abnormality as the major cause of mortality in first-trimester somatic cell cloned bovine fetuses. Biol Reprod. 2000; 63: 1787-94.

32. Constant F, Guillomot M, Heyman Y, Vignon X, Laigre P, Servely JL, et al. Large offspring or large placenta syndrome? Morphometric analysis of late gestation bovine placentomes from somatic nuclear transfer pregnancies complicated by hydrallantois. *Biol Reprod.* 2006; 75: 122-30.
33. Chavatte-Palmer P, Camous S, Jammes H, Le Cleac'h N, Guillomot M, Leed RSF. Review: Placental perturbations induce the developmental abnormalities often observed in bovine somatic cell nuclear transfer. *Placenta.* 2012; 33: S99-S104.
34. Suasnavas EA, Heywood S, Ward A, Cox L, O'Grady M, Zhao YF, et al. Isolation and characterization of trophoblast-derived stem-like cells from peri-implantation porcine embryos. *Anim Reprod Sci.* 2015; 154: 128-41.
35. Dyce PW, Zhu H, Craig J, Li J. Stem cells with multilineage potential derived from porcine skin. *Biochem Bioph Res Co.* 2004; 316: 651-8.
36. Sneddon IN. The relation between load and penetration in the axisymmetric boussinesq problem for a punch of arbitrary profile. *Int J Eng Sci.* 1965; 3: 47-57.
37. Butt HJ, Cappella B, Kappl M. Force measurements with the atomic force microscope: Technique, interpretation and applications. *Surf Sci Rep.* 2005; 59: 1-152.
38. Rosenbluth MJ, Lam WA, Fletcher DA. Force microscopy of nonadherent cells: A comparison of leukemia cell deformability. *Biophys J.* 2006; 90: 2994-3003.
39. Schulze HG, Konorov SO, Caron NJ, Piret JM, Blades MW, Turner RFB. Assessing Differentiation Status of Human Embryonic Stem Cells Noninvasively Using Raman Microspectroscopy. *Anal Chem.* 2010; 82: 5020-7.

40. Chan JW, Lieu DK, Huser T, Li RA. Label-Free Separation of Human Embryonic Stem Cells and Their Cardiac Derivatives Using Raman Spectroscopy. *Anal Chem.* 2009; 81: 1324-31.
41. Notingher I, Verrier S, Haque S, Polak JM, Hench LL. Spectroscopic study of human lung epithelial cells (A549) in culture: living cells versus dead cells. *Biopolymers.* 2003; 72: 230-40.
42. Movasaghi Z, Rehman S, Rehman IU. Raman spectroscopy of biological tissues. *Appl Spectrosc Rev.* 2007; 42: 493-541.
43. Yu C, Gestl E, Eckert K, Allara D, Irudayaraj J. Characterization of human breast epithelial cells by confocal Raman microspectroscopy. *Cancer Detect Prev.* 2006; 30: 515-22.
44. Stone N, Kendall C, Smith J, Crow P, Barr H. Raman spectroscopy for identification of epithelial cancers. *Faraday Discuss.* 2004; 126: 141-57; discussion 69-83.
45. Stone N, Kendall C, Shepherd N, Crow P, Barr H. Near-infrared Raman spectroscopy for the classification of epithelial pre-cancers and cancers. *J Raman Spectrosc.* 2002; 33: 564-73.
46. Cheng WT, Liu MT, Liu HN, Lin SY. Micro-Raman spectroscopy used to identify and grade human skin pilomatrixoma. *Microsc Res Techniq.* 2005; 68: 75-9.
47. Shetty G, Kendall C, Shepherd N, Stone N, Barr H. Raman spectroscopy: elucidation of biochemical changes in carcinogenesis of oesophagus. *Brit J Cancer.* 2006; 94: 1460-4.
48. Ruiz-Chica AJ, Medina MA, Sanchez-Jimenez F, Ramirez FJ. Characterization by Raman spectroscopy of conformational changes on guanine-cytosine and adenine-

- thymine oligonucleotides induced by aminoxy analogues of spermidine. *J Raman Spectrosc.* 2004; 35: 93-100.
49. Chan JW, Taylor DS, Zwerdling T, Lane SM, Ihara K, Huser T. Micro-Raman spectroscopy detects individual neoplastic and normal hematopoietic cells. *Biophys J.* 2006; 90: 648-56.
50. Chiriboga L, Xie P, Yee H, Vigorita V, Zarou D, Zakim D, et al. Infrared spectroscopy of human tissue. I. Differentiation and maturation of epithelial cells in the human cervix. *Biospectroscopy.* 1998; 4: 47-53.
51. Konorov SO, Glover CH, Piret JM, Bryan J, Schulze HG, Blades MW, et al. In situ analysis of living embryonic stem cells by coherent anti-stokes Raman Microscopy. *Anal Chem.* 2007; 79: 7221-5.
52. Puppels GJ, Demul FFM, Otto C, Greve J, Robertnicoud M, Arndtjovin DJ, et al. Studying Single Living Cells and Chromosomes by Confocal Raman Microspectroscopy. *Nature.* 1990; 347: 301-3.
53. Konorov SO, Schulze HG, Caron NJ, Piret JM, Blades MW, Turner RFB. Raman microspectroscopic evidence that dry-fixing preserves the temporal pattern of non-specific differentiation in live human embryonic stem cells. *J Raman Spectrosc.* 2011; 42: 576-9.
54. Tan Y KS, Schulze HG, Piret JM, Blades MW, Turner RF. Comparative study using Raman microspectroscopy reveals spectral signatures of human induced pluripotent cells more closely resemble those from human embryonic stem cells than those from differentiated cells. *Analyst* 2012: 5-34.

55. Harkness L, Novikov SM, Beermann J, Bozhevolnyi SI, Kassem M. Identification of Abnormal Stem Cells Using Raman Spectroscopy. *Stem Cells Dev.* 2012; 21: 2152-9.
56. Asanoma K, Rumi MA, Kent LN, Chakraborty D, Renaud SJ, Wake N, et al. FGF4-dependent stem cells derived from rat blastocysts differentiate along the trophoblast lineage. *Dev Biol.* 2011; 351: 110-9.
57. Scott IC, Anson-Cartwright L, Riley P, Reda D, Cross JC. The HAND1 basic helix-loop-helix transcription factor regulates trophoblast differentiation via multiple mechanisms. *Mol Cell Biol.* 2000; 20: 530-41.
58. McConnell BB, Ghaleb AM, Nandan MO, Yang VW. The diverse functions of Kruppel-like factors 4 and 5 in epithelial biology and pathobiology. *Bioessays.* 2007; 29: 549-57.
59. Moll, R., Cytokeratins as markers of differentiation. Expression profiles in epithelia and epithelial tumors. *Veroff Pathol.* 1993; 142: 1-197.

CHAPTER 3

IN VITRO EVALUATION OF THE ROLE OF BREAST CANCER METASTASIS SUPPRESSOR 1 (BRMS1) IN BREAST CNACER CELLS TO CHEMOTHERAPY USING A MULTIMODAL APPROACH

3.1 ABSTRACT

The Breast Cancer Metastasis Suppressor 1 (BRMS1) is a nucleo-cytoplasmic protein that suppresses cancer metastasis without affecting the growth of the primary tumor. Previous work has shown that it decreases the expression of protein mediators involved in chemoresistance. This study measured the biomechanical and biochemical changes in BRMS1 expression and the responses of BRMS1 to drug treatments on cancer cells in vitro. The results show that BRMS1 expression affects biomechanical properties by decreasing the Young's modulus and adhesion force of breast cancer cells after doxorubicin (DOX) exposure. Raman spectral bands corresponding to DNA/RNA, lipids and proteins were similar for all cells after DOX treatment. The expression of cytokines were similar for cancer cells after DOX exposure, although BRMS1 expression had different effects on the secretion of cytokines for breast cancer cells. The absence of significant changes on apoptosis, reactive oxygen species (ROS) expression and cell viability after BRMS1 expression shows that BRMS1 has little effect on cellular chemoresistance. Analyzing cancer protein expression is critical in evaluating therapeutics. Our study may provide evidence of the benefit of metastatic suppressor expression before chemotherapy.

3.2 INTRODUCTION

The most deadly feature of cancer cells is their metastatic property, which is controlled by metastasis suppressors. Clinical studies have reported that Breast Cancer Metastasis Suppressor 1 (BRMS1) affects disease progression and prognosis [1, 2]. BRMS1 is part of an expanding class of proteins called metastasis suppressors that stifle cancer metastasis without affecting the primary tumor growth [3]. A loss of BRMS1 is correlated with poor prognosis among cancer patients [4-6]. BRMS1 decreases the expression and activity of numerous mediators of chemoresistance such as NF- κ B activity [7] and AKT phosphorylation [8] in several cancer models [9-11]. Some reports studied BRMS1's effect on cellular biophysical and biocomponents differences [12, 13], but little research evaluates these biophysical and biochemical changes in response to drug treatments in presence of BRMS1. Thus, we compared the responses of cancer cells with and without BRMS1 to a therapeutic agent using multiple approaches.

Atomic force microscopy (AFM) is a scanning analytical technique that can measure the biomechanical and topographical characteristics of a sample at nanoscale resolution [14, 15]. Attractive or repulsive forces between tip and sample surface will cause a positive or negative bending of the cantilever. This alteration is detected by a laser, and reflected by a position photodetector [15, 16]. AFM has been used to detect biomechanical differences between human lung adenocarcinoma epithelial cell (A549) and human primary small airway epithelial cell (SAECs) after exposure to anticancer drugs [17]. Therefore, AFM was selected to study the biomechanical properties of cells.

Raman microspectroscopy (RM) is a spectroscopic technique based on inelastic scattering when a laser impinges upon a molecule, interacting with the electron cloud and

the bonds of that molecule. RM provides chemical information in the vibrational system, so it can identify chemical molecular compositions through characteristic fingerprints in living cells [18]. RM is used to study cells in near physiological conditions, without labeling or fixation [19], and has been applied to investigate the interaction between pharmaceuticals and living cells in toxicology studies [20]. Thus, RM is a suitable technique to collect the biochemical information of cells.

Apoptosis, ROS expression and cell viability tests were also applied to detect BRMS1's effect on cellular chemoresistance. Apoptosis is a universal and efficient suicide pathway in cells, and it might enhance a death cascade by a drug [21]. ROS, generated during cellular metabolism, are oxygen-containing molecules that can damage DNA, proteins, and lipids [22]. The viability of cancer cells will change according to the interaction conditions with anticancer drugs. Comparing the results of apoptosis, ROS expression and cell viability between parental and BRMS1-expressing cells though doxorubicin (DOX) exposure can reflect BRMS1 effect on chemosensitivity. In this work, using five different cell lines: metastatic MDA-MB-231 (231), metastatic MDA-MB-435 (435), non-metastatic MDA-MB-231/BRMS1 (231/BRMS1), non-metastatic MDA-MB-435/BRMS1 (435/BRMS1) and A549. We investigated the biomechanical and biochemical changes induced on BRMS1 expression when treated with the chemotherapeutic agent DOX. Knowledge of these differences could improve the understanding of metastasis suppressors and be of significant clinical benefit in human cancer therapy.

3.3 HYPOTHESIS

BRMS1 expression has limited impact on cellular physiological conditions when cancer cells were treated with anti-cancer drugs (DOX).

3.4 MATERIALS AND METHODS

3.4.1 Cell culture

To express BRMS1 cDNA, 231 and 435 cells were transfected with a lentiviral vector construct under a cytomegalovirus promoter. 231, 231/BRMS1, 435 and 435/BRMS1 cells were cultured in a 1:1 mixture of Dulbecco's-modified eagle's medium (DMEM) and Ham's F-12 medium supplemented with 5% fetal bovine serum (Thermo Fisher Scientific, Waltham, MA, USA). A549 cells (ATCC, Manassas, VA, USA) were cultured in F-12k medium containing 10% fetal bovine serum at 37 °C with 5% CO₂ in a humidified atmosphere. All cells were passaged at 80-90% confluency using 0.5% Trypsin-EDTA solution (Thermo Fisher Scientific).

3.4.2 Drug preparation and treatment

DOX was dissolved in deionized water. Stock solutions of DOX (8 µM) were stored at 4 °C according to instructions (Sigma-Aldrich, St. Louis, MO, USA). For final drug concentrations, solutions were serially diluted. The dose of DOX treatment for A549 is 71 nM, referring to the study of Kashkin et al [23]. Meantime, the IC₅₀ concentration of DOX corresponding to 231, 231/BRMS1, 435, and 435/BRMS1 cell is 49 nM, 71 nM, 122 nM, and 114 nM, respectively, referring to the research from Danney et al [24].

3.4.3 Immunofluorescence for detection of BRMS1 localization

435 and 435/BRMS1 cells were plated on cover slips (Thermo Fisher Scientific), washed with cold PBS (Thermo Fisher Scientific), fixed with 4% para-formaldehyde (Electron microscopy sciences, Hatfield, PA, USA) and permeabilized with 0.2% Triton X-

100 in PBS. After blocking with 5% Bovine serum albumin (BSA) in PBS for one hour, cells were incubated with anti-BRMS1 monoclonal antibody (1:100 dilution) in 5% BSA solution overnight at 4⁰C. After washing thrice with PBS, Alexa Fluor 488-labeled anti-mouse IgG (1:400 dilution, Thermo Fisher Scientific) was added and incubated at room temperature for 1 hour. After washing the cells thrice with PBS, the cover slips were mounted (Vector laboratories Inc., Burlingame, CA, USA) and observed under an Olympus IX-70 inverted fluorescence microscope (Olympus America Inc., Center Valley, PA, USA).

3.4.4 Raman spectroscopy

To avoid high near infrared (IR) Raman scattering and fluorescence background, magnesium fluoride (MgF₂, United Crystals Co., Port Washington, NY, USA) substrates were used. The cells were seeded on MgF₂ in culture medium overnight and treated with corresponding IC₅₀ concentration of DOX. Before measurements, cells were rinsed thrice in PBS, and maintained in EBSS (Thermo Fisher Scientific) for Raman spectra collection.

Before experiments began, LIVE/DEAD viability experiments were conducted to verify if the cells were alive on MgF₂. Raman spectra were recorded using a Renishaw inVia Raman spectrometer (Renishaw, Wotton-under-Edge, Gloucestershire, UK) equipped with a 63 × 0.9NA water immersion objective (Leica DMLM, Leica Microsystems, Buffalo Grove, IL, USA) and a 300 mW 785 nm near-IR laser. Spectra were collected in static mode for 1 accumulation at 10 s laser exposure over a wavenumber range of 600-1800 cm⁻¹. Eight cells per treatment were analyzed with micro-Raman spectroscopy. Cosmic rays of Raman spectra were removed by Renishaw WiRE 3.3 software (Renishaw).

3.4.5 Atomic force microscopy

Cells were detected by a contact mode PicoPlus AFM controlled by Picoview software (Agilent Technologies, Santa Clara, CA, USA). Biomechanical properties were calculated from *in situ* force-distance curve measurements in medium at room temperature. The radius of silicon nitride tips was 20 nm. Its spring constant was calibrated to 0.10~0.11 N/m by Thermo K Calibration (Agilent Technologies) and its corresponding deflection sensitivities were 45~50 nm/V. More than 10 cells were detected, collecting at least 15 force curves on the central area of different cells to avoid spurious detections [25, 26]. Scanning Probe Image Processor (SPIP) software (Image Metrology, Hørsholm, Denmark) was used to calculate Young's modulus by fitting the Sneddon variation of Hertz model [27-29]. Adhesion force (the force between tip and cellular surface during tip retracting) was calculated from deflection (nm) vs. distance (nm) curves by SPIP. The half cone-opening angle of tip was 36°, and cellular Poisson's ratio was 0.5. The detection was accomplished within 2 hours (h) to approximate physiological conditions.

$E_{\text{cell}} = 4 \cdot F_{(\Delta Z)} \cdot (1 - \eta_{\text{cell}}^2)/3 \cdot (\Delta Z)^{1.5} \cdot \tan \theta$, where E_{cell} : Young's modulus; F : loading force; η_{cell} : Poisson ratio; ΔZ : indentation; θ : tip half cone opening angle.

3.4.6 Cytokine and chemokine analysis

A total of 25 cytokines and chemokines were selected to analyze their expression. The samples were centrifuged at $250 \times g$ for 5 min, the supernatant was collected and stored at $-80 \text{ }^\circ\text{C}$ prior to the assay. The samples were tested as single batches on Q-Plex ArrayTM kits (Quansys Biosciences, Logan, UT, USA).

3.4.7 ROS and apoptosis assay

The ROS expression was detected by a Muse™ Oxidative Stress kit (EMD Millipore Co., Billerica, MA, USA), and apoptosis level was determined by a Muse™ Annexin V and Dead Cell kit (EMD Millipore Co.). Cells were cultured in 6-well plates to about 70% confluence, then the medium was replaced with DOX containing medium. Every treatment had three replicates. At each time point, the cells were collected and analyzed using a Muse Cell Analyzer (EMD Millipore Co.).

3.4.8 Cell viability assay

Cell viability was analyzed using LIVE/DEAD Viability/Cytotoxicity Assay Kit (Thermo Fisher Scientific). Calcein AM is retained within live cells producing green fluorescence; whereas, EthD-1 enters damaged membrane and binds to nucleic acids, producing red fluorescence. Every treatment has three replicates. After staining, cells were imaged using fluorescence microscope with DP30BW CCD camera (Olympus America Inc.) to analyze the relative proportion of live/dead cells.

3.5 RESULTS

3.5.1 BRMS1 distributed mainly in nucleus with some expression observed in the cytosol

To assess the biophysical and biochemical differences of breast cancer cells with and without BRMS1, it is important to pinpoint the distribution of BRMS1. Figure 3.1 shows the immunofluorescence images for 435 and 435/BRMS1 cells. BRMS1 is highly expressed (green) in (Figure 3.1B) 435/BRMS1 cells compared to 435 cells (Figure 3.1A). Further, it is

observed that BRMS1 is mainly distributed within cellular nucleus, which is consistent with previous research [30].

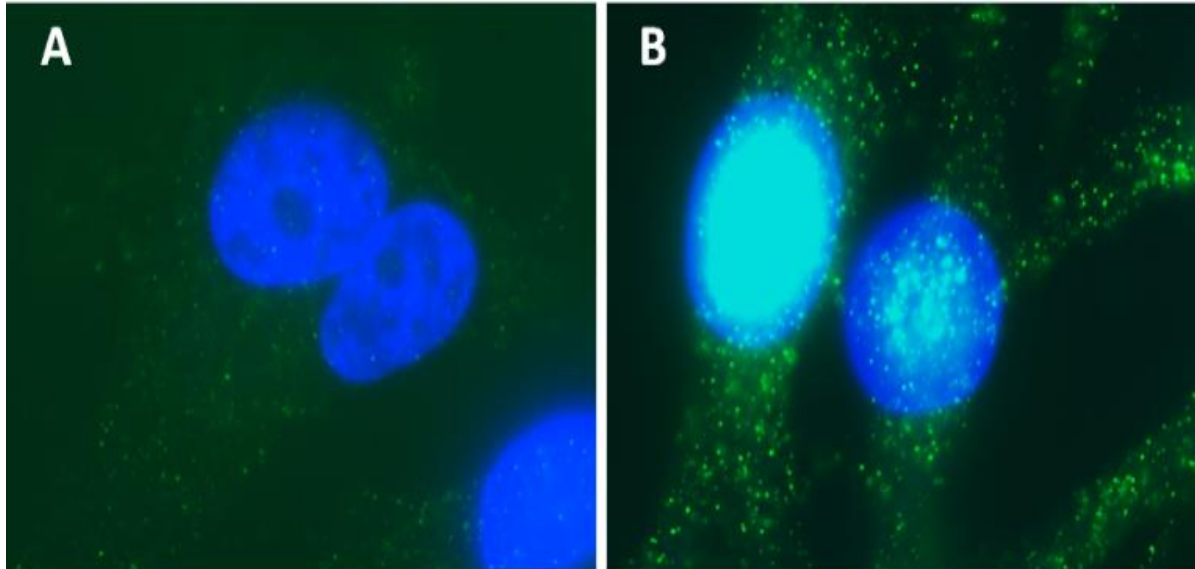


Figure 3.1 BRMS1 mainly distributed around the nucleus. Immunofluorescence images of (A) 435 and (B) 435/BRMS1 cells stained with anti-BRMS1 antibody (blue: nucleus; green: expression of BRMS1).

3.5.2 BRMS1 affects the biomechanical properties and the response of cancer cells to DOX

AFM was employed to quantify the biomechanical properties. The results are shown after 4 h DOX exposure where A549, 231 and 435 cells showed similar changes as both Young's modulus (Figure 3.2A) and adhesion forces increased (Figure 3.2B). However, both biomechanical properties of 231/BRMS1 and 435/BRMS1 moderately decreased. For 231 and 231/BRMS1 cells, the differences in the Young's modulus and adhesion force

corresponded to 7.5 kPa and 0.30 nN respectively. While for the 435 and 435/BRMS1 cells, the differences were 11.6 kPa and 0.29 nN respectively. However, after incubation with DOX, both the Young's modulus and adhesion forces decreased for both cell lines. The difference amounts to 2.8 kPa and 0.04 nN for 231 and 231/BRMS1 and, 2.6 kPa and 0.07 nN for 435 and 435/BRMS1.

These results suggest that BRMS1 expression affects the biomechanical properties of cancer cells and also induces a differential response when interacting with DOX.

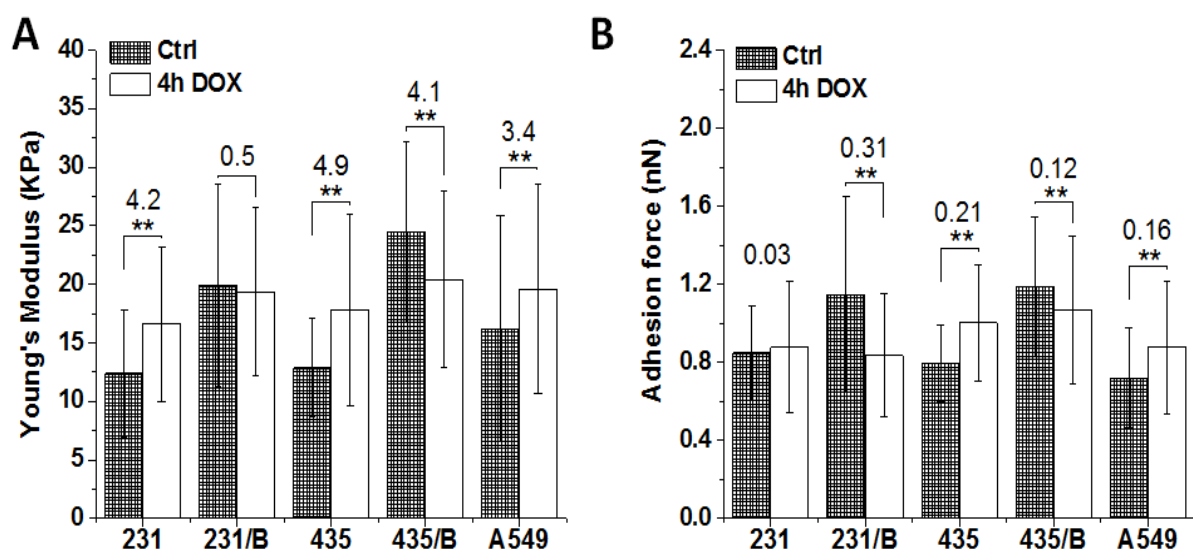


Figure 3.2 BRMS1 expression alters the biomechanical properties and the response of cancer cells to DOX. (A) Young's modulus and (B) adhesion force of 231, 231/BRMS1 (231/B), 435, 435/BRMS1 (435/B) and A549 cells without DOX treatment and treated with 4 h DOX group. Error bars are standard deviation of the mean ($N \geq 10$, $**p < 0.01$; B represents BRMS1).

3.5.3 BRMS1 has little effect on the biochemical changes of cancer cells to DOX

To compare the differences in biochemical information, Raman spectra of cells with and without DOX treatment were collected. A representative Raman video images of 231, 231/BRMS1, 435, 435/BRMS1 and A549 are shown in Figure 3.3A-E. The average Raman spectra were collected from over 24 spectra for each individual group, and all those spectra exhibited similar spectral peaks.

To identify the spectral differences, the spectrum of corresponding control group was subtracted from the average Raman spectra of different DOX groups (4 h, 12 h and 24 h) as shown in Figure 3.3A'-E'. Raman peaks at 786 cm^{-1} , 937 cm^{-1} , 1006 cm^{-1} , 1095 cm^{-1} , 1313 cm^{-1} , 1450 cm^{-1} , 1608 cm^{-1} and peak range from $1200\text{-}1300\text{ cm}^{-1}$ show significant differences when BRMS1 is expressed. The peak at 786 cm^{-1} arises from pyrimidine ring breathing mode. Raman peak at 937 cm^{-1} is assigned to α -helix and C-C stretching in the protein backbone. The peak at 1006 cm^{-1} belongs to the symmetric ring breathing mode of phenylalanine (Phe). Raman peak at 1095 cm^{-1} can be assigned to lipid, and the peak at 1313 cm^{-1} corresponds to guanine (G). The bands at 1450 cm^{-1} can be assigned to the CH_2 deformation (def) of lipid whereas the 1608 cm^{-1} corresponds to tryptophan (Tyr). The spectral region of $1200\text{-}1300\text{ cm}^{-1}$ belongs to Amide III. Table 3.1 lists the other major cellular biopolymers, i.e. nucleus acids, proteins, lipids and carbohydrates.

The Raman intensities were extracted as shown in Figure 3.4. Most of the peak intensities from BRMS1-expressing cells are larger than parental cells (Figure 3.4A-G). Meanwhile, these spectral intensities displayed a similar trend from control to 24 h DOX group.

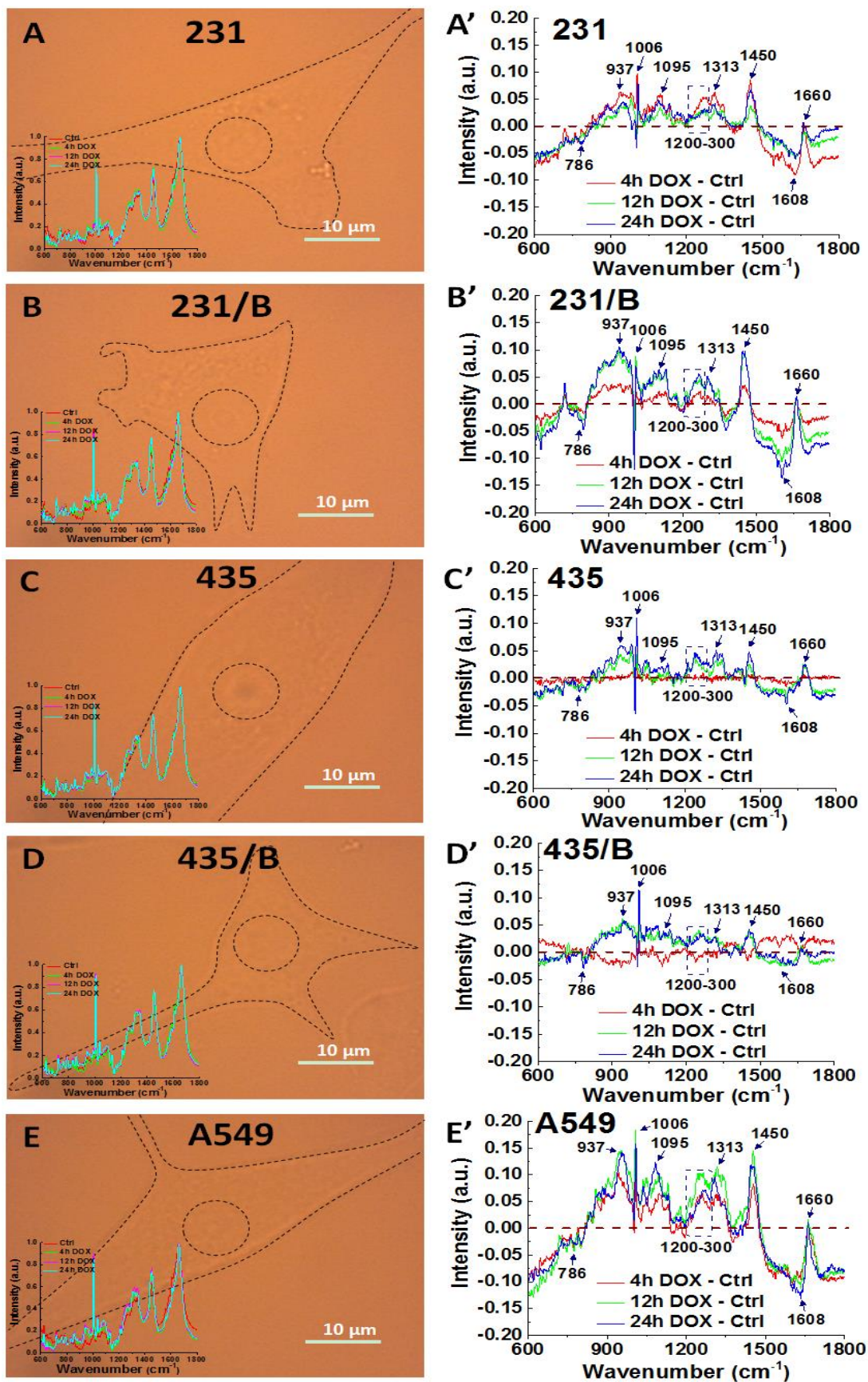


Figure 3.3 Similar Raman peaks corresponding to DNA/RNA, lipids and proteins between cell lines have noticeable changes for all cancer cells after DOX treatment. The representative Raman video images of (A) 231, (B) 231/BRMS1, (C) 435, (D) 435/BRMS1 and (E) A549 (inset in each image is the average Raman spectra from nucleus of control and treated with DOX for 4 h, 12 h and 24 h). Spectra difference between different time (4h, 12h and 24h) of DOX treated cells and control cells of (A') 231, (B') 231/BRMS1, (C') 435, (D') 435/BRMS1 and (E') A549 (B represents BRMS1).

The peak intensity at 786 cm^{-1} (Figure 3.4A) gradually reduces in all cell lines from control group to 24 h DOX exposure. After 24 h DOX exposure, the intensity at 786 cm^{-1} for 231, 231/BRMS1, 435, 435/BRMS1 and A549 slightly decreases 1.2, 1.2, 1.1, 1.1 and 1.2 folds respectively, compared to the corresponding control group. Interestingly, the intensity of 1313 cm^{-1} (Figure 3.4B) increases for all cells from control to 24 h DOX exposure. In the control group, the intensity of 1313 cm^{-1} for BRMS1-expressing cells is slightly larger than that of cells without BRMS1. All cells increase 1.1 fold at 1313 cm^{-1} after 24 h DOX treatment compared to control. Similarly, the peaks at 1095 cm^{-1} , 1450 cm^{-1} , 937 cm^{-1} and 1006 cm^{-1} (Figure 3.4C-F) all exhibit increasing intensity for all cells when compared to the control. However, the intensity at 1608 cm^{-1} of 231, 231/BRMS1, 435, 435/BRMS1 and A549 at 24 h group reduces 7%, 19%, 5%, 4% and 15% respectively compared to control. The spectral region of $1200\text{--}1300\text{ cm}^{-1}$ (Figure 3.4H) fluctuates over DOX exposure time, and the band areas of 12 h and 24 h DOX groups increase compared to control group for all cancer cell lines due to an alteration of proteins secondary structure. The band area ratios between the 1450 cm^{-1} and 1006 cm^{-1} in Figure 3.4I, A_{1450}/A_{1003} , can reveal a structural

modification [40]. Most of the cells have the largest mean ratio at 24 h DOX treatment, indicating the largest relative content of lipids at 24 h DOX incubation.

Overall, although BRMS1 expression changes the biochemical information of cancer cells, all cancer cells respond to DOX similarly over time.

Table 3.1 Tentative Raman band assignments of cells.

Raman shift (cm ⁻¹)	Band assignment
624	Phenylalanine
717	CN ⁻ (CH ₃) ₃ (lipids)
719	C-C-N ⁺ symmetric stretching in phosphatidylcholine
720	DNA
760	Tryptophan
786	DNA & phosphodiester bands DNA
813	Phosphodiester bands RNA
832	PO ₂ ⁻ stretch nucleic acids
854	Ring breathing tyrosine (proteins)
937	C-C stretching, α-helix (proteins)
961	Phosphate of HA; Calcium-phosphate stretch band
1006	Phenylalanine
1031	Phenylalanine
1057	Lipids
1066	PO ₂ ⁻ stretching; chain stretching; C-O, C-C stretching
1084	Phosphodiester groups in nucleic acids
1095	Lipid
1200-1300	Amide III (proteins)
1313	Guanine
1317-9	Guanine (B,Z-marker)
1335/6	Guanine
1400-30	γ(C=O) O ⁻ (amino acids aspartic & glutamic acid)
1450	CH ₂ deformation (lipids)
1579	Pyrimidine ring (nucleic acids)
1608	Phenylalanine, Tryptophan
1658/9	Amide I band (protein band)
1740	Collagen III

Band assignments refer from literature [31-39].

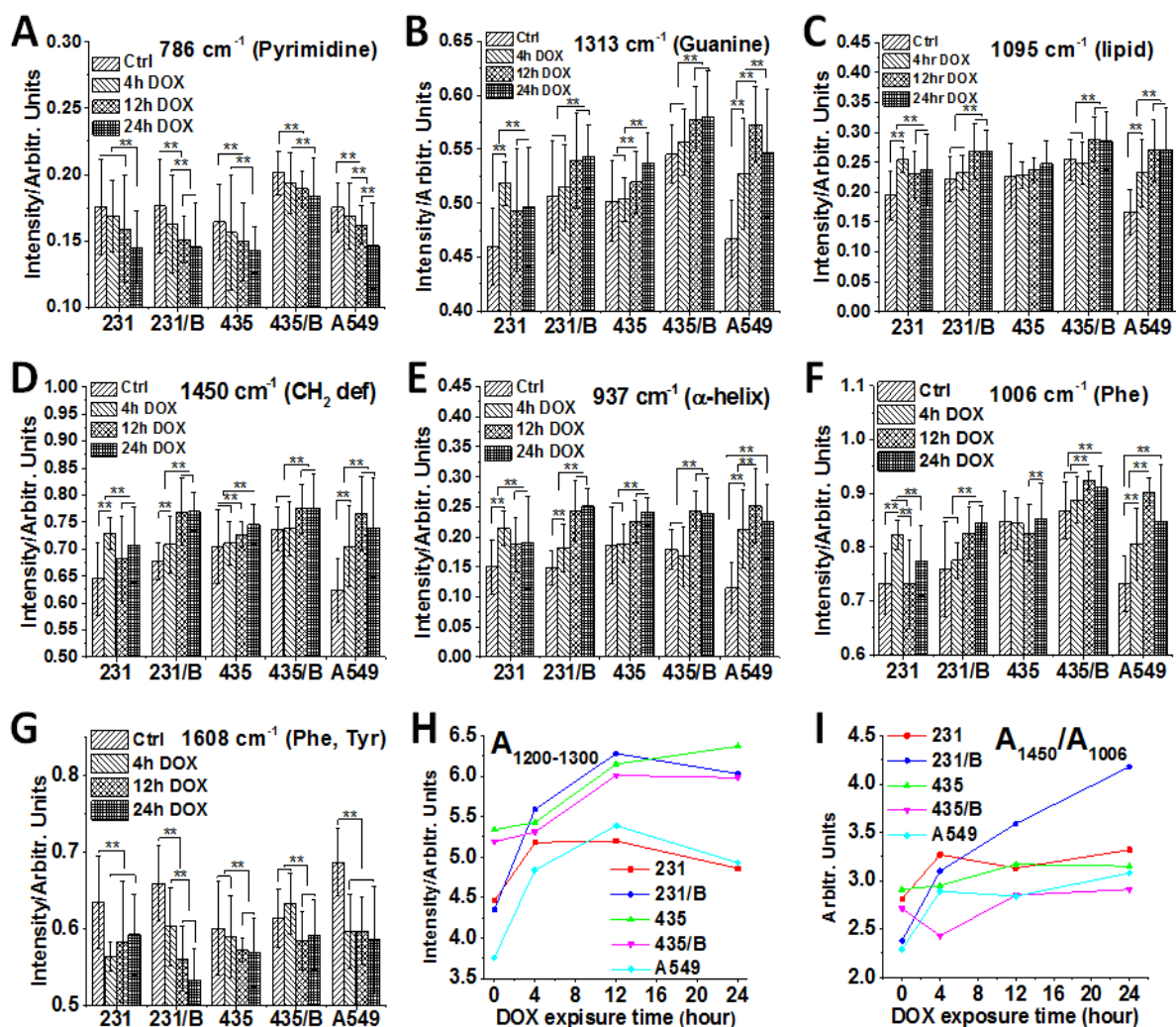


Figure 3.4 BRMS1 expression has little impact on the biochemical changes of cancer cells to DOX. Raman intensity analysis of five cancer cell lines at (A) 786 cm⁻¹ (pyrimidine), (B) 1313 cm⁻¹ (guanine), (C) 1095 cm⁻¹ (lipid), (D) 1450 cm⁻¹ (CH₂ deformation of lipid), (E) 937 cm⁻¹ (α-helix), (F) 1006 cm⁻¹ (phenylalanine) and (G) 1608 cm⁻¹ (phenylalanine and tryptophan) at different DOX exposure times (control, 4 h, 12 h and 24 h). Error bars are standard deviation of the mean. The band area of 1200-1300 cm⁻¹ (H) and the intensity ratio (I) between the 1450 cm⁻¹ and 1006 cm⁻¹ bands (A₁₄₅₀/A₁₀₀₆) of 231, 231/BRMS1, 435, 435/BRMS1 and A549 cells at different DOX exposure times (N ≥ 6, **p < 0.01, B represents BRMS1).

3.5.4 BRMS1 affects the expression of cytokine and chemokine

Multiplex ELISA was applied to analyze a total of 25 human cytokines and chemokines, and the majority of them were undetectable. However, several cytokines (IL-8, IL-15, RANTES, MCP-1, GRO α , GMCSF, IL-2 and TNF α) showed prominent expression levels after DOX treatments (Figure 3.5).

All cells expressed IL-8, IL-15, RANTES and MCP-1, while some of these cells did not release GRO α , GMCSF, IL-2 and TNF α . For 231 and 231/BRMS1, the expressions of IL-8, IL-15, RANTES and IL-2 are very similar from control to 24 h DOX group. However, the average expression of GRO α is 1041 and 5282 pg/mL for 231 and 231/BRMS1 respectively from control to 24 h DOX group, and 231 and 231/BRMS1 secrete an average of 135 and 9 pg/mL for GMCSF correspondingly. Similar to 231 and 231/BRMS1, these cytokines fluctuate from control to 24 h DOX group for 435 and 435/BRMS1. Among the eight cytokines 435 releases more than 435/BRMS1 except IL-2 that is undetectable. On average, 435 cells express about 2-fold more IL-15, 9-fold more RANTES, 85-fold higher MCP-1, 87-fold more IL-8, 93-fold higher TNF α , and 6308-fold more GRO α than the 435/BRMS1 from control to 24 h DOX group. Meanwhile, the average expression of GMCSF is 1687 pg/mL for 435 cells, while that of 435/BRMS1 is undetectable. For A549 cells, cytokine expression also varies. A549 cells express low level of IL-15, RANTES, GMCSF, IL-2 and TNF α (each one is less than 9 pg/mL on average) comparing to IL-8, MCP-1 and GRO α (83142, 975 and 27650 pg/mL on average, respectively) from control to 24 h DOX group.

Overall, different cell lines release different cytokines at varying levels from control to 24 h DOX group. Among the 25 cytokines and chemokines, many are expressed at a

negligible level. The eight cytokines discussed here indicate that 231 and 231/BRMS1 release similar levels of IL-8, IL-15, RANTES and IL-2, while 435 cells express cytokines at a much higher level than the 435/BRMS1 (except IL-2).

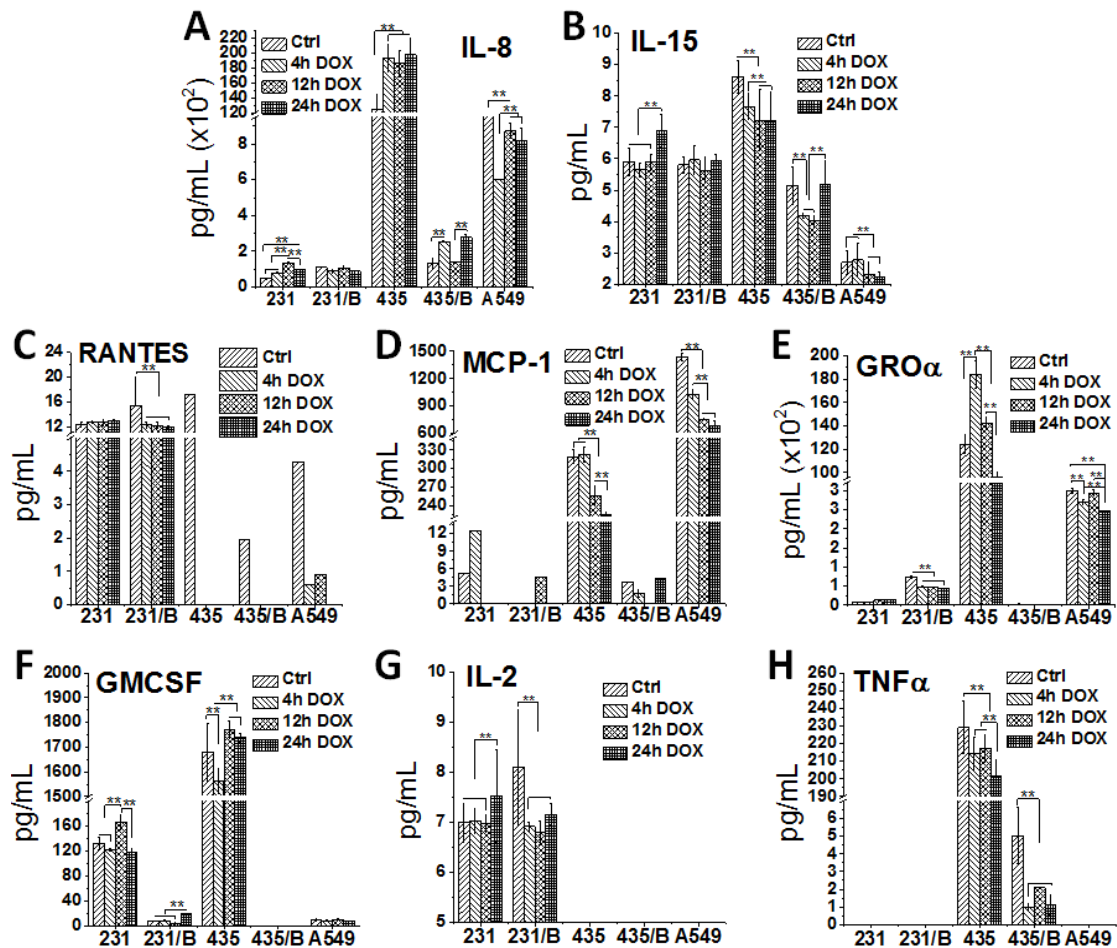


Figure 3.5 The expression of cytokine and chemokine was affected by BRMS1. Cytokines and chemokines analysis of (A) IL-8, (B) IL-15, (C) RANTES, (D) MCP-1, (E) GRO α , (F) GMCSF, (G) IL-2 and (H) TNF α released from 231, 231/BRMS1, 435, 435/BRMS1 and A549 cells. Cells were exposed to DOX for 0h (control), 4 h, 12 h and 24 h before measurement. Unit of Y-axis: pg/mL. Error bars are standard deviation of the mean (N = 3, ** $p < 0.01$, B represents BRMS1).

3.5.5 BRMS1 expression has little effect on apoptosis, ROS expression and cell viability of cancer cells from DOX

When DOX interacts with cancer cells, an apoptotic response, an increase in ROS, and reduced viability is triggered. These results also show that apoptosis, ROS expression and cell viability tests are all time-dependent, and the percentage variations of these three tests follow similar changes across all cell lines. In Figure 3.6A, there is a large increase in the number of apoptotic cells after 24 h DOX exposure, with a pronounced increase in 435 and 435/BRMS1 cells. For instance, at 12 h exposure, both 435 and 435/BRMS1 have a similar apoptosis percentage (ca. 5~6%); after 24 h exposure, the percentage of apoptotic cells increases to 24 % for 435, and 27% for 435/BRMS1. Plus, both are significantly higher than ~17% for both 231 and 231/BRMS1 at the same exposure time. Similarly, the production of ROS in five cells grew with the increase of DOX exposure time (Figure 3.6B). The overall level of ROS production for A549, 231, and 231/BRMS1 after 24 h DOX exposure was larger than those for 435 and 435/BRMS1 cells. For cell viability (Figure 3.6C), the viable cell percentages of 231, 231/BRMS1, 435, 435/BRMS1 and A549 decreased after DOX treatment, changing into 72.7%, 72.4%, 74.8%, 70.7% and 74.5% respectively after 24 h DOX incubation. After 4 h and 12 h DOX exposure, the differences of viability percentage between cancer cells and cancer cells with BRMS1 are ~3% and ~2.8%, correspondingly.

The apoptosis, ROS expression and cell viability changes of five cells display a similar pattern from control to 24 h DOX exposure, reflecting the similar responses between cancer cells and BRMS1-expressing cells to DOX treatment.

3.5.6 BRMS1 expression has little effect on apoptosis, ROS expression and cell viability of cancer cells from DOX

When DOX interacts with cancer cells, an apoptotic response, an increase in ROS, and reduced viability is triggered. These results also show that apoptosis, ROS expression and cell viability tests are all time-dependent, and the percentage variations of these three tests follow similar changes across all cell lines. In Figure 3.6A, there is a large increase in the number of apoptotic cells after 24 h DOX exposure, with a pronounced increase in 435 and 435/BRMS1 cells. For instance, at 12 h exposure, both 435 and 435/BRMS1 have a similar apoptosis percentage (ca. 5~6%); after 24 h exposure, the percentage of apoptotic cells increases to 24 % for 435, and 27% for 435/BRMS1. Plus, both are significantly higher than ~17% for both 231 and 231/BRMS1 at the same exposure time. Similarly, the production of ROS in five cells grew with the increase of DOX exposure time (Figure 3.6B). The overall level of ROS production for A549, 231, and 231/BRMS1 after 24 h DOX exposure was larger than those for 435 and 435/BRMS1 cells. For cell viability (Figure 3.6C), the viable cell percentages of 231, 231/BRMS1, 435, 435/BRMS1 and A549 decreased after DOX treatment, changing into 72.7%, 72.4%, 74.8%, 70.7% and 74.5% respectively after 24 h DOX incubation. After 4 h and 12 h DOX exposure, the differences of viability percentage between cancer cells and cancer cells with BRMS1 are ~3% and ~2.8%, correspondingly.

The apoptosis, ROS expression and cell viability changes of five cells display a similar pattern from control to 24 h DOX exposure, reflecting the similar responses between cancer cells and BRMS1-expressing cells to DOX treatment.

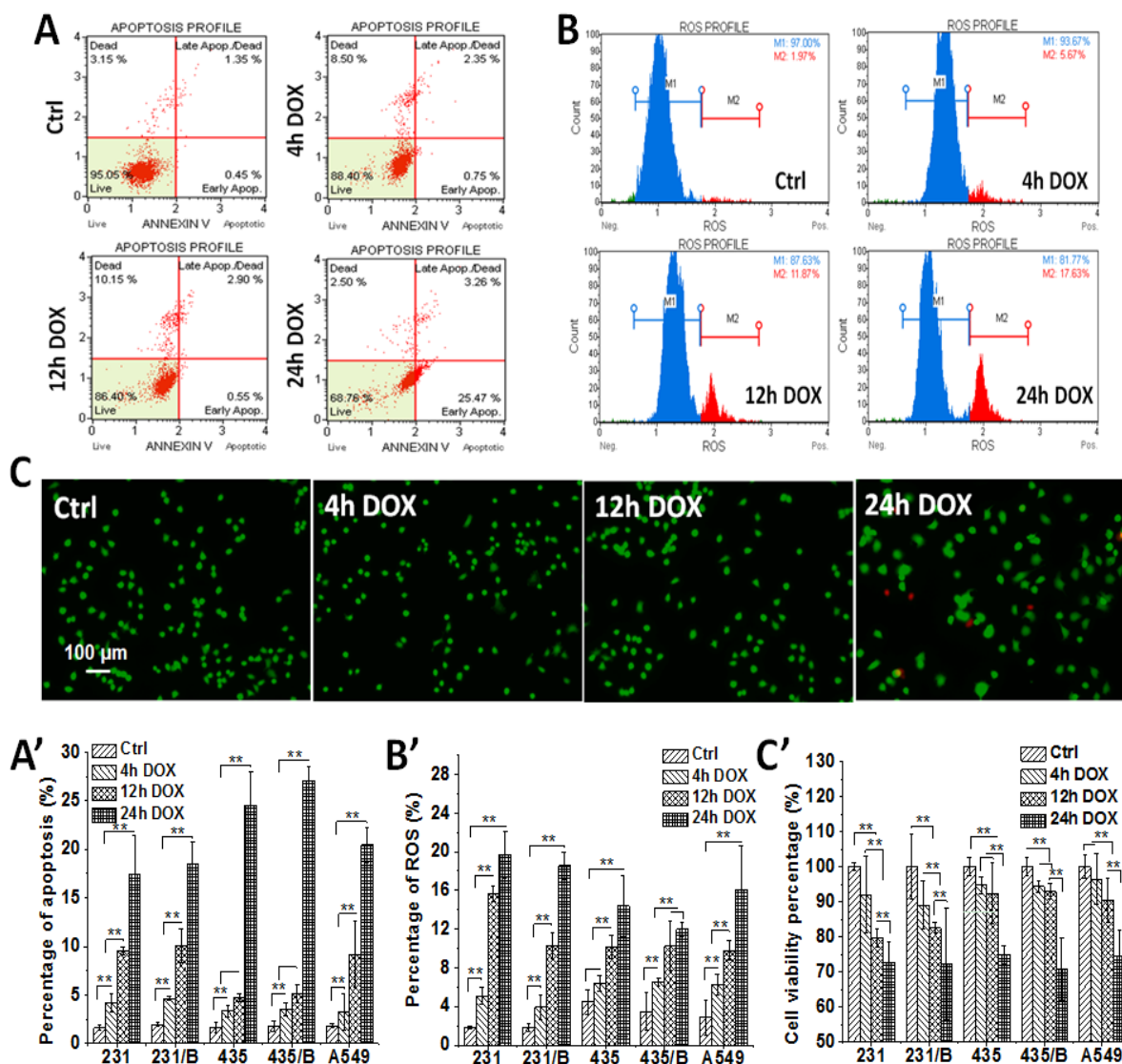


Figure 3.6 BRMS1 expression has little influence on apoptosis, ROS expression and cell viability of cancer cells from DOX. The representative (A) Apoptosis, (B) ROS expression and (C) cell viability images and the histogram of (A') Apoptosis, (B') ROS expression and (C') cell viability percentage from 231, 231/BRMS1, 435, 435/BRMS1 and A549 cells without DOX treatment and treated with 4 h, 12 h and 24 h DOX (Error bars are standard deviation of the mean; N = 3, ** $p < 0.01$, B represents BRMS1).

3.6 DISCUSSIONS

Studies were conducted to understand the effects of metastasis suppressors on cellular biomechanical and biochemical properties and its responses to chemotherapeutic drugs. To perform these studies, a representative metastasis suppressor, BRMS1, was selected. Immunolocalization experiments using BRMS1 antibody confirmed the high expression and localization of BRMS1 predominantly to the nucleus of MDA-MB-435/BRMS1 cells. BRMS1 is an important part of the SIN3-HDAC complexes, critical for deacylating histone proteins and condensing the chromatin machinery leading to reduced transcription of several genes [41, 42]. BRMS1 was also found, albeit at lower levels, in the cytosol, which is consistent with earlier reports categorizing BRMS1 as a nucleo-cytoplasmic protein [43].

It is reported that in BRMS1-expressing cells, the activation of focal adhesion kinase and $\beta 1$ integrin were reduced, leading to a decrease level of cellular adhesion and cytoskeletal reorganization [44]. Our results demonstrate that BRMS1 could affect cellular biomechanical properties. The Young's moduli of metastatic cancer cells (231, 435) are lower than that of non-metastatic cells (231/BRMS1, 435/BRMS1), which is consistent with reported studies [26, 45-47]. This distinction in cell elasticity is attributed to altered cytoskeletal organization, in particular the intermediate filament and actin filament structures, which have been identified as the main determinants of cell elasticity [48]. Furthermore, interaction with DOX results in an increase in Young's modulus for cancer cells; while decreasing it in BRMS1 expressing cells. Metastatic cancer cells (231, 435) possessed lower adhesion forces than BRMS1 expressing non-metastatic cells. In addition, interaction with DOX led to increased cell adhesion in metastatic A549, 231 and 435 cells, whereas a decrease was seen in non-metastatic 231/BRMS1 and 435/BRMS1 cells. The measured

adhesion force is associated with cell-surface biomolecules [49]. Alterations in cell adhesion after DOX treatment may be caused by cellular response to chemical stimulus leading to the variation of cell-surface macromolecules.

The Raman spectral results demonstrate that BRMS1 expression has an effect on cellular biochemical properties. However, after DOX treatment, the spectral changes of cancer cells with BRMS1 are similar to those without BRMS1. DOX incubation time also plays a critical role in changing spectral intensities. The results suggest that BRMS1 expression changes the cells' biochemical makeup without affecting chemotherapeutic sensitivity of these *in vitro* cancer cells. It is reported that the expression of BRMS1 largely enhances major histocompatibility complex (MHC) genes and significantly reduces the expression level of some genes related to protein localization and secretion [50]. This phenomenon is more obvious between 435 and 435/BRMS1, as shown in Figure 3.5. Although 231 and 231/BRMS1 secrete similar level of IL-8, IL-15, RANTES and IL-2, the level of GM-CSF for 231/BRMS1 is much less than that of 231. This result may indicate that the expression of BRMS1 in different cell lines has different effects on secretion of cytokines. In addition, the expression values of cytokines and chemokines for five cell lines are at similar magnitude comparing control to DOX treated groups, suggesting that DOX has similar influences on cancer cells with and without BRMS1. The results from apoptosis, ROS expression and cell viability reflect similar patterns for five cell lines upon DOX treatments, confirming that DOX has similar impacts on cancer cells with and without BRMS1.

In conclusion, this study demonstrates the distribution of BRMS1 within cells. It is also observed that BRMS1 has an influence on cellular biomechanical and biochemical properties. However, the effect on cellular biomechanical and biochemical information from

BRMS1 does not affect the chemotherapeutic sensitivity of cells with BRMS1 compared to cells without BRMS1. These findings have provided critical clues on the biomechanical and biochemical changes from BRMS1 expression and the following drug treatments, and confirmed that the drug treatment of breast cancer remains effective in the presence of BRMS1. Our future work is to study more metastasis suppressors and their effects on cellular levels, providing clinical cues for drug treatments.

3.7 REFERENCES

1. Slipicevic A, Holm R, Emilsen E, Rosnes AKR, Welch DR, Maelandsmo GM, et al. Cytoplasmic BRMS1 expression in malignant melanoma is associated with increased disease-free survival. *BMC Cancer*. 2012; 12; 73.
2. Frolova N, Edmonds MD, Bodenstine TM, Seitz R, Johnson MR, Feng R, et al. A Shift from Nuclear to Cytoplasmic Breast Cancer Metastasis Suppressor 1 Expression Is Associated with Highly Proliferative Estrogen Receptor-Negative Breast Cancers. *Tumor Biol*. 2009; 30: 148-59.
3. Stafford LJ, Vaidya KS, Welch DR. Metastasis suppressors genes in cancer. *Int J Biochem Cell Biol*. 2008; 40: 874-91.
4. Hicks DG, Yoder BJ, Short S, Tarr S, Prescott N, Crowe JP, et al. Loss of breast cancer metastasis suppressor 1 protein expression predicts reduced disease-free survival in subsets of breast cancer patients. *Clin Cancer Res*. 2006; 12: 6702-8.
5. Stark AM, Tongers K, Maass N, Mehdorn HM, Held-Feindt J. Reduced metastasis-suppressor gene mRNA-expression in breast cancer brain metastases. *J Cancer Res Clin Oncol*. 2005; 131: 191-8.

6. Zhang Z, Yamashita H, Toyama T, Yamamoto Y, Kawasoe T, Iwase H. Reduced expression of the breast cancer metastasis suppressor 1 mRNA is correlated with poor progress in breast cancer. *Clin Cancer Res.* 2006; 12: 6410-4.
7. Cicek M, Fukuyama R, Welch DR, Sizemore N, Casey G. Breast cancer metastasis suppressor 1 inhibits gene expression by targeting nuclear factor-kappaB activity. *Cancer Res.* 2005; 65: 3586-95.
8. Vaidya KS, Harihar S, Phadke PA, Stafford LJ, Hurst DR, Hicks DG, et al. Breast cancer metastasis suppressor-1 differentially modulates growth factor signaling. *J Biol Chem.* 2008; 283: 28354-60.
9. Cheng JQ, Lindsley CW, Cheng GZ, Yang H, Nicosia SV. The Akt/PKB pathway: molecular target for cancer drug discovery. *Oncogene.* 2005; 24: 7482-92.
10. Pham CG, Bubici C, Zazzeroni F, Knabb JR, Papa S, Kuntzen C, et al. Upregulation of Twist-1 by NF-kappaB blocks cytotoxicity induced by chemotherapeutic drugs. *Mol Cell Biol.* 2007; 27: 3920-35.
11. Sebens S, Arlt A, Schafer H. NF-kappaB as a molecular target in the therapy of pancreatic carcinoma. *Recent Results Cancer Res.* 2008; 177: 151-64.
12. Wu Y, McEwen GD, Harihar S, Baker SM, DeWald DB, Zhou A. BRMS1 expression alters the ultrastructural, biomechanical and biochemical properties of MDA-MB-435 human breast carcinoma cells: an AFM and Raman microspectroscopy study. *Cancer lett.* 2010; 293: 82-91.
13. McEwen GD, Wu Y, Tang M, Qi X, Xiao Z, Baker SM, et al. Subcellular spectroscopic markers, topography and nanomechanics of human lung cancer and

- breast cancer cells examined by combined confocal Raman microspectroscopy and atomic force microscopy. *Analyst*. 2013; 138: 787-97.
14. Binnig G, Quate CF, Gerber C. Atomic Force Microscope. *Phys Rev Lett*. 1986; 56: 930-3.
 15. Dorobantu LS, Gray MR. Application of atomic force microscopy in bacterial research. *Scanning*. 2010; 32: 74-96.
 16. Liu S, Wang Y. Application of AFM in microbiology: a review. *Scanning*. 2010; 32: 61-73.
 17. Xiao LF, Tang MJ, Li QF, Zhou AH. Non-invasive detection of biomechanical and biochemical responses of human lung cells to short time chemotherapy exposure using AFM and confocal Raman spectroscopy. *Anal Methods*. 2013; 5: 874-9.
 18. Ling J, Weitman SD, Miller MA, Moore RV, Bovik AC. Direct Raman imaging techniques for study of the subcellular distribution of a drug. *Appl Optics*. 2002; 41: 6006-17.
 19. Notingher L, Jell G, Notingher PL, Bisson I, Tsigkou O, Polak JM, et al. Multivariate analysis of Raman spectra for in vitro non-invasive studies of living cells. *J Mol Struct*. 2005; 744: 179-85.
 20. Owen CA, Selvakumaran J, Notingher I, Jell G, Hench LL, Stevens MM. In vitro toxicology evaluation of pharmaceuticals using Raman micro-spectroscopy. *J Cell Biochem*. 2006; 99: 178-86.
 21. Sellers WR, Fisher DE. Apoptosis and cancer drug targeting. *J Clin Invest*. 1999; 104: 1655-61.

22. Thannickal VJ, Fanburg BL. Reactive oxygen species in cell signaling. *Am J Physiol Lung Cell Mol Physiol.* 2000; 279: L1005-28.
23. Kashkin KN, Musatkina EA, Komelkov AV, Favorskaya IA, Trushkin EV, Shleptsova VA, et al. Expression profiling and putative mechanisms of resistance to doxorubicin of human lung cancer cells. *Dokl Biochem Biophys.* 2010; 430: 20-3.
24. Vaidya KS, Sanchez JJ, Kim EL, Welch DR. Expression of the Breast Cancer Metastasis Suppressor 1 (BRMS1) maintains in vitro chemosensitivity of breast cancer cells. *Cancer Lett.* 2009; 281: 100-7.
25. Cross SE, Jin YS, Lu QY, Rao JY, Gimzewski JK. Green tea extract selectively targets nanomechanics of live metastatic cancer cells. *Nanotechnology.* 2011; 22: 215101.
26. Cross SE, Jin Y-S, Rao J, Gimzewski JK. Nanomechanical analysis of cells from cancer patients. *Nat Nanotechnol.* 2007; 2: 780-3.
27. Sneddon IN. The relation between load and penetration in the axisymmetric boussinesq problem for a punch of arbitrary profile. *Int J Eng Sci.* 1965; 3: 47-57.
28. Butt HJ, Cappella B, Kappl M. Force measurements with the atomic force microscope: Technique, interpretation and applications. *Surf Sci Rep.* 2005; 59: 1-152.
29. Rosenbluth MJ, Lam WA, Fletcher DA. Force microscopy of nonadherent cells: A comparison of leukemia cell deformability. *Biophys J.* 2006; 90: 2994-3003.
30. Hurst DR, Xie Y, Thomas JW, Liu JZ, Edmonds MD, Stewart MD, et al. The C-Terminal Putative Nuclear Localization Sequence of BREast cancer Metastasis

- Suppressor 1, BRMS1, Is Necessary for Metastasis Suppression. *PLoS One*. 2013; 8: e55966.
31. Movasaghi Z, Rehman S, Rehman IU. Raman spectroscopy of biological tissues. *Appl Spectrosc Rev*. 2007; 42: 493-541.
 32. Yu C, Gestl E, Eckert K, Allara D, Irudayaraj J. Characterization of human breast epithelial cells by confocal Raman microspectroscopy. *Cancer Detect Prev*. 2006; 30: 515-22.
 33. Stone N, Kendall C, Smith J, Crow P, Barr H. Raman spectroscopy for identification of epithelial cancers. *Faraday Discuss*. 2004; 126: 141-57; discussion 69-83.
 34. Stone N, Kendall C, Shepherd N, Crow P, Barr H. Near-infrared Raman spectroscopy for the classification of epithelial pre-cancers and cancers. *J Raman Spectrosc*. 2002; 33: 564-73.
 35. Cheng WT, Liu MT, Liu HN, Lin SY. Micro-Raman spectroscopy used to identify and grade human skin pilomatrixoma. *Microsc Res Techniq*. 2005; 68: 75-9.
 36. Shetty G, Kendall C, Shepherd N, Stone N, Barr H. Raman spectroscopy: elucidation of biochemical changes in carcinogenesis of oesophagus. *Brit J Cancer*. 2006; 94: 1460-4.
 37. Ruiz-Chica AJ, Medina MA, Sanchez-Jimenez F, Ramirez FJ. Characterization by Raman spectroscopy of conformational changes on guanine-cytosine and adenine-thymine oligonucleotides induced by aminoxy analogues of spermidine. *J Raman Spectrosc*. 2004; 35: 93-100.

38. Chan JW, Taylor DS, Zwerdling T, Lane SM, Ihara K, Huser T. Micro-Raman spectroscopy detects individual neoplastic and normal hematopoietic cells. *Biophys J*. 2006; 90: 648-56.
39. Chiriboga L, Xie P, Yee H, Vigorita V, Zarou D, Zakim D, et al. Infrared spectroscopy of human tissue. I. Differentiation and maturation of epithelial cells in the human cervix. *Biospectroscopy*. 1998; 4: 47-53.
40. Guo J, Cai W, Du B, Qian M, Sun Z. Raman spectroscopic investigation on the interaction of malignant hepatocytes with doxorubicin. *Biophys Chem*. 2009; 140: 57-61.
41. Meehan WJ, Samant RS, Hopper JE, Carrozza MJ, Shevde LA, Workman JL, et al. Breast cancer metastasis suppressor 1 (BRMS1) forms complexes with retinoblastoma-binding protein 1 (RBP1) and the mSin3 histone deacetylase complex and represses transcription. *J Biol Chem*. 2004; 279: 1562-9.
42. Liu Y, Smith PW, Jones DR. Breast cancer metastasis suppressor 1 functions as a corepressor by enhancing histone deacetylase 1-mediated deacetylation of RelA/p65 and promoting apoptosis. *Mol Cell Biol*. 2006; 26: 8683-96.
43. Bodenshtein TM, Vaidya KS, Ismail A, Beck BH, Cook LM, Diers AR, et al. Homotypic Gap Junctional Communication Associated with Metastasis Suppression Increases with PKA Activity and Is Unaffected by PI3K Inhibition. *Cancer Res*. 2010; 70: 10002-11.
44. Khotskaya YB, Beck BH, Hurst DR, Han Z, Xia W, Hung MC, et al. Expression of metastasis suppressor BRMS1 in breast cancer cells results in a marked delay in cellular adhesion to matrix. *Mol Carcinog*. 2014; 53: 1011-26.

45. Cross SE, Jin YS, Tondre J, Wong R, Rao J, Gimzewski JK. AFM-based analysis of human metastatic cancer cells. *Nanotechnology*. 2008; 19: 384003.
46. Wu YZ, McEwen GD, Harihar S, Baker SM, DeWald DB, Zhou AH. BRMS1 expression alters the ultrastructural, biomechanical and biochemical properties of MDA-MB-435 human breast carcinoma cells: An AFM and Raman microspectroscopy study. *Cancer Lett*. 2010; 293: 82-91.
47. Lekka M, Laidler P, Gil D, Lekki J, Stachura Z, Hryniewicz AZ. Elasticity of normal and cancerous human bladder cells studied by scanning force microscopy. *Eur Biophys J*. 1999; 28: 312-6.
48. Leporatti S, Vergara D, Zacheo A, Vergaro V, Maruccio G, Cingolani R, et al. Cytomechanical and topological investigation of MCF-7 cells by scanning force microscopy. *Nanotechnology*. 2009; 20: 055103.
49. van der Aa BC, Michel RM, Asther M, Zamora MT, Rouxhet PG, Dufrene YF. Stretching cell surface macromolecules by atomic force microscopy. *Langmuir*. 2001; 17: 3116-9.
50. Champine PJ, Michaelson J, Weimer BC, Welch DR, DeWald DB. Microarray analysis reveals potential mechanisms of BRMS1-mediated metastasis suppression. *Clin Exp Metastasis*. 2007; 24: 551-65.

CHAPTER 4

DIESEL EXHASUT PARTICLES (DEP) INDUCED HUMAN LUNG CANCER CELLS DAMAGE AND THE STRUCTURE PROTECTIVE EFFECT OF RESVERATROL (RES)

4.1 ABSTRACT

In this study, scanning electron microscopy (SEM), confocal laser scanning microscopy and atomic force microscope (AFM), Raman spectroscopy (RM), multiplex ELISA, flow cytometry, were applied to analyze the biochemical and biophysical responses of *in vitro* human lung carcinoma epithelial cells (A549) treated with or without resveratrol (RES), followed by different time points (from 0 h to 48 h) of diesel exhaust particles (DEP) exposure. SEM identified the elements and size of DEP and the morphology of cells treated with DEP and RES. Confocal microscope and AFM results confirmed that DEP destroyed cellular structure and the protective effect from RES. AFM topography showed that RES protected cells from DEP-induced damage to cytoskeleton and cell architectures. Also, AFM force-distance measurements indicated that RES treatments attenuated DEP-induced alterations in cell elasticity and surface adhesion force over DEP incubation time. RM monitored the changes of characteristic Raman peak intensities of DNA and protein over DEP exposure time for both RES and non-RES treated groups. The cytokine and chemokine changes quantified by Multiplex ELISA revealed that the inflammatory responses were enhanced with the increase in DEP exposure time, and that RES attenuated the expression levels of cytokine and chemokine. In addition, DEP and RES changed the plasma membrane potential (PMP) and cell cycle of A549 cells. This work demonstrated that significant biophysical and biochemical changes induced by DEP may be relevant to early pathological

changes induced by DEP damage, and that the pretreatment of RES protected cellular damage and increased cellular sensitivity to DEP exposure, revealing the importance of antioxidant on the prevention of respiratory diseases.

4.2 INTRODUCTION

A relationship between lung cancer incidence, cardiopulmonary deaths, respiratory and cardiovascular diseases for adults living in metropolitan areas and the level of particulate matter (PM) has been reported [1-4]. One specific type of PM significant to public health is the diesel exhaust particle (DEP), which is characterized by a carbonic nucleus, in which some 18,000 high-molecular-weight organic compounds are adsorbed [5]. The mechanisms of DEP causing adverse health effects are involved with reactive oxygen species (ROS) generation, oxidative stress and inflammation [6], and these responses can lead to DNA damage [7].

Resveratrol (trans-3, 4, 5-trihydroxystilbene, RES) is a phenolic natural component of *Vitis vinifera L*, mainly abundant in the skin of the grapes and found to be present in higher concentration in red than in white wines. This natural compound has been found to show many pharmacologic effects, including lipoprotein metabolism modulation, platelet antiaggregation, anti-inflammation, anti-fungal, cancer chemopreventive, and anticancer properties [8-11]. Studies have shown RES can effectively inhibit oxidative damage [12, 13] and has been shown to scavenge free radicals such as lipid hydroperoxyl, hydroxyl ($\bullet\text{OH}$), and superoxide anion ($\text{O}_2^{\bullet-}$) radicals [14].

It is clinically important to study cellular responses when cells are exposed to DEP with or without RES because people are under the condition of taking up antioxidants by daily diet and being exposed to potential DEP-containing environment. The investigation of

DEP and RES on cellular biophysical and biochemical changes is needed to better understand the mechanisms of DEP and RES on mammalian cells. Atomic force microscopy (AFM) has proven to be a valuable tool to study single cells. With AFM measurement, cellular topography and mechanics properties (adhesion force and elasticity) can be measured and statistically analyzed [15-17], allowing researchers to better understand biophysical responses of mammalian cells under the different treatments. Previous applications of AFM in human lung carcinoma epithelial cells (A549) studies include elasticity modulus measurements [18, 19], recognition of surface heparin sulphate proteoglycan receptors [20], and photodynamic and sonodynamic effects [21, 22], demonstrating the feasibility and utility of AFM to detect cellular biophysical properties. Raman microspectroscopy (RM) is a spectroscopic technique that can be utilized to identify characteristic fingerprints of living cells based on chemical compositions and molecular structures [23]. When the light is scattered from a molecule, a small fraction of light (approximately 1 in 10^7 photons) is scattered at lower optical frequencies than the frequency of the incident photons. Raman scattering can occur with a change in vibrational, rotational or electronic energy of a molecule, Thus RM is a sensitive method to measure compounds in biological system and can provide supplementary information on cellular composition. Previous applications of RM were mainly focused on physical and structural investigations; more recently, it has gained popularity in the field of cellular biology [24, 25], suggesting that RM can provide cellular biochemical information for analysis.

The primary target tissue of inhaled DEP is lung epithelial cells, so this experiment was conducted by exposing A549 cells - as model of alveolar epithelial cells - to DEP and RES. The purpose of this work is to improve understanding of the cellular biomechanical and

biochemical changes and the connection with cellular responses by which DEP cause damage to the airway epithelium and the potential protection from RES to those DEP damaged cells. In order to address this, the effects of DEP and RES on cellular topography, cytoskeleton, biomechanics, biocomponents, inflammatory responses, plasma membrane potential and cell cycle of the human epithelial A549 cell line were investigated.

4.3 HYPOTHESIS

DEP could destroy cellular structure, and induce cellular inflammatory responses, while RES could alleviate DEP-induced destructive effect on cytoskeleton and enhance the inflammatory responses of cells.

4.4 MATERIALS AND METHODS

4.4.1 Preparation of human lung carcinoma epithelial A549 cells

Human lung carcinoma A549 cells (ATCC, Manassas, VA, USA) were cultured in F-12k medium containing 10% fetal bovine serum (Thermo Fisher Scientific, Waltham, MA, USA) at 37 °C with 5% CO₂ in a humidified atmosphere. Cells (approximately 10⁶ cells/mL) were passaged at 70-90% confluency and used for experiments.

RES was dissolved in complete cell growth media, and sonicated for 3 min at room temperature. Then 10 µM RES culture media was added directly into A549 cells for 24 hours. DEP was generously given by Dr. M. Ian Gilmour of the National Health and Environmental Effects Research Laboratory, U.S. Environmental Protection Agency (Research Triangle Park, NC, USA). DEP was suspended in complete cell growth media and underwent vortex for 10 s, and subsequently sonicated for 20 min at room temperature. Then 400 µg/mL DEP suspension was added 50 µL directly into 2 mL culture media. One group of cells was treated

with the DEP suspension for 0 hour (h) (no DEP treatment), 4 h, 8 h, 16 h, 24 h and 48 h, respectively. And the other group of cells was treated with RES for 24 hours in advance and then added the DEP suspension for 0 h, 4 h, 8 h, 16 h, 24 h and 48 h, respectively, at a final concentration of 10 $\mu\text{g}/\text{mL}$ DEP. DEP were characterized by scanning electron microscopy (SEM) and energy-dispersive X-ray spectra (EDX), which was recorded by FEI Quanta FEG 650 equipped with a FEG source (FEI Quanta FEG 650, FEI Company, Hillsboro, OR, USA). Cell samples of different treatments were stained for cytoskeletal (Alexa Flour® 488 phalloidin) and nuclear architecture (DAPI) according to manufacturer's protocol (Thermo Fisher Scientific), and were imaged by an LSM 710 confocal laser scanning microscopy (Carl Zeiss, Thornwood, NY, USA).

4.4.2 Raman Microspectroscopy

To minimize background in RM, a density of 1×10^5 cells per 2 mL of media was seeded on a sterilized magnesium fluoride (MgF_2) optical window (United Crystals Co., Port Washington, NY). Raman spectra were acquired with a Renishaw inVia Confocal Raman System coupled a Leica microscope (Leica DMLM, Leica Microsystems, Buffalo Grove, IL, USA) with a $63 \times$ water immersion objective. The Raman system (Renishaw, Wotton-under-Edge, Gloucestershire, UK) was equipped with a thermoelectrically cooled Renishaw RenCam NIR enhanced charge-coupled device (CCD) detector and a 785 nm near-IR laser was employed as excitation source. The Raman microscope was equipped with a motorized XYZ positioning stage (Prior Scientific, Cambridge, UK) with integrated position sensors on the X and Y axes with a 0.1 μm displacement capacity. Instrument control and data collection was performed with Renishaw WiRE 3.3 software. The confocal configuration placed a physical block or "pinhole" in the laser path and reduced the illuminated laser area

to a $\sim 3 \times 3 \mu\text{m}$ laser spot. Additional high confocality software settings allowed largely improved signal-to-noise in the final data. The spectrometer was calibrated with silicon at a static spectrum centered at 520.5 cm^{-1} for 1 s. Cells were cultured on 13 mm MgF_2 with $\sim 70\%$ confluency, then placed in a 50 mm glass Petri dish lined with a reflective metal substrate, with Earle's Balanced Salt Solutions (EBSS) as the imaging medium. Spectra were collected in a static mode for two accumulations at 20 s laser exposure over a wavenumber range of $600 - 1800 \text{ cm}^{-1}$ for cells and culture medium at the same focal plane [26]. If necessary, Cosmic Ray Removal (CRR) was performed. Four spectra per location and three locations for each cell were imaged (16 total spectra per location): nucleus, cytoplasm and cell membrane. The diffraction limited optical resolution for the $63 \times$ objective was calculated by the Abbe equation [23]. In this experiment, 48 spectra (4 replicates per location \times 3 locations per cells \times 4 individual cells) for each time treatment point were collected. Raman spectra are affected by the physical properties of the samples and background noise, so it is necessary to perform mathematical processes to reduce systematic noise, and enhance resolution of chemical compositions from target cells. Firstly, Raman spectra were smoothed by moving average smoothing to filter high-frequency noise. Then, second derivative of smoothed spectra was performed to eliminate baseline drifts and background interference. This method of data processing helps to distinguish overlapping peaks and improve resolution and sensitivity of spectra [27].

4.4.3 Measurement of cytokines and chemokines secretion by multiplex ELISA

To analyze the secretion of cytokines and chemokines, cell supernatants with different treatments were collected and centrifuged at $250 \times g$ for 5 min to remove cells and then centrifuged at $2500 \times g$ for 5 minutes to remove DEP prior to storage at -80°C . The

samples were tested as single batches on Quansys Biosciences' (Logan, UT, USA) Q-Plex Array™ kits for human cytokines and chemokines. The data were reported as mean \pm SD (standard deviation of the mean), and the statistical difference was analyzed by one-way ANOVA.

4.4.4 Flow Cytometry

Flow cytometry was performed with BD FACSAria II (BD Biosciences, San Jose, CA, USA), and data analysis was conducted by FACSDiva version 6.1.3 (BD Biosciences).

Protocol of Plasma membrane potential. The dye bis-(1, 3-Dibarbituric acid)-trimethine oxanol (DiBAC4(3)) (Ex/Em: 493/516 nm; Enzo Life Sciences, Farmingdale, NY, USA) was applied to detect the alterations in plasma membrane potential of A549 in the absence and presence of 10 μ M RES and 10 μ g/mL DEP. DiBAC4(3) serves as an indicator for the changes in membrane potential. An increase in fluorescence intensity indicates depolarization of cells, while a decrease in fluorescence intensity is indicative of cell hyperpolarization. The harvested DEP-treated cells were incubated in 5 μ M dye-PBS solution in 37°C incubator with 5% CO₂ for 30 min. Then stained cells were immediately tested by flow cytometry.

Protocol of Cell cycle. The floating and adherent cells were collected, washed twice with PBS before centrifuged. The pellet was fixed in 70% (v/v) ethanol for 24 h at 4 °C. The cells were washed once with PBS and resuspended in cold propidium iodide (PI; 50 μ g/ml) containing RNase A (0.1 mg/mL) in PBS (pH 7.4) for 30 min in the dark. Cellular DNA content was analyzed by flow cytometry. Forward light scatter characteristics were used to exclude cell debris from the analysis. At least 10,000 cells were used for each analysis.

4.4.5 Atomic Force Microscopy

The cells were seeded on poly-L-lysine coated glass bottom Petri dishes (MatTek Corp., Ashland, MA, USA) at a density of 1×10^5 cells per 2 mL of media. Cells with different treatments were then measured by AFM. For AFM measurements, the *in situ* approach was used to visualize cell topography and measure the mechanical properties such as adhesion force and Young's modulus; that is, cells grown on poly-D-lysine-coated glass bottom Petri dishes were directly transferred onto AFM scanner stage for measurements without any pretreatment, and whole measurements were conducted in culture media at room temperature within 2 h; the acquired imaging and data thus reflected the morphology and physiological status of the observed living cells.

The contact mode Picoplus AFM controlled by software PicoView 1.14 (Agilent Technologies, Santa Clara, CA, USA) was applied to perform measurements directly in cell culture media. The spring constant of the cantilever was calibrated at 0.06 ~ 0.11 N/m using the Thermal K Calibration Kit (Agilent Technologies). The length of tip with pyramid shape is approximately 3 μm , and the curvature radius of the Si_3N_4 tip is around 10 nm. Meanwhile, the approach/retract velocity applied throughout the experiments of deflection (nm) vs. distance (nm) curve acquirement was 6 $\mu\text{m/s}$. The values for the adhesion force (the detachment force between bare AFM tip and cell surface in the process of AFM cantilever retracting, which reflects alteration of cell membrane adhesion behavior/property or denaturation of membrane surface adhesion molecules) were extracted from curves of deflection (nm) vs. distance (nm) via the Scanning Probe Image Processor (SPIP) software (Image Metrology, Hørsholm, Denmark). Over 10 cells were measured, collecting at least 50 force curves of each individual cell. By applying the AFM tip to the cell surface, the

elasticity modulus of cells can be evaluated based on the slope of compliance portion of the deflection-distance curves. To analyze alterations in cell elasticity, Young's modulus was calculated according to the formula [15, 28, 29]:

$$E_{cell} = \frac{4 \cdot F_{(\Delta z)} \cdot (1 - \eta_{cell}^2)}{3 \cdot \Delta z^2 \cdot \tan \theta} \quad (1)$$

Where, E_{cell} , cellular Young's modulus; F , loading force; η_{cell} , Poisson ratio (assuming 0.5); Δz , indentation; θ is the tip half opening angle that equals to 36° .

Young's modulus and adhesion force were calculated based on hundreds of deflection-distance curves acquired for each group. Furthermore, to assess statistically significant differences in biomechanical properties including adhesion force and cellular elasticity between the two groups, the data were reported as mean \pm SE (standard error of the mean), and the statistical difference was analyzed by a Student's t-test. The data used to graph histogram were measured from the whole cell body, and the histograms were plotted by OriginPro 9.0 (OriginLab Corp., Northampton, MA, USA).

4.5 RESULTS

4.5.1 Characterization of DEP by SEM

From the EDX spectrum (Figure 4.1A), the DEPs used in this study consisted of non-metal element, metal and metal oxide compounds [30]. DEP size in culture medium ranged from nanometers to as large as micrometers (Figure 4.1A (inset)), which is similar to previous report [31].

Figure 4.1(B-D) illustrates the representative SEM images of A549 cells without treatment, treated with 24 h DEP, and treated with 24 h RES first and then 24 h DEP (black arrow points to DEP), respectively. It was found that after 24 h DEP exposure (Figure 4.1C) the filaments of the cells decreased compared to control (Figure 4.1B). However, the group of cells treated with 24 h RES first and followed by 24 h DEP exposure (Figure 4.1D) exhibited more well-defined filaments than that of 24 h DEP group (Figure 4.1C), suggesting that RES may play an important role in protecting cellular structure.

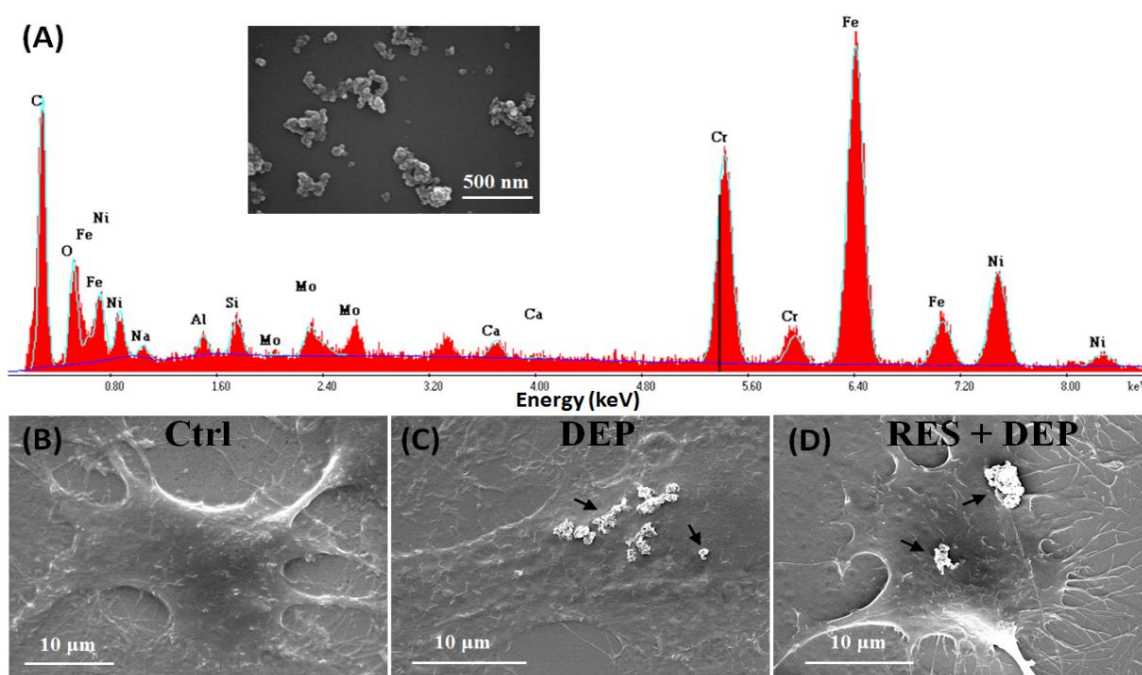


Figure 4.1 Energy-dispersive X-ray spectroscopy of DEP (A) used in this study (inset is the representative SEM image of DEP). Representative SEM images of A549 cells without treatment (B), treated with 24 h DEP (C) and treated with 24 h RES and 24 h DEP (D) (black arrow points to DEP).

4.5.2 Morphological comparison by confocal laser scanning microscopy

To further detect cytoskeletal alterations of A549 treated with DEP for different exposure times before and after RES pre-treatment, laser scanning confocal microscopy was applied to visualize cellular structure, as shown in Figure 4.2 (green fluorescence). DEP can be easily found in DIC images (black dots). It was observed that cytoskeleton was gradually obscure after 16 h DEP exposure in non-RES group (Figure 4.2A). Additionally, cell shape and cell architectures especially lamellipodia structures became obviously contracted over longer DEP exposure time. In contrast, cytoskeletal structures arranged in parallel can be readily seen in RES group (Figure 4.2B) under similar DEP exposure time (e.g., 16 h exposure timepoint), and the RES group possessed more cellular filamentous cytoskeleton or filopodia. These observations revealed the damage effect from DEP on cellular structures and protective effect of RES on cytoskeleton, confirming the findings from AFM results below.

4.5.3 RES attenuated DEP-induced biomechanical alterations of A549 cells by AFM

AFM was applied to imaging cellular topography and detect cell biomechanics for the cells under DEP and/or RES exposures, as shown in Figure 4.3. Figure 4.3(A-B) displayed cellular deflection topography images from different treatment times (from 4 h to 48 h) and the corresponding 3D view images (row 1 and row 2), respectively. Morphological changes due to DEP exposure were found in Figure 4.3A, and it was observed that cell size gradually reduced over DEP exposure time, compared to control cells. However, the RES treated group (Figure 4.3B) exhibited well-defined cytoskeleton and more cellular surrounding structures in comparison with non-RES treated group under similar DEP exposure time. For example, after 8 h exposure, RES/DEP treatment group presented more flat and filamentous

cytoskeleton than non-RES groups, suggesting that the presence of RES may maintain cellular morphology even under DEP exposure.

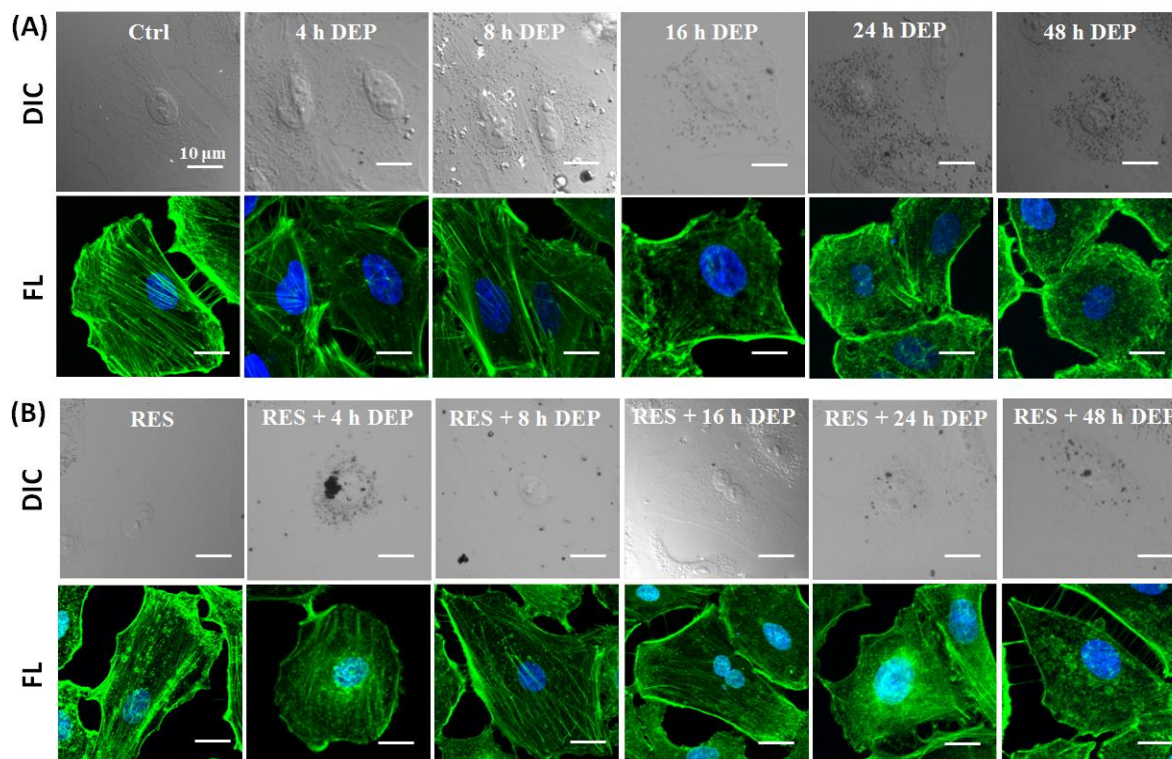


Figure 4.2 Differential interference contrast (DIC) images (row 1 and row 3) and corresponding fluorescence (FL) confocal images (row 2 and row 4) of A549 cells treated with DEP for different time and treated with RES and DEP for different time (scale bar: 10 μm; DEP: black spot in DIC images; nucleus: DAPI, blue; cytoskeleton: fluorescein phalloidin, green).

After observing the cytoskeletal changes, it was of interest to investigate the biomechanical properties of A549 in the absence and presence of RES, which would offer new insights into assessments of DEP cytotoxicity and RES role in protecting cells from DEP induced damage. Therefore, AFM was also used to quantify mechanical property changes

(including Young's modulus and membrane adhesion force) of A549 cells in culture medium, as shown in Figure 4.3(C-D). Furthermore, a statistical analysis of alterations of adhesion force and Young's modulus (cell elasticity) obtained from multiple cells was conducted. Both histograms of Young's modulus (Figure 4.3C) and adhesion force (Figure 4.3D) fluctuated over DEP exposure time in both non-RES and RES groups, and they both had peak values at 24 h DEP (19.16 kPa for non-RES group; 17.17 kPa for RES group). In addition, it was observed that Young's modulus in presence RES increased slightly over the exposure time except 16 h and 24 h (which slight decrease). In general, the presence of RES lead to the slight increase in adhesion force across all exposure time (Figure 4.3D), indicating that RES made cell tougher and difficult to migrate. For example, at 0 h DEP (control group) the value of Young's modulus and adhesion force for RES group was 1.3-fold and 1.2-fold than those of non-RES group, respectively; while at 48 h DEP treatment, the value of Young's modulus and adhesion force for RES group was 1.2-fold and 1.2-fold than those of non-RES group, respectively. The AFM results indicated that DEP damage lead to the changes of cytoskeleton and biomechanical properties, and RES may play a protective role in cellular structures from the DEP induced damage.

4.5.4 RES affected DEP-induced biochemical changes of A549 cells by Raman microspectroscopy

Raman representative bright-field images and the corresponding spectra of four time points (0 h, 4 h, 16 h and 48 h DEP exposure) with or without RES treatments were shown in Figure 4.4(A-B). Raman bright-field images exhibited the morphologic changes of A549 cells (labelled with white dash line) treated with different time points of DEP. Three averaged spectra (under each bright-field image) correspond to three locations on a single

cell were presented in color: nucleus (black), cytoplasm (red), and cell membrane (blue). Each spectrum was the averaged spectrum from four randomly selected cells. It was observed that the spectra of non-RES group and RES group are similar at 0 h and 48 h DEP. Both groups exhibited well-defined spectral peaks at 0 h DEP, while these characteristic peaks disappeared after 48 h DEP treatment, indicating the destructive effect from DEP. However, it was found that RES group displayed more spectral peaks than non-RES group at 4 h and 16 h DEP incubation, suggesting that RES may protect cellular biocomposition against DEP. To further compare these spectral differences, characteristic peaks were extracted for analysis.

A representative Raman spectrum of A549 cells without treatment is shown in Figure 4.4C. Two characteristic peaks at 786 cm^{-1} (DNA and phosphodiester) and 1660 cm^{-1} (Amide I) are selected to compare the spectral changes of cellular biopolymers due to DEP and RES exposure, and the change in peak intensities (normalized to the highest peak in the spectrum) from three cell locations is displayed in Figure 4.4(D-F). It was found that these peak intensities at nucleus, cytoplasm and cell membrane decreased with the increase of DEP exposure time. The peak intensity decrease of 786 cm^{-1} at nucleus (Figure 4.4D) indicated that extended DEP exposure could damage cellular DNA. Also, DEP could suppress the presence of Amide I at cytoplasm and membrane, as seen from Figure 4.4(E-F). In addition, RES treatment attenuated the decrease of the DEP-induced peak intensities, suggesting RES affects the cellular biocomponents of exposed cells.

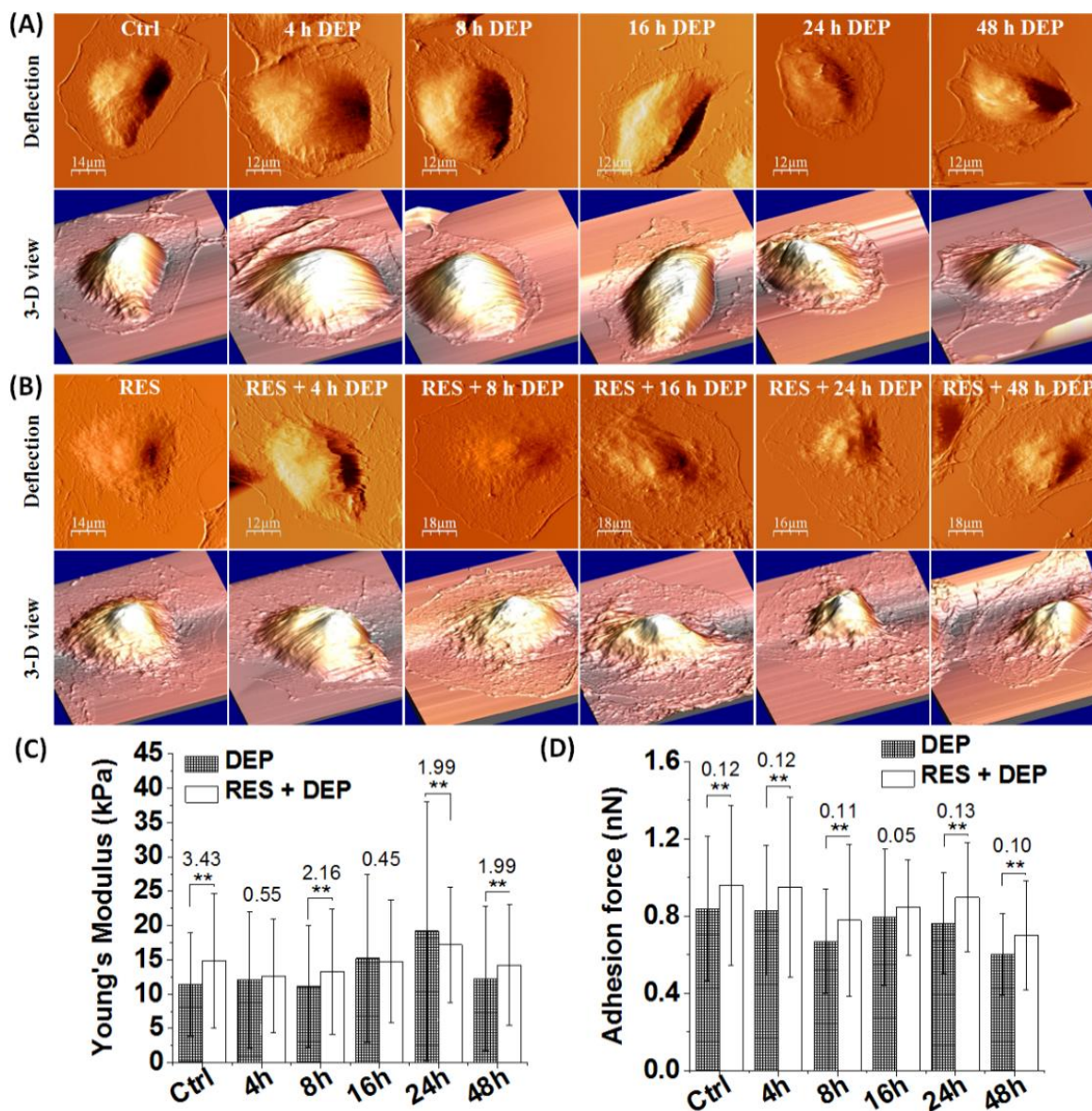


Figure 4.3 Representative AFM deflection images and corresponding 3-D images of A549 treated with 10 $\mu\text{g}/\text{mL}$ DEP (A) and treated with 10 μM RES and 10 $\mu\text{g}/\text{mL}$ DEP (B) for different times. Histograms of Young's modulus (C) and adhesion force (D) of A549 cells treated with different groups. The data of histograms were obtained from multiple individual cells (Error bars are standard deviation of the mean; $N \geq 10$, ** $p < 0.01$).

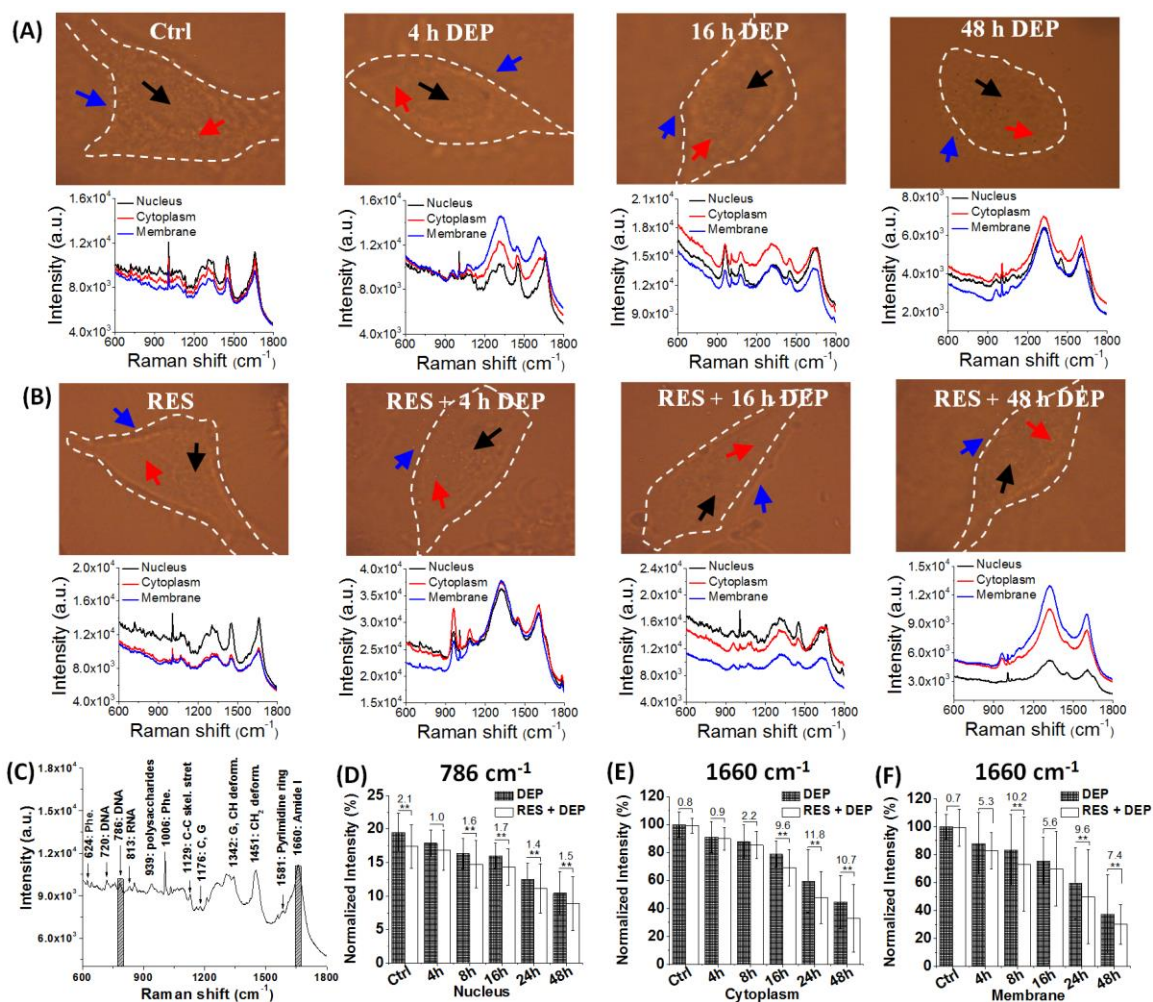


Figure 4.4 Raman bright-field images and spectra of A549 cells with 0 h, 4 h, 16 h and 48 h DEP treatment (A) and treated with 24 h RES in advance, followed by 0 h, 4 h, 16 h and 48 h DEP treatment (B). In row 1 of (A) and (B) white dash line illustrates cellular morphology; black arrow points to nucleus; red arrow points to cytoplasm; blue arrow points to membrane. Row 2 of (A) and (B) is the corresponding confocal Raman spectra at different cellular locations as assigned by different color: nucleus (black); cytoplasm (red) and cell membrane (blue). A representative Raman spectrum of A549 cells without treatment (C). Raman peak intensity changes for nucleus (D), cytoplasm (E) and membrane (F) at Raman peaks 786 and 1660 cm⁻¹ (Error bars of (D–F) are standard deviation of the mean; N ≥ 4, ***p* < 0.01).

4.5.5 Cytokine and Chemokine analysis of DEP-induced A549 cells before and after

RES treatment

Seven human cytokines and chemokines (IL-6, IL-8, MCP-1, RANTES, GRO α , GM-CSF and Eotaxin) assayed by multiplex ELISA were selected to compare the inflammatory changes among different treatments, as shown in Figure 4.5. It was noticed that the increase of DEP exposure time resulted in the elevated inflammatory responses, which were reflected by the increasing level of some important cytokines and chemokines secretion. As an example, from 0 h DEP to 48 h DEP exposure, it led to the expression of IL-6, IL-8, MCP-1, RANTES, GRO α , GM-CSF and Eotaxin increased 44.4%, 74.3%, 62.7%, 43.2%, 21.5%, 49.7% and 116.7%, respectively. As comparison, it was found that RES treatment increased the secretion of cytokines and chemokines of DEP-induced cells (even for control group), especially for IL-6, IL-8, MCP-1, RANTES and GRO α (Figure 4.5(A-E)). In control cells (0 h DEP), RES treatment exhibited an increase of 4.3-fold for IL-6, 3.3-fold for IL-8, 2.5-fold for MCP-1, 3.5-fold for RANTES, 2.0-fold for GRO α , 1.1-fold for GM-CSF, and 1.7-fold for Eotaxin than those of non-RES treatment.

Overall, the cytokines and chemokines levels for A549 cells were found to be elevated over DEP exposure time. Compared to non-DEP treated groups, A549 released higher levels of cytokines and chemokines in presence of RES. This observation suggested that the presence of RES seems to make the DEP damaged cells become “worse” with enhanced inflammatory responses, and it is possible that RES may play a different role in the regulation of cytokines/chemokines levels than the regulation of cell biomechanics over DEP exposure.

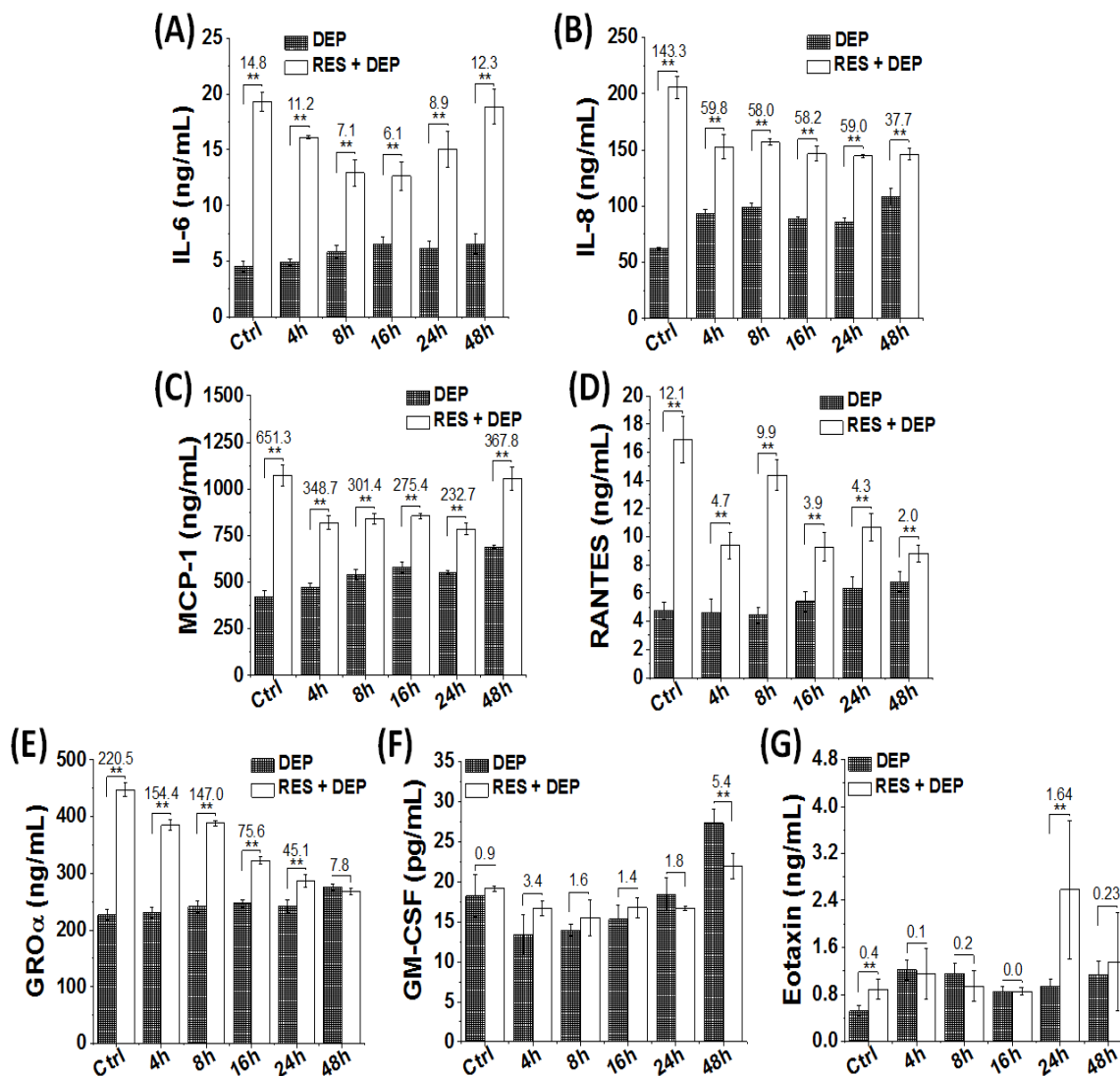


Figure 4.5 RES induced cytokines and chemokines release from A549 cells. Histograms of IL-6, IL-8, MCP-1, RANTES, GRO α , GM-CSF and Eotaxin (A-G) showed mean values of three independent experiments of both types of cells. Cells were exposed to 10 μ M RES for 24 h and 10 μ g/mL DEP for 0 h (no DEP treatment), 4 h, 8 h, 16 h, 24 h and 48 h, or only treated by 10 μ g/mL DEP 0 h (no DEP treatment), 4 h, 8 h, 16 h, 24 h and 48 h for before measurement (Error bars are standard deviation of the mean; N = 3, ** p < 0.01).

4.5.6 Plasma membrane potential and cell cycle analysis

To further evaluate the biophysical responses, flow cytometry was applied to investigate the effect of RES on plasma membrane potential (PMP) and cell cycle of DEP exposed A549 cells (Figure 4.6). These histograms of statistical analysis were based on three independent experiments of just DEP treated cells and RES combined with DEP treated cells.

In PMP measurement, the fluorescence of the dye DiBAC4(3) reflects the level of PMP. In depolarized cells, DiBAC4(3) can easily bind to intracellular proteins or membrane to exhibit higher fluorescence intensity, which corresponds to high PMP. Conversely, a decrease in fluorescence (low PMP) is indicative of cell hyperpolarization. The PMP of both cells with and without RES groups fluctuated over DEP exposure time (Figure 4.6A). Non-RES group (DEP only) showed the increasing trend up to 8 h at which PMP reached the largest (2.0-fold of 0 h DEP), and then decreased gradually till reached stable at 24 h through 48 h exposure time (67.9% of 0 h DEP). However, the presence of RES maintained the PMP stable in first 8 h of DEP exposure, then decreased till 16 h; slightly increased PMP (~9% of 0 h DEP) after 24 h DEP exposure was then observed. It was noticed that the PMP value of non-RES group was 2.0-fold at 8 h DEP and 1.9-fold at 16 h DEP than those of corresponding RES group. However, the PMP values of non-RES group at 24 h and 48 h DEP became 61.3% and 61.1% of those corresponding RES group. The fluctuation of PMP revealed that DEP can lead to cellular depolarization and hyperpolarization at different times of DEP exposure, and RES can decrease DEP-induced PMP over the first 16 h of DEP exposure, followed by the increase in PMP from 24 h to 48 h.

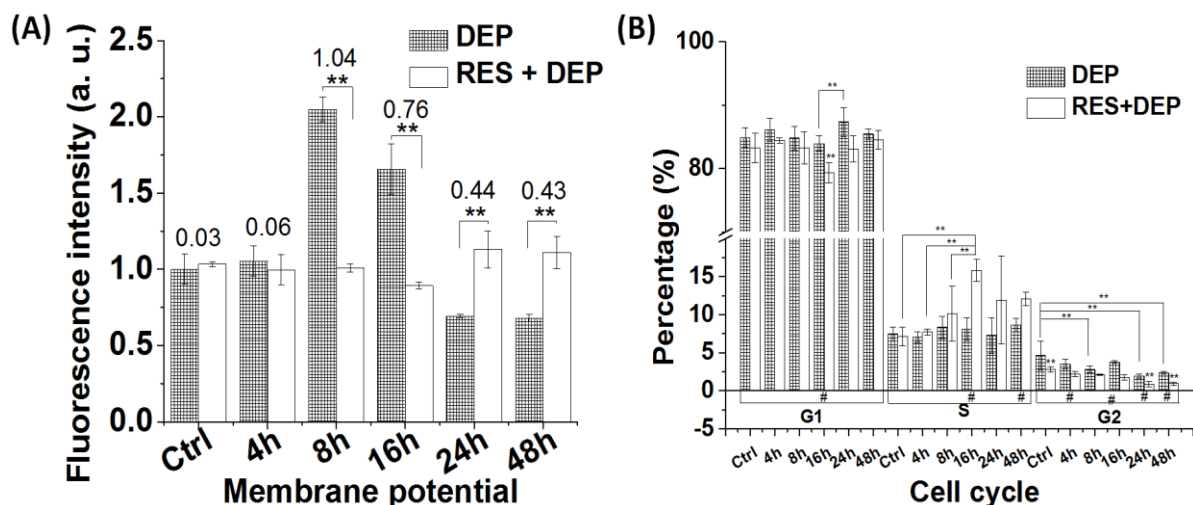


Figure 4.6 Changes of plasma membrane potential (A) (control group was normalized as 1) and cell cycle (B) of A549 cells treated with 10 $\mu\text{g}/\text{mL}$ DEP and treated with 10 μM RES and 10 $\mu\text{g}/\text{mL}$ DEP assayed by flow cytometry. Results represent the means of three separate experiments, and error bars represent the standard error of the mean. All experimental groups significantly differs from control group (Error bars are standard deviation of the mean; $N = 3$, $**p < 0.01$).

The regulation of the cell cycle plays an important role in cell survival because it can repair genetic damage and prevent uncontrolled cell division. To study the effect from RES on the cell cycle progression of A549 cells, the cells were stained with PI and then flow cytometry was performed on cells incubated with 10 μM RES for 24 h in advance then treated without DEP or treated with 10 $\mu\text{g}/\text{mL}$ DEP for 4 h, 8 h, 16 h, 24 h and 48 h (Figure 4.6B). It was observed that most of cells from non-RES and RES groups were resting cells (over 80% of cells for all treatments in G1 stage except cells treated with RES and 16 h DEP (79% of cells in G1)), and G2 stage had the least percentage of cells for all treatments. Cells treated with RES and 16 h DEP were significantly increased in the S phase. The percentages

of cells in G2 stage for both non-RES and RES groups decreased over DEP exposure time except the group of RES and 16 h DEP. In non-RES group the cells, G2 stage percentage decreased 75.9%, 60.2%, 81.4%, 42.4% and 50.9% at 4 h, 8 h, 16 h, 24 h and 48 h DEP, compared to control group, respectively. Similarly, compared to control group, G2 stage percentages in presence of RES also decreased 78.1%, 74.5%, 61.6%, 31.7% and 32.6% at 4 h, 8 h, 16 h, 24 h and 48 h DEP respectively. In comparison, it was found that the non-RES group had 1.6-fold, 1.6-fold, 1.3-fold, 2.1-fold, 2.2-fold and 2.6-fold more cells in G2 than the RES group at 0 h, 4 h, 8 h, 16 h, 24 h and 48 h DEP, respectively. These cell cycle results indicated that most of A549 cells from both non-RES and RES groups were arrested in the G1 phase of cell cycle over DEP exposure time. The percentages of cells in G2 phase decreased over DEP exposure time for both non-RES and RES groups, and RES group had less percentage of G2 stage cells than that of non-RES group at each DEP exposure time point.

4.6 DISCUSSION

Cytotoxicity of DEP evokes increasing concerns with adverse effects on human health, especially on the respiratory system. Antioxidant is an effective approach for protection against environmental factor-induced damage. RES has been well known for its antioxidant role and protective effects against oxidative damage [32]. Previous approaches to study cytotoxicity associated with DEP exposure and test the protective ability of RES were based mainly on traditional molecular biology methods (e.g., Microarray; microRNA; western blotting). However, very little information from these traditional methods can be provided with cell biophysical properties (cytoskeleton, cell architectures and cell biomechanics) and biochemical properties (biochemical components, cell surface

biomacromolecules/biopolymers), especially analysis of these properties at the single living cell level. Thus, investigations of such biophysical and biochemical information using our proposed instrument techniques would further elucidate the role of RES in potential protection of DEP induced cell damage.

Inspired by this motivation, first SEM was applied to confirm the localization of DEP on A549 cells and distinguish their structural differences (Figure 4.1). It was noticed that the size of DEP was not uniform and distributed randomly around the cells. There were obvious morphological differences between DEP group and RES/DEP combined treatment group: the later displayed more filaments and well-defined surrounding cellular structures. Confocal fluorescence microscopy images (Figure 4.2) showed that changes of cytoskeletal organization induced by DEP can be distinguished. The cytoskeletal structures of DEP treated cells became obscure and decreasing F-actin filaments after 8 h DEP exposure, implying denaturation of membrane molecules occurred at these time points, whereas cells of combined RES and DEP treatment group possessed a clear and intact cytoskeleton structures in the first 16 h.

Furthermore, AFM was utilized to detect biophysical changes at single cell level in the absence and presence of RES, and besides visualization of possible rearrangement and even destruction of cytoskeleton induced by DEP. Observations of membrane cytoskeleton indicated that DEP treatment induced significant alterations in cell architectures after 16 h treatment, and the topographical images revealed that the cell lamellipodia structures became obviously contracted over DEP exposure time. However, the group treated with combined RES/DEP possessed more cellular filamentous cytoskeleton or filopodia than the group treated with DEP only at the same DEP treatment duration (e.g., after 8 h DEP exposure),

and the topography images of combined RES with DEP group were similar to non-treatment group (Figure 4.3). Such observations and analyses revealed that 10 $\mu\text{g/ml}$ of DEP intervention could induce obvious changes in cell membrane cytoskeleton and cell topography, and 10 μM RES of 24 h incubation (before DEP exposure) could prevent the structural damage from DEP. In addition, cellular biomechanics (Young's modulus and adhesion force) were generally increased after treated with RES at most of DEP exposure timepoints, compared to non-RES group. It was reported that cancer cells normally have lower cellular biomechanics (cell stiffness and adhesion) than that of their normal counterparts, and these biomechanical differences can be indicative of early diagnosis of cancers [33, 34]. When first treated with RES before DEP exposure, the biomechanical properties of A549 cells were larger than these of non-RES group, which means RES treated A549 cells became less cancerous and would be more difficult to migrate. These observations implied that RES plays a significant role in the regulation of cellular cytoskeleton and prevention of cancer migration. Characterizations of these biophysical properties demonstrated the competence and utility of AFM as a force-sensitive nanotechnology in the study of DEP induced cellular damage and the potential protective effect of RES. Our work here supports the conclusion that cell nanomechanics [17] such as elasticity [35] could be a promising "biomarker" to reveal cellular phenotypic events [36] associated with cytoskeleton arrangement [15] and the decomposition of membrane surface molecules.

To assess how RES treatment affects the biochemical composition of A549 cells over DEP exposure time, RM was then used to evaluate spectral changes that directly reflect the biochemical alterations of individual A549 cell under various DEP treatment times (Figure

4.4). The Raman spectra from three locations (cell nucleus, cytoplasm, cell membrane) were selected to compare spectral changes in some characteristic peak intensities, as a function of DEP exposure time. It was noticed that Raman spectra at each location were distinctive with reproducible band differences. Spectra of non-DEP group (Ctrl and RES in Figure 4.4) illustrated well-defined Raman bands. Peak assignments of RM spectra of A549 cells have been given previously [37-41]. For RM spectra of cells treated with only DEP and DEP combined with RES, these characteristic peaks were significantly suppressed in all five DEP exposure timepoints (4, 8, 16, 24 and 48 h), suggesting DEP had destructed cellular surface structures. Statistical analysis of Raman characteristic peaks at 786 cm^{-1} (DNA) at nucleus and 1660 cm^{-1} (protein) at cytoplasm and membrane revealed that biochemical changes were time-dependent (Figure 4.4(D-F)). The gradual decrease of peak intensity at 786 cm^{-1} and 1660 cm^{-1} clearly indicated that DEP can damage cellular DNA and protein, which is consistent with previous studies that DEP exposure leads to DNA damage [42, 43]. Meantime, the DNA and protein decrease induced by DEP were attenuated for RES-treated cells, indicating A549 cells became more sensitive to DEP exposure after 24 h RES pre-treatment. It was reported that RES has the functions of chemopreventive and chemotherapeutic for lung cancer by inhibiting cancer cells growth and inducing considerable physiologic alterations (apoptosis, cell cycle, cell proliferation, etc.) [44, 45], which may account for the biophysical and biochemical differences between RES group and no-RES group. Our previous study found that normal cells are more sensitive to DEP exposure [46], suggesting RES treatment may turn cancer cells (A549) to less malignant cancer cells. Additionally, the higher expression of pro-inflammatory responses (cytokines/chemokines) in Figure 4.5 confirmed that RES treated cancer cells actually led to

more secretion of typical cytokines/chemokines, especially IL-6, IL-8, MCP-1, RANTES and GRO α . Higher levels of such cytokines and chemokines also implied greater protein changes in cells, which is supported by the RM results which showed that RES treated cells had larger change of characteristic protein peak intensities than those of non-RES treatment.

It was reported that among normal cells cellular depolarization and hyperpolarization can induce a decrease and an increase in cellular stiffness respectively [47, 48]. From AFM measurements (Figure 4.3.(C-D)), it was noticed that cellular Young's modulus at 8 h and 24 h DEP exposure was the least and largest within DEP treated groups, which can match with the largest and the least value of PMP at 8 h and 24 h DEP exposure (Figure 4.6(A)). However, it was difficult to find similar relationship in other groups. Although the changes of PMP measured by flow cytometry cannot fully match with the trend of cellular Young's modulus measured by AFM, our measurements still provide complimentary cell biomechanics information (cell elasticity) in addition to other biophysical properties (PMP). In Figure 4.6B cell cycles of both RES group and non-RES group arrest in the G1 phase, which can delay cell proliferation and migration. This observation is different from previous report that RES can cause an arrest cells in S phase of cell cycle [49], and this difference may come from different RES treatment conditions (time, concentration and so on), and the chemical structure difference between RES and RES analogue.

In summary, SEM, confocal, and AFM results confirmed the destructive effect of DEP on cellular structures and the protective role of RES in cytoskeleton. We successfully observed the biophysical and biochemical differences of cells under different DEP exposure duration with and without RES. DEP treatments can change cell stiffness and adhesion force, which is beneficial for the study of respiratory diseases at sub-cellular scale. RES can

strengthen cellular biomechanical properties, inhibiting cellular metastasis and making cells more sensitive to DEP. Characteristic Raman peak intensity changes revealed that DEP can decrease DNA and protein, and the presence of RES attenuated the decrease of DNA and protein induced by DEP. Cytokines and chemokines analysis indicated that RES pre-treatment can enhance the DEP-induced inflammatory responses of exposed cells, making cells more sensitive to DEP by secreting higher level of cytokines and chemokines. Combined RM and AFM measurements allowed us to quantitatively assess biochemical and biomechanical changes due to DEP-induced cytotoxicity and the effect from RES at single cell level. These findings indicated that DEP exposure induces significant biophysical and biochemical alterations that are relevant to early pathological development. Meantime, RES plays a protective role in DEP-induced lung cell structure damage. This work evaluates cellular biomechanical and biochemical changes, and provides an insightful information on the interaction between environmental pollution and antioxidant on a single cell, which is important for the research area of respiratory diseases.

4.7 REFERENCES

1. Kunzli N, Kaiser R, Medina S, Studnicka M, Chanel O, Filliger P, et al. Public-health impact of outdoor and traffic-related air pollution: a European assessment. *Lancet*. 2000; 356: 795-801.
2. Samet JM, Dominici F, Currier FC, Coursac I, Zeger SL. Fine particulate air pollution and mortality in 20 US Cities, 1987-1994. *New Engl J Med*. 2000; 343: 1742-9.

3. Pope CA, Thun MJ, Namboodiri MM, Dockery DW, Evans JS, Speizer FE, et al. Particulate Air-Pollution as a Predictor of Mortality in a Prospective-Study of Us Adults. *Am J Resp Crit Care*. 1995; 151: 669-74.
4. Brauer M, Henderson S. Diesel exhaust particles and related air pollution from traffic sources in the Lower Mainland. Health Canada, Environment and Sustainability Program: Willingdon Green. 2003: 1-28.
5. Mazarella G, Ferraraccio F, Prati MV, Annunziata S, Bianco A, Mezzogiorno A, et al. Effects of diesel exhaust particles on human lung epithelial cells: An in vitro study. *Resp Med*. 2007; 101: 1155-62.
6. Donaldson K, Mills N, MacNee W, Robinson S, Newby D. Role of inflammation in cardiopulmonary health effects of PM. *Toxicol Appl Pharmacol*. 2005; 207: 483-8.
7. Moller P, Folkmann JK, Forchhammer L, Brauner EV, Danielsen PH, Risom L, et al. Air pollution, oxidative damage to DNA, and carcinogenesis. *Cancer Lett*. 2008; 266: 84-97.
8. Soleas GJ, Diamandis EP, Goldberg DM. Resveratrol: A molecule whose time has come? And gone? *Clin Biochem*. 1997; 30: 91-113.
9. Middleton E, Kandaswami C, Theoharides TC. The effects of plant flavonoids on mammalian cells: Implications for inflammation, heart disease, and cancer. *Pharmacol Rev*. 2000; 52: 673-751.
10. Di Santo A, Mezzetti A, Napoleone E, Di Tommaso R, Donati MB, De Gaetano G, et al. Resveratrol and quercetin down-regulate tissue factor expression by human stimulated vascular cells. *J Thromb Haemost*. 2003; 1: 1089-95.

11. Baur JA, Sinclair DA. Therapeutic potential of resveratrol: the in vivo evidence. *Nat Rev Drug Discov.* 2006; 5: 493-506.
12. Pervaiz S. Resveratrol: from grapevines to mammalian biology. *Faseb J.* 2003; 17: 1975-85.
13. Sun AY, Simonyi A, Sun GY. The "French paradox" and beyond: Neuroprotective effects of polyphenols. *Free Radical Bio Med.* 2002; 32: 314-8.
14. Morelli R, Das S, Bertelli A, Bollini R, Lo Scalzo R, Das DK, et al. The introduction of the stilbene synthase gene enhances the natural antiradical activity of *Lycopersicon esculentum* mill. *Mol Cell Biochem.* 2006; 282: 65-73.
15. Wu YZ, McEwen GD, Harihar S, Baker SM, DeWald DB, Zhou AH. BRMS1 expression alters the ultrastructural, biomechanical and biochemical properties of MDA-MB-435 human breast carcinoma cells: An AFM and Raman microspectroscopy study. *Cancer Lett.* 2010; 293: 82-91.
16. Cross SE, Jin YS, Rao J, Gimzewski JK. Nanomechanical analysis of cells from cancer patients. *Nat Nanotechnol.* 2007; 2: 780-3.
17. Lee GYH, Lim CT. Biomechanics approaches to studying human diseases. *Trends Biotechnol.* 2007; 25: 111-8.
18. Alcaraz J, Buscemi L, Grabulosa M, Trepas X, Fabry B, Farre R, et al. Microrheology of human lung epithelial cells measured by atomic force microscopy. *Biophys J.* 2003; 84: 2071-9.
19. Rico F, Roca-Cusachs P, Gavara N, Farre R, Rotger M, Navajas D. Probing mechanical properties of living cells by atomic force microscopy with blunted pyramidal cantilever tips. *Phys Rev E.* 2005; 72.

20. Dupres V, Verbelen C, Raze D, Lafont F, Dufrene YF. Force Spectroscopy of the Interaction Between Mycobacterial Adhesins and Heparan Sulphate Proteoglycan Receptors. *Chemphyschem*. 2009; 10: 1672-5.
21. Tomankova K, Kolarova H, Bajgar R. Study of photodynamic and sonodynamic effect on A549 cell line by AFM and measurement of ROS production. *Phys Status Solidi A*. 2008; 205: 1472-7.
22. Tomankova K, Kolarova H, Bajgar R, Jirova D, Kejlova K, Mosinger J. Study of the Photodynamic Effect on the A549 Cell Line by Atomic Force Microscopy and the Influence of Green Tea Extract on the Production of Reactive Oxygen Species. *Ann Ny Acad Sci*. 2009; 1171: 549-58.
23. Ling J, Weitman SD, Miller MA, Moore RV, Bovik AC. Direct Raman imaging techniques for study of the subcellular distribution of a drug. *Appl Optics*. 2002; 41: 6006-17.
24. Yu CX, Gestl E, Eckert K, Allara D, Irudayaraj J. Characterization of human breast epithelial cells by confocal Raman micro spectroscopy. *Cancer Detect Prev*. 2006; 30: 515-22.
25. Krishna CM, Sockalingum GD, Kegelaer G, Rubin S, Kartha VB, Manfait M. Micro-Raman spectroscopy of mixed cancer cell populations. *Vib Spectrosc*. 2005; 38: 95-100.
26. Pyrgiotakis G, Bhowmick TK, Finton K, Suresh AK, Kane SG, Bellare JR, et al. Cell (A549)-particle (Jasada Bhasma) interactions using Raman spectroscopy. *Biopolymers*. 2008; 89: 555-64.

27. Barnes RJ, Dhanoa MS, Lister SJ. Standard Normal Variate Transformation and De-Trending of near-Infrared Diffuse Reflectance Spectra. *Appl Spectrosc.* 1989; 43: 772-7.
28. Rosenbluth MJ, Lam WA, Fletcher DA. Force microscopy of nonadherent cells: A comparison of leukemia cell deformability. *Biophys J.* 2006; 90: 2994-3003.
29. Wu YZ, Zhou AH. In situ, real-time tracking of cell wall topography and nanomechanics of antimycobacterial drugs treated *Mycobacterium JLS* using atomic force microscopy. *Chem Commun.* 2009: 7021-3.
30. Park EJ, Roh J, Kang MS, Kim SN, Kim Y, Choi S. Biological responses to diesel exhaust particles (DEPs) depend on the physicochemical properties of the DEPs. *PLoS One.* 2011; 6: e26749.
31. Wu Y, Yu T, Gilbertson TA, Zhou A, Xu H, Nguyen KT. Biophysical assessment of single cell cytotoxicity: diesel exhaust particle-treated human aortic endothelial cells. *PLoS One.* 2012; 7: e36885.
32. Kawada N, Seki S, Inoue M, Kuroki T. Effect of antioxidants, resveratrol, quercetin, and N-acetylcysteine, on the functions of cultured rat hepatic stellate cells and Kupffer cells. *Hepatology.* 1998; 27: 1265-74.
33. Suresh S. Nanomedicine: elastic clues in cancer detection. *Nat Nanotechnol.* 2007; 2: 748-9.
34. Cross SE, Jin YS, Rao J, Gimzewski JK. Nanomechanical analysis of cells from cancer patients. *Nat Nanotechnol.* 2007; 2: 780-3.
35. Suresh S. Nanomedicine - Elastic clues in cancer detection. *Nat Nanotechnol.* 2007; 2: 748-9.

36. Cross SE, Jin YS, Tondre J, Wong R, Rao J, Gimzewski JK. AFM-based analysis of human metastatic cancer cells. *Nanotechnology*. 2008; 19.
37. Notingher I, Verrier S, Haque S, Polak JM, Hench LL. Spectroscopic study of human lung epithelial cells (A549) in culture: Living cells versus dead cells. *Biopolymers*. 2003; 72: 230-40.
38. Verrier S, Notingher I, Polak JM, Hench LL. In situ monitoring of cell death using Raman microspectroscopy. *Biopolymers*. 2004; 74: 157-62.
39. Owen CA, Selvakumaran J, Notingher I, Jell G, Hench LL, Stevens MM. In vitro toxicology evaluation of pharmaceuticals using Raman micro-spectroscopy. *J Cell Biochem*. 2006; 99: 178-86.
40. Notingher I, Green C, Dyer C, Perkins E, Hopkins N, Lindsay C, et al. Discrimination between ricin and sulphur mustard toxicity in vitro using Raman spectroscopy. *J Roy Soc Interface*. 2004; 1: 79-90.
41. Notingher I, Selvakumaran J, Hench LL. New detection system for toxic agents based on continuous spectroscopic monitoring of living cells. *Biosens Bioelectron*. 2004; 20: 780-9.
42. Danielsen PH, Loft S, Moller P. DNA damage and cytotoxicity in type II lung epithelial (A549) cell cultures after exposure to diesel exhaust and urban street particles. *Part Fibre Toxicol*. 2008; 5: 6.
43. Danielsen PH, Loft S, Kocbach A, Schwarze PE, Moller P. Oxidative damage to DNA and repair induced by Norwegian wood smoke particles in human A549 and THP-1 cell lines. *Mutat Res*. 2009; 674: 116-22.

44. Whyte L, Huang YY, Torres K, Mehta RG. Molecular mechanisms of resveratrol action in lung cancer cells using dual protein and microarray analyses. *Cancer Res.* 2007; 67: 12007-17.
45. Bae S, Lee EM, Cha HJ, Kim K, Yoon Y, Lee H, et al. Resveratrol Alters microRNA Expression Profiles in A549 Human Non-Small Cell Lung Cancer Cells. *Mol Cells.* 2011; 32: 243-9.
46. Tang MJ, Li QF, Xiao LF, Li YP, Jensen JL, Liou TG, et al. Toxicity effects of short term diesel exhaust particles exposure to human small airway epithelial cells (SAECs) and human lung carcinoma epithelial cells (A549). *Toxicol Lett.* 2012; 215: 181-92.
47. Callies C, Fels J, Liashkovich I, Kliche K, Jeggle P, Kusche-Vihrog K, et al. Membrane potential depolarization decreases the stiffness of vascular endothelial cells. *J Cell Sci.* 2011; 124: 1936-42.
48. He DZZ, Dallos P. Somatic stiffness of cochlear outer hair cells is voltage-dependent. *Proc Natl Acad Sci U S A.* 1999; 96: 8223-8.
49. Chen Z, Jin K, Gao LY, Lou GD, Jin Y, Yu YP, et al. Anti-tumor effects of bakuchiol, an analogue of resveratrol, on human lung adenocarcinoma A549 cell line. *Eur J Pharmacol.* 2010; 643: 170-9.

CHAPTER 5

IN-VITRO BIOMECHANICAL PROPERTIES, FLUORESCENCE IMAGING, SURFACE- ENHANCED RAMAN SPECTROSCOPY, AND PHOTOTHERMAL THERAPY EVALUATION OF LUMINESCENT FUNCTIONALIZED CaMoO₄:Eu@Au HYBRID NANORODS ON HUMAN LUNG ADENOCARCINOMA EPITHELIAL CELLS

5.1 ABSTRACT

Highly dispersible Eu³⁺-doped CaMoO₄@Au-nanorod hybrid nanoparticles (HNPs) exhibit optical properties, such as plasmon resonances in the near-infrared region ~790 nm and luminescence ~615 nm, offering multimodal capabilities: fluorescence imaging, surface-enhanced Raman spectroscopy (SERS) detection and photothermal therapy (PTT). HNPs were conjugated with a Raman reporter (4-mercaptobenzoic acid), showing desired SERS signal (enhancement factor $\sim 4.76 \times 10^5$). The HNPs have heat conversion efficiency 25.6%, and hyperthermia temperature ~ 42 °C could be achieved by adjusting either concentration of HNPs, or laser power, or irradiation time. HNPs were modified with antibody specific to cancer biomarker epidermal growth factor receptor (EGFR), then applied to human lung cancer (A549) and mouse hepatocyte cells (AML12), and *in-vitro* PTT effect was studied. In addition, the biomechanical properties of A549 cells were quantified using atomic force microscopy. Together, this study shows the potential applications of these HNPs in fluorescence imaging, SERS detection, and PTT functionalities with good photostability and biocompatibility.

5.2 INTRODUCTION

Development of novel nanostructured materials with desired properties of luminescent, surface-enhanced Raman spectroscopy (SERS) and photothermal therapy (PTT) have drawn significant interest in clinical diagnosis and therapeutic monitoring in biological systems [1-5]. Ultrasensitive and non-invasive detection of specific bioanalytes in living cells can be achieved by SERS through increasing the weak inelastic scattering signal into a structurally sensitive probe [6]. To realize this SERS function with good stability and biocompatibility, the gold nanorods (GNRs) are conjugated with Raman reporter molecules followed by protective polymers (e.g., PEG) [7]. PTT reagents such as GNRs absorb near-infrared (NIR) photons which can be converted into heat energy (hyperthermia temperature ~ 42 °C) to destroy the cancer cells [8]. Hybrid nanoparticles (HNPs) exhibit fluorescence emission (~ 615 nm), good photothermal stability, and high biocompatibility are the potential good candidates for cancer therapy. Also, GNRs have high tissue penetration in the NIR region (700–850 nm). Recently, PTT agents such as GNRs [9], Au nanoshells [10], zinc ferrite spinel reduced graphene oxide ($\text{ZnFe}_2\text{O}_4\text{-rGO}$) [11], palladium nanostructures [12], CuS nanoparticles (NPs) [13], Cu_9S_5 nanocrystals [14], and other inorganic NPs have been intensively investigated. However, none of these nanostructured materials have fluorescence properties. It is also known that the proximity of GNRs on the surface of luminescent NPs (ex. lanthanide ion doped NPs) significantly enhances the luminescence efficiency [15]. HNPs were synthesized and can be used as prospective materials for killing tumor cells and diagnostic imaging applications.

The cellular biomechanics (Young's modulus and adhesion) can be considered as an indicator of early diagnosis of cancers, where cancer cells have lower Young's modulus than

their normal counterparts [16]. When the NPs interact with cells, the proteins present in the cell membrane bind to the surface of NPs and form a coating known as the protein corona. Rapid corona formation affects NPs uptake and the death of endothelial cell at an early stage [17]. Although many NPs for therapeutic applications have been studied, a little is known about the morphological and biomechanical changes of cancer cells induced by NPs. Moreover, attaining specific targeting of NPs in tumor site is particularly important. It can be achieved by conjugating antibodies (Ab) to the HNPs. Epidermal growth factor receptor (EGFR), one of the cell surface biomarkers for targeting in Ab-based cancer therapy, is a transmembrane receptor protein embedded in the plasma membrane of many types of cancer cells. Overexpression of EGFR (>50%) is observed in lung cancer patients [18, 19]. Recent studies have shown that NPs labelled with anti-EGFR Ab could effectively kill the target cancer cells when irradiated by laser light with a wavelength around the nanoparticle absorption peak [20, 21].

Herein, we demonstrate the potential use of $\text{CaMoO}_4:\text{Eu}@G\text{NR}$ (CMO:Eu@GNR) HNPs as multi-functional probes for optical imaging, and SERS and as a PTT agent. The specificity of anti-EGFR Ab coated CMO:Eu@GNR is used for the enabled targeting of EGFR over-expressing human lung cancer cells (A549 cell). Also, the effect of CMO:Eu@GNR on cellular biomechanics and biocompatibility of the cancer cells were studied. The SERS enhancement factor (EF), photothermal responses and efficiency of light-to-heat conversion of the CMO:Eu@GNR were evaluated. Also, we investigated the influence of HNPs on the PTT of A549, AML12, and white blood cells (WBC) cells illuminated at an 808 nm laser for *in-vitro* cancer killing study.

5.3 HYPOTHESIS

The synthesized NPs could specifically image, detect and kill A549 cells by the mechanism of antibody-receptor binding.

5.4 MATERIALS AND METHODS

5.4.1 Materials

Calcium nitrate tetrahydrate, ($\text{Ca}(\text{NO}_3)_2 \cdot 4\text{H}_2\text{O}$, 99%, Alfa Aesar, Ward Hill, MA, USA), ammonium molybdate ($\text{H}_8\text{MoN}_2\text{O}_4$, 99.99%, Alfa Aesar), europium(III) nitrate hydrate ($\text{Eu}(\text{NO}_3)_3 \cdot x\text{H}_2\text{O}$, 99.99%, Sigma Aldrich), oleic acid (Alfa Aesar), 1-octadecene (95%, Alfa Aesar), NaOH pellet (Merck & Co., Kenilworth, NJ, USA), hydrochloric acid (HCl, Sigma-Aldrich, St. Louis, MO, USA), HS-PEG-COOH (MW = 5000, Nanocs Inc., New York, NY, USA), mPEG-SH (MW = 5000, Nanocs Inc.), *N*-(3-dimethylaminopropyl)-*N'*-ethylcarbodiimide hydrochloride ($\text{C}_8\text{H}_{17}\text{N}_3\text{HCl}$, MW = 191.7 g/mol, Sigma-Aldrich) (EDC), *N*-hydroxysuccinimide ($\text{C}_4\text{H}_5\text{NO}_3$, Sigma-Aldrich, MW = 115.09 g/mol) (NHS), 4-mercaptobenzoic acid (MBA, Sigma-Aldrich), anti-human epidermal growth factor receptor (EGFR) antibody (Thermo Fisher Scientific, Waltham, MA, USA), and phosphate buffered saline (1X) (PBS) (Thermo Fisher Scientific) were used for HNPs synthesis. Human (*homo sapiens*) lung carcinoma (A549 cells) (ATCC, Manassas, VA, USA), Mouse hepatocyte cells (AML12, normal hepatocyte from liver tissue), 0.5% trypsin-EDTA solution (Thermo Fisher Scientific), LIVE/DEAD Viability/Cytotoxicity Assay Kit (Thermo Fisher Scientific), Earle's balanced salt solution (EBSS, Thermo Fisher Scientific) and PBS were used for cell experiments.

5.4.2 Coating GNRs on CaMoO₄:Eu NPs

Twenty mg of the CMO:Eu NPs were dispersed in 5 mL of 0.1 M HCl, and the mixture was sonicated for 1 h. To this, 2 mL of diethyl ether was added and sonicated for 30 min. The resulting solution was centrifuged at 6000 rpm for 15 min. The obtained precipitate was washed twice with ethanol and redispersed in 5 mL of PBS solution. To this, 20 mg of HS-PEG-COOH was added and sonicated for 1 h. The PEGylated capped NPs were collected by centrifugation and washed with PBS solution for three times to remove the excess of HS-PEG-COOH present in the sample. The final precipitate obtained was redispersed in a PBS solution. For the synthesis of HNPs, GNRs with 10 nm in diameter and 35 nm in length were purchased from Nanopartz. First, 4 mL of the GNRs was centrifuged at 13,000 rpm for 30 min and then redispersed in PBS. Centrifugation was repeated for three times to reduce the excess of cetyltrimethylammonium bromide (CTAB) present on the surface of the GNRs. Four mL of GNRs dispersed in PBS was added to 1 mL of the PEGylated CMO:Eu NPs under continuous stirring and then sonicated for 1 h. The resulting solution was centrifuged, and the HNPs precipitated was collected. These particles were washed with a PBS solution for three times and redispersed in PBS.

5.4.3 Raman reporter labeling and antibody conjugation

The synthesized NPs were labeled with MBA by adding 200 μ L of a MBA solution (2 mM) into 1 mL of the synthesized NPs solution. After 30 min sonication, the MBA-labelled CMO:Eu@GNR NPs were collected. For conjugating the anti-human EGFR antibody with the MBA-labelled CMO:Eu@GNR NPs, 10 μ L HS-PEG-COOH of 1 mg/mL concentration was added into the MBA-labelled NPs. After 15

min sonication, 40 μL mPEG-SH of 1 mg/mL was added for 2 h incubation followed by 30 min sonication. The prepared NPs were centrifuged for 15 min at 13,000 rpm and then resuspended in water. Next, 10 μL EDC (10 mM) and 10 μL NHS (25 mM) were added and sonicated for 30 min. The prepared NPs were centrifuged for 15 min of 13,000 rpm and then resuspended in PBS. Then, the prepared NPs were labelled with antibody (20 μL , 0.2 mg/mL) with 1 h sonication. After 15 min centrifugation at 13,000 rpm, the prepared NPs were resuspended in PBS and stored at 4 °C for further experiments.

5.4.4 Characterization of synthesized NPs

Transmission electron microscopy (TEM) images and energy-dispersive X-ray spectroscopy spectrum (EDX) were collected using an FEI Titan 80–300 kV (S) TEM equipped with a spherical aberration (Cs) image corrector. All the images were collected at 300 kV. For the TEM measurements, the powder samples were ground and dispersed in methanol. A drop of the dispersed particles was placed over a carbon-coated copper grid and evaporated to dryness at room temperature.

UV-visible spectra were recorded using a Multiskan UV-visible spectrophotometer. All the luminescence spectra were recorded using a Horiba FluoroMax-3 fluorescence spectrophotometer. A zeta potentiometer (ZetaPALS, Brookhaven Instrument, Holtsville, NY, USA) was used to measure the surface charge of the particles. Hydrodynamic diameter and particle size distributions of the HNPs were determined by dynamic light scattering (DLS) measurements using a DynaPro NanoStar (Wyatt Technology Corp., Santa Barbara, CA, USA) instrument at 25 ± 0.1 °C. Disposable cuvettes were used for the measurements.

The temperature changes of the CMO:Eu@GNR solutions irradiated by an 808 NIR laser (Xi'an Sampling Laser Technik Institute, Xi'an, Shanxi, China) were collected by a portable fiber optic thermometer (Qualitrol, Fairport, NY, USA). The photothermal images of the CMO:Eu@GNR solutions were recorded using an FLIR A20 camera (FLIR Systems, Inc., Wilsonville, OR, USA), and the laser power was measured using a handheld laser power meter (Edmund Optics, Barrington, NJ, USA).

5.4.5 Calculation of Raman enhancement factor (EF) of CMO:Eu@GNR-MBA

$$EF = \frac{I_{SERS}}{I_{RS}} \times \frac{N_{RS}}{N_{SERS}} \text{ --- (1)}$$

Using the above equation, N_{SERS} was calculated from the results of TEM and concentration analyses. First, the laser-activated volume (V_{laser}) in the micro-Raman experiment was calculated from the laser spot diameter [$d_{spot} = 0.61\lambda/NA = 1.2 \mu\text{m}$; $\lambda = 785 \text{ nm}$, NA (numerical aperture) = 0.9] and the penetration depth ($p_d = x \mu\text{m}$), resulting in a V_{laser} value of $0.942x \mu\text{m}^3$. From the commercial sample, the surface area and weight of one GNR (length = 38 nm, diameter = 10 nm) were determined as $1350 \times 10^{-6} \mu\text{m}^2$, and $5.2 \times 10^{-14} \text{ g}$, respectively. The concentration of the CMO:Eu@GNR-MBA solution was about 20 Au $\mu\text{g/mL}$, which corresponds to $3.85 \times 10^8 \text{ GNRs/mL} = 3.85 \times 10^{-4} \text{ GNRs}/\mu\text{m}^3$. Therefore, the CMO:Eu@GNR-MBA solution in V_{laser} contained $3.62 \times 10^{-4} \text{ GNRs}$, which indicates that the SERS spectra were generated by $3.62 \times 10^{-4} \text{ CMO:Eu@GNR-MBA molecules}$. On the other hand, the surface area of the MBA was 0.33 nm^2 as a monolayer [22] and therefore the number of MBA molecules absorbed onto one GNR was approximately 4091 and consequently $1.5x \text{ MBA molecules}$, which is N_{SERS} in the above equation, were absorbed onto the GNRs present in V_{laser} .

The density of MBA used in regular Raman detection was approximately 3.1×10^{-6} g/mL. Thus, the number of MBA molecules in V_{laser} for regular Raman detection was 1.13×10^4 MBA. Finally, we determined the Raman enhancement factor (EF) as

$$R_{EF} = \frac{N_{RS}}{N_{SERS}} \times \frac{I_{SERS}}{I_{RS}} = \frac{1.13 \times 10^4 x}{1.5x} \times \frac{58,495}{925} \approx 4.76 \times 10^5$$

5.4.6 Heat transfer efficiency of synthesized NPs

The change in the temperature of the HNPs was estimated by the heat input from the NIR laser via GNRs and heat dissipated into the ambient atmosphere, which can be expressed as follows:

$$\sum_{i=2} m_i C_i \frac{dT}{dt} = Q_{in} - Q_{out} \quad (2)$$

where m_i and C_i are the mass and specific heat capacity of sample i , respectively. T is the temperature of the HNPs on NIR irradiation at time t . The mass of HNPs is significantly smaller than that of water (1 g), and the specific heat capacity of GNRs and water are ~ 0.129 $\text{Jg}^{-1}\text{K}^{-1}$ and 4.18 $\text{Jg}^{-1}\text{K}^{-1}$, respectively [23]. By neglecting the specific heat capacity of GNR, eq. (i) can be modified as follows:

$$C_i \frac{dT}{dt} = Q_{in} - Q_{out} \quad (3)$$

where $Q_{in} = (I_0 - I_{tr})\eta$ and $Q_{out} = \sum hS[T(t) - T_0]$, I and I_{tr} are the NIR laser power before and after transmitting through the HNPs, h is the heat transfer efficiency, and S is the surface area of the interference between the HNPs and external environment. The increase in the temperature of the HNPs at any time t can be estimated as follows:

$$T(t) = T_0 + \frac{(I_0 - I_{tr})\eta}{mCB} (1 - e^{-Bt}) \quad (4)$$

where T_m is the maximum stable temperature of the HNPs at which laser is turned off, η is the photothermal conversion efficiency, and B is the heat dissipation constant.

The dissipation constant (B) was calculated using the temperature decay profile after the laser was turned off as follows:

$$T(t) = T_0 + (T_m - T_0)e^{-Bt} \quad (5)$$

In thermal equilibrium condition, $Q_{in} = Q_{out}$

i.e., $\eta = mCB \frac{\Delta T}{\Delta t}$ (6), all symbols have their usual meanings.

5.4.7 Cell culture and NPs treatment

A549 cells (ATCC) were cultured in F-12k medium containing 10% fetal bovine serum at 37°C with 5% CO₂ in a humidified atmosphere. Mouse hepatocyte cells (AML12, normal hepatocyte from liver tissue) purchased from American Type Culture Collection (ATCC) were cultured in a 1:1 mixture of Dulbecco's modified Eagle's medium and Ham's F12 medium (ATCC) with 0.005 mg/ml insulin, 0.005 mg/ml transferrin, 5 ng/ml selenium, 40 ng/ml dexamethasone (Sigma-Aldrich) and 10% fetal bovine serum (ATCC) at 37°C with 5% CO₂ in a humidified atmosphere.

Both cells were passaged at 70–90% confluency using 0.5% Trypsin-EDTA solution, and the cell number was estimated by a hemocytometer to be $\sim 1 \times 10^5$ cells/mL. A549 and AML12 cells ($\sim 1 \times 10^5$ cells/mL) were treated with 100 μ L prepared NPs (20 μ g/mL) for two hours incubation at 37 °C. Then, cells were washed to remove non-bound NPs. The binding of the NPs onto the cells was verified by fluorescence and SERS spectra. The fluorescence images were captured under a fluorescence microscope with DP30BW CCD camera (Olympus IX71, Olympus

America Inc., Center Valley, PA, USA) with an excitation at 450 nm and an emission at 630 nm.

5.4.8 Atomic force microscopy

A549 cells were detected by AFM contact mode controlled by Picoview software (Picoplus, Agilent Technologies, Santa Clara, CA, USA). AFM probe was applied silicon nitride with 20 nm tip radius (Bruker Corp., Billerica, MA, USA), and its spring constant was calibrated as 0.06–0.10 N/m and deflection sensitivities were 30–40 nm/V. The biomechanical properties (Young's modulus and adhesion force) of cells were calculated using a Scanning Probe Image Processor (SPIP) software (Image Metrology, Hørsholm, Denmark) by Sneddon's modification of the Hertz model from the force curves for the elastic indentation in a soft sample [24, 25]. The model describes the relationship between applied loading force F and indentation depth δ :

$$F = \frac{2}{\pi} \times \tan(\alpha) \times \frac{E_{cell}}{1 - \gamma^2} \times \delta^2$$

where E_{cell} : Young's modulus; F : loading force; γ : Poisson ratio (its value was 0.5); and α : tip half cone opening angle (its value was set to 36°). The force was obtained by the cantilever deflection $d(z)$ and the spring constant of the cantilever k : $F = k \times d(z)$. The indentation depth was calculated from the z -height and the cantilever deflection: $\delta = z - d(z)$. The Young's modulus were obtained from the force curves transformation and the linear regression fitted by the Hertz model [26]. For each group, at least 25 force curves of each cell (the total cells are over 20) were detected, and the detection was accomplished within 2 h to approximate cellular physiological conditions. For

deflection and 3D view images, the AFM images were imported into a WSXM software (Nanotec Electrónica S.L., Tres Cantos, Madrid, Spain).

5.4.9 SERS measurements of cells treated with synthesized NPs

SERS spectra were recorded using a Renishaw inVia Raman spectrometer (WIRE 3.3 software, Renishaw, Wotton-under-Edge, Gloucestershire, UK) equipped with a 300 mW, 785 nm NIR laser. Cells were cultured on magnesium fluoride (MgF₂, United Crystals Co., Port Washington, NY, USA) and imaged in EBSS through a 63 × (NA = 0.90) water immersion objective (Leica DMLM, Leica Microsystems, Buffalo Grove, IL, USA). For Raman streamline mapping, the data were acquired at 1 accumulation with 10 s exposure, and the peak at 1078 cm⁻¹ from MBA was selected for mapping. On each group, the cells were detected within 2 h at room temperature. Renishaw Wire 3.3 software (Renishaw) performed for Raman spectra baseline corrected, spectral smoothed, and normalized at maximum peaks. The processed spectra were imported to OriginPro 9 software (OriginLab Corp., Northampton, MA, USA) for analysis.

5.4.10 NIR photothermal therapy on cells

For NIR PTT, A549 and AML12 cells ($\sim 1 \times 10^5$ cells/mL) were incubated with about 100 μ L prepared NPs (20 μ g/mL CMO:Eu@GNR-MBA-Ab and CMO:Eu@GNR-MBA, respectively) for two hours incubation at 37 °C. Next, the cells were rinsed with PBS thrice and then exposed to the 808 nm laser irradiation at 1 W/cm² power densities for 5 min. For cell viability test, the cells with triplicates were stained using a LIVE/DEAD viability/cytotoxicity Assay Kit (Thermo Fisher Scientific)

according to the instruction. After staining, the cells were imaged using a fluorescence microscope equipped with a DP30BW CCD camera (Olympus IX71) at 10× objective to analyze the relative proportion of live/dead cells.

5.4.11 Zeta Potential and DLS studies

The colloidal stability of the NPs was estimated using a zeta potential (the potential close to the particle surface and thus the electrostatic stabilization) in PBS solvent. The average zeta potential of the GNR particles in a CTAB solution was found to be ~41.12 mV. The value slightly decreased when the particles were dispersed in PBS (~35.5 mV), whereas the PEGylated CMO:Eu NPs showed a negative zeta potential of ~-29.5 mV. The CMO:Eu@GNR HNPs showed a zeta potential of ~27.6 mV. This indicates that positive charge is present on the surface of HNPs. It confirms the high stability of the particles in PBS.

5.4.12 White blood cell (WBC) count experiment

EDTA stabilized human whole blood were freshly obtained from Innovative Research (Novi, MI, USA). Whole blood and serum were used for white blood cell (WBC) count analysis.

5.4.13 Statistics analysis

Data are presented as mean \pm standard deviation of error. Differences were considered significant at $p < 0.01$. The OriginPro 9 software (OriginLab Corp.) was used for one-way ANOVA for significance test.

5.5 RESULTS

5.5.1 Characterization of HNPs

Transmission electron microscopy (TEM) and high-resolution transmission electron microscopy (HRTEM) images of the CMO:Eu@GNR NPs and selected area electron diffraction pattern (SAED) are shown in Figure 5.1(A–D). The TEM image confirms the formation of hybrid nanostructures where GNRs are attached to the surface of CaMoO₄:Eu NPs (Figure 5.1(B)). The average sizes of CaMoO₄:Eu found to be ~10–15 nm and GNRs with an average diameter of ~8–12 nm and a length of ~40 nm. The distance between lattice planes ~2.283 Å corresponding to the lattice spacing in the (211) plane of tetragonal CaMoO₄, JCPDS card No. 29–0351 (Figure 5.1(C)) was calculated using ImageJ Software v1.47. The bright circular spots in the SAED patterns confirm the presence of both CaMoO₄ and GNRs phases in the CMO:Eu@GNR (Figure 5.1(D)). Furthermore, the energy dispersive X-Ray analysis (EDX) spectrum confirms the presence of Ca, Mo, O, Eu, and Au elements in the hybrid sample. Figure 5.1(E) shows the UV-visible spectra of CMO:Eu@GNR with and without Ab between 200–1000 nm. Three characteristic peaks were observed ~260, 530, and 790 nm. The absorption band ~260 nm was assigned to the Mo–O charge-transfer band (CTB) [27], and the bands ~530 and 790 nm can be attributed to the surface plasmon resonance (SPR) of GNRs [3]. The inset of Figure 5.1(E) shows the comparison of the normalized SPR absorption spectrum between 400–1000 nm. Figure 5.1(F) depicts the photoluminescence spectra of the CMO:Eu@GNR with and without Ab coating at a fixed excitation of 464 nm (${}^7F_0 \rightarrow {}^5D_2$) and show a strong red luminescence ~612 nm. Inset shows a digital photograph of HNPs under UV light. HNPs show a strong excitation spectrum at

~275 nm, which is assigned to O→Mo CTB (Mo–O CTB), and two sharp peaks at ~394 and 464 nm are assigned to the $^7F_0 \rightarrow ^5L_6$ and $^7F_0 \rightarrow ^5D_2$ transitions of Eu^{3+} , respectively [8].

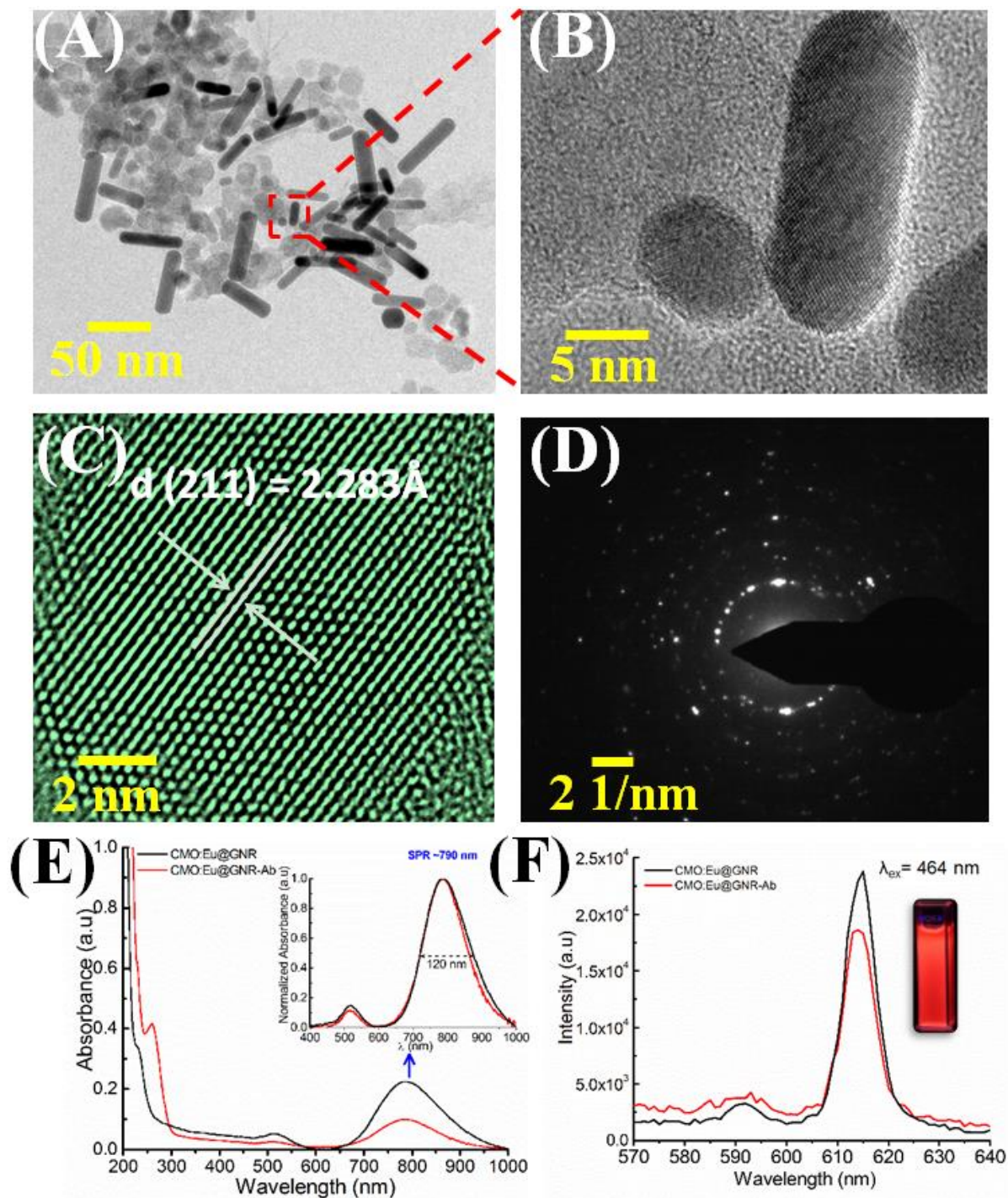


Figure 5.1 (A) TEM and (B) HRTEM images of CMO:Eu@GNR. (C) HRTEM image of CaMoO₄:Eu NPs and (D) SAED pattern for (A). (E) UV–visible and (F) photoluminescence ($\lambda_{\text{ex}} = 464$ nm) spectra of CMO:Eu@GNR without (black) and with Ab (red). Inset in (E) shows the comparison of normalized absorption spectrum at an SPR of ~ 790 nm. Digital photograph of the CaMoO₄:Eu NPs dispersed in PBS under a UV-lamp ($\lambda_{\text{ex}} = 254$ nm), shown in the inset of (F).

5.5.2 Photothermal properties of HNPs

The PTT abilities of HNPs were investigated using 808 nm NIR laser irradiation. Figure 5.2(A) shows a thermal image of phosphate buffered saline (PBS) and CMO:Eu@GNR solution placed in a 1 cm quartz cuvette using a forward looking infrared (FLIR) thermal imaging camera on irradiation with a NIR laser (~ 1 mm spot size, 1 W/cm^2) after 900 s at room temperature. As the irradiation time increased, the color of the thermal images of HNPs is gradually changed from dark blue to bright yellow (high temperature). In contrast, the thermal images for the PBS solution changed slightly over time as compared to those HNPs. Thermal images confirms that the NIR light could be absorbed by the CMO:Eu@GNR and converted to heat energy. It consists of a fiber-optic thermocouple temperature sensor (accuracy ± 0.1 °C) for temperature measurement, a FLIR thermal imaging camera, and an 808 nm NIR laser.

Figure 5.2(B, C) show the temperature kinetic curves at different concentrations. The bright circular spots in the SAED patterns ($0 \sim 28$ $\mu\text{g/mL}$ of GNRs) and excitation powers ($0 \sim 1.1.2 \text{ W/cm}^2$) of the CMO:Eu@GNR irradiated with NIR laser for 900 s (ΔT is the

temperature change, sample temperature ~ 27 °C). The temperature of the HNPs solution exponentially increases with the concentration of GNRs, and the similar temperature increasing profile is observed with the increase of excitation power. CMO:Eu@GNR achieved a PTT temperature of ~ 42 °C ($\Delta T = 15$ °C) in $\sim 210, 258, 377,$ and 481 s for $28, 21, 14,$ and 7 $\mu\text{g/mL}$ of GNRs, respectively (Figure 5.2(B)). In the case of 0 $\mu\text{g/mL}$ of GNRs (pure PBS), ΔT was found to be ~ 4.4 °C in 900 s, which is $\sim 87.5\%$ lesser than PTT temperature obtained using CMO:Eu@GNR (28 $\mu\text{g/mL}$ GNRs). The heating ability of the CMO:Eu@GNR at various laser irradiation powers for ~ 28 $\mu\text{g/mL}$ of GNRs concentration, is shown in Figure 5.2(C). The required PTT temperature of ~ 42 °C ($\Delta T = 15$ °C) was obtained in $\sim 136, 237, 351,$ and 673 s for $1.2, 1.0, 0.8,$ and 0.6 W/cm^2 of NIR laser power, respectively. Thus, by increasing the NIR laser power, the time required for the desired PTT temperature can be decreased. Moreover, the increase in the temperature of the PBS solution was significantly less than required PTT temperature.

Heat conversion efficiency (η) can be determined by plotting ΔT vs. ΔI as reported by *Pinchuk and co-workers* (Eq. 2-6) [23]. The value of heat dissipation rate constant (B) was further analyzed using the cooling temperature profile when the laser was turned off. The natural log of $(T(t)-T_0)/(T_m-T_0)$ as a function of time after the laser was turned off. The average value of B was found to be $\sim 1.58 \times 10^{-3} \text{ s}^{-1}$ with $R^2 = 0.99923$. Recently, *Pinchuk and co-workers* reported a B value of $\sim 4.66 \times 10^{-3} \text{ s}^{-1}$ for spherical Au particles with an SPR of ~ 530 nm. It was reported that the value of B depended on the volume of the NPs in the cuvette and was almost independent of the amount of the NPs present in the sample [23]. The η value was found to be $\sim 25.6\%$. However, a slight deviation in the ΔT was observed at a higher NIR laser irradiation power.

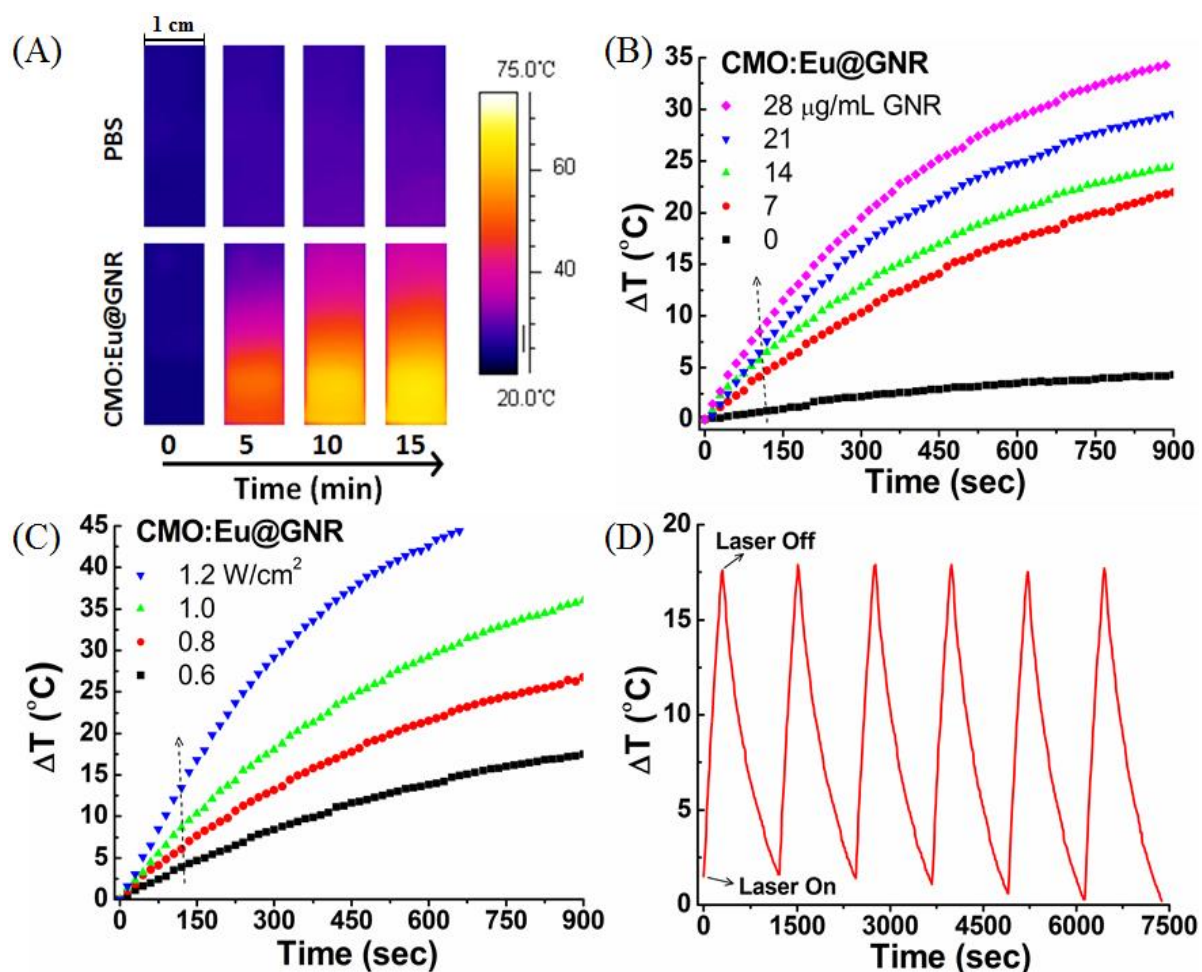


Figure 5.2 (A) Infrared images of PBS and CMO:Eu@GNR aqueous solutions exposed to 808 nm laser (1 W cm⁻²) for 900 s recorded at different time intervals. (B) Photothermal responses of CMO:Eu@GNR NPs at different concentrations in aqueous solution for 900 s NIR laser (808 nm, 1 W/cm²). (C) Photothermal responses of 808 nm laser irradiation with different power densities for 900 s at fixed CMO:Eu@GNR NP concentration (28 μg/mL GNR). (D) Temperature change of CMO:Eu@GNR solution at 1 W/cm² 808 nm laser irradiation over six LASER ON/OFF cycles. Experiment was carried out at room temperature.

To understand the photostability of HNPs, six cycles of ON/OFF NIR laser irradiations were performed ($\sim 1 \text{ W/cm}^2$ for 300 s (laser ON), followed by naturally cooling for 900 s (laser OFF) (Figure 5.2(D)). It was found that the temperature (ΔT) increased by $17.6 \text{ }^\circ\text{C}$ in the first laser ON condition of the CMO:Eu@GNR (GNR concentration $\sim 28 \text{ }\mu\text{g/mL}$). During six cycles of laser ON/OFF, the temperature elevations remained almost the same as in the first cycle within the limits of error bar, indicating the good photostability of HNPs. Furthermore, the effect of laser ON/OFF on luminescence emission was measured ($\lambda_{\text{ex}} = 464 \text{ nm}$) on the start and end of each cycle. A slight decrease in the emission of $\sim < 2\%$ was observed at the end of the sixth cycle.

The biocompatibility of the HNPs was investigated using the LIVE/DEAD viability/cytotoxicity assay kit. Cells has high viability ($> 90\%$) at lower concentrations of the CMO:Eu@GNR ($2.5\text{--}20 \text{ }\mu\text{g/mL}$) incubated for 24 h and decreased to $\sim 84\%$ as the concentration increased to $40 \text{ }\mu\text{g/mL}$. The decrease in cell viability at high concentration of CMO:Eu@GNR can be attributed to the production of hydroxyl radicals from $\text{CaMoO}_4\text{:Eu}$ [28]. Hydroxyl radicals can generate reactive oxygen species (ROS), causing cellular apoptosis [29, 30].

5.5.3 Cell biomechanical properties

To investigate the interactions between cells and the HNPs (without and with Ab), the cellular morphological effects were observed by atomic force microscopy (AFM) and compared with control cells (Figure 5.3). In case of control group (Figure 5.3(A-A')), its surrounding cytoskeleton structures were less visible than the NPs treated groups (Figure 5.3(B-B', C-C')). The short black arrows in these treated groups

indicate the filamentous actin bundles, which suggests that the mechanical properties of cells vary with the interaction of HNPs.

The comparison of biomechanical properties of different groups were shown in Figure 5.3(D, E). The control group has the largest Young's modulus $\sim 13.7 \pm 8.3$ kPa, while the CMO:Eu@GNR-Ab group has the least Young's modulus $\sim 11.3 \pm 6.2$ kPa. Furthermore, the CMO:Eu@GNR-Ab group has the largest adhesion force $\sim 0.53 \pm 0.20$ nN and control group has the least adhesion force $\sim 0.34 \pm 0.22$ nN. These results implied that the CMO:Eu@GNR-Ab has significant effects on the cellular biomechanics. One-way ANOVA for significance test was applied.

5.5.4 Fluorescence imaging of HNPs treated cells

To investigate the bioimaging application, CMO:Eu@GNR and CMO:Eu@GNR-Ab were incubated with A549 cells for 2 and 16 h, respectively. Red fluorescence from the CMO:Eu@GNR ($\lambda_{em}=615$ nm) was observed from A549 cells on excitation ~ 464 nm (5D_2 level of Eu^{3+} ion). Figure 5.4 shows phase contrast, fluorescence, and overlay of phase contrast and fluorescence images of control, A549 cells incubated with CMO:Eu@GNR NPs for 2 and 16 h (with and without Ab). It was found that the fluorescence intensity from the cells after 16 h incubation is larger than that of 2 h incubation; and no fluorescence was observed from the control cells under similar conditions. The increase in the fluorescence intensity with time may be due to more uptake of the CMO:Eu@GNR by the A549 cells. The Ab-conjugated CMO:Eu@GNR after 16 h incubation showed the strongest fluorescence compared to other groups. This result showed the specificity of CMO:Eu@GNR-Ab as compared to the control and CMO:Eu@GNR groups. The fluorescence emission from Eu^{3+} doped NPs was

similar to previous studies that used Ab-coated NPs for enhanced fluorescence imaging [31-33].

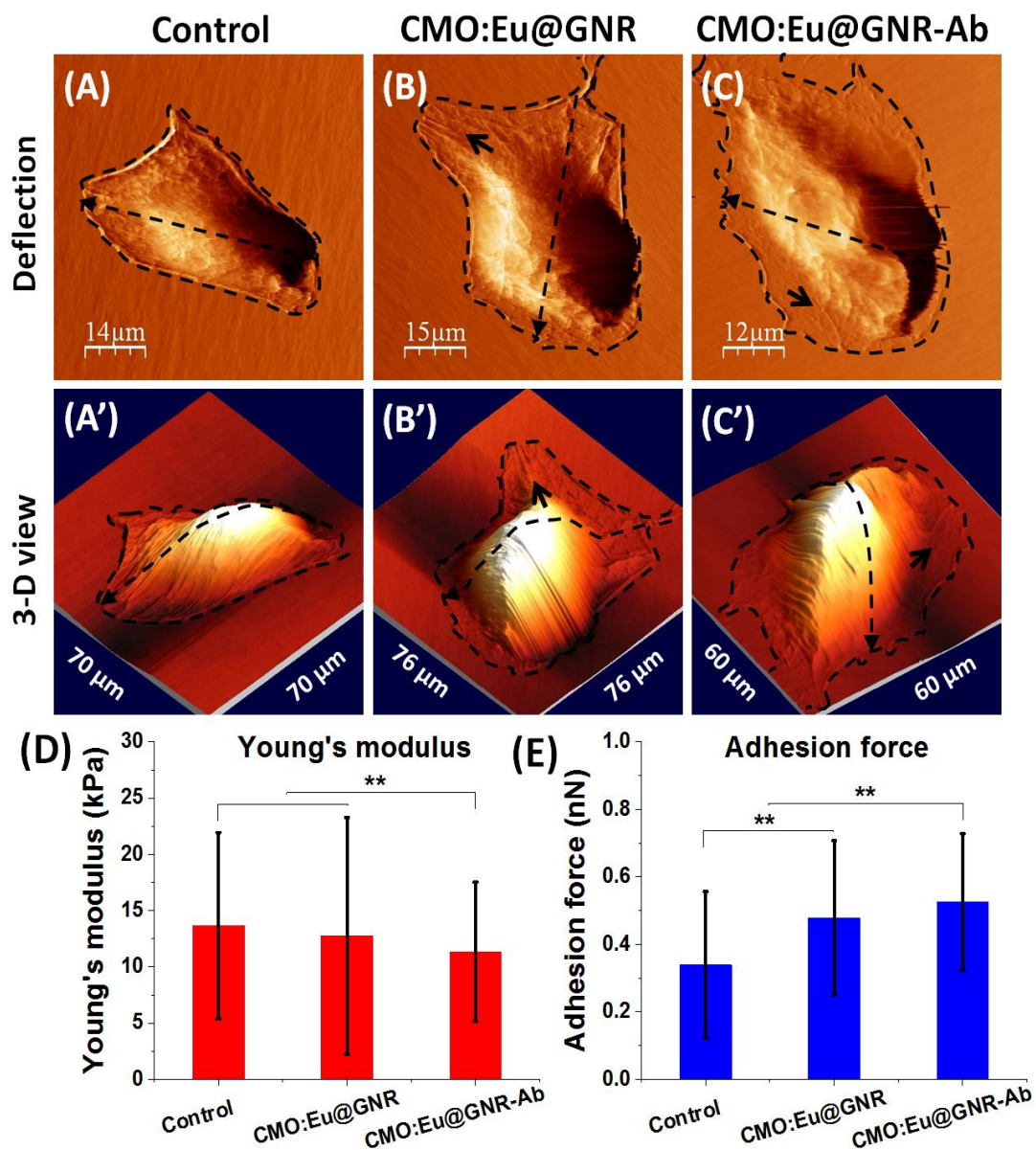


Figure 5.3 Atomic force microscopy detection of A549 cells (A) without treatment, (B) treated with CMO:Eu@GNR, or (C) CMO:Eu@GNR-Ab for 2 h; (A'–C') are 3D view images of (A–C); (D) Young's modulus and (E) adhesion force of cells. Error bar: standard deviation of the mean; $N \geq 20$, $**P < 0.01$.

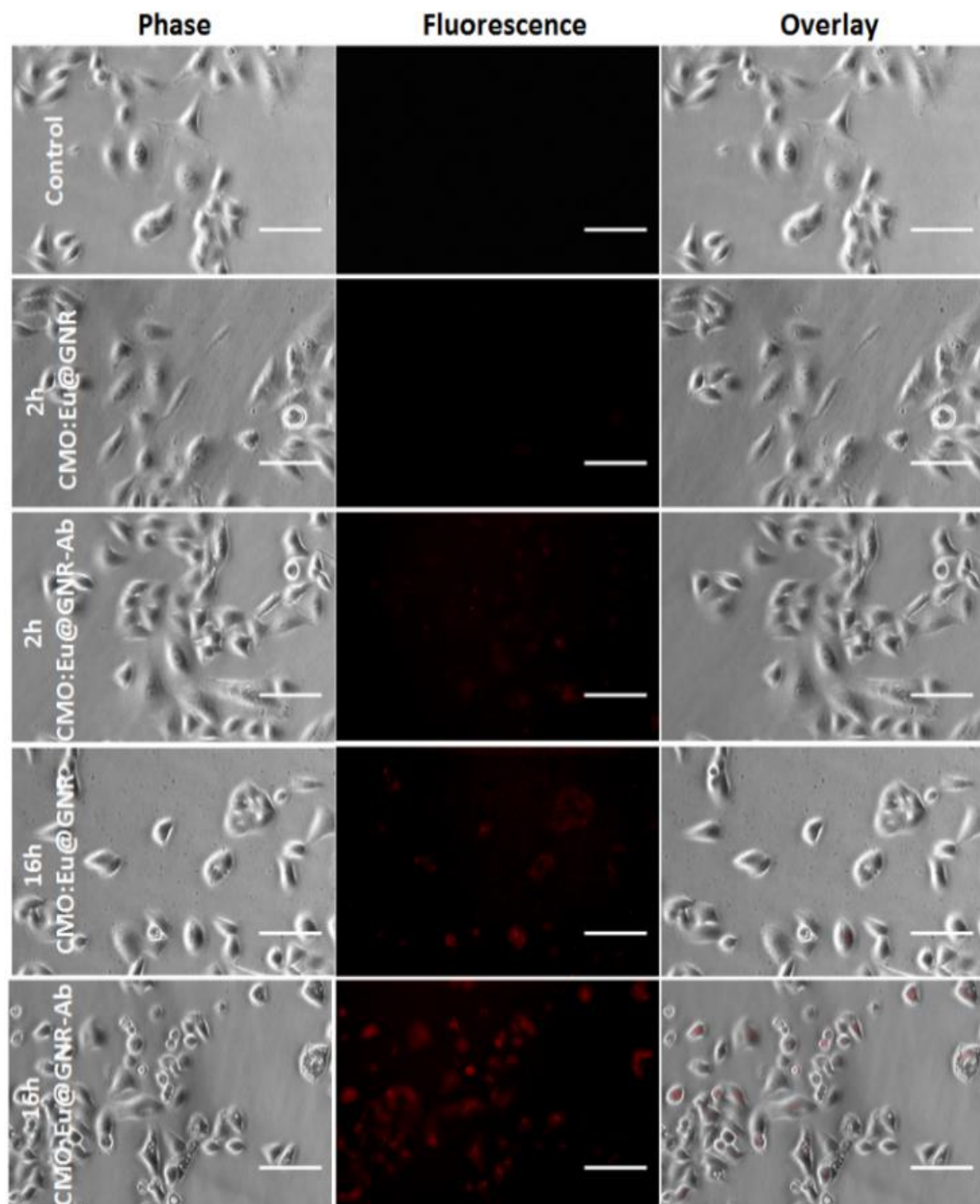


Figure 5.4 Phase, fluorescence, and overlay images of A549 cells without treatment and treated with CMO:Eu@GNR or CMO:Eu@GNR-Ab for 2 h and 16 h. Scale bar: 100 μm .

5.5.5 SERS measurement

Gold nanomaterials have been widely applied as Raman signal enhancement substrates due to their good biocompatibility and strong SERS signal [34, 35]. 4-mercaptobenzoic acid (MBA) was selected as the Raman reporter molecule to evaluate the SERS ability of the CMO:Eu@GNR for its well-established strong Raman peak $\sim 1078\text{ cm}^{-1}$ (aromatic ring vibration) [36]. To estimate the EF, we calculated the EF per MBA molecule as the ratio of the intensity of 1078 cm^{-1} obtained from the CMO:Eu@GNR-MBA NPs and the Raman intensity of the MBA without NPs under excitation 785 nm laser by eq. (1) in Materials and Methods part. SERS signals are enhanced by many orders of magnitude stronger than intrinsic cellular Raman signals. The average EF of the CMO:Eu@GNR calculated using eq. (1) was $\sim 4.76 \times 10^5$, demonstrating the SERS capability of the CMO:Eu@GNR (the EF calculation was based on the SERS signal of MBA on the CMO:Eu@GNR NPs).

The HNPs were conjugated with Ab for the enhancement of specificity. Figure 5.5 shows the Raman bright-field image, Raman streamline mapping and Raman spectrum ($900\text{--}1250\text{ cm}^{-1}$) from SERS negative (black cross) and SERS positive (red cross) sites on a single live A549 cell incubated with CMO:Eu@GNR. Raman mapping for a live cell was performed by selection of 1078 cm^{-1} (a characteristic peak from Raman reporter molecule MBA). The Raman spectra obtained from SERS positive and negative spots are shown in Figure 5.5(C). The SERS positive spectra from both CMO:Eu@GNR-MBA and CMO:Eu@GNR-MBA-Ab groups show a strong characteristic peak from MBA at 1078 cm^{-1} . The order of strong Raman mapping pixel intensity is found to be control $<$ CMO:Eu@GNR-MBA $<$ CMO:Eu@GNR-MBA-Ab. The bright color spots in the Raman

mapping indicates the distribution of EGFR biomarkers on single live cell (Figure 5.5(B)). The high pixel intensity in Raman mapping for CMO:Eu@GNR-MBA-Ab group confirms the higher cellular distribution of HNPs compared to non-Ab group. A few CMO:Eu@GNR were still distributed around the cellular membrane edges in CMO:Eu@GNR-MBA group due to nonspecific binding. In contrast, more NPs were bound to the cells in CMO:Eu@GNR-MBA-Ab group. As expected, no SERS signal was detected from the control group (no NPs treatment) except a lowest intensity characteristic peak $\sim 1004\text{ cm}^{-1}$, which is assigned to the phenylalanine from the cell [37]. CMO:Eu@GNR were also applied to the AML12 cells (EGFR negative) for SERS detection, as shown in Figure 5.6. It was found that a few NPs were distributed around AML12 live cell membrane of both CMO:Eu@GNR-MBA and CMO:Eu@GNR-MBA-Ab groups, indicating nonspecificity binding of NPs. The spectra from Figure 5.6(C) confirmed these Raman positive spots were CMO:Eu@GNR due to presence of the characteristic peak from Raman reporter MBA molecule. These SERS results compared the spectral differences among the three groups, illustrating the specificity of the Ab-conjugated NPs and the distribution of these NPs.

5.5.6 Photothermal treatment of cells

NPs with strong NIR absorption are considered to be a relatively noninvasive and effective treatment of cancer compared to the current cancer treatments (chemotherapy, radiotherapy, surgery, and so on), which usually result in severe adverse effects and cancer recurrence [38-41]. In PTT, the malignant cells were killed by localized hyperthermia generated by the conversion of absorbed light to heat. The distribution of cancer biomarker EGFR (via CMO:Eu@GNR) into A549 cells was confirmed by Raman results (Figure 5.5),

cells were treated with CMO:Eu@GNR (without and with Ab) and irradiated by a NIR laser for 5 min (1 W/cm^2). Figure 5.7(A) shows the fluorescence images of phase, live (green), and dead (red) cells with and without NPs treatments. Most of the cells were alive in control group, whereas a few dead in CMO:Eu@GNR groups, but complete cell death was observed in CMO:Eu@GNR-Ab group within the external 808 nm laser exposure area. Moreover, there was no significant difference in the cell viability between no-laser and laser control groups, suggesting that 808 nm NIR laser has negligible effect on the cells under similar conditions. Besides being tested on cancer cells A549, noncancerous hepatocyte AML12 cells were also treated with CMO:Eu@GNR (with and with Ab).

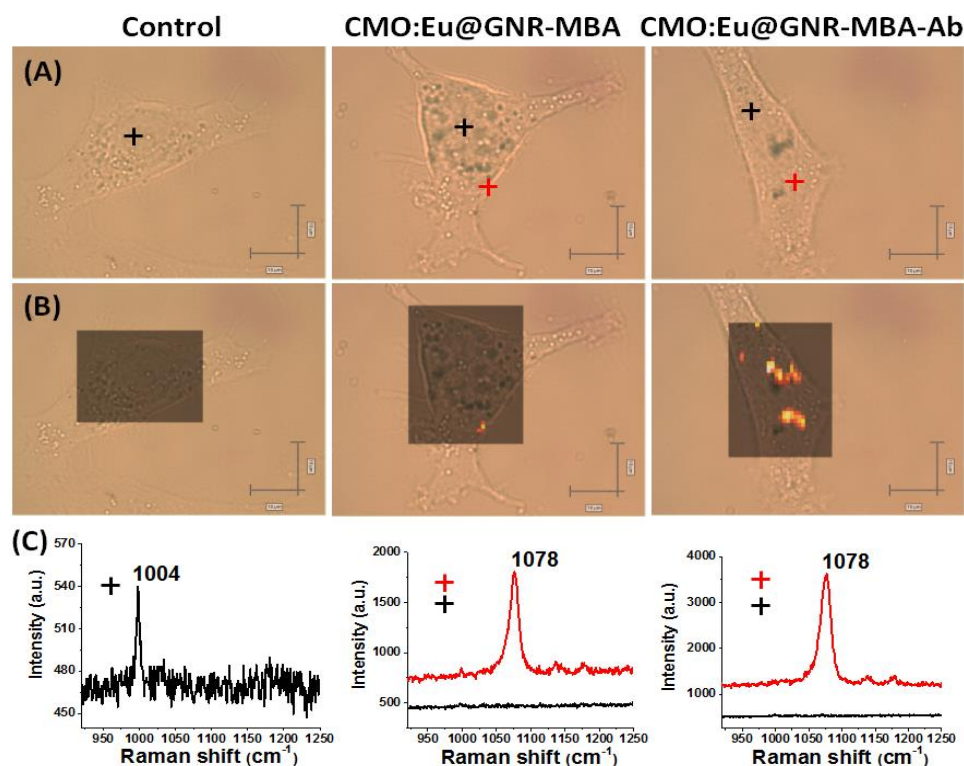


Figure 5.5 (A) Raman bright-field images of A549 cells without treatment and treated with CMO:Eu@GNR-MBA or CMO:Eu@GNR-MBA-Ab for 2 h (peak at 1078 cm^{-1})

from MBA was selected for mapping). Scale bar: 10 μm (horizontal), 5 μm (vertical). (B) Raman streamline mapping and (C) corresponding Raman spectra of A549 cells without treatment and treated with CMO:Eu@GNR-MBA or CMO:Eu@GNR-MBA-Ab NPs for 2 h.

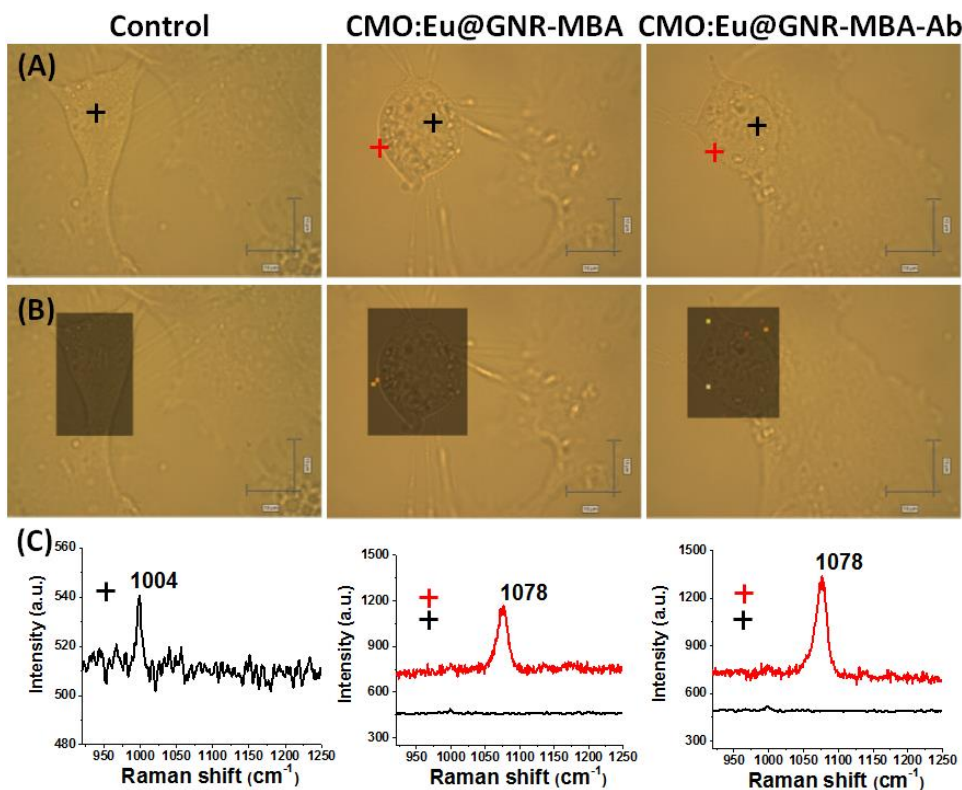


Figure 5.6 (A) Raman Bright-field images of AML12 cells without treatment and treated with 2-h CMO:Eu@GNR-MBA or CMO:Eu@GNR-MBA-Ab (peak at 1078 cm^{-1} from MBA was selected for mapping). Scale bar: 10 μm (horizontal), 5 μm (vertical). (B) Raman streamline mapping (Black cross: SERS negative; red cross: SERS positive) and (C) the corresponding Raman spectra of AML12 cells without treatment and treated with 2-h CMO:Eu@GNR-MBA or CMO:Eu@GNR-MBA-Ab NPs at 63 \times water immersion objective.

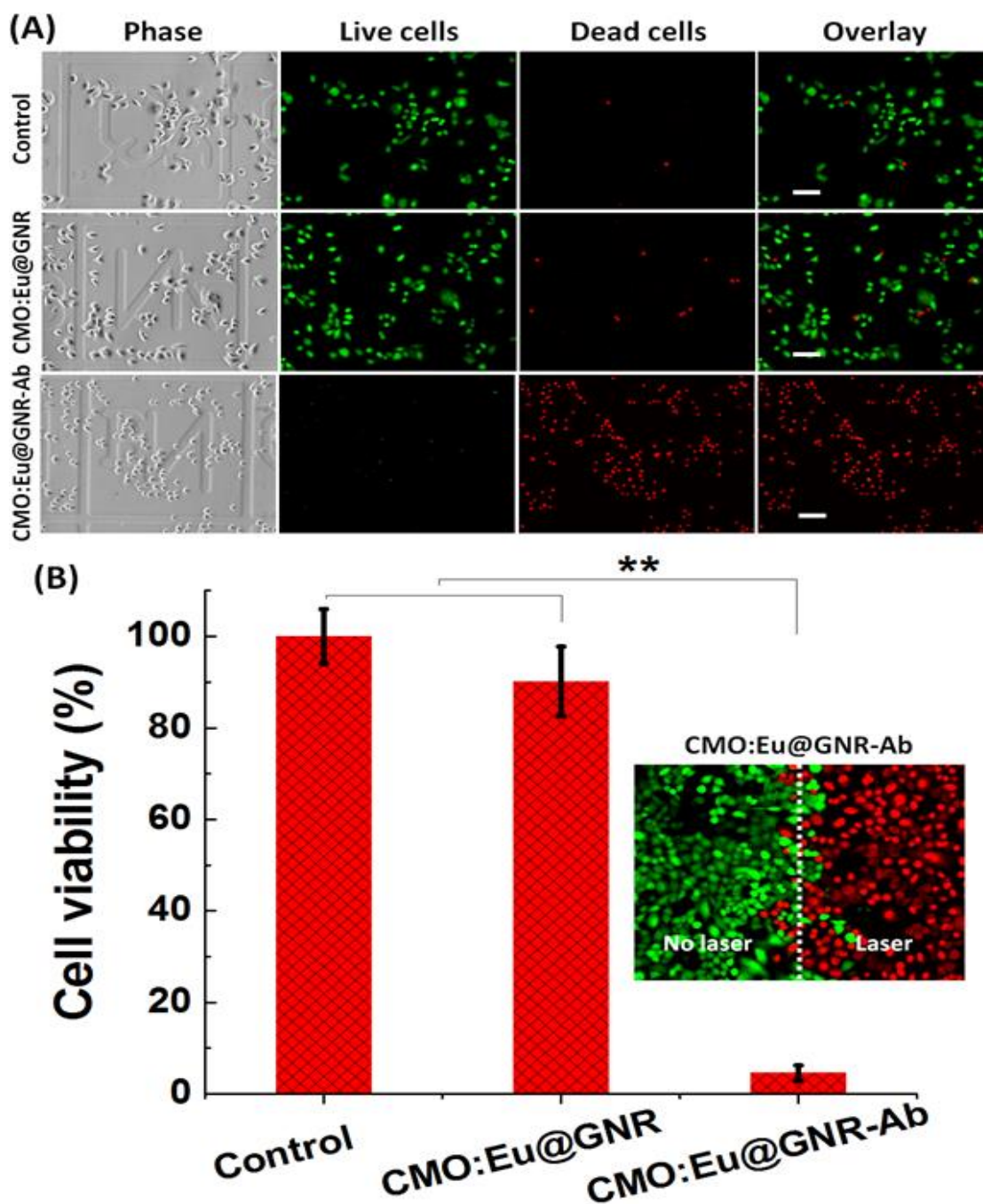


Figure 5.7 (A) Photothermal therapy. A549 cells were incubated without NPs (control), with CMO:Eu@GNR or CMO:Eu@GNR-Ab for 2 h; after that, cells were irradiated under 1 W/cm^2 808 nm laser for 5 min (green: live cells; red: dead cells. Scale bar: $100 \mu\text{m}$). (B) Cell viability of A549 cells without treatment and treated with CMO:Eu@GNR or CMO:Eu@GNR-Ab for 2 h; after that, irradiation for 5 min under 1 W/cm^2 808 nm laser.

Inset shows the fluorescence image of A549 cells treated with CMO:Eu@GNR-Ab NPs for 2 h, then irradiated without/with laser; Error bar: standard deviation of the mean; $N = 3$, $**P < 0.01$.

As shown in Figure 5.8, it was also found that the CMO:Eu@GNR have no PTT effect on AML12 cells, suggesting the HNPs with conjugated anti-EGFR antibodies are specific to cancer cells that overexpressed EGFR. The quantitative cell viability of A549 cells without and with treated (CMO:Eu@GNR and CMO:Eu@GNR-Ab) groups for 2 h was studied on 5 min 1 W/cm^2 808 nm laser irradiation (Figure 5.7(B)). The CMO:Eu@GNR group shows a slight toxicity (viability $\sim 90.2 \pm 7.6\%$), compared to control group. However, CMO:Eu@GNR-Ab group shows the least percentage of viability ($\sim 4.6 \pm 1.7\%$), indicating the high PTT effect from the Ab-labelled NPs. Inset of the Figure 5.7(B) shows the fluorescence images of the A549 cells incubated with the CMO:Eu@GNR-Ab NPs where the laser spot edge (white dashed line) shows a boundary between green (no laser) and red (laser) fluorescence regions. Within the laser spot, almost all cells were killed and displayed red color (dead cells). These results demonstrated that the CMO:Eu@GNR-Ab NPs could effectively and specifically kill A549 cells. This was because the CMO:Eu@GNR-Ab CMO:Eu@GNR can target the A549 cells via the interactions between the Ab and EGFR on the cancer cell surface. Thus, the CMO:Eu@GNR with high specificity and PTT efficiency may be of great importance for cancer treatments and have a potential to apply in clinical cancer therapy.

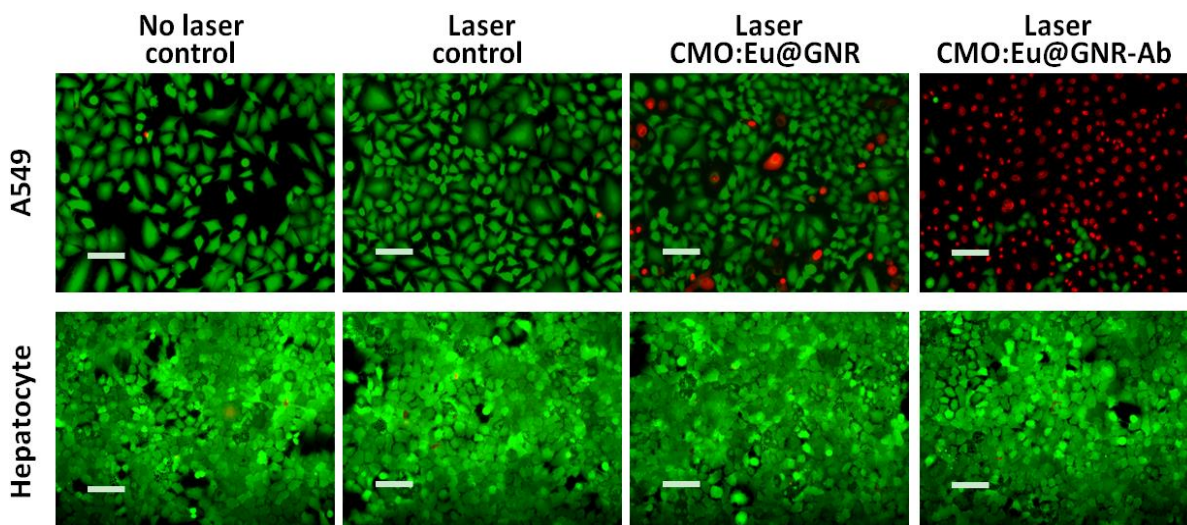


Figure 5.8 Fluorescence images of A549 and hepatocyte cells control without laser and with 5 min 1 W/cm^2 808 nm laser irradiation and treated with 2 h CMO:Eu@GNR or CMO:Eu@GNR-Ab, then for 5 min 1 W/cm^2 808 nm laser irradiation (Green: live cells; red: dead cells. Scale bar: 100 μm).

5.6 DISCUSSION

Hybrid nanomaterials with fluorescence in red region with NIR–SPR properties are increasingly attractive in theranostics of cancer that combines both diagnostic and therapeutic functions in recent years. NIR radiation is used as emerging tool in the fight against cancer [42]. We synthesized $\text{CaMoO}_4\text{:Eu}$ NPs having a strong luminescence at $\sim 615 \text{ nm}$ and conjugated with GNRs having NIR absorption at $\sim 790 \text{ nm}$. When these HNPs are uptaken at the tumor site, the temperature increase ($\sim 42 \text{ }^\circ\text{C}$) on NIR irradiation can kill the cancer cells. HNPs synthesized in this way have a great advantage in PTT tumor ablation. The HNPs were coated with anti-EGFR Ab for the selectively targeting of A549 cancer cells. Antibody conjugation to HNPs was further

confirmed by redshift in Mo–O CTB (~15 nm) and SPR band (~0.5 nm) (Figure 5.1(E)). The decrease in SPR band absorption for the Ab-conjugated NPs implies that the surface of the GNRs has different environment than Ab free NPs. El-Sayed and his co-workers studied the in detailed analysis of with and without anti-EGFR conjugated Au NPs to distinguish between cancerous and noncancerous cells using red shift [43]. Moreover, Ab conjugated Au NPs were specifically and homogeneously bind to the surface of the cancer cells 600% greater affinity than to the noncancerous cells [43]. Furthermore, a slight decrease in the luminescence intensity of Eu^{3+} ion was observed after Ab conjugation (Figure 5.1(F)). Asymmetric ratio ($A_{21} = \int^5\text{D}_{0\rightarrow7}\text{F}_2 / \int^5\text{D}_{0\rightarrow7}\text{F}_1$) values for without and with Ab coated NPs are found to be ~8.6 and 5.3, respectively. The luminescence of HNPs is slightly higher than $\text{CaMoO}_4:\text{Eu}$, this is due to proximity effect of GNRs [15]. The high colloidal stability (zeta potential) and uniform hydrodynamic size distribution of the HNPs were shown in Figure 5.9 and Figure 5.10. Indeed, the HNPs are good candidates for the development of PTT and imaging agents due to its easy access, simple conjugation procedures and low toxicity.

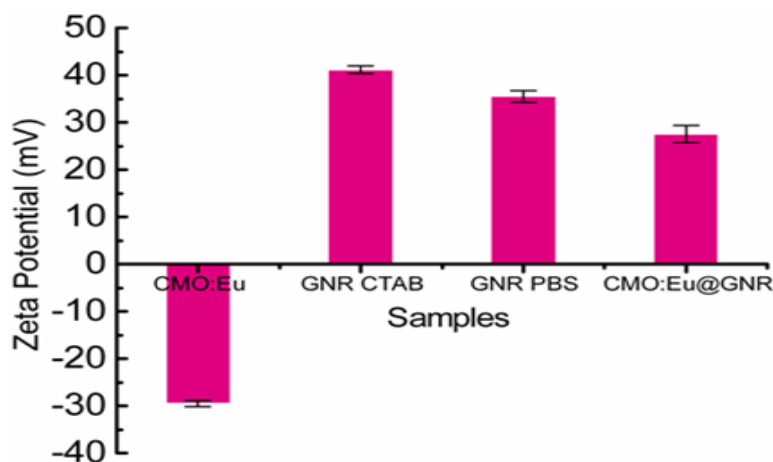


Figure 5.9 Zeta potentials of different samples at pH ~7.

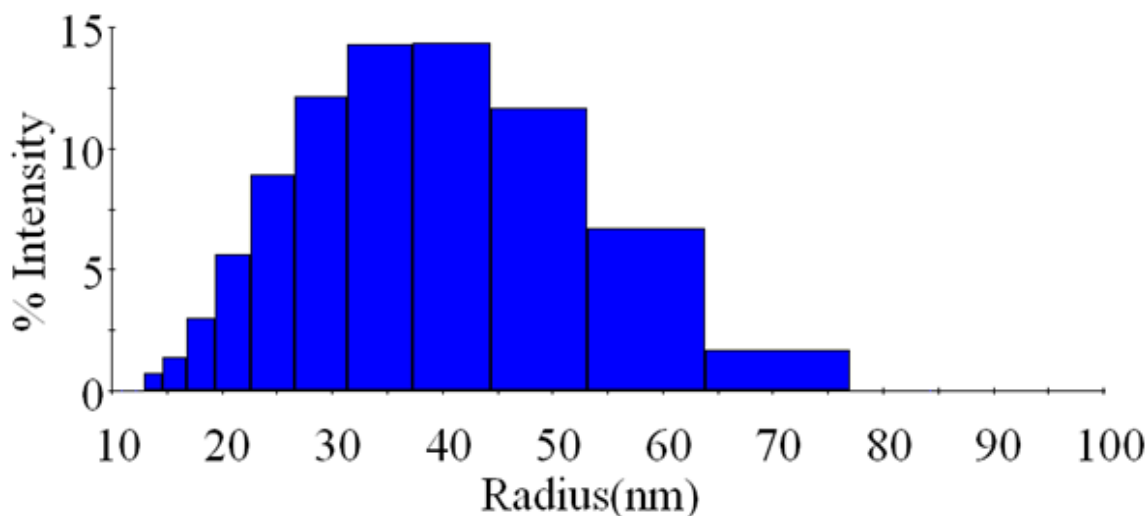


Figure 5.10 DLS data of CMO:Eu@GNR NPs.

HNPs with plasmon-enhanced fluorescence properties have attracted much attention as imaging nanoprobe for PTT due to its small size and deeper tumor permeation. Our HNPs have PTT conversion efficiency of $\sim 25.6\%$ and a sharp luminescence peak at ~ 615 nm. Recently, Sun and co-workers synthesized GNRs and gold nanostars (GNSs) with strong NIR absorption ~ 800 nm [44]. They concluded that pure GNRs show a higher η value, which varies in the range 69.7–94.2%. It is well known that pure gold particles exhibit strong PTT activity. Self-assembled WO_{3-x} hierarchical nanostructures ranging from 700–1400 nm were prepared with $\eta \sim 28\%$ by Hu and co-workers [45], and the same research group prepared CuS NPs with $\eta \sim 38\%$ [13]. Although various nanostructures have been evaluated as PTT agents, HNPs offer additional favorable properties that enable their use for cancer therapy. More importantly, the HNPs synthesized here not only have a high η value, but also have good NIR photostability (Figure 5.2(D)) and fluorescence properties (Figure 5.1(F)). These results demonstrate that the CMO:Eu@GNR could be used as a photothermal and imaging agent for cancer therapy applications.

Biomechanical properties played important roles in cellular morphogenesis, focal adhesion, motility, and metastasis [46-48], but also useful in medicine to understand the formation and stage of tumor development. The biomechanical properties of the cancer cells were investigated at singular cell level on incubation with HNPs. The biomechanical values of the control group were similar to our previous studies [49, 50]. Our AFM results (Figure 5.3) revealed that the interaction of HNPs with cells showed more surrounding cytoskeleton structures, much softer cell membrane and increased surface adhesion force compared to control cells. These alterations in cell topography and biomechanics indicate that the HNPs affected the cellular biophysical properties within a short time (2 h) under similar experimental conditions.

HNPs-MBA shows high sensitive SERS properties which arises from the interaction of MBA molecules with GNRs. Several factors (*e.g.*, substrate types, aspect ratios, plasmon absorption, reporter molecules, excitation source) [51] may affect the value of EF. The average EF value (4.76×10^5) of our HNPs was similar to previous reports [51, 52]. Raman streamline mapping in Figure 5.5 and Figure 5.6 consist of over 1000 spectra detected over 80% of the cell area. HNPs without Ab are partly attached to the cellular surface, suggesting that there was still nonspecific binding to cells due to long incubation time. Nevertheless, the nonspecific cellular binding of CMO:Eu@GNR NPs was significantly less than that of CMO:Eu@GNR-Ab with high specificity. To confirm this both cancerous (A594) and noncancerous cells (AML12) were treated with HNPs (with and without Ab) and irradiated with 808 nm NIR laser for 5 min (Figure 5.8). it was found that most of the cancer cells were killed and noncancerous cells were still alive. Furthermore, WBC

were treated with HNPs to evaluate their biocompatibility. WBC count demonstrates that HNPs treated groups (HNPs, HNPs-Ab, HNPs + laser, HNPs-Ab + laser) show a slight decrease in count by ~9% as compared to control group (Figure 5.11). The decrease of WBC count for NPs treated groups largely comes from the immune function of WBC to protect cells against foreign invaders (HNPs). However, the numbers of WBC for HNPs treated groups are still within normal range (~4000–11,000 white blood cells/ μL) [53] after this slight decrease, indicating the good biocompatibility of HNPs. These results indicate that rationally engineered HNPs having fluorescence in red region ($\lambda_{\text{ex}} = 464 \text{ nm}$) and PTT conversion efficiency ($\lambda_{\text{ex}} = 808 \text{ nm}$) can be used as efficient PTT agents. Meantime, the HNPs stand out because of its efficient NIR light absorption between 700–850 nm and their small size leading to the higher possibility of deeper tumor penetration. These properties of HNPs make them favorable for *in vivo* study in future experiments.

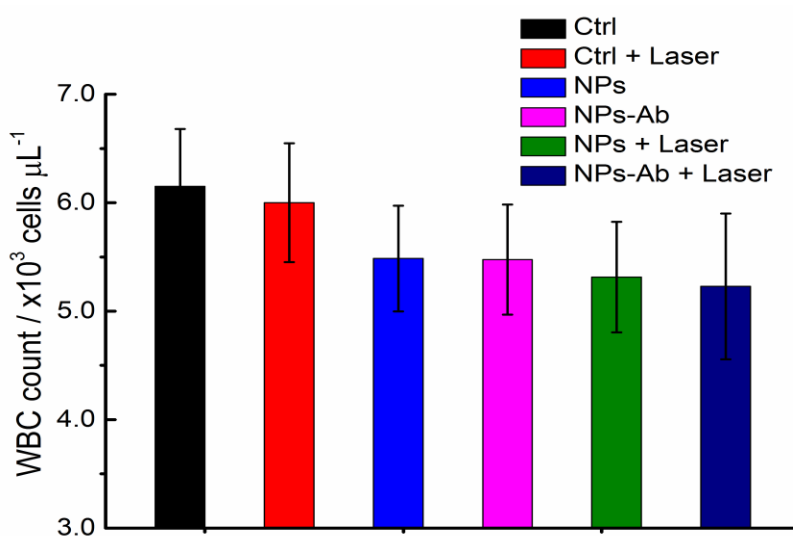


Figure 5.11 The effect of different treatments on the WBC counts (NPs: CMO:Eu@GNR;

** $p < 0.01$, $N = 3$, error bar: standard deviation of the mean).

In summary, multifunctional HNPs were synthesized for *in vitro* fluorescence imaging, SERS detection, and PTT cancer therapy applications. Fluorescence images show the fluorescent function of the HNPs with fluorescence at 615 nm (${}^5D_0 \rightarrow {}^7F_2$) on excitation ~ 464 nm. Ab was coated on the surface of the HNPs to enhance the cellular uptake. The biomechanical experiments shows that the Young's modulus of the A549 cells decreased whereas the adhesive force increased with the interactions between the HNPs and cells, and these changes further increased in the group of HNPs combined with Ab (CMO:Eu@GNR-Ab). Raman mapping confirmed the distribution of HNPs around the nucleus and membrane region using SERS characteristic peak of MBA at 1078 cm^{-1} , and the EF was found to be $\sim 4.76 \times 10^5$. Moreover, these HNPs effectively suppressed A549 cell viability upon 808 nm laser irradiation. However, no significant decrease in cell viability of noncancerous cells (AML12) was observed. The PTT efficiency of CMO:Eu@GNR were found to be $\sim 25.6\%$. Thus, a combination of fluorescence imaging, SERS and the NIR photothermal ablation of targeted tumor cells would allow multimodal imaging and PTT *in vivo* for the future applications.

5.7 REFERENCES

1. Bardhan M, Satpati B, Ghosh T, Senapati D. Synergistically controlled nano-templated growth of tunable gold bud-to-blossom nanostructures: a pragmatic growth mechanism. *J Mater Chem C*. 2014; 2: 3795-804.
2. Austin LA, Mackey MA, Dreaden EC, El-Sayed MA. The optical, photothermal, and facile surface chemical properties of gold and silver nanoparticles in biodiagnostics, therapy, and drug delivery. *Arch Toxicol*. 2014; 88: 1391-417.

3. Seo SH, Kim BM, Joe A, Han HW, Chen XY, Cheng Z, et al. NIR-light-induced surface-enhanced Raman scattering for detection and photothermal/photodynamic therapy of cancer cells using methylene blue-embedded gold nanorod@SiO₂ nanocomposites. *Biomaterials*. 2014; 35: 3309-18.
4. Zhang Y, Wei W, Das GK, Tan TTY. Engineering lanthanide-based materials for nanomedicine. *J Photochem Photobiol C*. 2014; 20: 71-96.
5. Niu N, He F, Ma PA, Gai SL, Yang GX, Qu FY, et al. Up-Conversion Nanoparticle Assembled Mesoporous Silica Composites: Synthesis, Plasmon-Enhanced Luminescence, and Near-Infrared Light Triggered Drug Release. *ACS Appl Mater Interfaces*. 2014; 6: 3250-62.
6. Alvarez-Puebla RA, Liz-Marzan LM. SERS-based diagnosis and biodetection. *Small*. 2010; 6: 604-10.
7. Maiti KK, Dinish US, Fu CY, Lee JJ, Soh KS, Yun SW, et al. Development of biocompatible SERS nanotag with increased stability by chemisorption of reporter molecule for in vivo cancer detection. *Biosens Bioelectron*. 2010; 26: 398-403.
8. Parchur AK, Ansari AA, Singh BP, Hasan TN, Syed NA, Rai SB, et al. Enhanced luminescence of CaMoO₄:Eu by core@shell formation and its hyperthermia study after hybrid formation with Fe₃O₄:cytotoxicity assessment on human liver cancer cells and mesenchymal stem cells. *Integr Biol*. 2014; 6: 53-64.
9. Mackey MA, Ali MRK, Austin LA, Near RD, El-Sayed MA. The Most Effective Gold Nanorod Size for Plasmonic Photothermal Therapy: Theory and In Vitro Experiments. *J Phys Chem B*. 2014; 118: 1319-26.

10. Trinidad AJ, Hong SJ, Peng Q, Madsen SJ, Hirschberg H. Combined Concurrent Photodynamic and Gold Nanoshell Loaded Macrophage-Mediated Photothermal Therapies: An In Vitro Study on Squamous Cell Head and Neck Carcinoma. *Laser Surg Med.* 2014; 46: 310-8.
11. Akhavan O, Meidanchi A, Ghaderi E, Khoei S. Zinc ferrite spinel-graphene in magneto-photothermal therapy of cancer. *Journal of Materials Chemistry B.* 2014; 2: 3306-14.
12. Xiao JW, Fan SX, Wang F, Sun LD, Zheng XY, Yan CH. Porous Pd nanoparticles with high photothermal conversion efficiency for efficient ablation of cancer cells. *Nanoscale.* 2014; 6: 4345-51.
13. Liu XJ, Li B, Fu FF, Xu KB, Zou RJ, Wang Q, et al. Facile synthesis of biocompatible cysteine-coated CuS nanoparticles with high photothermal conversion efficiency for cancer therapy. *Dalton Trans.* 2014; 43: 11709-15.
14. Tian QW, Jiang FR, Zou RJ, Liu Q, Chen ZG, Zhu MF, et al. Hydrophilic Cu₉S₅ Nanocrystals: A Photothermal Agent with a 25.7% Heat Conversion Efficiency for Photothermal Ablation of Cancer Cells in Vivo. *Acs Nano.* 2011; 5: 9761-71.
15. Bardhan R, Chen WX, Perez-Torres C, Bartels M, Huschka RM, Zhao LL, et al. Nanoshells with Targeted Simultaneous Enhancement of Magnetic and Optical Imaging and Photothermal Therapeutic Response. *Adv Funct Mater.* 2009; 19: 3901-9.
16. Cross SE, Jin YS, Lu QY, Rao J, Gimzewski JK. Green tea extract selectively targets nanomechanics of live metastatic cancer cells. *Nanotechnology.* 2011; 22: 215101.

17. Tenzer S, Docter D, Kuharev J, Musyanovych A, Fetz V, Hecht R, et al. Rapid formation of plasma protein corona critically affects nanoparticle pathophysiology. *Nat Nanotechnol.* 2013; 8: 772-781.
18. Yarom N, Jonker DJ. The Role of the Epidermal Growth Factor Receptor in the Mechanism and Treatment of Colorectal Cancer. *Discov Med.* 2011; 57: 95-105.
19. Morgensztern D, Politi K, Herbst RS. EGFR mutations in non-small-cell lung cancer: Find, divide, and conquer. *JAMA Oncol.* 2015; 1: 146-8.
20. Black KCL, Yi J, Rivera JG, Zelasko-Leon DC, Messersmith PB. Polydopamine-enabled surface functionalization of gold nanorods for cancer cell-targeted imaging and photothermal therapy. *Nanomedicine.* 2013; 8: 17-28.
21. Kuo WS, Chang CN, Chang YT, Yang MH, Chien YH, Chen SJ, et al. Gold Nanorods in Photodynamic Therapy, as Hyperthermia Agents, and in Near-Infrared Optical Imaging. *Angew Chem Int Ed Engl.* 2010; 49: 2711-5.
22. Sisco PN, Murphy CJ. Surface-coverage dependence of surface-enhanced raman scattering from gold nanocubes on self-assembled monolayers of analyte. *J Phys Chem A.* 2009; 113: 3973-8.
23. Jiang K, Smith DA, Pinchuk A. Size-Dependent Photothermal Conversion Efficiencies of Plasmonically Heated Gold Nanoparticles. *J Phys Chem C.* 2013; 117: 27073-80.
24. Sneddon IN. The relation between load and penetration in the axisymmetric Boussinesq problem for a punch of arbitrary profile. *Int J Eng Sci.* 1965; 3: 47-57.
25. Hertz H. Ueber die Berührung fester elastischer Körper. *J. Reine Angew. Math* 1882; 1882: 156-171.

26. Radmacher M, Fritz M, Kacher CM, Cleveland JP, Hansma PK. Measuring the viscoelastic properties of human platelets with the atomic force microscope. *Biophys J*. 1996; 70: 556-67.
27. Singh BP, Parchur AK, Ningthoujam RS, Ansari AA, Singh P, Rai SB. Enhanced photoluminescence in $\text{CaMoO}_4:\text{Eu}^{3+}$ by Gd^{3+} co-doping. *Dalton Trans*. 2014; 43: 4779-89.
28. Hussain SM, Hess KL, Gearhart JM, Geiss KT, Schlager JJ. In vitro toxicity of nanoparticles in BRL 3A rat liver cells. *Toxicol In Vitro*. 2005; 19: 975-83.
29. Li P, Zhao QL, Wu LH, Jawaid P, Jiao YF, Kadowaki M, et al. Isofraxidin, a potent reactive oxygen species (ROS) scavenger, protects human leukemia cells from radiation-induced apoptosis via ROS/mitochondria pathway in p53-independent manner. *Apoptosis*. 2014; 19: 1043-53.
30. Krifka S, Spagnuolo G, Schmalz G, Schweikl H. A review of adaptive mechanisms in cell responses towards oxidative stress caused by dental resin monomers. *Biomaterials*. 2013; 34: 4555-63.
31. Ansari AA, Hasan TN, Syed NA, Labis JP, Parchur AK, Shafi G, et al. In-vitro cytotoxicity, geno-toxicity, and bio-imaging evaluation of one-pot synthesized luminescent functionalized mesoporous $\text{SiO}_2@\text{Eu}(\text{OH})(3)$ core-shell microspheres. *Nanomedicine*. 2013; 9: 1328-35.
32. Hui JF, Zhang XY, Zhang ZC, Wang SQ, Tao L, Wei Y, et al. Fluoridated $\text{HAp}:\text{Ln}(3+)$ ($\text{Ln} = \text{Eu}$ or Tb) nanoparticles for cell-imaging. *Nanoscale*. 2012; 4: 6967-70.

33. Singh NS, Kulkarni H, Pradhan L, Bahadur D. A multifunctional biphasic suspension of mesoporous silica encapsulated with YVO₄:Eu-3(+) and Fe₃O₄ nanoparticles: synergistic effect towards cancer therapy and imaging. *Nanotechnology*. 2013; 24.
34. Xiao LF, Harihar S, Welch DR, Zhou AH. Imaging of epidermal growth factor receptor on single breast cancer cells using surface-enhanced Raman spectroscopy. *Anal Chim Acta*. 2014; 843: 73-82.
35. Tong LM, Zhu T, Liu ZF. Approaching the electromagnetic mechanism of surface-enhanced Raman scattering: from self-assembled arrays to individual gold nanoparticles. *Chem Soc Rev*. 2011; 40: 1296-304.
36. Yan ML, Xiang YC, Liu LL, Chai LY, Li XB, Feng T. Silver nanocrystals with special shapes: controlled synthesis and their surface-enhanced Raman scattering properties. *RSC Advances*. 2014; 4: 98-104.
37. Movasaghi Z, Rehman S, Rehman IU. Raman spectroscopy of biological tissues. *Appl Spectrosc Rev*. 2007; 42: 493-541.
38. Lu WT, Singh AK, Khan SA, Senapati D, Yu HT, Ray PC. Gold Nano-Popcorn-Based Targeted Diagnosis, Nanotherapy Treatment, and In Situ Monitoring of Photothermal Therapy Response of Prostate Cancer Cells Using Surface-Enhanced Raman Spectroscopy. *J Am Chem Soc*. 2010; 132: 18103-14.
39. Coates A, Abraham S, Kaye SB, Sowerbutts T, Frewin C, Fox RM, et al. On the Receiving End Patient Perception of the Side-Effects of Cancer Chemotherapy. *Eur J Cancer Clin Oncol*. 1983; 19: 203-8.

40. Zachariah B, Balducci L, Venkattaramanabalaji GV, Casey L, Greenberg HM, DelRegato JA. Radiotherapy for cancer patients aged 80 and older: A study of effectiveness and side effects. *Int J Radiat Oncol Biol Phys.* 1997; 39: 1125-9.
41. In H, Bilimoria KY, Stewart AK, Wroblewski KE, Posner MC, Talamonti MS, et al. Cancer Recurrence: An Important but Missing Variable in National Cancer Registries. *Ann Surg Oncol.* 2014; 21: 1520-9.
42. Ayala-Orozco C, Urban C, Knight MW, Urban AS, Neumann O, Bishnoi SW, et al. Au Nanomaterials as Efficient Near-Infrared Photothermal Transducers for Cancer Treatment: Benchmarking against Nanoshells. *ACS Nano.* 2014; 8: 6372-81.
43. El-Sayed IH, Huang XH, El-Sayed MA. Surface plasmon resonance scattering and absorption of anti-EGFR antibody conjugated gold nanoparticles in cancer diagnostics: Applications in oral cancer. *Nano Lett.* 2005; 5: 829-34.
44. Wang XC, Li GH, Ding Y, Sun SQ. Understanding the photothermal effect of gold nanostars and nanorods for biomedical applications. *Rsc Adv.* 2014; 4: 30375-83.
45. Li B, Zhang YX, Zou RJ, Wang Q, Zhang BJ, An L, et al. Self-assembled WO₃-x hierarchical nanostructures for photothermal therapy with a 915 nm laser rather than the common 980 nm laser. *Dalton Trans.* 2014; 43: 6244-50.
46. Nelson CM, Jean RP, Tan JL, Liu WF, Sniadecki NJ, Spector AA, et al. Emergent patterns of growth controlled by multicellular form and mechanics. *Proc Natl Acad Sci U S A.* 2005; 102: 11594-9.
47. du Roure O, Saez A, Buguin A, Austin RH, Chavrier P, Siberzan P, et al. Force mapping in epithelial cell migration. *Proc Natl Acad Sci U S A.* 2005; 102: 2390-5.

48. Suresh S. Biomechanics and biophysics of cancer cells. *Acta Biomaterialia*. 2007; 3: 413-38.
49. Xiao LF, Tang MJ, Li QF, Zhou AH. Non-invasive detection of biomechanical and biochemical responses of human lung cells to short time chemotherapy exposure using AFM and confocal Raman spectroscopy. *Anal Methods*. 2013; 5: 874-9.
50. Tang MJ, Li QF, Xiao LF, Li YP, Jensen JL, Liou TG, et al. Toxicity effects of short term diesel exhaust particles exposure to human small airway epithelial cells (SAECs) and human lung carcinoma epithelial cells (A549). *Toxicol Lett*. 2012; 215: 181-92.
51. Orendorff CJ, Gearheart L, Jana NR, Murphy CJ. Aspect ratio dependence on surface enhanced Raman scattering using silver and gold nanorod substrates. *Phys Chem Chem Phys*. 2006; 8: 165-70.
52. Nikoobakht B, El-Sayed MA. Surface-enhanced Raman scattering studies on aggregated gold nanorods. *J Phys Chem A*. 2003; 107: 3372-8.
53. Rezende SM, Lijfering WM, Rosendaal FR, Cannegieter SC. Hematologic variables and venous thrombosis: red cell distribution width and blood monocyte count are associated with an increased risk. *Haematologica*. 2014; 99: 194-200.

CHAPTER 6

NEAR-INFRARED PHOTOTHERMAL THERAPY OF PRUSSIAN BLUE COATED MULTIFUNCTIONAL $\text{CaMoO}_4\text{:Eu@SiO}_2/\text{Au}$ NANOSTRUCTURES FOR TARGETING HUMAN EPIDERMAL GROWTH FACTOR RECEPTOR 2 EXPRESSING CANCER CELLS

6.1 ABSTRACT

Here we report the synthesis, characterization and application of Prussian blue (PB) functionalized $\text{CaMoO}_4\text{:Eu@SiO}_2\text{@Au}$ -nanorod hybrid nanoparticles (NPs) having multimodal capabilities such as fluorescence imaging, surface-enhanced Raman spectroscopy (SERS) detection and photothermal therapy (PTT). The average size of $\text{CaMoO}_4\text{:Eu@SiO}_2$ nanoparticles was found to be ~206 nm. Hybrid particles are highly dispersible in water for several weeks without settling and show a strong absorption in NIR region which is overlap of Prussian blue absorption between 600–1000 nm and surface plasmon resonance of Au nanorods around 800 nm. Upon 808 nm laser excitation particles shows hyperthermia temperature (43 °C). Also, PB NPs can be used in clinical trials for treatment of radioactive exposure, and PB acts as a Raman reporter molecule (2152 cm^{-1} characteristic peak) with good biosafety and stability in the human body. In addition, using both SiO_2 NPs and Au nanorods to coat on the surface of $\text{CaMoO}_4\text{:Eu}$ nanoparticles increases the biocompatibility. Furthermore, the PTT efficiency of HER2 (human epidermal growth factor receptor 2) antibody conjugated hybrid nanoparticles on MDA-MB-435 cancerous cells is significantly higher than and hepatocyte cells (non-cancerous). This is due to more uptake of hybrid nanoparticles in cancerous cells than non-cancerous cells. Together, this study

shows the potential applications of these HNPs in fluorescence imaging, SERS detection, and PTT functionalities with good photostability and biocompatibility.

6.2 INTRODUCTION

The combination of diagnostic and therapeutic functions into a single construct is an emerging field to further promote clinical diagnosis and therapeutic processes. This construct can image and detect a specific target, measure the biological changes and conduct the therapeutic processes. In this way, specificity and selectivity can be significantly facilitated followed by high therapeutic efficacy while decreasing deleterious side effects. Recently, we developed hybrid materials with the properties of fluorescence, surface-enhanced Raman spectroscopy (SERS) and photothermal therapy (PTT) potential. Different from traditional fluorophores restricted by the limitation of photobleaching and short lifetime [1], the synthesized inorganic hybrid materials do not experience these problems. In addition, the hybrid materials exhibit enhancement in luminescence intensity (λ_{em} : ~615 nm) due to metal (GNR) proximity effect [2], and this luminescence feature is from Eu^{3+} ion ($^5\text{D}_2$ level of Eu^{3+} ion). Moreover, the Raman-labeled hybrid materials can be applied as sensitive SERS probes for Raman imaging in living cells. Similarly, Raman imaging techniques are not limited by photobleaching or solvent and environmental effects because of the need for only one irradiation source and the narrow spectral peaks [3]. When the absorption band of a Raman-labeled construct overlaps with the laser excitation, the SERS signal can be greatly intensified [4]. Furthermore, the hybrid materials have the property of PTT potential, which is a non-invasive laser-based approach applied to 'burn' tumor cells by converting the photon energy into thermal energy (hyperthermia temperature ~42 °C) [5]. Therefore, the combination of fluorescence, Raman imaging and PTT might be important for increasing the

curative rates of cancer treatments and has a potential for application in clinical cancer therapy.

Mesoporous silica nanoparticles (NPs) with the features of high surface area, adjustable pore size and chemically modifiable surfaces have been widely applied as efficient drug delivery carriers with good biocompatibility [6, 7]. Prussian blue (PB) is not only an inorganic pigment containing ferric ferrocyanide, but it is also an antidote for heavy metal poisoning [8]. Moreover, PB is very useful as an FDA approved treatment for radioactive exposure [9]. In addition, recent studies have indicated that PB could efficiently transform irradiation laser into heat for cancer treatment [10, 11], and its low price promotes its use in practical applications. The soluble PB is loaded onto silica NPs as well as the surface of GNR through electrostatic interactions. The conjugation of PB can greatly increase the PTT efficacy because the absorption bands of PB and GNR used in this work are both close to the NIR laser wavelength. Meantime, PB can be applied as a Raman reporter molecule for SERS imaging. The synergistic PTT effect from PB and GNR could provide us with new insight in fighting against cancer.

The HER2 (human epidermal growth factor receptor 2) protein is over-expressed in 25% to 30% of human breast cancers [12]. A monoclonal antibody (mAb), anti-HER2, was conjugated onto the external surface of PB modified $\text{CaMoO}_4:\text{Eu}@\text{SiO}_2@\text{GNR}$ (HNP-PB) to selectively recognize HER2/neu glycoproteins that are usually overexpressed on breast cancer cells. The specific targeting capability of HNP-PB-Ab is strongly affected by the mAb density on the outer surface of HNP-PB, and the mAb was modified with a polyethylene glycol (PEG) spacer to reduce non-specific binding to other cells without the receptor.

Herein, the synthesized hybrid materials are characterized first, then applied for imaging and PTT with an enhanced specificity when conjugating HER2 antibodies, and their biocompatibility is also evaluated.

6.3 HYPOTHESIS

The developed silica coated NPs could effectively visualize, detect and treat human breast cancer cells by the mechanism of antibody-receptor binding with enhanced biocompatibility.

6.4 MATERIALS AND METHODS

6.4.1 Materials

Calcium nitrate tetrahydrate, ($\text{Ca}(\text{NO}_3)_2 \cdot 4\text{H}_2\text{O}$, 99%, Alfa Aesar, Ward Hill, MA, USA), ammonium molybdate ($\text{H}_8\text{MoN}_2\text{O}_4$, 99.99%, Alfa Aesar), europium(III) nitrate hydrate ($\text{Eu}(\text{NO}_3)_3 \cdot x\text{H}_2\text{O}$, 99.99%, Sigma-Aldrich, St. Louis, MO, USA), oleic acid (OA, Alfa Aesar), 1-octadecene (95%, Alfa Aesar), NaOH pellet (Merck & Co., Kenilworth, NJ, USA), hydrochloric acid (HCl, Sigma-Aldrich), HS-PEG-COOH (MW = 5000, Nanocs Inc., New York, NY, USA), mPEG-SH (MW = 5000, NANOCS), *N*-(3-dimethylaminopropyl)-*N'*-ethylcarbodiimide hydrochloride ($\text{C}_8\text{H}_{17}\text{N}_3\text{HCl}$, MW = 191.7 g/mol, Sigma-Aldrich) (EDC), *N*-hydroxysuccinimide ($\text{C}_4\text{H}_5\text{NO}_3$, Sigma-Aldrich, MW = 115.09 g/mol) (NHS), Prussian blue (PB) (Sigma-Aldrich, USA), human epidermal growth factor receptor 2 (HER2) antibody (Santa Cruz Biotechnology Inc., Dallas, TX, USA), and phosphate buffered saline (1X) (PBS) (Thermo Fisher Scientific, Waltham, MA, USA) were used for HNPs synthesis. MDA-MB-435 human breast carcinoma (435 cells), mouse hepatocyte cells (AML12, normal hepatocyte from liver tissue, ATCC, Manassas, VA, USA), 0.5%

trypsin-EDTA solution (Thermo Fisher Scientific), LIVE/DEAD Viability/Cytotoxicity Assay Kit (Thermo Fisher Scientific), Earle's balanced salt solution (EBSS, Thermo Fisher Scientific) and PBS were used for cell experiments.

6.4.2 Synthesis of CaMoO₄:Eu@SiO₂@GNR core/shell Nanoparticles

CaMoO₄:Eu (2 at.%; CMO:Eu) nanoparticles were synthesized by a thermolysis process. A detailed method of synthesis was discussed elsewhere [submitted for publication]. To remove the unwanted oleic acid (OA) capped on the surface of the particles, 20 mg of the CMO:Eu nanoparticles were dispersed in 5 mL of 0.1 M HCl, and the mixture was sonicated for 1 h. To this, 2 mL of diethyl ether was added and sonicated for 30 min. The resulting solution was centrifuged at 6000 rpm for 15 min. The obtained precipitate was washed four times with ethanol. For the silica-coating on the surface of CaMoO₄:Eu nanoparticles, 200 mg of CMO:Eu nanoparticles was added to 100 mL of deionized water and 25 mL of NH₄OH aqueous solution added and sonicated for 30 min. To this 8 ml of Tetraethyl orthosilicate (TEOS) added drop wise and the reaction mixture was vigorously stirred for 24 h. Resulting precipitate was collected by centrifugation and washed with water to remove the unwanted reactants present on the surface of the particles and redispersed in 50 ml of distilled (DI) water.

For the synthesis of CMO:Eu@SiO₂@GNR hybrid nanoparticles, we used commercially available Au nanorods (GNRs; Nanopartz Inc., Loveland CO, USA) with 10 nm in diameter and 43 nm in length. First, 4 mL of the GNR was centrifuged at 13,000 rpm for 30 min and then redispersed in DI water. Centrifugation was repeated for three times to reduce the excess of cetyltrimethylammonium bromide

(CTAB) present on the surface of the GNR. Secondly, 10 mg of HS-PEG-COOH was added to 10 ml of CMO:Eu@SiO₂ and sonicated for 1 h and the resulting solution was centrifuged three times with DI water to remove the excess of HS-PEG-COOH present in the sample. The precipitate obtained was redispersed in a 10 ml of DI water followed by sonication for 2 h. To this GNRs were added dropwise and stirred for 24 h. Finally, CMO:Eu@SiO₂@GNR hybrid nanoparticles (non-PEGylation) were centrifuged at 13000 rpm for 15 min and redispersed in DI water. To this, 200 ml of 100 μ M mPEG-SH was added and stirred for 12 h. Finally, nanoparticles solution was centrifuged and redispersed in DI water. This step is used to control the surface charge on the particles.

6.4.3 Prussian blue labeling and antibody conjugation

The synthesized NPs were labeled with PB by adding 100 μ L PB solution (2 mM) into 1 mL of non-PEGylated NPs solution. After 30 min sonication, the PB-labelled CMO:Eu@SiO₂@GNR NPs were centrifuged for 15 min of 13,000 rpm to remove extra PB molecule and then resuspended in PBS for antibody conjugation. For conjugating the HER2 antibody (Ab) with the PB-labelled CMO:Eu@SiO₂@GNR NPs, 10 μ L HS-PEG-COOH of 1 mg/mL concentration was added into the PB-labelled NPs. After 15 min sonication, 40 μ L mPEG-SH of 1 mg/mL was added for 2 h incubation followed by 30 min sonication. The prepared NPs were centrifuged for 15 min at 13,000 rpm and then resuspended in water. Next, 10 μ L EDC (10 mM) and 10 μ L NHS (25 mM) were added and sonicated for 30 min. The prepared NPs were centrifuged for 15 min of 13,000 rpm and then resuspended in PBS. Then, the prepared NPs were labelled with antibody (20 μ L, 0.2 mg/mL) with 1 h sonication.

After 15 min centrifugation at 13,000 rpm, the prepared NPs were resuspended in PBS and stored at 4 °C for further experiments.

6.4.4 Characterization of synthesized NPs

X-ray diffraction (XRD) patterns of the powder samples were examined at room temperature using a PANalytical X'Pert X-ray diffractometer equipped with Ni filtered CuK α ($\lambda = 1.54056 \text{ \AA}$) radiation as the X-ray source. XRD patterns of the powder sample were examined at room temperature. The microstructure and morphology of the nanoparticles were analyzed using Scanning Electron Microscopy (SEM) (FEI Quanta FEG 650, FEI Company, Hillsboro, OR, USA) integrated with the energy dispersive analysis of X-ray (EDX) spectrometer operated at accelerating voltage of 20 kV. Scanning transmission electron microscopy (STEM) of single particles was measured using Titan TEM with ChemiSTEM capability. Fourier transform infrared spectroscopy (FTIR) spectrum was measured with a FT-IR spectrometer (Bomem MB 102, Agilent technologies, Santa Clara, CA, USA). UV-visible spectra were recorded using a Multiskan UV-visible spectrophotometer (Thermo Scientific). All the luminescence spectra were recorded using a Jobin Yvon Horiba Fluoromax-3 at room temperature. A zeta potentiometer (ZetaPALS, Brookhaven Instrument, Holtsville, NY, USA) was used to measure the surface charge of the particles. Hydrodynamic diameter of the HNPs was determined by dynamic light scattering (DLS) measurements using a DynaPro NanoStar (Wyatt Technology Corp., Santa Barbara, CA, USA) instrument at $25 \pm 0.1 \text{ }^\circ\text{C}$. Disposable cuvettes were used for the measurements.

The surface area and the total pore volume were evaluated using the BET (Brunauer–Emmett–Teller) model and the pore size was evaluated using the BJH (Barrett–Joyner–Halenda) model (Lucideon, Schenectady, NY, USA). The temperature changes of the

CMO:Eu@GNR solutions irradiated by an 808 NIR laser (Xi'an Sampling Laser Technik Institute, Xi'an, Shanxi, China) were collected by a portable fiber optic thermometer (Qualitrol, USA), and the laser power was measured using a handheld laser power meter (Edmund Optics, Barrington, NJ, USA).

6.4.5 Heat transfer efficiency of synthesized NPs

The change in the temperature of the HNPs was estimated by the heat input from the NIR laser via GNRs and heat dissipated into the ambient atmosphere, which can be expressed as follows:

$$\sum_{i=2} m_i C_i \frac{dT}{dt} = Q_{in} - Q_{out} \quad (1)$$

where m_i and C_i are the mass and specific heat capacity of sample i , respectively. T is the temperature of the HNPs on NIR irradiation at time t . The mass of HNPs is significantly smaller than that of water (1 g), and the specific heat capacity of GNRs and water are $\sim 0.129 \text{ Jg}^{-1}\text{K}^{-1}$ and $4.18 \text{ Jg}^{-1}\text{K}^{-1}$, respectively.[13] By neglecting the specific heat capacity of GNR, eq. (i) can be modified as follows:

$$C_i \frac{dT}{dt} = Q_{in} - Q_{out} \quad (2)$$

where $Q_{in} = (I_0 - I_{tr})\eta$ and $Q_{out} = \sum hS[T(t) - T_0]$, I and I_{tr} are the NIR laser power before and after transmitting through the HNPs, h is the heat transfer efficiency, and S is the surface area of the interference between the HNPs and external environment. The increase in the temperature of the HNPs at any time t can be estimated as follows:

$$T(t) = T_0 + \frac{(I_0 - I_{tr})\eta}{mCB} (1 - e^{-Bt}) \quad (3)$$

where T_m is the maximum stable temperature of the HNPs at which laser is turned off, η is the photothermal conversion efficiency, and B is the heat dissipation constant.

The dissipation constant (B) was calculated using the temperature decay profile after the laser was turned off as follows:

$$T(t) = T_0 + (T_m - T_0)e^{-Bt} \quad (4)$$

In thermal equilibrium condition, $Q_{in} = Q_{out}$

i.e., $\eta = mCB \frac{\Delta T}{\Delta t}$ (5), all symbols have their usual meanings.

6.4.6 Cell culture and NPs treatment

435 cells were cultured in a 1:1 mixture of Dulbecco's-modified eagle's medium (DMEM) and Ham's F-12 medium supplemented with 5% fetal bovine serum (ThermoFisher Scientific). Mouse hepatocyte cells (AML12, normal hepatocyte from liver tissue) purchased from American Type Culture Collection (ATCC) were cultured in a 1:1 mixture of Dulbecco's modified Eagle's medium and Ham's F12 medium (ATCC) with 0.005 mg/ml insulin, 0.005 mg/ml transferrin, 5 ng/ml selenium, 40 ng/ml dexamethasone (Sigma-Aldrich) and 10% fetal bovine serum (ATCC) at 37°C with 5% CO₂ in a humidified atmosphere.

Both cells were passaged at 70–90% confluency using 0.5% Trypsin-EDTA solution, and the cell number was estimated by a hemocytometer to be $\sim 1 \times 10^5$ cells/mL. 435 and AML12 cells ($\sim 1 \times 10^5$ cells/mL) were treated with 100 μ L prepared NPs (20 μ g/mL) for two hours incubation at 37 °C. Then, cells were washed with PBS to remove non-bound NPs. 435 cells without treatment, treated with HNP-PB or HNP-PB-Ab were fixed first, then measured by scanning electron microscopy (SEM) and energy-

dispersive X-ray spectra (EDX), which was controlled by FEI Quanta FEG 650 equipped with a FEG source (FEI Company). The fluorescence images were captured under a fluorescence microscope with DP30BW CCD camera (Olympus IX71, Olympus America Inc., Center Valley, PA, USA) with an excitation at 450 nm and an emission at 630 nm. EDTA stabilized human whole blood were freshly obtained from Innovative Research (Novi, MI, USA). Whole blood and serum were used for white blood cell (WBC) count analysis.

6.4.7 SERS measurements of cells treated with synthesized NPs

SERS spectra were recorded using a Renishaw inVia Raman spectrometer (WIRE 3.3 software, Renishaw, Wotton-under-Edge, Gloucestershire, UK) equipped with a 300 mW, 785 nm NIR laser. Cells were cultured on magnesium fluoride (MgF_2 , United Crystals Co., Port Washington, NY, USA) and imaged in EBSS through a $63\times$ ($\text{NA} = 0.90$) water immersion objective (Leica Microsystems, Buffalo Grove, IL, USA). For Raman streamline mapping, the data were acquired at 1 accumulation with 10 s exposure, and the peak at 2152 cm^{-1} from PB was selected for mapping. On each group, the cells were detected within 2 h at room temperature.

6.4.8 NIR photothermal therapy on cells

For NIR PTT, 435 and AML12 cells ($\sim 1 \times 10^5$ cells/mL) were incubated with about 100 μL prepared NPs (20 $\mu\text{g/mL}$ $\text{CMO:Eu@SiO}_2\text{@GNR-PB-Ab}$ (HNP-PB-Ab) and $\text{CMO:Eu@SiO}_2\text{@GNR-PB}$ (HNP-PB), respectively) for two hours incubation at 37 °C. Next, the cells were rinsed with PBS thrice and then exposed to the 808 nm laser irradiation at 0.8 W/cm^2 power densities for 5 min. For cell viability test, the

cells with triplicates were stained using a LIVE/DEAD viability/cytotoxicity Assay Kit (Thermo Fisher Scientific) according to the instruction. After staining, the cells were imaged using a fluorescence microscope equipped with a DP30BW CCD camera (Olympus IX71) at 10× objective to analyze the relative proportion of live/dead cells.

6.4.9 Apoptosis and reactive oxygen species (ROS) analysis

The apoptosis level was recorded by a Muse™ Annexin V and Dead Cell kit (EMD Millipore Co., Billerica, MA, USA), and ROS level was measured by a Muse™ Oxidative Stress kit (EMD Millipore Co.). Cells were cultured in 6-well plates to about 70% confluence, and every treatment had three replicates. The cells were collected and analyzed using a Muse Cell Analyzer (EMD Millipore Co.).

6.4.10 Statistics analysis

Data are exhibited as mean \pm standard deviation of error. One-way ANOVA is conducted for significance test by OriginPro 9 software (OriginLab Corp., Northampton, MA, USA).

6.5 RESULTS AND DISCUSSIONS

6.5.1 Characterization of HNP-PB

Figure 6.1(A) shows the X-ray diffraction (XRD) pattern of CMO:Eu@SiO₂ hybrid NPs. All diffraction peaks are well matches with tetragonal structure of CaMoO₄ (JCPDF No: 29-0351 having space group I4_{1/a} (88) and Z = 4) [14] and a broad peak between 15–30° centered at ~23° was assigned to porous silica present on the surface of the CMO:Eu nanoparticles [15]. The intensity of the diffraction peak centered at ~23° weak as

compared to that of CaMoO_4 due to the amorphous nature of SiO_2 on the surface of CaMoO_4 . No impurity phases were detected. In this way luminescence functionalized CMO:Eu nanoparticles are capped by SiO_2 shell. Similar results were reported on mesoporous SiO_2 functionalized with luminescent core or Fe_3O_4 magnetic nanoparticles [16, 17].

The structural and morphological properties of the CMO:Eu@SiO_2 (Figure 6.1(B)) and $\text{CMO:Eu@SiO}_2\text{@GNR}$ (Figure 6.1(C)) nanoparticles were examined by SEM. A mesoporous spherical SiO_2 shell with uniform thickness was formed over CMO:Eu core. The average diameter of CMO:Eu@SiO_2 nanoparticles was found to be ~ 206 nm. However, SEM micrographs were not able to resolve the thickness of SiO_2 shell and CMO:Eu core. It was confirmed by using STEM micrograph (inset of Figure 6.1(B)). Moreover, the presence of SiO_2 shell on the surface of CMO:Eu nanoparticles significantly enhanced the dispersion ability of the nanoparticles in distilled water. Furthermore, all the particles were spherical in shape and no irregular shaped particles were observed. Thickness of the SiO_2 shell can be varied simply changing the concentration of TEOS in the reaction [15]. The obtained CMO:Eu@SiO_2 nanoparticles possessed uniform pore size of ~ 2.2 nm and high surface area $380 \text{ m}^2/\text{g}$. SEM micrograph of $\text{CMO:Eu@SiO}_2\text{@GNR}$ hybrid nanoparticles was shown in Figure 6.1(C). On average each CMO:Eu@SiO_2 nanoparticles was surrounded by ~ 5 GNRs. The presence of elements in CMO:Eu@SiO_2 nanoparticles was further confirmed by Energy-dispersive X-ray spectroscopy (EDX) spectrum as shown in Figure 6.1(D). Inset of Figure 6.1(D) shows the Fourier transform infrared spectroscopy (FTIR) spectra of (i) $\text{CaMoO}_4\text{:Eu}^{3+}$ and (c) CMO:Eu@SiO_2 nanoparticles. The absorption peaks at 1642 and 3450 cm^{-1} are attributed to bending and stretching vibrations water molecules present on the

surface of nanoparticles [18]. The band at $\sim 816\text{ cm}^{-1}$ is attributed to asymmetric stretching vibrations of O–Mo–O of MoO_4^{2-} tetrahedral [14]. The absorption band $\sim 1110\text{ cm}^{-1}$ is due to stretching vibrations of Si–O–Si which arises from hybrid nanoparticles [16].

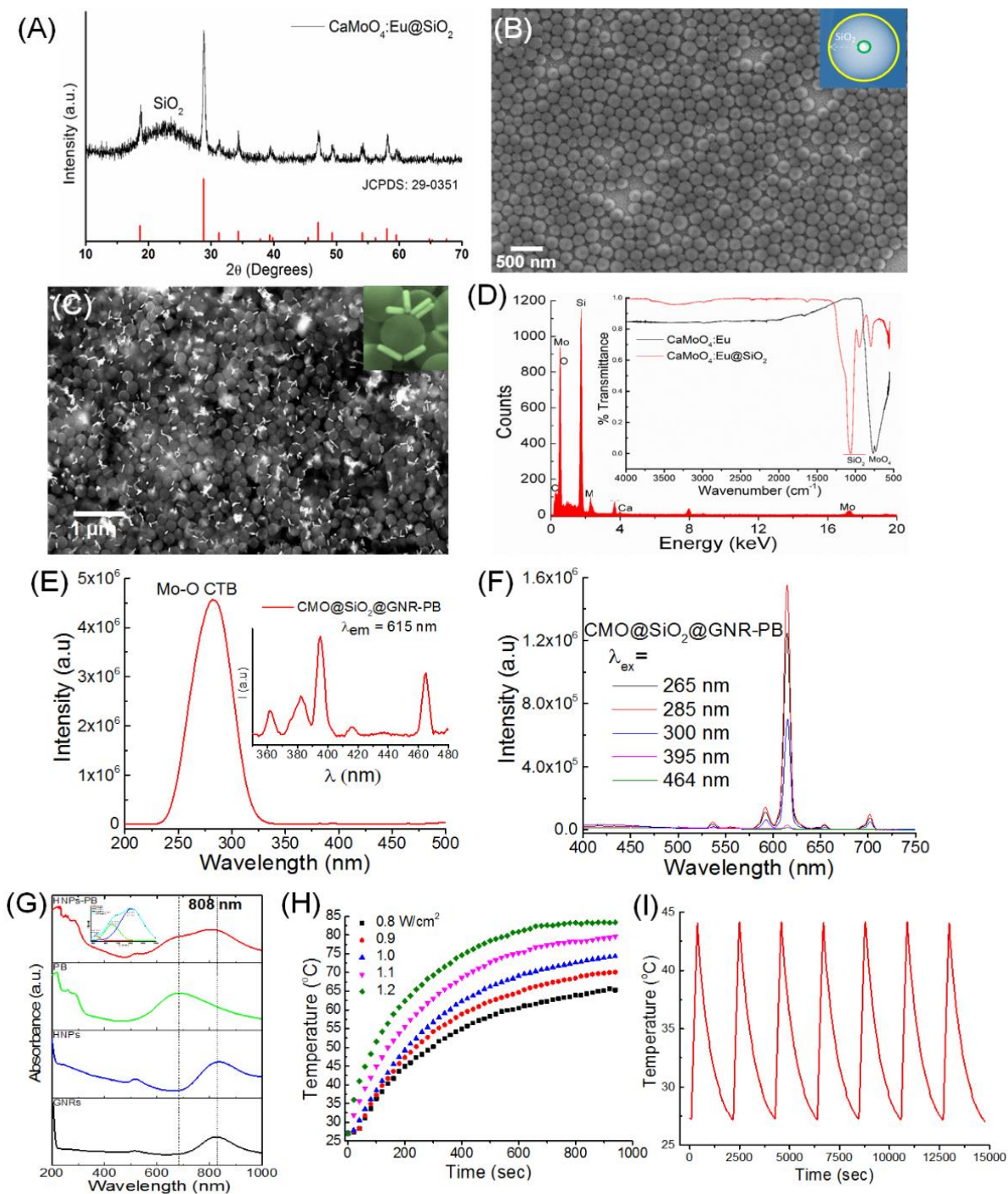


Figure 6.1 (A) XRD (B) SEM of Silica coated CMO nanoparticles and (C) Silica coated CMO nanoparticles conjugated with gold nanorods, Inset of (B) shows the STEM of CMO@SiO₂; Inset of (C) shows the SEM of single CMO@SiO₂@GNR. (D) EDX spectrum of CMO@SiO₂. (E) Excitation, and (F) Luminescence spectra of CMO@SiO₂@GNR-PB nanoparticles under different excitations. (G) UV–visible spectra of GNR, CMO@SiO₂@GNR, PB and CMO@SiO₂@GNR-PB. (H) Photothermal responses of 808 nm laser irradiation with different power densities for 900 s at fixed CMO@SiO₂@GNR-PB concentration (28 µg/mL GNR). (I) Temperature change of CMO@SiO₂@GNR-PB solution with 28 µg/mL GNR at 0.8 W/cm² 808 nm laser irradiation over seven LASER ON/OFF cycles. Experiment was carried out at room temperature.

The excitation (monitoring emission at 615 nm) and emission (excitation at 265, 285, 300, 395 and 464 nm) spectra of CMO@SiO₂@GNR-PB hybrid nanoparticles are shown in Figure 6.1(E-F). Excitation consists of a strong and broad absorption in the range of 225–350 nm, peak centered at 285 nm is attributed to Mo–O charge transfer (CT). Inset of the Figure 6.1(E) shows the expansion the excitation spectrum between 350 to 480 nm. The sharp absorption peaks ~395 (⁷F₀→⁵L₆) and 464 nm (⁷F₀→⁵D₂) are due to the f–f transitions of Eu³⁺ ion [19]. Figure 6.1(F) shows the emission spectra of bare CMO@SiO₂@GNR-PB hybrid nanoparticles at different excitation wavelengths. Emission spectra consist of sharp emission peaks which are assigned to ⁵D_{0,1}→⁷F_i, i=0–4, transitions of Eu³⁺ ion. The emission at 595 and 615 nm correspond to the magnetic (⁵D₀→⁷F₁) and electric dipole transitions (⁵D₀→⁷F₂) of Eu³⁺ ion, respectively, where the emission intensity of the electric dipole transition is significantly higher than other transitions. When Eu³⁺ ions occupy the

Ca^{2+} lattice sites in CaMoO_4 host, only the magnetic dipole transition should be allowed according to Judd–Ofelt theory, but the non-inversion center leads to a dominant hypersensitive electric dipole transition at 615 nm. Moreover, there is a significant enhancement in the luminescence intensity of $\text{CMO@SiO}_2\text{@GNR-PB}$ hybrid nanoparticles as compared to CMO@SiO_2 . This may be due to proximity of GNRs on the surface of luminescent NPs that significantly enhance the luminescence efficiency [2]. Figure 6.1(G) shows the UV-visible spectra of GNR, $\text{CMO@SiO}_2\text{@GNR}$, PB and $\text{CMO@SiO}_2\text{@GNR-PB}$ between 200–1000 nm. Two characteristic peaks were observed ~ 530 and 808 nm, which are assigned to surface plasmon resonance (SPR) of GNRs. Bare GNRs and $\text{CMO@SiO}_2\text{@GNR}$ hybrid nanoparticles show almost no any absorbance around 680 nm whereas Prussian blue shows a strong absorption at 680 nm which arises due to a charge-transfer absorption band from Fe(II) to Fe(III) peculiar to Prussian blue [20]. The $\text{CMO@SiO}_2\text{@GNR-PB}$ hybrid nanoparticles show a broad absorption from 500–1000 nm which arises due to overlap of PB absorption and SPR band of GNRs, which enable the use of hybrid nanoparticles as a potential agent for NIR mediated PTT agent [21].

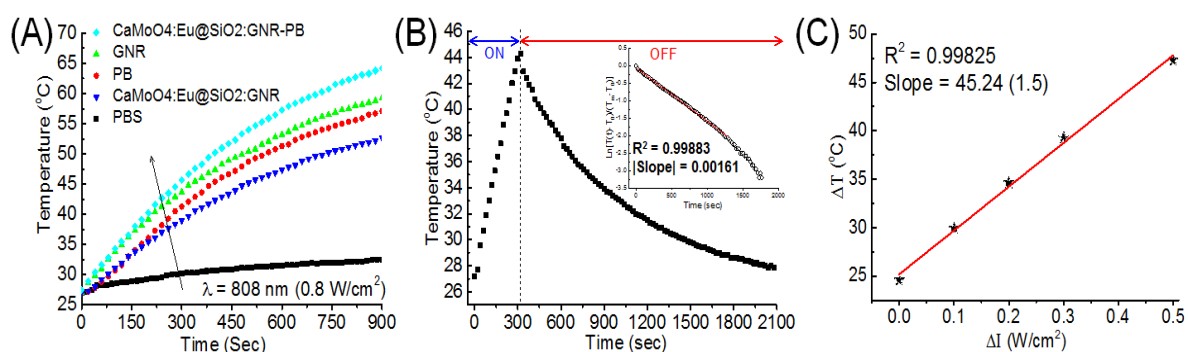


Figure 6.2 (A) Photothermal responses of PBS, GNR, PB, $\text{CMO@SiO}_2\text{@GNR}$ and $\text{CMO@SiO}_2\text{@GNR-PB}$ for 900 s at fixed 0.8 W/cm^2 . (B) The photothermal response of the

CMO@SiO₂@GNR-PB solution (28 µg/mL GNR) was recorded for an NIR laser (808 nm, 0.8 W/cm²), and then the laser was turned off. (C) Temperature increase of synthesized CMO@SiO₂@GNR-PB solution as a function of laser power extinction.

The photothermal properties of CMO@SiO₂@GNR-PB hybrid nanoparticles were investigated by monitoring the temperature of 1 mL water containing CMO@SiO₂@GNR-PB NPs (28 µg/mL GNRs) under 808 nm NIR light for 900 s at different irradiation powers (0.8–1.2 W/cm²) (Figure 6.1(H)). Temperatures increased between 25 to 65 °C on NIR irradiation (0.8 W/cm²) to the hybrid nanoparticles for 900 s. It was also found that the temperature of hybrid nanoparticles was exponentially increased with time and laser irradiation power. The comparison of photothermal responses of 808 nm laser irradiation at PBS, GNR, PB, CMO@SiO₂@GNR and CMO@SiO₂@GNR-PB for 900 s at fixed 0.8 W/cm² was shown in Figure 6.2(A). No significant difference in temperature change was observed when PBS was irradiated with an 808 nm NIR radiation. It was found that the order of PTT heating efficiency follows CMO@SiO₂@GNR < PB < GNR < CMO@SiO₂@GNR-PB. To understand the photostability of CMO@SiO₂@GNR-PB hybrid nanoparticles, seven cycles of ON/OFF NIR laser irradiations were performed (~0.8 W/cm² for 300 s (laser ON), followed by naturally cooling for 1800 s (laser OFF) (Figure 6.1(I)). It was found that the temperature increased to 43 °C in the first laser ON condition of the CMO@SiO₂@GNR-PB. After the seventh cycle of laser ON/OFF, the temperature elevations remained almost the same as in the first cycle within the limits of error bar. It confirms the excellent photothermal stability of CMO@SiO₂@GNR-PB hybrid nanoparticles. The PTT heat conversion efficiency (η) of

CMO@SiO₂@GNR-PB hybrid nanoparticles was determined using the previous report by Pinchuk and co-workers (Eq. 1-5) [13]. PTT effect of CMO@SiO₂@GNR-PB hybrid nanoparticles on an 808 nm NIR laser, in which the irradiation lasted for 300 s, and then the laser was shut off and allowed to cool the nanoparticles up to 1800 s (Figure 6.2(B)). Inset of Figure 6.2(B) shows log of $(T(t)-T_0)/(T_m-T_0)$ versus time obtained from cooling curve and the value of heat dissipation rate constant (B) was calculated using the cooling temperature profile when the laser was turned off. The average value of B was found to be $\sim 1.61 \times 10^{-3} \text{ s}^{-1}$ by linear fitting to Figure 6.2(B) with $R^2 = 0.99883$. Figure 6.2(C) shows the linear relationship between ΔT and ΔI . The η value was found to be $\sim 30.6\%$. Furthermore, there is no significant difference in luminescence emission was measured on 464 nm excitation to the hybrid nanoparticles at the start and end of each cycle (Figure 6.1(I)).

6.5.2 Zeta potential/hydrodynamic diameter properties

Moreover, for the cellular uptake of the hybrid nanoparticles, its surface charge and dispersion ability play essential factors. Bare GNRs show a positive charge of $\sim 43.9 \text{ mV}$. CMO@SiO₂ nanoparticles show a negative charge of -26.6 mV , this is may be due to the presence of $-\text{OH}$ groups present on the surface of nanoparticles. Further, zeta potential of CMO@SiO₂@GNR-PB hybrid nanoparticles shifted to $+16 \text{ mV}$. This high value reveals the good colloidal stability of the hybrid nanoparticles but minimum surface charge is required for the better tumor penetration. Recently, Joshi and Halas group demonstrated that the PEGylated gold nano-shell (-5.4 mV) and nanomatryoshkas (-4.4 mV) shows more tumor uptake as compared to bare gold nano-shell (-57 mV) and bare nanomatryoshkas (-46.7 mV) nanoparticles [22]. Also, mesoporous silica coated gold nanoparticles with zeta potential -22.5 mV have been successfully tested for both *in-vitro* and *in-vivo* applications [23].

6.5.3 Characterization of HNP-PB distributed on cells by SEM

To understand the distribution of nanoparticles in cell environment, 435 cells were treated with HNP-PB and HNP-PB-Ab nanoparticles. Figure 6.3(A) illustrates the representative SEM images of 435 cells without treatment, treated with HNP-PB and treated with HNP-PB-Ab (black arrow points to NPs) and its EDX spectra were displayed in Figure 6.3(B). The scale of HNP-PB and HNP-PB-Ab group in Figure 6.3(B) is slightly different, which is caused by the distribution of NPs, but both groups confirm the distribution of NPs on cells. After 2 h NPs incubation, cells treated with HNP-PB-Ab group exhibited a strong EDX signal which confirms the presence of highest occupancy NPs distributed around the cell surface as compared to control and HNP-PB groups, indicating the specificity of HNP-PB-Ab. Few NPs were still observed on HNP-PB treated cells because of non-specific binding.

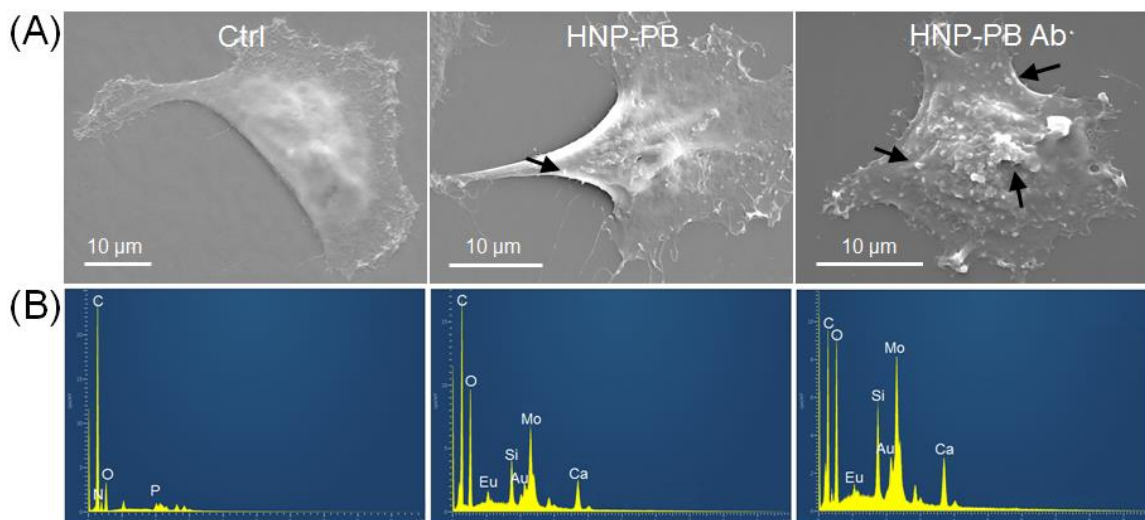


Figure 6.3 (A) Representative SEM images of 435 cells without treatment, treated with HNP-PB or HNP-PB-Ab (black arrow points to NPs). (B) Corresponding energy-dispersive X-ray spectroscopy of 435 cells without treatment, treated with HNP-PB or HNP-PB-Ab.

6.5.4 Fluorescence imaging of HNP-PB on cells

Figure 6.4 exhibits phase contrast, fluorescence, and overlay of phase contrast and fluorescence images of 435 and AML12 cells without treatment (control), treated with 2 h HNP-PB (with or without Ab). In 435 cells (Figure 6.4(A)) there was no obvious fluorescence red color in the groups of control and 2 h HNP-PB; while a strong red color was observed in the group of 2 h HNP-PB-Ab, demonstrating the fluorescence function of synthesized NPs with strong specificity once conjugated with antibodies. To further investigate the specificity of HNP-PB-Ab, non-cancerous cells (AML12, HER2 negative) were treated with the same groups (Figure 6.4(B)). Still no red fluorescence was detected under the groups of control and 2 h HNP-PB. However, there was a slight red fluorescence color in the group of 2 h HNP-PB-Ab. When compared to 435 cells of 2 h HNP-PB-Ab group with the group of AML12 cells, it was evident that 435 cells possessed much more red color than AML12 cells, indicating the over-expression of HER2 on 435 cells than AML 12 cells. This also further confirmed the specificity of HNP-PB-Ab for 435 breast cancer cells.

The red fluorescence was observed in the group of 435 and AML12 cells treated with HNP-PB-Ab by ~464 nm excitation and 615 nm emission, and this fluorescence property is from Eu^{3+} ion ($^5\text{D}_2$ level of Eu^{3+} ion). Previous studies also demonstrated the fluorescence emission from Eu^{3+} doped NPs for enhanced imaging [15, 16]. Compared to 435 cells with AML12 cell line, 435 cells over-express HER2 [24], and AML12 cell line was derived from normal liver and is non-tumorigenic [25]. The 435 cells of 2 h HNP-PB-Ab group exhibited the strongest fluorescence compared to other groups.

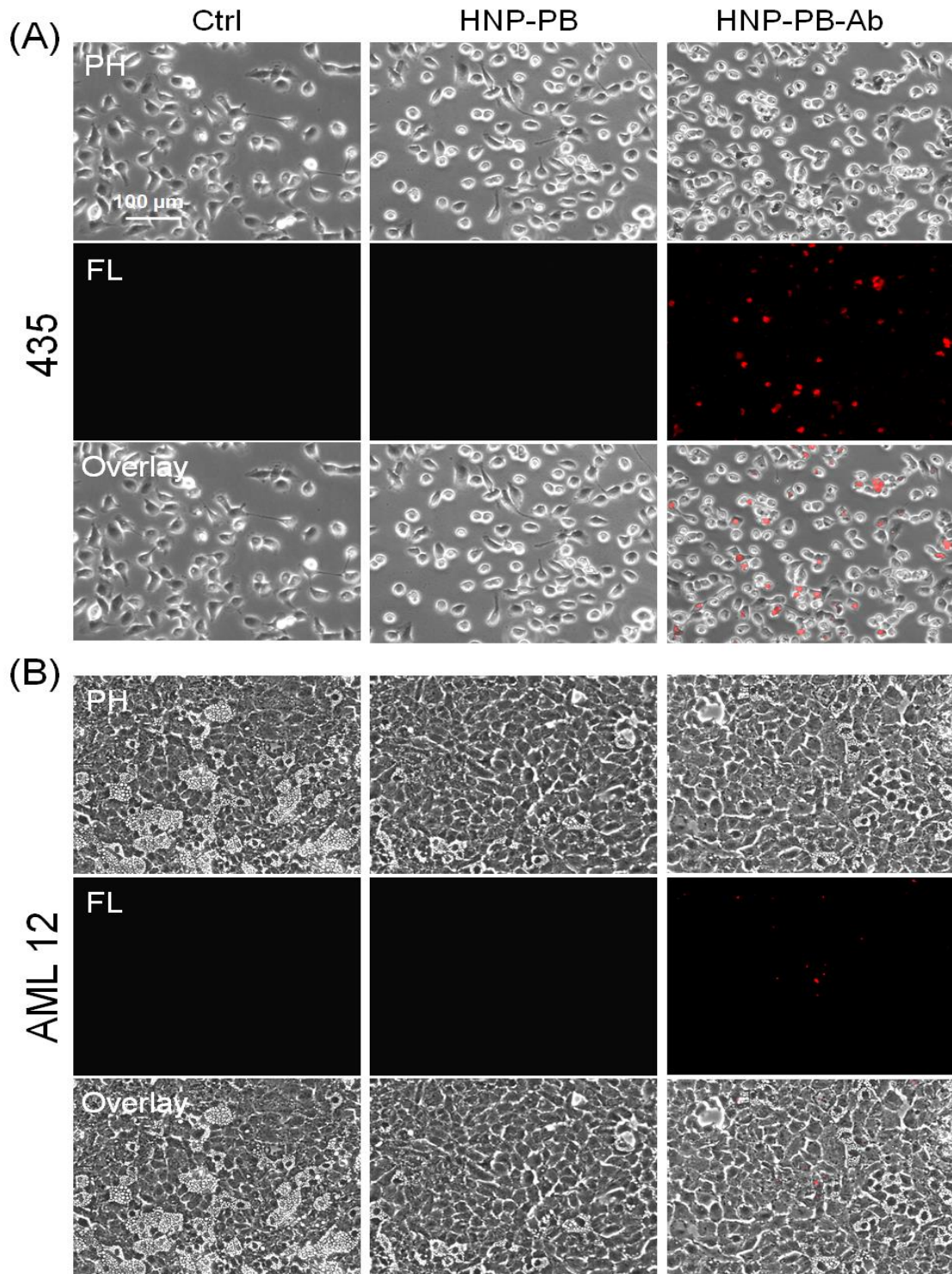


Figure 6.4 Phase (PH), fluorescence (FL), and overlay images of 435 (A) and AML12 cells (B) without treatment and treated with HNP-PB or HNP-PB-Ab for 2 h. Scale bar: 100 μm .

6.5.5 Distribution of HNP-PB on cells detected by SERS

HNP-PB possess SERS function due to GNR conjugation, and GNR has been largely utilized to enhance Raman intensity [26, 27]. Prussian blue (PB) was selected to evaluate the SERS ability as the Raman reporter molecule for its strong Raman vibrational band at $\sim 2152\text{ cm}^{-1}$ (stretching vibration of carbon nitrogen triple bond group) [28]. Raman mapping for live 435 and AML12 cells was performed by selection of 2152 cm^{-1} (a characteristic peak from PB). The HNP-PB were conjugated with Ab for the enhancement of specificity. Figure 6.5 shows the Raman bright-field image, the corresponding Raman streamline mapping and representative Raman spectrum ($2000\text{--}2300\text{ cm}^{-1}$) from SERS negative (green cross) and SERS positive (red cross) sites of single living 435 (Figure 6.5(A)) and AML12 cell (Figure 6.5(B)). It was observed that 435 cells treated with HNP-PB-Ab illustrated the strongest distribution of NPs (bright yellow color indicated), suggesting the specificity of synthesized HNP-PB-Ab. Few NPs were still distributed around the 435 cells treated with HNP-PB due to non-specific binding. NPs were also applied to the AML12 for comparison (Figure 6.5(B)). It was found that few NPs were located around AML12 cells in both HNP-PB and HNP-PB-Ab groups, indicating non-specific binding of NPs. These SERS results verified the specificity of HNP-PB-Ab and the distribution of these NPs on cancerous cells (e.g., 435 cells) but not on non-cancerous cells (e.g., AML 12 cells).

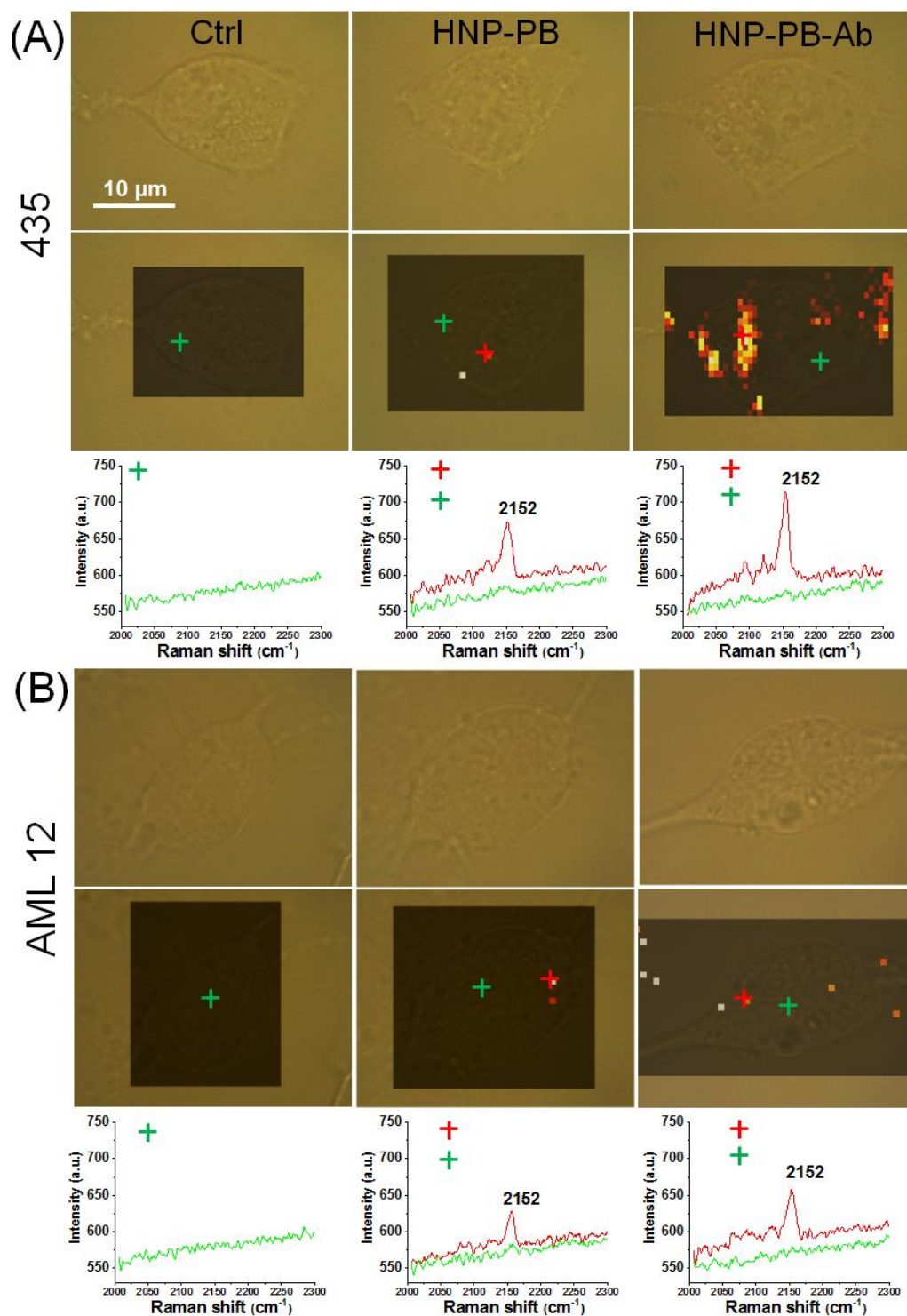


Figure 6.5 Raman streamline mapping of 435 (A) and AML12 cells (B) without treatment and treated with HNP-PB or treated with HNP-PB-Ab for 2 h (peak at 2152 cm^{-1} from PB was selected for mapping). Scale bar: 10 μm .

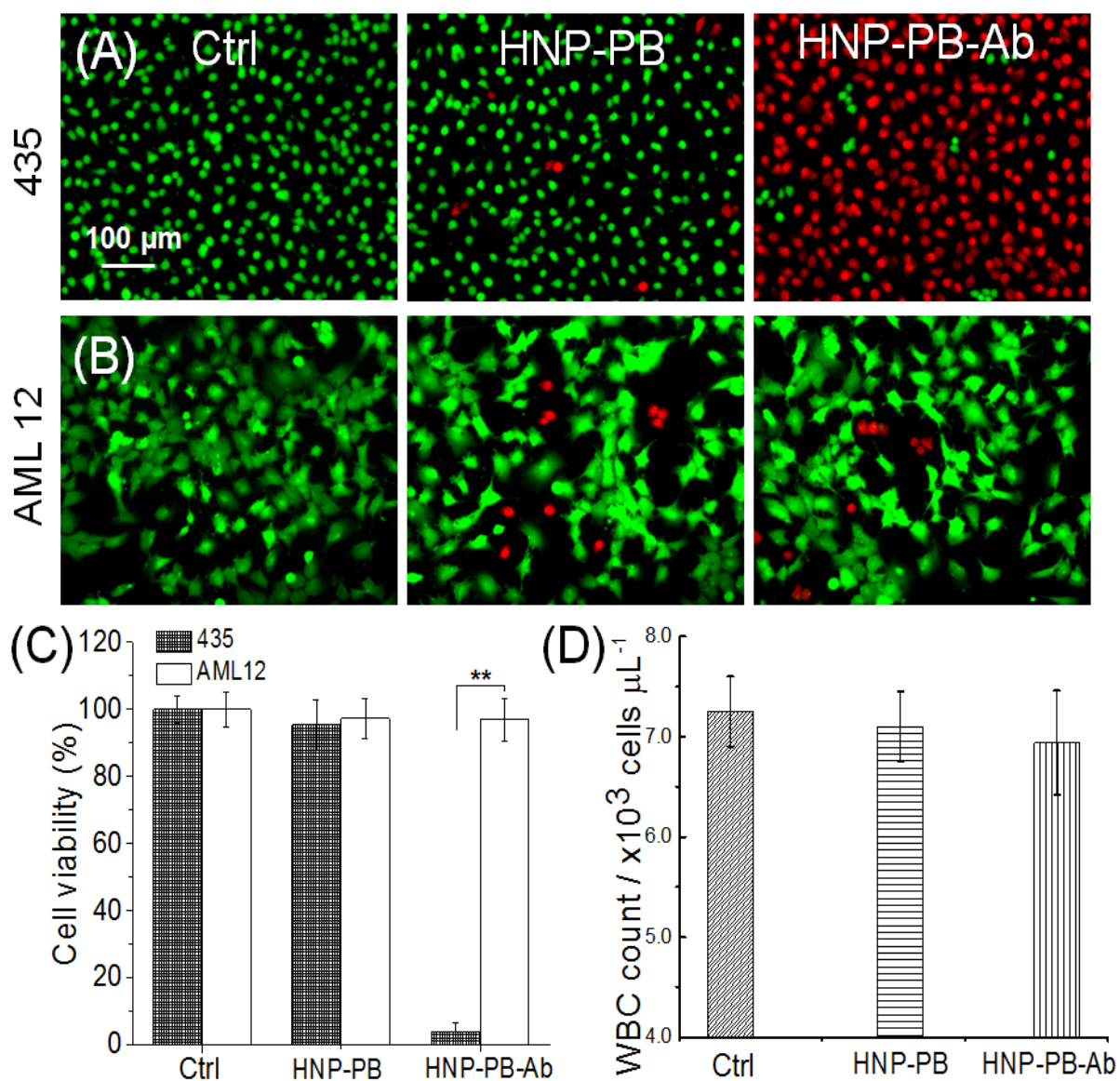


Figure 6.6 (A) Photothermal effect and biocompatibility. 435 and AML12 cells were incubated without NPs (control), with HNP-PB or HNP-PB-Ab for 2 h; after that, cells were irradiated under 0.8 W/cm^2 808 nm laser for 5 min (green: live cells; red: dead cells. Scale bar: $100 \mu\text{m}$). (C) Cell viability of 435 and AML12 cells (Error bar: standard deviation of the mean; $N = 3$, $**P < 0.01$). (D) Human white blood count.

6.5.6 Photothermal effect and biocompatibility of HNP-PB

The photothermal effect of HNP-PB and HNP-PB-Ab NPs on HER2 positive 435 cells and HER2 negative cells is presented in Figure 6.6. Cells were treated with HNP-PB (without or with Ab) and irradiated by an 808 nm NIR laser for 5 min (0.8 W/cm^2). Figure 6.6(A-B) exhibits the fluorescence images (live cells: green; dead cells: red) of 435 and AML12 cells without or with NPs treatments (HNP-PB or HNP-PB-Ab). Cells were alive in the control group, whereas a few dead cells were observed in the HNP-PB group when treated to both types of cells. As expected, almost all cells were dead when HNP-PB-Ab was applied to 435 cancer cells (Figure 6.6(A)). However, only few dead AML12 cells in HNP-PB-Ab group were observed (Figure 6.6(B)), indicating that HNP-PB-Ab can specifically target and kill 435 cancer cells that overexpressed HER2.

The quantitative cell viability of 435 and AML12 cells without and with treated (HNP-PB or HNP-PB-Ab) groups for 2 h was studied on 5 min 0.8 W/cm^2 808 nm laser irradiation (Figure 6.6(C)). There was no significant viability differences for AML12 cells among these three group. However, 435 cells treated with HNP-PB-Ab had the least percentage of viability ($\sim 4.0 \pm 2.8\%$) comparing to control and HNP-PB group, demonstrating the specificity and high PTT efficiency from HNP-PB-Ab. Moreover, HNP-PB with or without Ab were treated with WBC to evaluate their biocompatibility, as shown in Figure 6.6(D). WBC count reveals that there was no significant viability differences among these three groups, and the numbers of WBC for all treated groups were within normal range ($\sim 4000\text{--}11,000$ white blood cells/ μL) [29], indicating the good biocompatibility of synthesized HNP-PB.

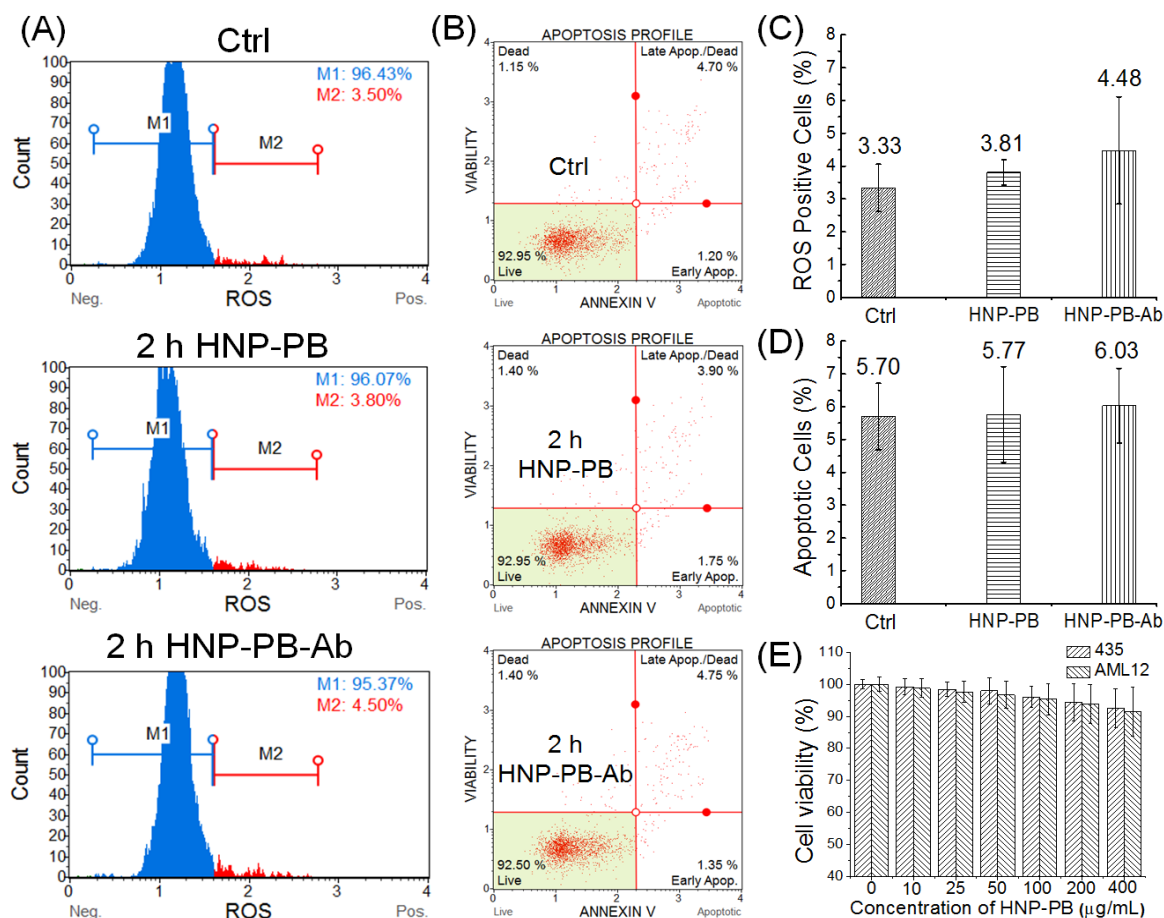


Figure 6.7 Cytotoxicity of synthesized HNP-PB. (A) The histograms show the percentages of ROS- (M1) and ROS+ (M2) for one experiment. 435 cells were incubated without NPs (control), with HNP-PB or HNP-PB-Ab for 2 h; after that the formation of ROS was measured using the Muse flow cytometry-based oxidative stress assay™. (B) The scattered apoptosis blots represent one experiment. 435 cells were incubated without NPs (control), with HNP-PB or HNP-PB-Ab for 2 h; after that apoptosis was evaluated after staining with FITC-annexin-V/7ADD. (C) The graph displays the summary ROS+ cells from three independent experiments. (D) The graph represents the summary mean percentages \pm SD of apoptosis (early and late apoptosis) of three independent experiments. (E) Cell viability of 435 and AML12 cells: control and treated with different concentrations of HNP-PB for 24 h (Error bars are standard deviation of the mean; N = 3, ** $P < 0.01$).

The PTT results indicated that the HNP-PB-Ab could kill 435 cells with high specificity, PTT efficiency and biocompatibility. The high specificity comes from the binding interactions between the Ab and HER2 on the cancer cell, the advanced PTT efficiency is from the synergistic effect of GNR and PB that can convert light to heat effectively, and the good biocompatibility of HNP-PB-Ab is caused by the inert property of SiO₂ and GNR and the stability of PB. Therefore, the HNP-PB-Ab with high specificity, PTT efficiency and biocompatibility could be used as a potential approach for cancer treatment and may apply in clinical cancer therapy.

6.5.7 Cytotoxicity of synthesized HNP-PB

To evaluate the cytotoxicity of synthesized HNP-PB, ROS, apoptosis and cell viability were measured for the cells exposed to these NPs. Figure 6.7(A) is the representative result of ROS expression from flow cytometry, and Figure 6.7(C) compares ROS+ cells from three independent experiments. The representative apoptosis result is shown in Figure 6.7(B), and Figure 6.7(D) exhibits the summary mean percentages of apoptotic cells of three independent experiments. Figure 6.7(E) analyzes the cell viability of 435 and AML12 cells incubated with HNP-PB for 24 h at different concentrations (from 0 to 400 µg/mL). In Figure 6.7(C) the cell population with ROS+ cells in control group is $3.33 \pm 0.72\%$, and there is a slight increase in HNP-PB without ($3.81 \pm 0.38\%$) or with antibody ($4.48 \pm 1.63\%$) groups. There is no significant difference among them for ROS expression.

Similarly, there is no significant difference in NPs-induced apoptosis among the three groups (Figure 6.7(D)): control group ($5.70 \pm 1.01\%$), cells treated with HNP-PB ($5.77 \pm 1.46\%$) and HNP-PB-Ab ($6.03 \pm 1.14\%$), respectively.

The effect of HNP-PB on cell viability (Figure 6.7(E)) was evaluated using the LIVE/DEAD viability/cytotoxicity assay kit. Even though cell viability decreased slightly with the increase of HNP-PB concentration, it still remains >90% up to 400 $\mu\text{g/mL}$ of the HNP-PB incubated for 24 h. This observation is similar to previous study that mesoporous silica nanoparticles have little impact on cellular activities (viability, mitochondrial activity, membrane integrity) with good biocompatibility [30]. The slight decrease of cell viability at high concentration (400 $\mu\text{g/mL}$) of HNP-PB may be attributed to CMO:Eu, which has been reported to produce hydroxyl radicals at high concentration [31]. Hydroxyl radicals can generate ROS which induces cellular apoptosis [32, 33]. However, the concentration of HNP-PB used in this study is under 50 $\mu\text{g/mL}$, so the impact of cytotoxicity of higher NP concentration is limited.

Overall, the cytotoxic effect of HNP-PB on cancerous and non-cancerous cells was negligible, further demonstrating the good biocompatibility of synthesized NPs.

6.6 CONCLUSION

In summary, PB coated $\text{CaMoO}_4\text{:Eu@SiO}_2\text{@Au}$ -nanorod hybrid nanoparticles were prepared and used as a fluorescence, SERS and PTT probe for biomedical applications. The nanostructures were heated up to hyperthermia temperature (43 °C) on excitation with NIR light and can be used to kill cancer cells. Also, electric dipole transition of Eu^{3+} ion (615 nm) can be used for imaging cancer cells on excitation with 464 nm. Surface functionalized GNRs and SiO_2 shell make hybrid particles more biocompatible. Core/shell features of the particles were demonstrated by STEM. Finally, *in-vitro* results suggest that HER2 antibody functionalized hybrid nanoparticles may induce more cell death as compared to bare nanoparticles on 808 nm laser excitation. Also, the porous SiO_2 structure may useful for

loading drug and NIR fluorophores into the porous structure. This method can be used to prepare various other upconversion core functionalized mesoporous nanostructures decorated with GNRs and could be used for different biomolecules in biological and biomedical applications. In addition, the ROS generation, apoptosis level and cell viability changes induced from the synthesized construct were evaluated, confirming the good biocompatibility of synthesized materials. Thus, this work demonstrates the promising potential of CMO:Eu@SiO₂@GNR-PB nanocomposites that potentially benefit the area of cancer therapy.

6.7 REFERENCES

1. Wang F, Tan WB, Zhang Y, Fan XP, Wang MQ. Luminescent nanomaterials for biological labelling. *Nanotechnology*. 2006; 17: R1-R13.
2. Bardhan R, Chen WX, Perez-Torres C, Bartels M, Huschka RM, Zhao LL, et al. Nanoshells with Targeted Simultaneous Enhancement of Magnetic and Optical Imaging and Photothermal Therapeutic Response. *Adv Funct Mater*. 2009; 19: 3901-9.
3. Keren S, Zavaleta C, Cheng Z, de la Zerda A, Gheysens O, Gambhir SS. Noninvasive molecular imaging of small living subjects using Raman spectroscopy. *Proc Natl Acad Sci U S A*. 2008; 105: 5844-9.
4. Yuan HK, Liu Y, Fales AM, Li YL, Liu J, Vo-Dinh T. Quantitative Surface-Enhanced Resonant Raman Scattering Multiplexing of Biocompatible Gold Nanostars for in Vitro and ex Vivo Detection. *Anal Chem*. 2013; 85: 208-12.

5. Gollavelli G, Ling YC. Magnetic and fluorescent graphene for dual modal imaging and single light induced photothermal and photodynamic therapy of cancer cells. *Biomaterials*. 2014; 35: 4499-507.
6. Tsai CP, Chen CY, Hung Y, Chang FH, Mou CY. Monoclonal antibody-functionalized mesoporous silica nanoparticles (MSN) for selective targeting breast cancer cells. *J Mater Chem*. 2009; 19: 5737-43.
7. Shi SG, Zhu XL, Zhao ZX, Fang WJ, Chen M, Huang YZ, et al. Photothermally enhanced photodynamic therapy based on mesoporous Pd@Ag@mSiO₂ nanocarriers. *J Mater Chem B*. 2013; 1: 1133-41.
8. Rios C, Monroyoyola A. D-Penicillamine and Prussian Blue as Antidotes against Thallium Intoxication in Rats. *Toxicology*. 1992; 74: 69-76.
9. Shokouhimehr M, Soehnlén ES, Hao JH, Griswold M, Flask C, Fan XD, et al. Dual purpose Prussian blue nanoparticles for cellular imaging and drug delivery: a new generation of T₁-weighted MRI contrast and small molecule delivery agents. *J Mater Chem*. 2010; 20: 5251-9.
10. Fu GL, Liu W, Feng SS, Yue XL. Prussian blue nanoparticles operate as a new generation of photothermal ablation agents for cancer therapy. *Chem Commun*. 2012; 48: 11567-9.
11. Jia X, Cai X, Chen Y, Wang S, Xu H, Zhang K, et al. Perfluoropentane-encapsulated hollow mesoporous prussian blue nanocubes for activated ultrasound imaging and photothermal therapy of cancer. *ACS Appl Mater Interfaces*. 2015; 7: 4579-88.
12. Cobleigh MA, Vogel CL, Tripathy D, Robert NJ, Scholl S, Fehrenbacher L, et al. Multinational study of the efficacy and safety of humanized anti-HER2 monoclonal

- antibody in women who have HER2-overexpressing metastatic breast cancer that has progressed after chemotherapy for metastatic disease. *J Clin Oncol.* 1999; 17: 2639-48.
13. Jiang K, Smith DA, Pinchuk A. Size-Dependent Photothermal Conversion Efficiencies of Plasmonically Heated Gold Nanoparticles. *J Phys Chem C.* 2013; 117: 27073-80.
 14. Parchur AK, Ningthoujam RS. Preparation and structure refinement of Eu³⁺ doped CaMoO₄ nanoparticles. *Dalton Trans.* 2011; 40: 7590-4.
 15. Ansari AA, Hasan TN, Syed NA, Labis JP, Parchur AK, Shafi G, et al. In-vitro cytotoxicity, geno-toxicity, and bio-imaging evaluation of one-pot synthesized luminescent functionalized mesoporous SiO₂@Eu(OH)₃ core-shell microspheres. *Nanomedicine.* 2013; 9: 1328-35.
 16. Singh NS, Kulkarni H, Pradhan L, Bahadur D. A multifunctional biphasic suspension of mesoporous silica encapsulated with YVO₄:Eu-3(+) and Fe₃O₄ nanoparticles: synergistic effect towards cancer therapy and imaging. *Nanotechnology.* 2013; 24.
 17. Deng Y, Qi D, Deng C, Zhang X, Zhao D. Superparamagnetic high-magnetization microspheres with an Fe₃O₄@SiO₂ core and perpendicularly aligned mesoporous SiO₂ shell for removal of microcystins. *J Am Chem Soc.* 2008; 130: 28-9.
 18. Singh BP, Parchur AK, Ningthoujam RS, Ansari AA, Singh P, Rai SB. Influence of Gd³⁺ co-doping on structural property of CaMoO₄:Eu nanoparticles. *Dalton Trans.* 2014; 43: 4770-8.

19. Raju GSR, Pavitra E, Nagaraju G, Yu JS. Versatile properties of CaGd₂ZnO₅:Eu³⁺ nanophosphor: its compatibility for lighting and optical display applications. *Dalton Trans.* 2015; 44: 1790-9.
20. Samain L, Silversmit G, Sanyova J, Vekemans B, Salomon H, Gilbert B, et al. Fading of modern Prussian blue pigments in linseed oil medium. *J Anal Atom Spectrom.* 2011; 26: 930-41.
21. Jing LJ, Liang XL, Deng ZJ, Feng SS, Li XD, Huang MM, et al. Prussian blue coated gold nanoparticles for simultaneous photoacoustic/CT bimodal imaging and photothermal ablation of cancer. *Biomaterials.* 2014; 35: 5814-21.
22. Ayala-Orozco C, Urban C, Knight MW, Urban AS, Neumann O, Bishnoi SW, et al. Au Nanomatryoshkas as Efficient Near-Infrared Photothermal Transducers for Cancer Treatment: Benchmarking against Nanoshells. *Acs Nano.* 2014; 8: 6372-81.
23. Monem AS, Elbially N, Mohamed N. Mesoporous silica coated gold nanorods loaded doxorubicin for combined chemo-photothermal therapy. *Int J Pharmaceut.* 2014; 470: 1-7.
24. Subik K, Lee JF, Baxter L, Strzepek T, Costello D, Crowley P, et al. The Expression Patterns of ER, PR, HER2, CK5/6, EGFR, Ki-67 and AR by Immunohistochemical Analysis in Breast Cancer Cell Lines. *Breast Cancer (Auckl).* 2010; 4: 35-41.
25. Dumenco L, Oguey D, Wu J, Messier N, Fausto N. Introduction of a Murine P53 Mutation Corresponding to Human Codon-249 into a Murine Hepatocyte Cell-Line Results in Growth Advantage, but Not in Transformation. *Hepatology.* 1995; 22: 1279-88.

26. Hu XG, Cheng WL, Wang T, Wang YL, Wang EK, Dong SJ. Fabrication, characterization, and application in SERS of self-assembled polyelectrolyte-gold nanorod multilayered films. *J Phys Chem B*. 2005; 109: 19385-9.
27. Orendorff CJ, Gearheart L, Jana NR, Murphy CJ. Aspect ratio dependence on surface enhanced Raman scattering using silver and gold nanorod substrates. *Phys Chem Chem Phys*. 2006; 8: 165-70.
28. Farah AM, Shooto ND, Thema FT, Modise JS, Dikio ED. Fabrication of Prussian Blue/Multi-Walled Carbon Nanotubes Modified Glassy Carbon Electrode for Electrochemical Detection of Hydrogen Peroxide. *Int J Electrochem Sc*. 2012; 7: 4302-13.
29. Rezende SM, Lijfering WM, Rosendaal FR, Cannegieter SC. Hematologic variables and venous thrombosis: red cell distribution width and blood monocyte count are associated with an increased risk. *Haematologica*. 2014; 99: 194-200.
30. Slowing II, Vivero-Escoto JL, Wu CW, Lin VSY. Mesoporous silica nanoparticles as controlled release drug delivery and gene transfection carriers. *Adv Drug Deliv Rev*. 2008; 60: 1278-88.
31. Hussain SM, Hess KL, Gearhart JM, Geiss KT, Schlager JJ. In vitro toxicity of nanoparticles in BRL 3A rat liver cells. *Toxicol In Vitro*. 2005; 19: 975-83.
32. Li P, Zhao QL, Wu LH, Jawaid P, Jiao YF, Kadowaki M, et al. Isofraxidin, a potent reactive oxygen species (ROS) scavenger, protects human leukemia cells from radiation-induced apoptosis via ROS/mitochondria pathway in p53-independent manner. *Apoptosis*. 2014; 19: 1043-53.

33. Krifka S, Spagnuolo G, Schmalz G, Schweikl H. A review of adaptive mechanisms in cell responses towards oxidative stress caused by dental resin monomers. *Biomaterials*. 2013; 34: 4555-63.

CHAPTER 7

TROPHOBLAST DERIVED CELLS BIOPHYSICAL AND BIOCHEMICAL CHANGES ON TiO₂ NT ARRAYS COATED WITH GOLD NANOPARTICLES (TiO₂ NTs-Au)

7.1 ABSTRACT

Trophoblast derived cells (TE) are interesting model of stem-like cell research for their regenerative properties, indefinite passage, and foreign DNA receptivity. In this work, vertically orientated TiO₂ nanotube (NT) arrays coated with gold nanoparticles were fabricated, and trophoblast cells were grown on the surface of these TiO₂ NT fabricated substrates. Fluorescence microscopy, Raman spectroscopy, and scanning electron microscopy were applied to study cell viability, cellular biochemical information and morphology of TE cells grown on TiO₂ NTs surface up to 30 days. This study will benefit efforts to design and fabricate new biomimetic materials for regenerative medicine, and provide new insight into the nature of trophoblast cells-nanotopography interaction.

7.2 INTRODUCTION

Titanium surfaces have been widely applied in clinical implantations for the purpose of bone, joint, or tooth replacements [1]. Compared with a non-textured titanium surface, a thin TiO₂ nanotube (NT) layer formed on Ti substrate has desirable bioactive (bone-growth) properties [2]. In recent years TiO₂ NT arrays have gained much attention as a potential biomaterial for their superior biocompatibility to induce specific cell responses.

TiO₂ NT surfaces with nanoscale spacing models can be utilized for size-dependent cellular response [3]. The nanostructure also offered nanoscale cues to enhance cellular

probing, cell sensing, and cell migration. For bovine aortic endothelial cells (BAECs) grown on TiO₂ NT, it is of benefit to probe the surface and interlock cellular extensions. Extracellular matrix (ECM) deposition and a more natural “vascular bed” were stimulated by TiO₂ NT, which also induced unidirectional cytoskeletons and more organized lamellipodia, indicating the TiO₂ nanotopography facilitated endothelialization and endothelial cell migration, evidenced especially in the raised formation of ECM and increased level of nitric oxide/endothelin ratio [4]. The size of TiO₂ NT also can regulate the differentiation of human mesenchymal stem cell (hMSC) towards an osteoblast lineage without osteogenic inducing factors. In a relatively confined diameter range (30 nm ~ 100 nm), TiO₂ NT size is correlated with the hMSC oriented differentiation vs. adhesion and growth [5]. Nanoscale TiO₂ surface topography is associated with the proliferation, vitality, and motility of mesenchymal stem cells (MSCs) and their differentiation to bone-forming cells was associated specifically with NT with diameters between 15 and 100nm [6]. It was reported that 15-nm TiO₂ NT can maximally induce the adhesion, proliferation, migration, and differentiation of MSCs, while 100-nm NT have the opposite effect, inducing cell death [3].

Cellular interactions with the extracellular matrix and other cells, are induced by integrins that regulate all major cellular activities including adhesion, differentiation, cellular shape changes, proliferation, migration, gene expression, and apoptosis in a synergistic approach with hormones and growth factors [7, 8]. Due to cell adhesion to the extracellular matrix, integrins cluster into focal adhesion complexes, causing activation of intracellular signaling cascades into the cytoskeleton and to the nucleus [9, 10]. Various kinds of proteins such as FAK, paxillin, tensin, p130Cas, and others are recruited by functional focal adhesion complexes, which grow in size and complexity with time of adhesion [9, 11]. On 15 nm TiO₂

NT the phosphorylation of focal adhesion kinase FAK and the ERK kinase was highest in growing stem cells, while lowest on 100 nm NT. The concentration and topography of cell adhesion sites in the extracellular matrix are critical for integrin clustering and activation [6].

Porcine trophoblast derived cells have possessed a feature of stem cell - self-renewal, and they are valuable tools for studying the molecular basis of early embryo physiology. In serum-free medium these cells grow in colonies that form domes, self-regenerate, and can be passaged indefinitely, but in serum medium these cells fail to self-regenerate, undergo wide-ranging morphological changes, and ultimately senesce. In this study, we designed and synthesized three-dimensional TiO₂ NT coated with gold nanoparticles (Au) to study the biochemical and morphological alterations of trophoblast-derived stem-like cells treated with serum and serum-free media grown on this substrate at different time points. This study provided the new insight into the trophoblast cell-nanotopography interaction that would be of benefit in the design and fabrication of new biomimetic materials for regenerative medicine.

7.3 HYPOTHESIS

Three-dimensional nanostructures have stronger effects on the morphological and functional development of TE cells over two-dimensional Petri dishes.

7.4 MATERIALS AND METHODS

7.4.1 Synthesis of TiO₂ and TiO₂ NT coated with gold nanoparticles

Anodization methods were applied to prepared TiO₂ NT arrays substrate. First titanium foils (0.5 mm thick, 99.6% purity, 1 cm × 1 cm, Alfa Aesar, Ward Hill, MA, USA) were immersed into acetone and ethanol for 30 min ultrasound in order to thoroughly

degrease. Then a solution consisting of HF:HNO₃:H₂O = 10:30:60 (vol%) was used to chemically polish titanium foils. The anodization solution was prepared with a mixture (90:10 vol%) of glycerol and deionized water (18.2 MΩ cm⁻¹). The cleaned titanium foils were anodized for 3 h using a two electrode electrochemical system with a platinum foil as the cathode at a constant potential (20 V) with a direct current power supply (Agilent Technologies, Santa Clara, CA, USA). After that the TiO₂ NTs substrate was annealed for 2 h at 400 °C.

To attach gold nanoparticles, the prepared TiO₂ NTs substrate was immersed in a 0.02 M SnCl₂ solution with concentrated HCL and deionized water for 5 min. After being rinsed with deionized water and ethanol, respectively, the air dried TiO₂ NTs substrate was immersed in a 0.02 M HAuCl₄ solution three times (each time 2 min) to deposit Au seeds onto the substrate by reduction. 0.10 M cetyltrimethyl ammonium bromide (CTAB), 2.5 × 10⁻⁴ M HAuCl₄ and 0.10 M freshly prepared ascorbic acid were mixed to make the growth solution. The treated substrate was immersed into growth solution for 2 min, then exposed to 30 min UV irradiation. After that the substrate was re-immersed into the growth solution in a 38 °C water bath for 16 h. Finally the substrates with gold particles were ready to be prepared for characterization and cell growth experiments.

7.4.2 Trophoblast-derived stem-like cell preparation

Porcine trophoblast-derived stem-like cells were processed as described previously [12]. Though no animals were used in the current experiments, the authors can assert that the cells utilized herein were collected in strict accordance with the animal welfare guidelines reviewed and approved by the Institutional Animal Care and Use Committee at Utah State University (Protocol #2239). Briefly, cells were harvested from pig embryos on gestational

day 13, dissociated into small clumps of cells using mechanical (vortex) and enzymatic (trypsin) means, and cultured in a defined (fetal bovine serum-free) medium at 39 °C with 5% CO₂ in air. The detailed formula of medium is in Table 7.1. The serum-free medium consists of 49% (v:v) Dulbecco's Modified Eagle Medium (DMEM; Corning/Mediatech; Manassas, VA, USA), 49% (v:v) Ham's F12 Nutrient Mixture (Corning), and 2% (v:v) B-27 Supplement (50X; Invitrogen, Carlsbad, CA, USA) supplemented with 20 ng/ml Epidermal Growth Factor (Sigma-Aldrich, St. Louis, MO, USA), 40 ng/ml FGF2 (Sigma-Aldrich), and 20 µg/ml gentamicin. Cells were cultured under these conditions until utilized for the experiments detailed here. Upon initiation of the current work, cells were subpassaged and plated onto the prepared TiO₂ NTs or TiO₂ NTs-Au substrate cell culture well inserts in either the serum-free medium mentioned earlier, or a presumptive 'differentiation' medium that consists of 85% (v:v) DMEM base medium, 15% (v:v) fetal bovine serum, 2 ng/ml FGF2, and 20 µg/ml gentamicin.

7.4.3 Fluorescence microscopy

Bright field and fluorescence images were collected by an Olympus IX71 inverted fluorescence microscope (Olympus America Inc., Center Valley, PA, USA) equipped with an Olympus DP30BW CCD camera using Olympus DP-BSW Controller and Manager Software. Images were acquired via a 10× lens (Olympus). LIVE/DEAD Viability/Cytotoxicity Assay Kit (Thermo Fisher Scientific, Waltham, MA, USA) was used to image cell viability.

7.4.4 Raman microspectroscopy

Raman spectra were recorded using a Renishaw inVia Raman spectrometer (Renishaw, Wotton-under-Edge, Gloucestershire, UK) equipped with a $63 \times 0.9\text{NA}$ water immersion objective (Leica Microsystems, Buffalo Grove, IL, USA) and a 785 nm near-IR laser. Cells cultured onto TiO_2 NT coated with gold nanoparticles were placed under the Raman microspectrometer. Cells were maintained in medium during Raman measurements. The wavenumber of $520.5 \pm 0.1 \text{ cm}^{-1}$ with silicon at a static spectrum was the standard calibration for the spectrometer. Spectra were then collected in static mode for 1 accumulation at 10 s laser exposure over a wavenumber range of 600–1800 cm^{-1} .

Cosmic rays of Raman spectra were removed by Renishaw Wire 3.3 software. Due to the interferences from background and other factors, mathematical approaches were employed to reduce systematic noise and amplify the signal of biochemical compositions in target cells.

7.4.5 Scanning electron microscope

The substrates were characterized by a Hitachi S4000 scanning electron microscopy (SEM, Hitachi America Ltd, Tarrytown, NY, USA). X-ray photo-electron spectroscopy (XPS) was performed with a Kratos Axis Ultra DLD instrument using a monochromatic Al $\text{K}\text{-}\alpha$ source. Powder X-ray diffraction (XRD, X'PertPRO/cubix PRO, PANalytical) was obtained using Cu $\text{K}\text{-}\alpha$ radiation.

7.5 RESULTS AND DISCUSSION

7.5.1 Characterization of TiO₂ NTs and TiO₂ NTs-Au substrates

The synthetic TiO₂ NTs had around 63 nm inner diameter (Figure 7.1A) and a 540 nm length (Figure 7.1B). It is reported that TiO₂ NTs with small diameter (~ 30 nm) can promote the adhesion of hMSC without affecting differentiation, while TiO₂ NTs with large diameter ((~ 70 to 100 nm) can induce hMSC selective differentiation into osteoblast-like cells [5]. In this study, TiO₂ NTs with ~63 nm diameter were selected to study the effect of 3D substrate on the growth of trophoblast cells.

Gold nanoparticles have been considered as biocompatible *in vitro* [13], and they are suitable candidates for nanomedicine because of their noncytotoxic, nonimmunogenic and good biocompatible properties. In addition, gold nanoparticles can be applied to enhance the Raman signal of reporter molecule [14]. To increase the biocompatibility and Raman signal, gold nanoparticles were coated onto the surface of TiO₂ NTs. It was found that the gold nanoparticles, randomly distributed on the surface of TiO₂ NTs (Figure 7.1C), were mainly hexagonal in shape with ~140 nm diameter (Figure 7.1D). The gold nanoparticles and gold cluster covered most of the TiO₂ NTs surface area. TiO₂ NTs-Au substrates were sterilized before culturing trophoblast-derived stem-like cells for further detection.

7.5.2 Biochemical analysis of trophoblast-derived stem-like cells grown on TiO₂ NTs-Au substrates

To evaluate cellular biochemical information on three-dimensional substrates, trophoblast-derived stem-like cells were seeded on TiO₂ NTs-Au substrates. TiO₂ NTs-Au substrates were chosen because gold nanoparticles on the surface of TiO₂ NTs could enhance the Raman signal from cells, while cells grown on TiO₂ NTs substrates only displayed the

signal from TiO₂ NTs substrates, as shown in Figure 7.2. For example, the Raman peak at 639 cm⁻¹ was from the TiO₂ NTs substrate (labelled with black dash line). However, cells grown on TiO₂ NTs-Au substrates exhibited the enhanced Raman peaks from cells.

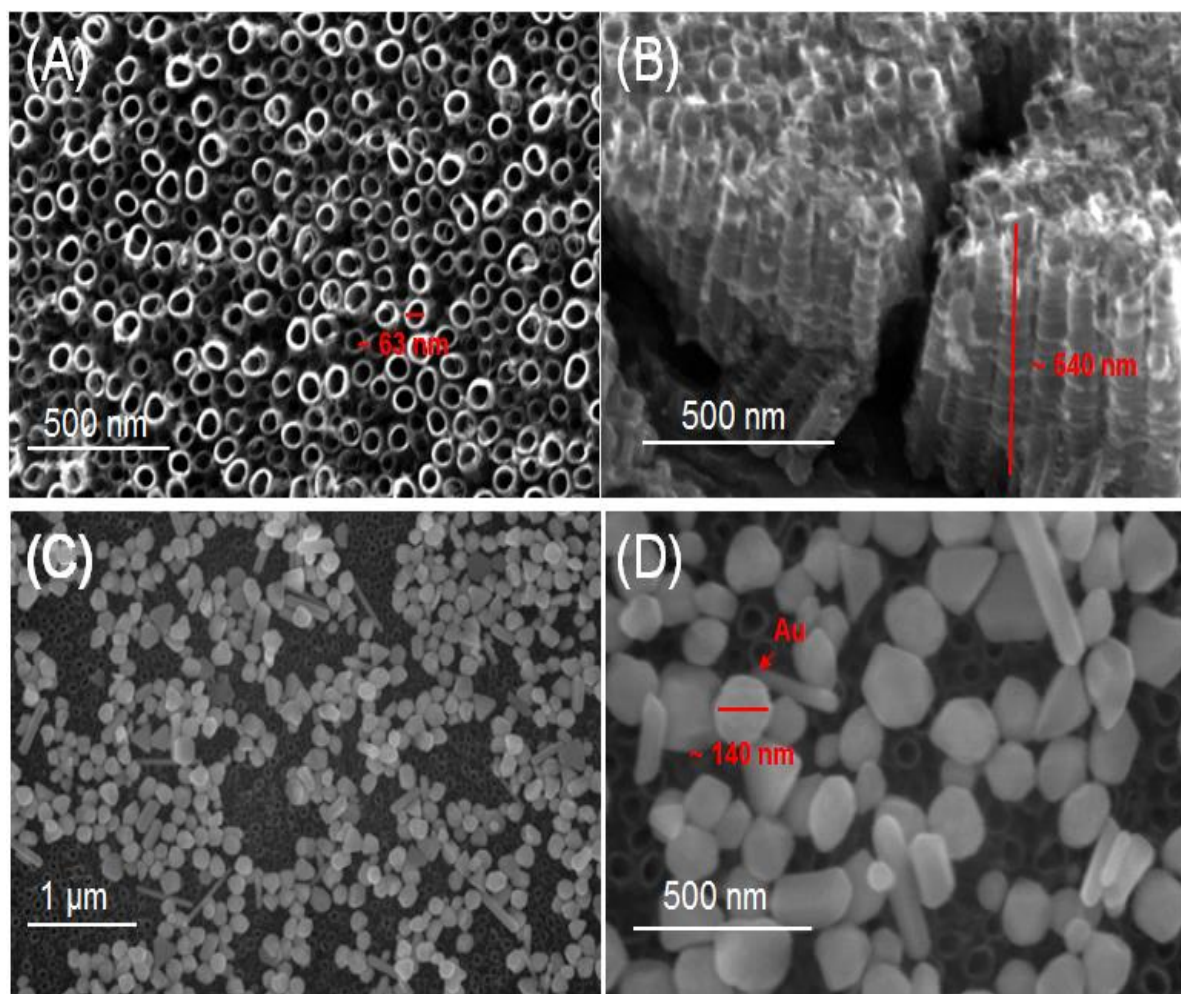


Figure 7.1 (A) The SEM top view of TiO₂ NTs, (B) cross section of TiO₂ NTs, (C) the top view of TiO₂ NTs-Au, (D) the enlarged top view of TiO₂ NTs-Au.

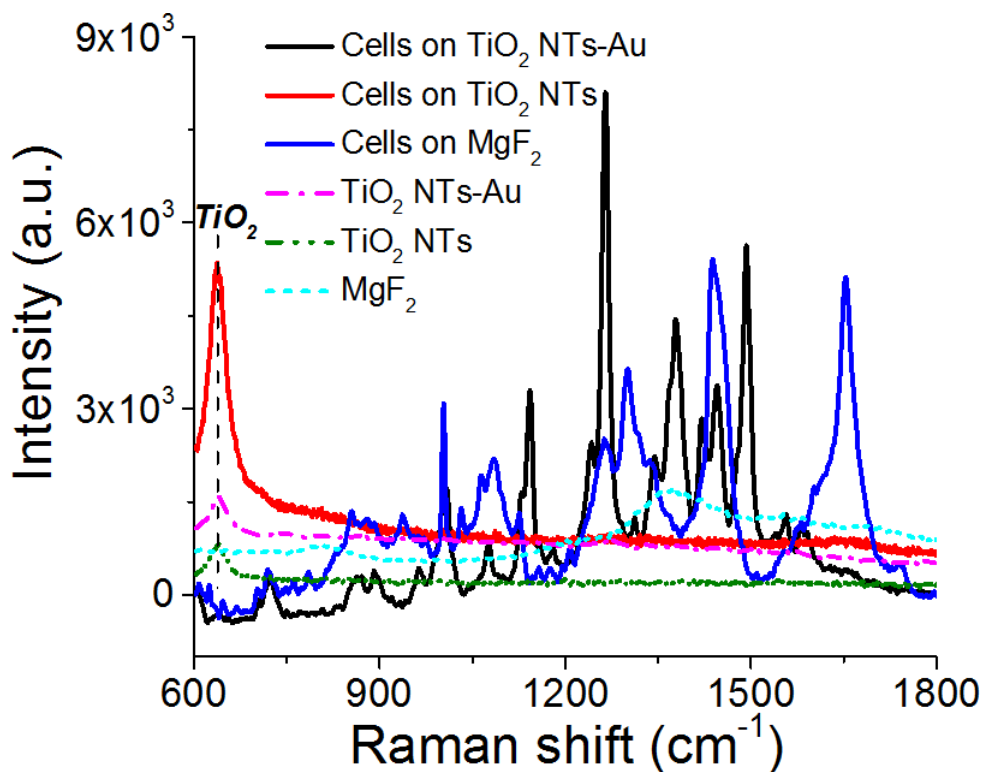


Figure 7.2 Raman spectra of trophoblast-derived stem-like cells grown on TiO₂ NTs-Au NPs, TiO₂ NTs and MgF₂ substrates (black dash line indicates the peak from TiO₂).

The smallest size of trophoblast cell was around 20 μm under undifferentiated status, so the cells of all groups covered the area coated with gold nanoparticles to receive enhanced Raman signal from cells. Raman average spectra of cells on TiO₂ NTs-Au at day 3, 5, 7, 10, 15 and 30 on serum-free and serum media were illustrated in Figure 7.3. The characteristic Raman peaks were labelled, and Raman signal was intensified because of the surface plasmon resonance effects from gold nanoparticles. The Raman spectra of both serum-free and serum groups at different days exhibited the characteristic peaks at 720 cm^{-1} (DNA), 854 cm^{-1} (Tyrosine), 1006 cm^{-1} (Phenylalanine), 1129 cm^{-1} (C-C skeletal stretch transconformation), 1158 cm^{-1} (Lipids and nucleic acids), 1213 cm^{-1} (Tyrosine, phenylalanine), 1260 cm^{-1} (Protein band), 1341 cm^{-1} (CH deformation (proteins and

carbohydrates)), 1374 cm^{-1} (Ring breathing modes of DNA/RNA), 1490 cm^{-1} (nucleic acids), 1582 cm^{-1} (Phenylalanine).

The difference between serum and serum-free groups was the Raman peak at 1446 cm^{-1} (CH_2 deformation (proteins & lipids)) as shown in Figure 7.3B. There was no Raman peak at 1446 cm^{-1} from day 3 to day 30 for cells with serum-free media groups. However, at day 7, 10 and 15 the Raman peak at 1446 cm^{-1} was more apparent on serum groups than serum-free groups, but decreased at day 3, 5 and 30 on serum groups. This Raman peak could be a potential biochemical marker to distinguish undifferentiated and differentiated trophoblast cells from day 7 to day 15.

Raman spectroscopy is able to monitor the biopolymer changes of trophoblast cells *in situ* and in real-time. It is reported that the Raman intensity of nucleic acids can be indicative of stem cells differentiation that the intensity of nucleic acids for differentiated stem cells is significantly less than that of undifferentiated cells [15, 16]. In this study, the most significant difference between differentiated and undifferentiated cells was the CH_2 deformation (proteins & lipids) indicated by Raman peak at 1446 cm^{-1} . This observation was different from above reported stem cells research, and the reasons may be accounted for the differences in cell type and the effect of substrate (TiO_2 NTs-Au) used in this study.

7.5.3 Cell viability analysis of trophoblast-derived stem-like cells grown on TiO_2 NTs-Au substrates

As shown in Figure 7.4, viabilities of the TE cells grown on TiO_2 NTs-Au at day 3, 5, 7, 10, 15 and 30 on serum and serum-free media (green: live; red: dead; scale bar: $100\text{ }\mu\text{m}$) were compared. Firstly the cells on both media were alive among 30 days, suggesting the good biocompatibility of TiO_2 NTs-Au substrates. Secondly the size of cells in serum-free

medium (Figure 7.4A) was less than that of cells in serum medium (Figure 7.4B), suggesting that cells in serum-free media still maintained undifferentiated state up to 30 days. However, the size of cells in serum medium was larger and more stretched over time as compared with cells in serum-free medium.

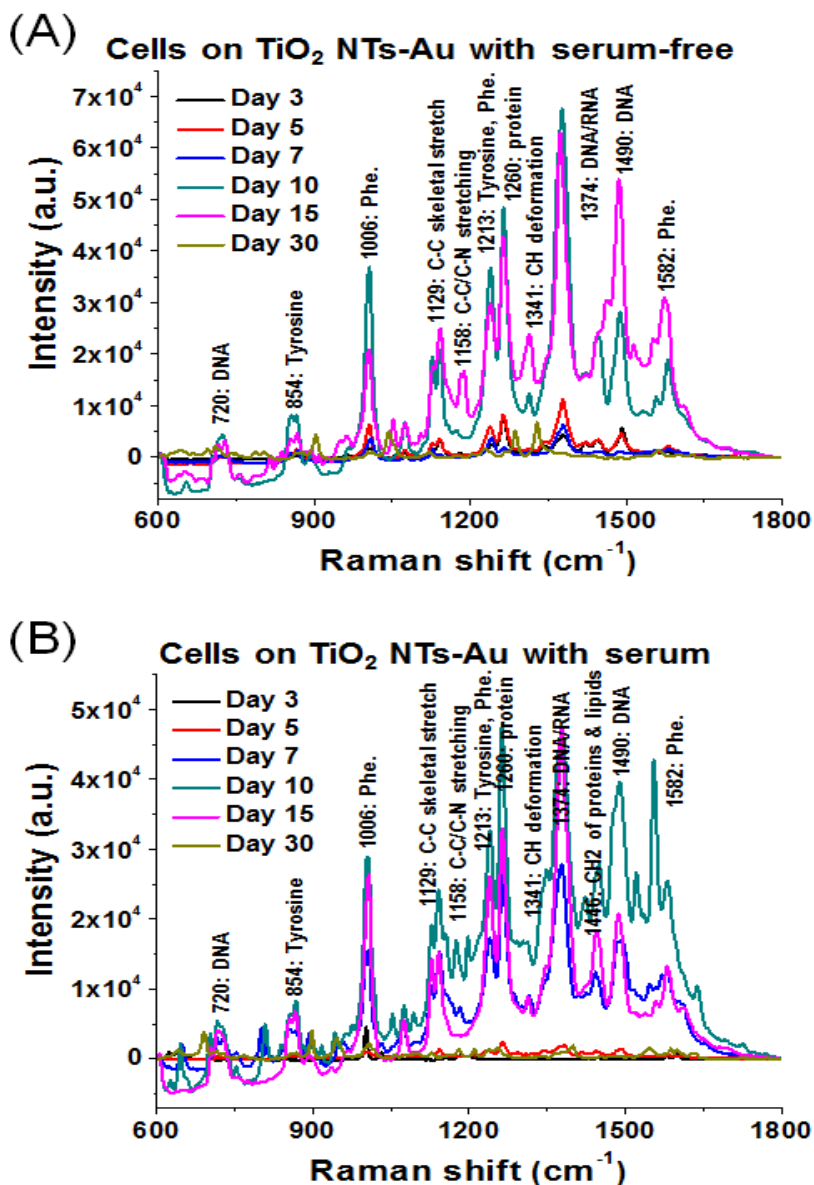


Figure 7.3 Raman spectra of trophoblast-derived stem-like cells on TiO₂ NTs-Au at day 3, 5, 7, 10, 15 and 30 on (A) serum-free and (B) serum media.

Previous study reported that the adhesion of hMSC grown on TiO₂ NTs with small diameter can be increased, and the differentiation of hMSC grown on TiO₂ NTs with large diameter can be facilitated [5]. In this study the TiO₂ NTs-Au substrates affected little on cellular morphology and differentiation, and the reasons may be the diameter of TiO₂ NTs used in this work which was between 30 nm to 100 nm, gold nanoparticles coating, cell line differences or the role of culture medium. Thus, these observations indicated the good biocompatibility of substrate and limited impact on cellular morphology and differentiation.

7.5.4 Morphological characterization of trophoblast-derived stem-like cells grown on different substrates

To compare the influence from substrates on cellular structure, three substrates (TiO₂ NTs-Au NPs, TiO₂ NTs and flat Petri dish substrate as control), one time point (3 days) and one medium type (serum-free medium) were selected. Trophoblast cells with similar cell density were seeded on these three substrates with serum-free medium. After three days, cells were fixed first and then imaged by SEM to visualize the morphological changes.

Figure 7.5 illustrated the SEM images of trophoblast cell grown on TiO₂ NTs-Au NPs (A), TiO₂ NTs (B) and Petri dish (C). Firstly it was observed that cells grown on three-dimensional TiO₂ NTs-Au NPs and TiO₂ NTs substrates presented more cellular structures, like more filaments, compared to cells grown on flat Petri dish. In addition, there were lots of cytoskeleton structures expanded along the substrates for cells grown on three-dimensional substrates. Together, these observations from SEM images indicated that cells grown on three-dimensional substrates may undergo more aggressive proliferative process as compared with cells on flat Petri dish in the same medium.

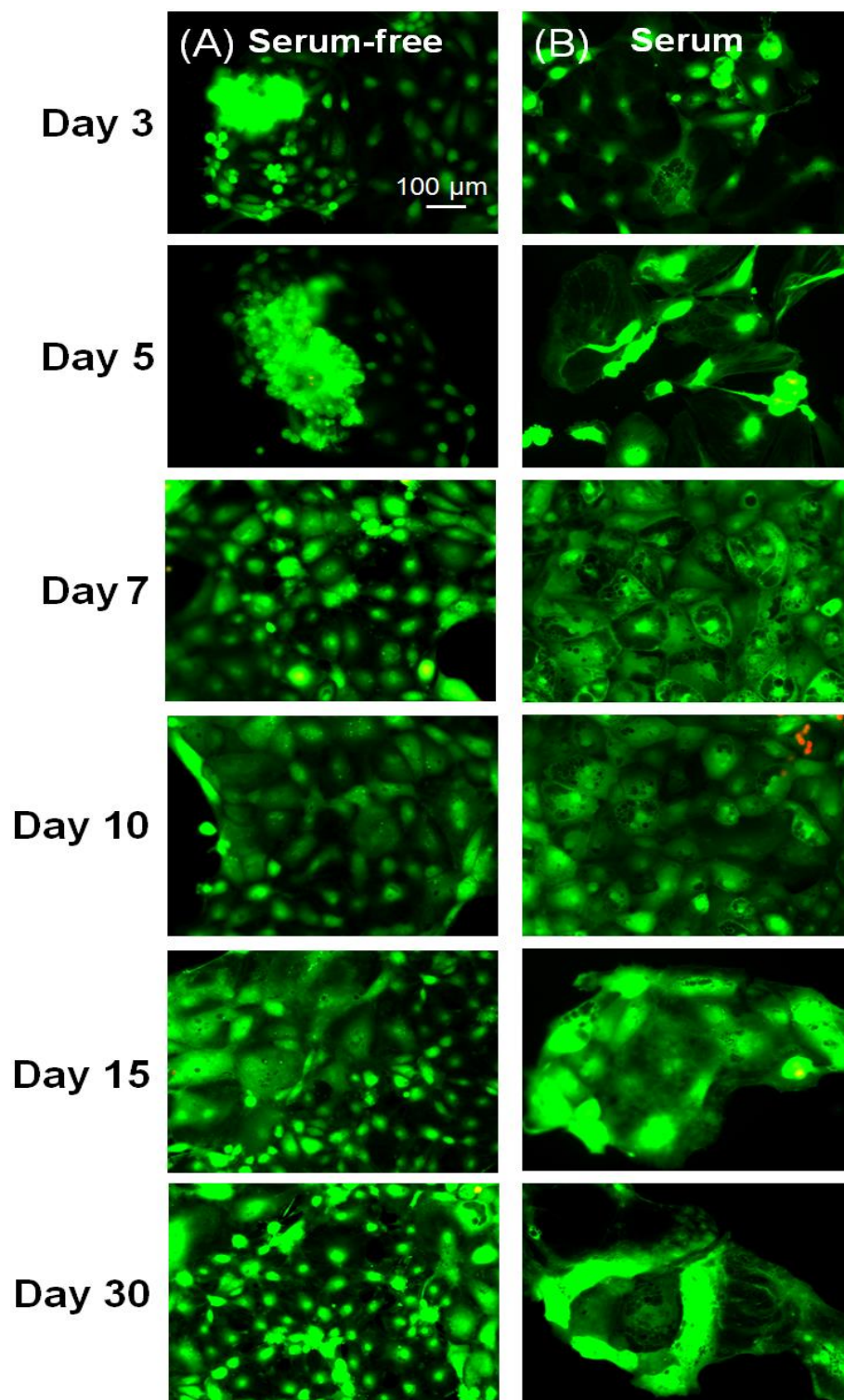


Figure 7.4 Cell viability of trophoblast-derived stem-like cells on TiO₂ NTs-Au at day 3, 5, 7, 10, 15 and 30 on (A) serum-free and (B) serum media (green: live; red: dead; scale bar: 100 μm).

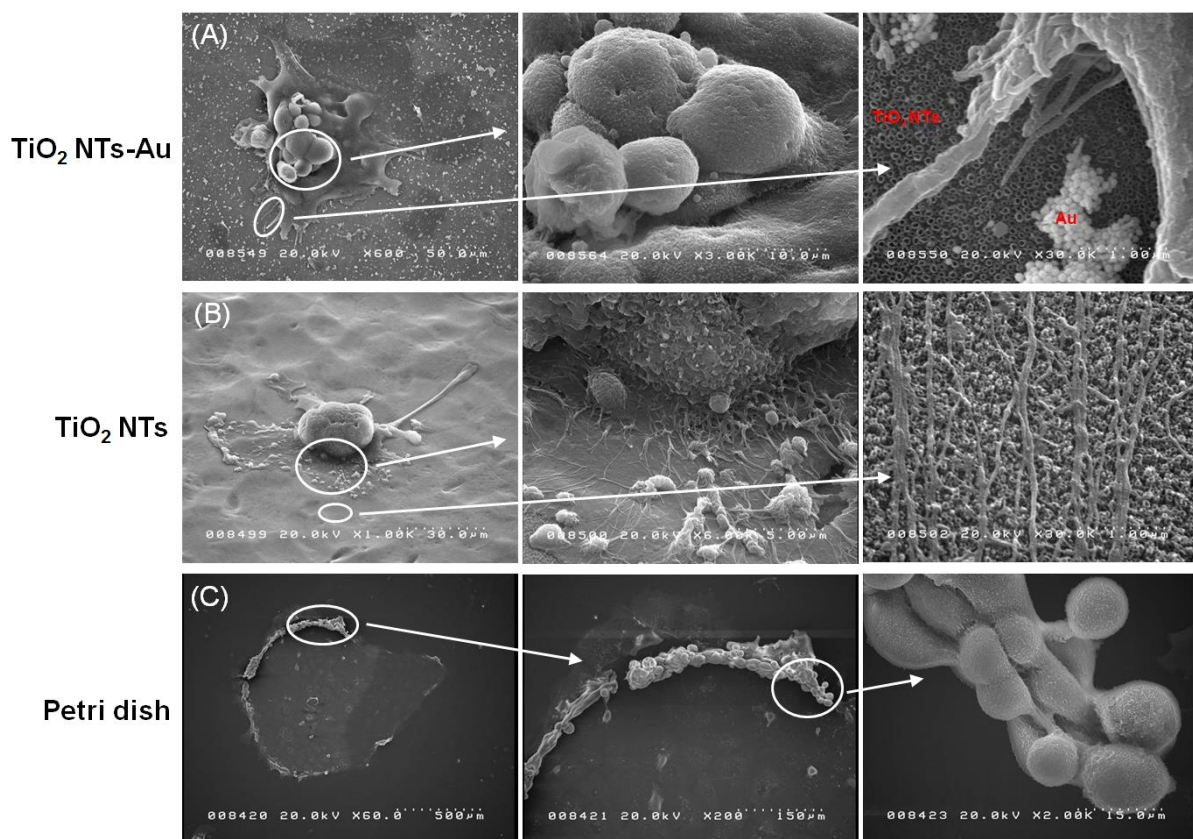


Figure 7.5 SEM images of trophoblast-derived stem-like cells on (A) TiO₂ NTs-Au NPs, (B) TiO₂ NTs and (C) Petri dish substrate (Cells were grown in serum-free medium).

Research conducted by Schmuki *et al.* reported that cell adhesion and spreading were increased for nanotube diameters between 15 and 30 nm, while cell activities were reduced for diameters larger than 50 nm, and the diameter of nanotube played more dominant role than surface modification onto the nanotube in affecting cellular function [17]. From our observation (SEM images), the activity of trophoblast cells did not exhibit obvious decay, which was different from Schmuki *et al.* finding [17]. However, it was found that trophoblast cells grown on three-dimensional TiO₂ NTs-Au NPs and TiO₂ NTs substrates both possessed more filaments, compared to cells grown on the flat Petri dish.

Thus, the SEM results showed that cells grown on nanostructures had more cellular filaments, suggesting more vigorous interaction with substrates during the growth and attachment, compared to cells grown on the flat Petri dish, implying that three-dimensional substrates played an important role in the development of cellular morphology, cytoskeleton and function under similar conditions. These observations motivated us to seek other biology method, like qPCR or gene microarray, to examine the ECM-related gene expression that may help understand the molecular mechanisms of TE cells-TiO₂ NTs interaction.

7.6 CONCLUSIONS

In this work we evaluated the behavior of trophoblast cells on nanoscale topographies of TiO₂ NTs. We developed aligned TiO₂ NTs layers with ~63 nm diameter and TiO₂ NTs coated with ~140 nm gold nanoparticles on the surface to explore the influence of surface structures. Cells grown on TiO₂ NTs substrates only displayed the Raman peak from TiO₂. To study the biochemical information on three-dimensional substrates, trophoblast cells were grown on TiO₂ NTs-Au substrates because gold nanoparticles can enhance the Raman signal from cell. It was found that the most significant difference between differentiated and undifferentiated cells was the Raman peak at 1446 cm⁻¹ (CH₂ deformation (proteins & lipids)), and this Raman peak could be a potential biochemical marker to distinguish undifferentiated and differentiated trophoblast cells grown on TiO₂ NTs-Au NPs substrates from day 7 to day 15. In addition, cell viability results showed that cells would be alive on TiO₂ NTs-Au NPs substrates up to 30 days, demonstrating the good biocompatibility of fabricated substrates. SEM images of trophoblast cells grown on three different substrates (TiO₂ NTs-Au NPs, TiO₂ NTs and Petri dish substrate) were compared, and it was found that cells grown on TiO₂ NTs-Au and TiO₂ NTs substrates both had more cellular filaments and

more spread on substrates. Integrin may play important roles in the morphological and functional differences of trophoblast cells grown on three-dimensional nanostructures or two-dimensional Petri dishes. The predicted size of an integrin heterodimer is about 10 nm diameter [18]. It is reported that a 15-20 nm spacing of nanotubes will force integrin clustering into the closest packing, resulting in integrin activation, and the activation of integrin-mediated signaling pathways induced by nanotubes could control cell proliferation, migration, differentiation, and cell survival [6]. In conclusion, this study would benefit to design and fabricate new biomimetic materials for regenerative medicine and tissue engineering, providing new understanding of the trophoblast cells-nanotopography interaction.

7.7 REFERENCES

1. Linder L, Carlsson A, Marsal L, Bjursten LM, Branemark PI. Clinical aspects of osseointegration in joint replacement. A histological study of titanium implants. *J Bone Joint Surg Br.* 1988; 70: 550-5.
2. Satsangi A, Satsangi N, Glover R, Satsangi RK, Ong JL. Osteoblast response to phospholipid modified titanium surface. *Biomaterials.* 2003; 24: 4585-9.
3. Park J, Bauer S, Schlegel KA, Neukam FW, von der Mark K, Schmuki P. TiO₂ nanotube surfaces: 15 nm--an optimal length scale of surface topography for cell adhesion and differentiation. *Small.* 2009; 5: 666-71.
4. Brammer KS, Oh S, Gallagher JO, Jin S. Enhanced cellular mobility guided by TiO₂ nanotube surfaces. *Nano Lett.* 2008; 8: 786-93.
5. Oh S, Brammer KS, Li YS, Teng D, Engler AJ, Chien S, et al. Stem cell fate dictated solely by altered nanotube dimension. *Proc Natl Acad Sci U S A.* 2009; 106: 2130-5.

6. Park J, Bauer S, von der Mark K, Schmuki P. Nanosize and vitality: TiO₂ nanotube diameter directs cell fate. *Nano Lett.* 2007; 7: 1686-91.
7. Burridge K, Chrzanowska-Wodnicka M. Focal adhesions, contractility, and signaling. *Annu Rev Cell Dev Biol.* 1996; 12: 463-518.
8. Giancotti FG. A structural view of integrin activation and signaling. *Dev Cell.* 2003; 4: 149-51.
9. Schlaepfer DD, Hauck CR, Sieg DJ. Signaling through focal adhesion kinase. *Prog Biophys Mol Biol.* 1999; 71: 435-78.
10. DeMali KA, Wennerberg K, Burridge K. Integrin signaling to the actin cytoskeleton. *Curr Opin Cell Biol.* 2003; 15: 572-82.
11. Mitra SK, Hanson DA, Schlaepfer DD. Focal adhesion kinase: in command and control of cell motility. *Nat Rev Mol Cell Biol.* 2005; 6: 56-68.
12. Suasnavas EA, Heywood S, Ward A, Cox L, O'Grady M, Zhao YF, et al. Isolation and characterization of trophoblast-derived stem-like cells from peri-implantation porcine embryos. *Anim Reprod Sci.* 2015; 154: 128-41.
13. Sperling RA, Rivera Gil P, Zhang F, Zanella M, Parak WJ. Biological applications of gold nanoparticles. *Chem Soc Rev.* 2008; 37: 1896-908.
14. Eustis S, El-Sayed MA. Why gold nanoparticles are more precious than pretty gold: Noble metal surface plasmon resonance and its enhancement of the radiative and nonradiative properties of nanocrystals of different shapes. *Chem Soc Rev.* 2006; 35: 209-17.
15. Nottingher L, Bisson I, Polak JM, Hench LL. In situ spectroscopic study of nucleic acids in differentiating embryonic stem cells. *Vib Spectrosc.* 2004; 35: 199-203.

16. Notingher I, Bisson I, Bishop AE, Randle WL, Polak JMP, Hench LL. In situ spectral monitoring of mRNA translation in embryonic stem cells during differentiation in vitro. *Anal Chem.* 2004; 76: 3185-93.
17. Bauer S, Park J, Faltenbacher J, Berger S, von der Mark K, Schmuki P. Size selective behavior of mesenchymal stem cells on ZrO₂ and TiO₂ nanotube arrays. *Integr Biol.* 2009; 1: 525-32.
18. Takagi J, Petre BM, Walz T, Springer TA. Global conformational rearrangements in integrin extracellular domains in outside-in and inside-out signaling. *Cell.* 2002; 110: 599-611.

CHAPTER 8

SUMMARY AND FUTURE DIRECTION

8.1 SUMMARY

The focus of this dissertation is on *in vitro*, non-invasive imaging and detection of single living mammalian cells interacting with bio-nano-interfaces. We studied the biophysical and biochemical alterations and cellular responses of mammalian cells (e.g. human cancer cells and porcine trophoblast-derived stem-like cells) upon external stimuli (e.g. anticancer drug, diesel exhaust particles, antioxidant, nanoparticles, serum-free media and nanotubes). This dissertation research of six technical chapters (chapter 2-7) can be summarized as follows:

- Classification of differentiated and undifferentiated trophoblast-derived stem-like cells grown on Petri dish by biomechanical, biochemical and genetic properties.
- Single living cell imaging, biomechanical and biochemical detection and cellular responses measurement upon different treatments.
- Development and synthesis of multifunctional hybrid nanoparticles with the functions of fluorescence, SERS and photothermal properties for different cancer biomarkers detection and specifically targeting cancer cells for PTT.
- Development and synthesis of three-dimensional TiO₂ nanotubes coated with Au to study the morphological and biochemical alterations of trophoblast-derived stem-like cells grown on this substrate.

In chapter 2, AFM, RM and qPCR were applied to distinguish between undifferentiated and differentiated trophoblast-derived stem-like cells grown on Petri dish.

Cellular biomechanical, biochemical changes were measured and cellular biophysical and biochemical properties can be used as differentiation markers to classify cellular differentiation.

In Chapter 3, the responses of five cancer cells with and without BRMS1 (MDA-MB-231, MDA-MB-435, MDA-MB-231/BRMS1, MDA-MB-435/BRMS1 and A549 cells) treated with anticancer drug (Doxorubicin) were studied by a multimodal approach. It was found that BRMS1 expression changes cellular biochemical and biomechanical properties. BRMS1 expression induces a differential biomechanical response when interacting with 4 h DOX. Cancer cells with or without BRMS1 show similar biochemical changes upon DOX treatment. ROS, apoptosis expression and cell viability changes of five cells display a similar pattern from control to 24 h DOX exposure, indicating that BRMS1 has no effect on cellular chemoresistance.

In chapter 4, diesel exhaust particles (DEP) and an antioxidant resveratrol (RES) were treated with cells to study the destructive effect from DEP and protective function from RES by measuring cellular biophysical and biomechanical changes as well as cellular plasma membrane potential and cell cycles. It was found that RES can alleviate DEP damage on cellular structure and increase DEP-induced biomechanical changes. In addition, RES could significantly prevent hyperpolarization of A549 cells, increase DEP-induced ROS generation and change DEP-induced cell cycle.

In chapter 5, a hybrid nanoparticle with the properties of fluorescence imaging, SERS detection and PTT was synthesized for single living cell analysis of epidermal growth factor receptor (EGFR) and specifically killing cancer cells with high EGFR expression. Fluorescence images demonstrated fluorescence function of NPs with fluorescence at 615 nm

($^5D_0 \rightarrow ^7F_2$) on excitation ~ 464 nm. The distribution of EGFR on single living cell was visualized by SERS mapping. These NPs effectively suppressed A549 cell viability upon 808 nm laser irradiation with good biocompatibility.

In chapter 6, silica coated nanoparticles conjugated with anti-human epidermal growth factor receptor 2 (HER2) antibody were developed to increase surface area, light-heat conversion efficiency and biocompatibility, applying for fluorescence imaging, SERS detection and PTT. SERS mapping demonstrated the distribution of HER2 on single living cell with HER2 expression. These NPs can kill 435 cells upon 808 nm laser irradiation with better biocompatibility. These NPs have the potential for cancer diagnostics, treatment and therapy.

In chapter 7, a three-dimensional TiO₂ NTs with or without Au substrate was synthesized for trophoblast-derived stem-like cell growth. The cell viability, morphology and biochemical changes were analyzed.

8.2 FUTURE DIRECTIONS

8.2.1 AFM/RM system combined with traditional biological methods to characterize cells

The biophysical and biochemical changes were detected in this dissertation by AFM/RM system in a non-invasive way, demonstrating the advantage of AFM/RM system for single living cell biomechanics and biopolymers characterization. AFM/RM system, as a novel technique, should be complementary with the conventional biological approaches (e. g. western blot, PCR, flow cytometry) to provide additional cell information for us to analyze. For example, AFM measures the biophysical properties (topography, Young's modulus,

adhesion force) of single living cell. Cellular biomechanics should also be measured in a large-scale way to make the AFM results more conclusive, although large-scale measurement of living cells biomechanics is not available currently. Alternatively, cytoskeleton can be recorded by fluorescence imaging, and cellular biophysical information collected from AFM and fluorescence imaging can be compared, even cells will be fixed first before fluorescence imaging. Darling *et al.* have applied AFM to detect the elastic and viscoelastic properties of undifferentiated adipose-derived stem cells (ASCs), combining with the detection of lineage-specific metabolite production to purify tissue-specific cells for cell-based regenerative therapies [1].

RM can record the biochemical information of single living cell without any label by characteristic Raman peak collection. Traditional methods, like flow cytometry or qPCR were incorporated to detect the cell responses or genetic changes, trying to find the connection between cellular biocomponent changes and cellular responses. Turner *et al.* have found that undifferentiated human embryonic stem cells possess higher Raman intensities of nucleic acids than differentiated cells; conversely, differentiated cells have more protein-related Raman intensities than undifferentiated cells [2]. These differences were associated with the cellular biopolymers changes that specifically overlapped with collagen, proline and hydroxyproline, consistent with *Coll1a1* gene downregulation in stem cells [3].

In summary, AFM/RM system has the advantage of single living mammalian cell detection, providing additional information for further characterization of biological systems compared with traditional biological techniques. Therefore, AFM/RM system combining conventional biological techniques is still a future research direction.

8.2.2 Application of hybrid nanoparticles with good biocompatibility

In chapter 5 and chapter 6, our laboratory developed two hybrid nanoparticles conjugated with two different antibodies (CaMoO₄:Eu@Au conjugated with EGFR antibodies and Silica coated CaMoO₄:Eu@GNR conjugated with HER2 antibodies). These hybrid nanoparticles can be applied to locate the distribution of these receptors at single living cell level by RM because of the surface plasmon resonance effect from metallic nanoparticles (GNR).

One future direction in this part is multiplex imaging. By modifying these hybrid nanoparticles with different antibodies, we can measure the interaction between receptors on single living cells. For example, one ongoing project in our laboratory is to apply multiplex SERS detection to track two receptors (GPR120 and CD36) and their interaction because these two receptors play a critical role in the chemoreception of fatty acids, which is important to the research area of obesity therapy.

Another future direction is nanoparticle based therapy (e. g. photothermal therapy (PTT); photodynamic therapy (PDT); drug delivery and controlled release). The hybrid nanoparticles of chapter 4 and chapter 5 were applied for PTT after confirming the specific targeting of cancer cells. By external laser irradiation, the temperature of hybrid nanoparticles rapidly increases, suppressing the viability of cancer cells by hyperthermia. Similarly, the PDT effect of selectively killing diseased cells comes from the photosensitizer to produce reactive oxygen species (ROS) by an appropriate light source irradiation. Application of hybrid nanoparticles in this area can increase PDT efficiency due to the surface area increase. PTT and PDT can be combined to more effectively kill diseased cells due to the synergistic effect. Additional, drug molecules can be loaded into a porous

nanostructure as a carrier for deliver and controlled release. By nanostructure modification, the drug molecule can be released at target environment (e. g. cancer thrives in an acidic environment).

These nanostructures must be biocompatible for the human body before the above applications. So far, we tested the effect of hybrid nanoparticles on cell viability, apoptosis, cell cycle and ROS level *in vitro*. To apply these hybrid nanoparticles *in vivo*, we need to conduct more experiments (e.g. white blood cell count; distribution and stability of nanoparticles in body, retention time) in the future.

8.2.3 Fate control of stem-like cell by substrate modification

In chapter 7, three-dimensional TiO₂ nanotubes with or without Au substrates were synthesized for trophoblast-derived stem-like cell growth. One future research in this direction is to find the potential correlations between structure, function and mechanisms of cells interacting with nano-interfaces. Previous studies have reported that the size of TiO₂ nanotubes can affect the differentiation, proliferation and migration of stem cells [4]. However, few literature reported about the biochemical and genetic changes of stem cells grown on these nanostructures, and that is the direction we are planning to do in the future.

Another future research on TiO₂ nanotubes is to load growth factor or molecules into the nanotubes to direct the growth of trophoblast-derive stem-like cells growth. It is reported that TiO₂ nanotubes can integrate polymer micelles as drug nanocarriers to load more poorly water soluble drugs [5], which opens the door for the application of controlling the development of stem cells by modifying the surface of nanotubes with different molecules.

In summary, the future direction is the fate control of trophoblast-derive stem-like cells by modifying the size of three-dimentional TiO₂ nanotubes, coating chemicals or loading molecules into nanotubes.

8.3 REFERENCES

1. Gonzalez-Cruz RD, Fonseca VC, Darling EM. Cellular mechanical properties reflect the differentiation potential of adipose-derived mesenchymal stem cells. *Proc Natl Acad Sci U S A*. 2012; 109: E1523-E9.
2. Schulze HG, Konorov SO, Caron NJ, Piret JM, Blades MW, Turner RFB. Assessing Differentiation Status of Human Embryonic Stem Cells Noninvasively Using Raman Microspectroscopy. *Anal Chem*. 2010; 82: 5020-7.
3. Palmqvist L, Glover CH, Hsu L, Lu M, Bossen B, Piret JM, et al. Correlation of murine embryonic stem cell gene expression profiles with functional measures of pluripotency. *Stem Cells*. 2005; 23: 663-80.
4. Park J, Bauer S, Schlegel KA, Neukam FW, von der Mark K, Schmuki P. TiO₂ nanotube surfaces: 15 nm--an optimal length scale of surface topography for cell adhesion and differentiation. *Small*. 2009; 5: 666-71.
5. Aw MS, Simovic S, Addai-Mensah J, Losic D. Polymeric micelles in porous and nanotubular implants as a new system for extended delivery of poorly soluble drugs. *J Mater Chem*. 2011; 21: 7082-9.

APPENDIX

**Corporate Information**[Core Businesses](#)[Directors and Officers](#)[History](#)[Locations](#)[Corporate Governance](#)[Business Conduct and Ethics Policy](#)[Corporate Giving](#)[Wiley Foundation](#)[Logos and Graphic Identity](#)**[Rights & Permissions](#)****[Permissions & Reprints](#)**[Accessibility](#)[Subsidiary Rights Licenses](#)[Internet Resources](#)[Home](#) / [Corporate Information](#) / [Rights & Permissions](#)

Permissions & Reprints

The quick and easy way to clear permissions via RightsLink®, the Copyright Clearance Center's online service

You can now obtain permission to reproduce or make copies of Wiley content, for commercial or non-commercial re-use, directly from the point of content on Wiley's websites.

For journal or online book content please locate the material you wish to reuse on [Wiley Online Library](#). For all other Wiley book content, please locate the title www.wiley.com.

This service is also available for [The Cochrane Library](#).

Please follow the easy instructions below:

- Click on the 'Request Permission' link on the content you wish to reproduce
- Follow the online instructions and select your requirements from the drop down options to gain a 'quick quote'
- Create a RightsLink® account to complete and pay for your transaction (if you do not already have one)
- Read and accept our Terms & Conditions and Download your license

For further information please view the [RightsLink® Slideshow](#).

Please note that some content will not contain the Permissions link. To request permission for this content, or for any Wiley content that is not available online please contact us directly at the address below or complete the online [request form](#).

Wiley Authors

[Authors who publish in any Wiley title retain a wide range of reproduction rights without having to ask our permission.](#) Please refer to your Copyright Transfer Agreement for journal articles or your book contract. If you require a formal republication license for your material, you may obtain this online using the Rightslink® service.

Educational institutions and Course material requests

Requests can be cleared using RightsLink®, but if you're an instructor/professor who has adopted (required) a book for your course and wishes to use content or ancillary material for your course, if the book will not arrive before the start of your semester, or you are located outside the United States please complete the [Educational Request Form](#). Or contact us directly at:

Permissions Department
John Wiley & Sons Inc.
111 River St. MS 4-02
Hoboken, NJ 07030-5774
Email: permissions@wiley.com

Fax: (201) 748-6008

Copyright Clearance Center

<http://www.wiley.com/WileyCDA/Section/id-403426.html>

Permission Letter

Edison Suasnavas
Department of Animal, Dairy & Veterinary Sciences
Utah State University
Logan, UT 84322-4815

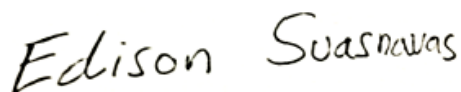
September 22, 2015

Qifei Li
Department of Biological Engineering
Utah State University
Logan, UT 84322-4105

This letter grants my permission to Qifei Li to use the following publication in part or in full for inclusion in his Ph.D. dissertation.

Qifei Li, E. Suasnavas, L. Xiao, S. Heywood, X. Qi, A. Zhou*, S. C. Isom*, "Label-free and non-invasive monitoring of porcine trophoblast derived cells: differentiation in serum and serum-free media". *J. of Biophotonics* 8 (2015) 638-645.

Sincerely,

A handwritten signature in black ink that reads "Edison Suasnavas". The signature is written in a cursive, slightly slanted style.

Edison Suasnavas

Permission Letter

Lifu Xiao
Department of Biological Engineering
Utah State University
Logan, UT 84322-4205

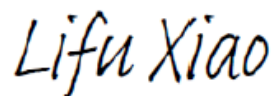
September 22, 2015

Qifei Li
Department of Biological Engineering
Utah State University
Logan, UT 84322-4105

This letter grants my permission to Qifei Li to use the following publication in part or in full for inclusion in his Ph.D. dissertation.

Qifei Li, E. Suasnavas, L. Xiao, S. Heywood, X. Qi, A. Zhou*, S. C. Isom*, "Label-free and non-invasive monitoring of porcine trophoblast derived cells: differentiation in serum and serum-free media". *J. of Biophotonics* 8 (2015) 638-645.

Sincerely,

A handwritten signature in black ink that reads "Lifu Xiao". The script is cursive and fluid.

Lifu Xiao

Permission Letter

Sierra Heywood
Department of Animal, Dairy & Veterinary Sciences
Utah State University
Logan, UT 84322-4815

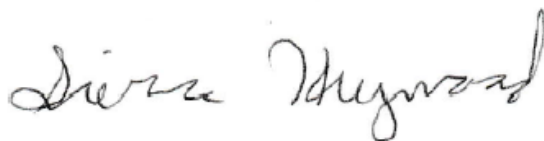
September 22, 2015

Qifei Li
Department of Biological Engineering
Utah State University
Logan, UT 84322-4105

This letter grants my permission to Qifei Li to use the following publication in part or in full for inclusion in his Ph.D. dissertation.

Qifei Li, E. Suasnavas, L. Xiao, S. Heywood, X. Qi, A. Zhou*, S. C. Isom*, "Label-free and non-invasive monitoring of porcine trophoblast derived cells: differentiation in serum and serum-free media". *J. of Biophotonics* 8 (2015) 638-645.

Sincerely,

A handwritten signature in black ink that reads "Sierra Heywood". The signature is written in a cursive, flowing style.

Sierra Heywood

Permission Letter

Dr. Xiaojun Qi

Professor

Department of Computer Science

Utah State University

Logan, UT 84322-4205


September 22, 2015

Qifei Li
Department of Biological Engineering
Utah State University
Logan, UT 84322-4105

This letter grants my permission to Qifei Li to use the following publication in part or in full for inclusion in his Ph.D. dissertation.

Qifei Li, E. Suasnavas, L. Xiao, S. Heywood, X. Qi, A. Zhou*, S. C. Isom*, "Label-free and non-invasive monitoring of porcine trophoblast derived cells: differentiation in serum and serum-free media". *J. of Biophotonics* 8 (2015) 638-645.

Sincerely,



Xiaojun Qi

Permission Letter

Dr. S. Clay Isom

Assistant Professor

Department of Animal, Dairy & Veterinary Sciences

Utah State University

Logan, UT 84322-4815

September 22, 2015

Qifei Li
Department of Biological Engineering
Utah State University
Logan, UT 84322-4105

This letter grants my permission to Qifei Li to use the following publication in part or in full for inclusion in his Ph.D. dissertation.

Qifei Li, E. Suasnavas, L. Xiao, S. Heywood, X. Qi, A. Zhou*, S. C. Isom*, "Label-free and non-invasive monitoring of porcine trophoblast derived cells: differentiation in serum and serum-free media". *J. of Biophotonics* 8 (2015) 638-645.

Sincerely,



S. Clay Isom

CURRICULUM VITAE

Qifei Li

Address: 1379E 1000N, SU304EF, Logan UT 84321
Phone: +1 (435) 881-3337
Email: qifei.li@aggiemail.usu.edu or lee_qifei@hotmail.com
LinkedIn: <https://www.linkedin.com/pub/qifei-li/3a/573/665>

EDUCATION:

Degree	Year	Institute	GPA
PhD. Biological Engineering	Attending	Utah State University, Utah, USA	3.69/4
PhD. Medical Genetics (transferred)	2010-11	State Key Laboratory of Medical Genetics, China	85.4/100
B.Sc. in Biological Science	2006-10	Central South University, China	87.9/100

RESEARCH EXPERIENCE / SUMMER TRAINING:

- **Molecular and Cellular Sensing and Imaging Laboratory (Aug'11- present)**

Dr. Anhong Zhou, Department of Biological Engineering, Utah State University, Logan, UT.

RESEARCH: working on the biophysical and biochemical alterations of cells (e.g. human cancer cells, human hepatocyte cell, porcine trophoblast cell and mouse stem cell) upon context changes (e.g. anticancer drug, diesel exhaust particles, antioxidant, nanoparticles, serum-free media and nanotubes). The biophysical and biochemical properties between control cells and treated cells are distinguished by AFM and RM, respectively, and these biophysical and biochemical differences could be applied as “biomarkers” for identification purpose (e.g. benign and malignant cancer cells, cellular differentiation). Presently, synthesizing multifunctional hybrid nanoparticles (CaMoO₄:Eu@GNR and CaMoO₄:Eu@SiO₂-GNR) with plasmon resonances in the near-infrared (NIR) region ~790 nm and luminescence ~615 nm to offer multimodal capabilities: fluorescence imaging, surface-enhanced Raman spectroscopy detection and photothermal therapy. The biomechanical properties of these nanoparticles-treated cancer cells are evaluated by AFM, and these nanoparticles distribution on cells are identified by RM.

TECHNIQUES: Atomic force microscopy, Raman microspectroscopy, Fourier transform infrared spectroscopy, scanning electron microscopy, fluorescence microscope, flow cytometry, UV-visible spectrometry, Zeta potential, dynamic light scattering, cancer cell culture, nanoparticles synthesize, surface modification.

- **State Key Laboratory of Medical Genetics (Aug'10- Jul'11)**

Dr. Desheng Liang, clone group, Central South University, Changsha, China.

RESEARCH: Involved in the construction of human ribosomal DNA (hrDNA) targeting plasmids with various therapeutic genes and transferred into stem cells, screened stem cells with positive hrDNA for gene therapy purpose.

TECHNIQUES: plasmid transformation and purification, nucleofection, western blotting, gel electrophoresis, MTT, cell screening, mouse stem cells culture.

- **Molecular and Genetic Epidemiology for Chronic Diseases Workshop (Jul'10)**

Prof. Xiao-Ou Shu and other professors, Department of Life Sciences, Fudan University, Shanghai, China.

RESEARCH: Participated in a workshop held by Fudan University and Vanderbilt University; learned the Principles of Molecular Epidemiology, Molecular Epidemiology Methods, Genetic Epidemiology and Genetic Association Studies, Genome-Wide Association Studies (GWAS) and Post-GWAS.

TECHNIQUES: apply bioinformatics software Golden Helix to Genome-Wide Association Studies

- **National Training Base in Life Science and Technology (Feb'09- Jul'10)**

Prof. Pan Qian, molecular and cellular group, Central South University, Changsha, China.

RESEARCH: Having access to peripheral blood for genetic disease diagnosis. Learned the technology of PCR amplification, DNA extraction from peripheral blood; involved with the establishment of genetic disease database, got familiar with experimental instruments, such as ABI 3130 and Genome Analyzer; had a good grasp of chromosome banding technique and the identification of chromosome 320-550 band; and completed the undergraduate thesis: Integration blood coagulation factor FIX into mouse embryonic stem cells by targeting vector of ribosomal gene region.

TECHNIQUES: PCR, qPCR, DNA sequencing, DNA extraction and process, blood cell culture

LIST OF PUBLICATIONS:

1. M. Tang, **Qifei Li**, L. Xiao, Y. Li, J. L. Jensen, T. G. Liou, A. Zhou*, "Toxicity effects of short term diesel exhaust particles exposure to human small airway epithelial cells (SAECs) and human lung carcinoma epithelial cells (A549)", *Toxicology Letters* **215** (2012) 181-192.
2. L. Xiao, M. Tang, **Qifei Li**, A. Zhou*, "Non-invasive detection of biomechanical and biochemical responses of human lung cells to short time chemotherapy exposure using AFM and confocal Raman spectroscopy", *Analytical Methods* **5** (2013) 874-879.
3. S. Swaminathan, M. Bullough, **Qifei Li**, A. Zhou, Y. Cui*, "Non-lithographic patterning of phage-displayed peptides with wrinkled elastomers", *J. of the Royal Society Interface* **11** (2014) 91.
4. R. Li, S. E. Williams, **Qifei Li**, J. Zhang, C. Yang, A. Zhou*, "Photoelectrocatalytic Degradation of Ofloxacin Using Highly Ordered TiO₂ Nanotube Arrays", *Electrocatalysis* **5** (2014) 379-386.
5. **Qifei Li**, E. Suasnavas, L. Xiao, S. Heywood, X. Qi, A. Zhou*, S. C. Isom*, "Label-free and non-invasive monitoring of porcine trophoblast derived cells: differentiation in serum and serum-free media", *J. of Biophotonics* **8** (2015) 638-645.
6. L. Xiao, X. Tian, S. Harihar, **Qifei Li**, L. Li, D. R. Welch, A. Zhou*, "Gd₂O₃-doped silica @ Au Nanoparticles as Probes for In Vitro Cancer Cell Imaging Biomarkers Using Surface-Enhanced Raman Spectroscopy", *J. of Biomedical Optics* (In revision)
7. **Qifei Li**, E. Suasnavas, S. Heywood, L. Xiao, A. Zhou*, S. C. Isom*, "Biochemical, biophysical and genetic changes of porcine trophoblast derived cells during differentiation as evaluated using Raman microspectroscopy, Atomic force microscopy and quantitative polymerase chain reaction", *Genesis, the J. of Genetics and Development* (In revision)

8. **Qifei Li**, L. Xiao, S. Harihar, D. R. Welch, E. Vargis, A. Zhou*, “*In vitro* biophysical, microspectroscopic and cytotoxic evaluation of metastatic and non-metastatic cancer cells in responses to anti-cancer drug”. (**Under review**)
9. **Qifei Li**, M. Tang, A. Zhou*, “Diesel exhaust particles induced human lung carcinoma epithelial cells damage and the structure protective effect of resveratrol”. (**Submitted**)
10. **Qifei Li**, A. K. Parchur, A. Zhou*, “*In-vitro* biomechanical properties, fluorescence imaging, surface-enhanced Raman spectroscopy, and photothermal therapy evaluation of luminescent functionalized CaMoO₄:Eu@Au hybrid nanorods on human lung adenocarcinoma epithelial cells”. (**To be submitted**)
11. A. K. Parchur, **Qifei Li**, A. Zhou*, “Near-infrared photothermal therapy of Prussian blue coated multifunctional CaMoO₄:Eu@SiO₂/Au nanostructures for targeting human epidermal growth factor receptor 2 expressing cancer cells”. (**To be submitted**)

CONFERENCES:

PODIUMS

1. **Qifei Li**, Abdul K. Parchur, Anhong Zhou, “Multifunctional CaMoO₄:Eu-Au hybrid nanorods for photothermal therapy and imaging of human lung adenocarcinoma epithelial cells”, IBE annual meeting. St. Louis, Missouri, March 7, 2015.
2. **Qifei Li**, Abdul K. Parchur, Anhong Zhou, “Multifunctional PEGylated CaMoO₄:Eu@Au core/shell nanoparticles for imaging, surface-enhanced Raman spectroscopy (SERS) detection and photo-thermal therapy (PTT) applications”, *SPIE Photonics West BIOS*. San Francisco, California, February 8, 2015.
3. **Qifei Li**, Sierra Heywood, Edison Suasnavas, Spencer Williams, Ruizhen Li, S. Clay Isom, Anhong Zhou, “Trophoblast derived cells behaviors on TiO₂ nanotube arrays coated with gold nanoparticles (Au NPs-TiO₂ NTs) by Raman spectroscopy, fluorescence microscopy, gene expression”, *245th ACS National Meeting & Exposition*. New Orleans, Louisiana, April 7, 2013.
4. **Qifei Li**, Mingjie Tang, Lifu Xiao, Anhong Zhou, “Q-Plex Array for analysis of cytokines and chemokines: complementary with Raman microspectroscopy for detection of DEP-induced cytotoxicity and anticancer drug interaction”, *Quansys Bioscience Annual Multiplex Assay Conference*. Logan, Utah, March 7, 2013.

POSTERS

1. **Qifei Li**, Abdul K. Parchur, Anhong Zhou, “Near-Infrared Photothermal Therapy of Prussian blue (PB) Coated Multifunctional CaMoO₄:Eu@SiO₂/Au Nanostructures for Targeting Epidermal Growth Factor Receptor (EGFR) Expressing Cancer”, *IBE 20th Annual Conference*. Crowne Plaza St. Louis-Clayton, St. Louis, Missouri. March 5-7, 2015.
2. **Qifei Li**, Abdul K. Parchur, Anhong Zhou, “Multifunctional highly dispersible PEGylated Eu³⁺-doped CaMoO₄@Au-nanorods core/shell nanoparticles for fluorescence imaging, surface-enhanced Raman spectroscopy (SERS) detection, and photo-thermal therapy (PTT) applications of human lung cancer cells”, *SPIE Photonics West BIOS*. The Moscone Center, San Francisco, California. February 7-12, 2015.
3. **Qifei Li**, Sierra Heywood, Lifu Xiao, Mingjie Tang, Anhong Zhou, S. Clay Isom, “Atomic force microscopy (AFM), Raman microspectroscopy (RM) and gene chip monitoring of porcine trophoblast derived cells differentiation”, *SPIE Photonics West BIOS*. The Moscone Center, San Francisco, California. February 7-12, 2015.
4. Lifu Xiao, Abdul K. Parchur, Han Xu, **Qifei Li**, Timothy A. Gilbertson, Anhong Zhou, “Lanthanide (Ln³⁺)-doped calcium molybdate nanoparticle (CaMoO₄:Ln³⁺, Ln=Eu, Tb) based SERS-fluorescence bimodal imaging probes for detection and imaging of fatty acid responsive GPR120 and CD36 receptors”, *SPIE Photonics West BIOS*. The Moscone Center, San Francisco, California. February 7-12, 2015.

5. **Qifei Li**, Lifu Xiao, Anhong Zhou, “Assessment of the anti-cancer drug chemoresistance by Raman microspectroscopy and atomic force microscopy (AFM)”, *SPIE Photonics West BIOS*. The Moscone Center, San Francisco, California. February 1-6, 2014.
6. Lifu Xiao, **Qifei Li**, Anhong Zhou, “Multimodal nano-bioprobes for imaging EGFR on single human cancer cells”, *SPIE Photonics West BIOS*. Moscone Center, San Francisco, California. February 1-6, 2014.
7. **Qifei Li**, Edison Suasnavas, Lifu Xiao, S. Clay Isom, Xiaojun Qi, Anhong Zhou, “Biochemical and biophysical properties of cellular differentiation of transfected porcine trophoblast derived cells by Raman microspectroscopy and atomic force microscopy”, *Institute of Biological Engineering Western Regional Conference*. Utah State University, Logan, Utah. October 26, 2012.
8. **Qifei Li**, Lifu Xiao, Mingjie Tang, Anhong Zhou, “Investigation on the chemoresistance of breast cancer cells with breast cancer metastasis suppressor 1 (BRMS1) by Raman Microspectroscopy and Atomic Force Microscopy (AFM)”, *Intermountain Graduate Research Symposium*. Utah State University, Logan, Utah. April 5-6, 2012.
9. Lifu Xiao, **Qifei Li**, Mingjie Tang, Anhong Zhou, “Probe biomechanical response and cellular biochemical composition changes of human lung epithelial cells to short time chemotherapy drug exposure using AFM and Raman Micro-Spectroscopy”, *Intermountain Graduate Research Symposium*. Utah State University, Logan, Utah. April 5-6, 2012.
10. **Qifei Li**, Mingjie Tang, Yangzhe Wu, Qian Chen, Anhong Zhou, “Diesel exhaust particles induced alterations of cell bio-mechanics and cytoarchitectures in human lung carcinoma epithelial A549”, *Institute of Biological Engineering Western Regional Conference*. Utah State University, Logan, Utah. October 28, 2011.